

UNIVERSITÄT BONN

Physikalisches Institut

Search for Supersymmetry and kinematic endpoint measurement in final states with two tau leptons with the ATLAS detector at the LHC

von
Carolin Zendler

Abstract

Discovery prospects for Supersymmetry in final states with at least two tau leptons and large missing transverse energy are evaluated for LHC proton-proton collisions measured with the ATLAS detector. In a first study based on Monte Carlo simulation, a Supersymmetry signal selection is developed for fully hadronic, semileptonic and fully leptonic di-tau decays in events produced in proton-proton collisions with a center-of-mass energy of $\sqrt{s} = 10$ TeV. The prospects of measuring the kinematic endpoint of the di-tau invariant mass distribution assuming an integrated luminosity of $\int L dt = 1 \text{ fb}^{-1}$ are evaluated for different mSUGRA scenarios along with the discovery reach. In a second study, a search for Supersymmetry in the fully hadronic channel is performed, using $\int L dt = 35 \text{ pb}^{-1}$ of ATLAS data collected with proton-proton collisions at $\sqrt{s} = 7$ TeV between June 24th and October 29th 2010. Two events are observed, which is consistent with the Standard Model background expectation of $N_{\text{SM}} = 0.77 \pm 0.19^{(\text{stat})} {}^{+0.55}_{-0.33} (\text{syst})$. Interpreted in mSUGRA, limits on m_0 and $m_{1/2}$ are set for $\tan\beta = 40$, a positive higgsino mixing parameter and $A_0 = 0$ GeV or $A_0 = -500$ GeV. These limits constitute the first results of SUSY searches with tau leptons within the ATLAS experiment.

Post address:
Nussallee 12
53115 Bonn
Germany



BONN-IR-2011-12
Bonn University
September 2011
ISSN-0172-8741

Angefertigt mit Genehmigung der Mathematisch-Naturwissenschaftlichen Fakultät der
Rheinischen Friedrich-Wilhelms-Universität Bonn

1. Gutachter: Prof. Dr. Klaus Desch
2. Gutachter: Prof. Dr. Jochen Dingfelder

Tag der Promotion: 11.08.2011
Erscheinungsjahr: 2011

Abstract

Discovery prospects for Supersymmetry in final states with at least two tau leptons and large missing transverse energy are evaluated for LHC proton-proton collisions measured with the ATLAS detector. In a first study based on Monte Carlo simulation, a Supersymmetry signal selection is developed for fully hadronic, semileptonic and fully leptonic di-tau decays in events produced in proton-proton collisions with a center-of-mass energy of $\sqrt{s} = 10$ TeV. The prospects of measuring the kinematic endpoint of the di-tau invariant mass distribution assuming an integrated luminosity of $\int L dt = 1 \text{ fb}^{-1}$ are evaluated for different mSUGRA scenarios along with the discovery reach. In a second study, a search for Supersymmetry in the fully hadronic channel is performed, using $\int L dt = 35 \text{ pb}^{-1}$ of ATLAS data collected with proton-proton collisions at $\sqrt{s} = 7$ TeV between June 24th and October 29th 2010. Two events are observed, which is consistent with the Standard Model background expectation of $N_{\text{SM}} = 0.77 \pm 0.19^{(\text{stat})} \begin{smallmatrix} +0.55 \\ -0.33 \end{smallmatrix}^{(\text{syst})}$. Interpreted in mSUGRA, limits on m_0 and $m_{1/2}$ are set for $\tan \beta = 40$, a positive higgsino mixing parameter and $A_0 = 0$ GeV or $A_0 = -500$ GeV. These limits constitute the first results of SUSY searches with tau leptons within the ATLAS experiment.

Zusammenfassung

Das Entdeckungspotential von Supersymmetrie mit Endzuständen aus mindesten zwei Tau Leptonen und fehlender Transversalenergie in Proton-Proton Kollisionen wird untersucht, sowie die Möglichkeit einer Messung des Endpunktes der invarianten Masse der beiden Tau-Leptonen evaluiert. Hierfür werden am LHC erzeugte und mit dem ATLAS-Detektor gemessene Ereignisse verwendet. Eine erste Studie basierend auf Monte Carlo Simulation entwickelt eine Supersymmetrie-Ereignisselektion für voll hadronische, semileptonische und voll leptonische Zerfälle der Tau-Paare für Ereignisse, die in Proton-Kollisionen mit einer Schwerpunktsenergie von $\sqrt{s}=10$ TeV produziert werden. Die Aussicht auf eine erfolgreiche Messung des kinematischen Endpunktes des Spektrums der invarianten Masse der Tau-Paare mit einer integrierten Luminosität von $\int L dt = 1 \text{ fb}^{-1}$ wird in verschiedenen mSUGRA Modellen untersucht und das Entdeckungspotential bestimmt. In einer zweiten Studie werden $\int L dt = 35 \text{ pb}^{-1}$ an ATLAS-Daten ausgewertet, die in Proton-Kollisionen mit $\sqrt{s}=7$ TeV zwischen dem 24. Juni und dem 29. Oktober 2010 aufgenommen wurden, und nach Hinweisen für Supersymmetrie im voll hadronischen Kanal gesucht. Die beobachtete Anzahl selektierter Ereignisse ist mit 2 Ereignissen in guter Übereinstimmung mit der Standardmodellerwartung von $N_{\text{SM}} = 0.77 \pm 0.19^{(\text{stat}) +0.55^{(\text{syst})}_{-0.33}}$ Ereignissen. Dieses Ergebnis wird im mSUGRA Modell interpretiert, und es werden Grenzen für m_0 und $m_{1/2}$ im mSUGRA-Parameterraum mit $\tan\beta = 40$, einem positiven Higgsino-Mischungsparameter und $A_0 = 0$ GeV oder $A_0 = -500$ GeV gesetzt. Dies stellt das erste Ergebnis der ATLAS SUSY Suche mit Tau Leptonen dar.

Contents

1. Introduction	1
2. Supersymmetry	3
2.1. The Standard Model of particle physics	3
2.1.1. Shortcomings of the Standard Model	6
2.2. Supersymmetric extension of the Standard Model	8
2.2.1. Minimal Supersymmetric Standard Model (MSSM)	9
2.2.2. Minimal Supergravity (mSUGRA)	12
2.3. mSUGRA phenomenology	16
2.3.1. Tau final states	19
3. The ATLAS detector at the LHC	21
3.1. The Large Hadron Collider	21
3.1.1. Event topology of proton-proton collisions	23
3.2. The ATLAS Experiment	24
3.2.1. Magnet System	25
3.2.2. The Inner Detector	26
3.2.3. Calorimetry	27
3.2.4. Muon System	29
3.2.5. Forward Detectors	30
3.2.6. Trigger System	31
4. Event simulation and reconstruction	33
4.1. Event generation	33
4.1.1. QCD dijets: PYTHIA	34
4.1.2. SUSY signal events: HERWIG	35
4.1.3. W and Z bosons: ALPGEN	35
4.1.4. Top quark pair production: MC@NLO	35
4.2. Detector simulation	35
4.2.1. Full detector simulation	36
4.2.2. Fast detector simulation	36
4.3. Event reconstruction and definition of physics objects	36
4.3.1. Inner Detector Tracks	37
4.3.2. Jets	37
4.3.3. Tau leptons	39
4.3.4. Electrons	44
4.3.5. Muons	45
4.3.6. Overlap removal	46
4.3.7. Missing transverse energy	46
4.3.8. Derived quantities	47
5. Endpoint measurement of a $\tau\tau$ invariant mass spectrum	49
5.1. Introduction	49
5.2. Di-tau SUSY signature at the LHC	49
5.2.1. Standard Model background	51

5.3.	Invariant mass of two hadronic tau leptons in $\sqrt{s}=14$ TeV collisions	52
5.3.1.	Starting point: previous work	52
5.3.2.	Further developement of the analysis	54
5.4.	Extension to leptonic tau lepton decays in $\sqrt{s}=10$ TeV collisions	57
5.4.1.	Starting point: preceding work regarding (semi-)leptonic spectra	58
5.4.2.	Event selection for $\sqrt{s}=10$ TeV	59
5.4.3.	Endpoint measurement	65
5.4.4.	Systematic uncertainties	67
5.4.5.	Alternative fit method: unbinned maximum likelihood fit	71
5.4.6.	Scan of mSUGRA parameter space	75
5.5.	Summary and conclusions	79
6.	Search for Supersymmetry with $\sqrt{s}=7$ TeV collisions	81
6.1.	Introduction	81
6.2.	Data and Monte Carlo simulated samples	81
6.2.1.	ATLAS data 2010	81
6.2.2.	Monte Carlo simulation	82
6.3.	Tau identification	82
6.4.	Event selection	85
6.4.1.	Trigger	85
6.4.2.	Event cleaning	87
6.4.3.	SUSY event selection	88
6.5.	MC validation with data	92
6.5.1.	QCD background estimation	92
6.5.2.	Non-QCD BG validation	101
6.6.	Systematic uncertainties	104
6.6.1.	Jet energy scale	104
6.6.2.	Jet energy resolution	105
6.6.3.	Tau energy scale and resolution	105
6.6.4.	Tau efficiency and fake rate	106
6.6.5.	Pile-up	108
6.6.6.	Other sources of systematic uncertainties	109
6.7.	Results	109
6.7.1.	Expectations in the signal region	109
6.7.2.	Observation	112
6.7.3.	Interpretation	112
6.8.	Conclusions and Outlook	118
7.	Summary	121
A.	Monte Carlo Datasets	123
A.1.	Samples with $\sqrt{s}=14$ TeV	124
A.1.1.	SUSY benchmark points and SM background	124
A.2.	Samples with $\sqrt{s}=10$ TeV	125
A.2.1.	SUSY benchmark points and SM background	125
A.2.2.	mSUGRA grid ($\sqrt{s}=10$ TeV)	126
A.3.	Samples with $\sqrt{s}=7$ TeV	131
A.3.1.	SUSY benchmark points and SM background	131
A.3.2.	mSUGRA grid ($\sqrt{s}=7$ TeV)	132
B.	Supplementing material	135
B.1.	Addition to chapter 5	135
B.1.1.	Cut-flow ($\sqrt{s}=10$ TeV)	135

B.1.2. Significance Z_n in different mSUGRA regions ($\sqrt{s}=10$ TeV selection) . .	136
B.2. Addition to chapter 6	138
B.2.1. Systematic uncertainties and cut-flow ($\sqrt{s}=7$ TeV)	138
C. mSUGRA limits	141
C.1. Limits from B decays	141
C.2. Limits from other ATLAS SUSY search channels	142
D. One-tau and semileptonic event selection	143
D.1. Tau identificaon	143
D.2. SUSY event selection	143
D.2.1. One-tau channel	143
D.2.2. Semileptonic channel	144

1. Introduction

*We shall not cease from exploration
And the end of all our exploring
Will be to arrive where we started
And know the place for the first time.*

- T.S. Eliot, Little Gidding

According to the Big Bang theory, particles were created from energy in an early stage of the hot expanding universe, and combined to form matter as the universe cooled off. Initial matter density fluctuations led to gravitational accumulation, causing stars to ignite and to produce elements which later built the Earth, and forming the structure of galaxy filaments and voids observed today.

It is deeply rooted in human nature to ask questions like “what is the world made of?” and “where does it come from?”. Both the humanities and natural sciences seek to describe the diversity of Nature from a set of fundamental principles. Yet while philosophy is constrained to reason, physics can employ experiments to test the accuracy of its theories.

With ever higher center-of-mass energies, high-energy particle colliders probe deeper into the structure of matter, an evolution culminating in the Large Hadron Collider (LHC) at the European Organization for Nuclear Research (CERN). The LHC began to deliver proton-proton collisions with a center-of-mass energy of $\sqrt{s} = 7$ TeV in March 2010. When operating at its design performance it will produce collisions with twice that energy, enabling the investigation of particle behaviour under conditions realized early in the universe, about 10^{-12} seconds after the Big Bang. The LHC experiments have thus started exploring the so-called *terascale*, an energy regime in which not only new physics theories are expected to reveal themselves, but also the last missing piece of the Standard Model of particle physics must be found, or the Standard Model has to be fundamentally revised.

The Standard Model contains the current knowledge of elementary particles and their interactions in a quantum field theory describing three out of the four fundamental forces: the electromagnetic, the weak and the strong force. It is able to compute electroweak particle physics processes with remarkable precision, and all particles it has predicted have been observed but for one exception: the Higgs boson, which is needed to allow for particle masses. All properties of the Higgs boson are predicted by the Standard Model save its mass, but experimental lower bounds and theoretical upper bounds place the possible Higgs mass right within the reach of the LHC.

However, some questions remain unanswered by the Standard Model, therefore it is assumed to be an effective approximation of a more fundamental underlying theory. For example, the known particles of the Standard Model seem to account for only about 5 % of the energy density in the universe, the strong force is not yet described in a unified way with the electroweak theory, gravity is not included at all, and the Higgs boson is sensitive to large radiative corrections implying an unnatural fine-tuning in order to stabilize its mass.

One possible extension to the Standard Model is Supersymmetry, which elegantly solves some of the most pressing problems of the Standard Model through the introduction of a symmetry between fermions and bosons such that every particle has a supersymmetric partner particle with identical mass and quantum numbers but a spin differing by $\frac{1}{2}$. This causes the fermionic and bosonic contributions to the Higgs mass corrections to cancel exactly, and thus avoids the fine-tuning problem mentioned above. Furthermore, the energy dependence of the coupling constants,

which depends on the particle content of a theory, is altered by the additional supersymmetric particles such that the electromagnetic, weak and strong coupling can be united at a high energy scale. In addition, those Supersymmetry models which contain a well motivated symmetry called *R-parity* predict a stable massive particle constituting an ideal candidate for Dark Matter, thus possibly describing up to another 23 % of the energy density of the universe.

Supersymmetry has already been searched for at the electron-positron collider LEP and at the proton-antiproton collider Tevatron, as well as implicitly in direct and indirect Dark Matter searches. Since supersymmetric partners of the known particles have not been observed so far, the symmetry must be broken and the supersymmetric partner particles must be too heavy to be within the reach of former collider experiments. If the masses of these new particles are heavier than the masses accessible at the LHC, however, Supersymmetry loses its capacity to solve the fine-tuning problem it is designed for. Thus assuming these particles are light enough to be produced at the LHC, and further assuming they respect R-parity conservation, they are expected to be produced in pairs at the LHC and decay successively into Standard Model particles and the lightest supersymmetric particle, which is stable and leads to a characteristic signature of missing energy.

Decays into the supersymmetric partner of the tau lepton might be favoured in Supersymmetry depending on the parameters of the theory, leading to an enhanced production of tau leptons at the LHC. Besides the contribution to a discovery of Supersymmetry, tau lepton final states can further be exploited to obtain information not accessible otherwise.

In this thesis, final states with tau leptons accompanied by large missing transverse energy are investigated in order to search for evidence for the existence of supersymmetric particles, as well as to extract information about the underlying supersymmetric model by measuring the kinematic endpoint of the di-tau invariant mass. While the latter is completely based on Monte Carlo simulation, the former uses an integrated luminosity of 35 pb^{-1} of proton-proton collisions recorded by the ATLAS detector between June and October 2010. This study includes the first results of Supersymmetry searches with tau leptons using ATLAS data.

In *chapter 2*, an introduction to Supersymmetry is given, *chapter 3* describes the ATLAS detector at the LHC accelerator, and *chapter 4* explains how processes occurring in proton-proton collisions at the LHC can be simulated and how physics objects are reconstructed from detector signals. *Chapter 5* uses Monte Carlo simulated data to investigate the prospects of a kinematic endpoint measurement in di-tau spectra in the fully hadronic, the semileptonic and the fully leptonic decay channel. In *chapter 6*, a Supersymmetry signature is searched for in the fully hadronic di-tau channel with ATLAS data recorded in 2010.

2. Supersymmetry

Today's knowledge of elementary particles and interactions between them is theoretically formulated in the so-called Standard Model of particle physics, a theory capable of describing almost all phenomena observed in the context of particle physics experiments with formidable precision. There are, however, essential shortcomings such as e.g. the fact that particles described by the Standard Model only account for less than 5% of the total energy density of the universe. Out of several extensions to the Standard Model that have been proposed, Supersymmetry solves the most pressing problems of this theory in an elegant way: it assumes a symmetry between fermions and bosons, which constitute matter particles and force carriers and are therefore fundamentally different particles in the Standard Model.

In the following, the Standard Model will shortly be recapitulated, motivating the necessity of an extension by slightly emphasizing its shortcomings in the first part of this chapter. More detailed information than possible in this context can be found in the respective literature, e.g. [1, 2]. The second part gives an introduction to supersymmetric models, concentrating on the so-called minimal Supergravity model, which has promising signatures that are in reach of the LHC. A more elaborate derivation of supersymmetry can be found for example in [3, 4]. The phenomenology expected in proton-proton collisions at centre-of-mass energies realized at the LHC will be described in the third part of this chapter.

2.1. The Standard Model of particle physics

The Standard Model of particle physics (SM) describes properties and behaviour of point-like elementary particles, the interactions of which in principle determine all physics processes. The mathematical description is a $SU(3)_C \otimes SU(2)_L \otimes U(1)_Y$ gauge theory, in which particles are represented by quantum fields and forces are determined by symmetries of the action.

Elementary particles can be classified as force carriers, so-called bosons with integer spin, or matter particles, so-called fermions with half-integral spin. The force carriers of the electromagnetic, the strong and the weak interaction are photons, gluons and the Z and W bosons, respectively. Fermions can further be classified as leptons, which are electrically charged, quarks which are additionally coloured, and neutrinos which are neither but interact only via the weak force. All known fermions can be ordered into three families, the first of which builds up all stable matter. Particles of the second and third family differ from their corresponding first generation partners only by their masses, which vary over several orders of magnitude and cannot be predicted by the Standard Model, but are free parameters which have to be measured experimentally. Masses are generated by the Higgs mechanism, which is incorporated in the Standard Model but predicts one particle that has not been experimentally confirmed yet, the Higgs boson.

The gravitational force could not be integrated in the formalism of particle physics so far. In proton-proton interactions at the LHC, however, gravitation is negligibly small¹ compared to the other, aforementioned forces, so it will not be treated explicitly in the following.

The particle content of the Standard Model is summarized in table 2.1. Not shown are different quark color states, and antiparticles of the fermions, which are charge conjugate but otherwise have the same characteristics as their partners.

¹Some extensions to the Standard Model assume the existence of extra dimensions, thereby opening the possibility for measurable gravitational effects at the LHC.

			Q	T_3
$\begin{pmatrix} \nu_e \\ e \end{pmatrix}_L$	$\begin{pmatrix} \nu_\mu \\ \mu \end{pmatrix}_L$	$\begin{pmatrix} \nu_\tau \\ \tau \end{pmatrix}_L$	0	$\frac{1}{2}$
e_R	μ_R	τ_R	-1	$-\frac{1}{2}$
$\begin{pmatrix} u \\ d \end{pmatrix}_L$	$\begin{pmatrix} c \\ s \end{pmatrix}_L$	$\begin{pmatrix} t \\ b \end{pmatrix}_L$	-1	0
u_R	c_R	t_R	$\frac{2}{3}$	$\frac{1}{2}$
d_R	s_R	b_R	$-\frac{1}{3}$	$-\frac{1}{2}$

(a) SM fermions.

	effect	spin
γ	electromagn. force	1
W^\pm, Z^0	weak force	1
$g_i, i \in \{1, 8\}$	strong force	1
H	mass	0

(b) SM gauge and higgs bosons.

Table 2.1. – Particle content of the Standard Model.

The classification of particles with respect to their spin and interactions as described above can be derived phenomenologically, yet also follows from the mathematical formulation of the Standard Model in the framework of Lagrangian field theory: by replacing the discrete generalized coordinates q_i, \dot{q}_i of the classical Lagrange formalism with continuous fields $\Phi_i, \partial_\mu \Phi_i$, i.e. $L(q_i, \dot{q}_i, t) \rightarrow \mathcal{L}(\Phi_i, \partial_\mu \Phi_i, t)$, the transition to relativistic field theory can be made in analogy to classical mechanics, with the Euler-Lagrange equations of motion following from the variation of the action $S = \int \mathcal{L} d^4x$. (The Lagrangian density \mathcal{L} is usually called Lagrangian only for simplicity.)

Interactions are now derived from the principle of local gauge invariance: when demanding e.g. the Lagrangian of a free fermion field $\mathcal{L} = \bar{\Psi}(i\gamma^\mu \partial_\mu - m)\Psi$ to be invariant under local phase transformations $\Psi \rightarrow \Psi' = e^{i\alpha(x)} \Psi$, it has to be modified to $\mathcal{L} = \bar{\Psi}(i\gamma^\mu D_\mu - m)\Psi$ with the covariant derivative $D_\mu = \partial_\mu + igA_\mu(x)$ introducing a vector field $A_\mu(x)$ which has to transform as $A_\mu(x) \rightarrow A'_\mu(x) = A_\mu(x) - \frac{1}{g}\partial_\mu \alpha(x)$ to cancel terms that otherwise prevent phase invariance of the Lagrangian. Here, Ψ is a four-component spinor, $\bar{\Psi} = \Psi^\dagger \gamma_0$ its adjoint and m the mass of the fermion. Transformations $U(x) = e^{i\alpha(x)}$ form the unitary abelian group $U(1)$. Imposing local gauge invariance on the Lagrangian of a free fermion thus necessitates an additional interaction term $-g\bar{\Psi}\gamma^\mu A_\mu \Psi$, which in quantum electrodynamics (QED) describes the interaction of a fermion field via a vector coupling γ^μ to a photon field A_μ , and g can be interpreted as coupling strength and identified with the electric charge Q . Interpretation of A_μ as photon field only holds if a kinetic term of the photon is added, which takes the form $-\frac{1}{4}F^{\mu\nu}F_{\mu\nu}$ with the field strength tensor $F_{\mu\nu} = \partial_\mu A_\nu - \partial_\nu A_\mu$. An additional mass term $m^2 A_\mu A^\mu$ would violate gauge invariance, thus the photon stays massless.

Similarly, electroweak interactions can be described by transformations under the group $SU(2)_L \otimes U(1)_Y$, where the $U(1)$ part is now formulated via the weak hypercharge Y , which is related to the electrical charge Q and the weak isospin T_3 by $Q = T_3 + \frac{Y}{2}$. $SU(2)_L$ acts only on left-handed fermions, while $U(1)_Y$ does not differentiate between left- and right-handed particles. The four gauge fields arising from this theory, an $SU(2)$ triplet $W^{1,2,3}$ and a $U(1)$ singlet B , form the experimentally observed gauge bosons W^\pm, Z and γ via the Weinberg angle θ_W :

$$W_\mu^\pm = \frac{1}{\sqrt{2}}(W_\mu^1 \mp iW_\mu^2) \quad (2.1)$$

$$\begin{pmatrix} A_\mu \\ Z_\mu \end{pmatrix} = \begin{pmatrix} \cos \theta_W & -\sin \theta_W \\ \sin \theta_W & \cos \theta_W \end{pmatrix} \begin{pmatrix} B_\mu \\ W_\mu^3 \end{pmatrix}. \quad (2.2)$$

Since $SU(2)$ is non-abelian, the corresponding gauge bosons are self-interacting.

Again, the absolute value of θ_W is not predicted by the theory, but has to be determined experimentally.

The strong force can be described by $SU(3)_C$ transformations, leading to a gluon octet. Due to the non-abelian nature of $SU(3)$, the gluons are colored and show self-coupling. Quarks are

color triplets, while other fermions are color singlets. Color eigenstates of quarks are not identical to electroweak eigenstates, but are related via the Cabibbo-Kobayashi-Maskawa (CKM) matrix.

Higgs mechanism

As mentioned above, inserting mass terms in the Standard Model Lagrangian leads to a violation of local gauge invariance. Since most particles of the Standard Model are experimentally known to be massive, this model is inconsistent with experimental observation if masses cannot be generated in a gauge invariant manner.

In the Higgs mechanism, particles gain their masses by coupling to a scalar field, the Higgs field. A complex $SU(2)$ -doublet Φ with four degrees of freedom

$$\Phi(x) = \sqrt{\frac{1}{2}} \begin{pmatrix} \Phi_1(x) + i\Phi_2(x) \\ \Phi_3(x) + i\Phi_4(x) \end{pmatrix} \quad (2.3)$$

and the potential

$$V(\Phi) = \mu^2 |\Phi(x)|^2 + \lambda |\Phi(x)|^4 \quad (2.4)$$

are postulated, leading to the Lagrangian

$$\mathcal{L} = |D_\mu \Phi(x)|^2 - V(\Phi) = |D_\mu \Phi(x)|^2 - \left(\mu^2 |\Phi(x)|^2 + \lambda |\Phi(x)|^4 \right). \quad (2.5)$$

For $\mu^2 < 0$ and $\lambda > 0$, the potential 2.4 is minimal at

$$\Phi^\dagger(x)\Phi(x) = \frac{1}{2}(\Phi_1(x)^2 + \Phi_2(x)^2 + \Phi_3(x)^2 + \Phi_4(x)^2) = -\frac{\mu^2}{2\lambda} \equiv v^2. \quad (2.6)$$

In order to use perturbation theory, a particular minimum has to be chosen about which $\Phi(x)$ can be expanded. It is common to choose $\Phi_1(x) = \Phi_2(x) = \Phi_4(x) = 0$, $\Phi_3(x) = v$, which after expansion yields

$$\Phi(x) = \sqrt{\frac{1}{2}} \begin{pmatrix} 0 \\ v + H(x) \end{pmatrix} \quad (2.7)$$

with a scalar field $H(x)$. Since the symmetry under $SU(2)$ which was obvious in equation 2.6 is now hidden, fixing a particular ground state is called spontaneous symmetry breaking.

Inserting Φ into the Lagrangian leads to the required mass terms for the W and Z bosons,

$$\frac{1}{2} \left(\frac{vg}{2} \right)^2 \left(2W_\mu^- W^{\mu+} + \frac{Z_\mu Z^\mu}{\cos^2 \theta_W} \right), \quad (2.8)$$

with $m_W = \frac{vg}{2}$ and $m_Z = \frac{vg}{2 \cos \theta_W} = \frac{m_W}{\cos \theta_W}$. Additionally, the term $-\frac{1}{2}(2\lambda v^2)H^2(x)$ is generated, which describes a scalar particle with mass $m_H = \sqrt{2\lambda v^2}$, the Higgs boson.

Fermion masses can now be generated via coupling to the Higgs field, where the strength of this Yukawa coupling defines the mass. However, these couplings have to be inserted into the Lagrangian “by hand” rather than following directly from the Higgs mechanism, and the coupling constants are free parameters of the model to be determined by experiment. Furthermore, the Higgs boson predicted by this mechanism has yet to be discovered.

The mass of the Standard Model Higgs boson is theoretically constrained by unitarity conditions in WW scattering and by electroweak precision measurements of the W and top quark mass to be around the weak scale [5]. This places the Standard Model Higgs boson in direct reach of the LHC experiments.

An experimental lower bound on the Higgs mass is given by LEP experiments with 114.4 GeV at 95 % C.L. [6], and the Tevatron has excluded Higgs masses between 158 GeV and 175 GeV with 95 % C.L. [7].

Combining electroweak precision measurements with these results of direct Higgs searches, a global fit yields a most probable Higgs mass of $m_H = 120.6^{+17.0}_{-5.2}$ GeV [8, 9].

2.1.1. Shortcomings of the Standard Model

Although the Standard Model can successfully describe most observed phenomena with high precision, the need for an underlying theory at high energies becomes obvious in some details described in this section. Supersymmetry (SUSY) extends the Standard Model such that some of the most pressing problems are addressed.

While the Higgs mechanism is necessary to complete the Standard Model by introducing particle masses, it also causes its most profound problem: the Higgs boson predicted by this theory introduces loop corrections that are quadratically divergent in a cut-off scale Λ . Dirac fermions with mass m_f and coupling λ_f to the Higgs field contribute mass correction terms

$$\Delta m_H^2 = \frac{|\lambda_f|^2}{16\pi^2} (-2\Lambda^2 + 6m_f^2 \ln \frac{\Lambda}{m_f} + \dots) . \quad (2.9)$$

The cut-off scale Λ has to be introduced as upper limit when integrating over all possible four-momenta in the loop to keep the integral finite, and can therefore be interpreted as the scale up to which the Standard Model Lagrangian \mathcal{L}_{SM} describes physics processes correctly. A problem arises if the Standard Model is not the final theory, which is generally believed to be the case due to evidence described below. If the Standard Model is valid up to very high energies, e.g. the Planck mass, independent loop contributions to Δm_H^2 of the order m_{plank}^2 have to nearly exactly cancel the bare Higgs mass $m_{H,0}$ in all orders of perturbation theory to give a finite Higgs mass of $\lesssim 1$ TeV, as required by the constraints described above. This is referred to as the *fine-tuning* or *hierarchy problem*.

If the scale Λ is small, so are the mass correction terms, but this means that the Standard Model is only valid up to this scale and a new, underlying theory has to come into effect then. If any symmetry or method that remedies the hierarchy problem is not exact in the low-energy limit, it has to be kept in mind that it must take effect at this scale, which leads to constraints on e.g. the Supersymmetry breaking scale. Supersymmetry avoids an infinite Higgs mass by introducing new scalar particles, which give additional mass correction terms

$$\Delta m_H^2 = \frac{\lambda_S}{16\pi^2} (\Lambda^2 - 2m_S^2 \ln \frac{\Lambda}{m_S} + \dots), \quad (2.10)$$

with analog denotation as above [3]. Fermionic and bosonic loops corresponding to these correction terms are shown in figure 2.1(a). Forcing the total number of bosonic and fermionic degrees of freedom to be equal, contributions from 2.9 and 2.10 quadratic in Λ exactly cancel in supersymmetric theories. Every fermion is accompanied by two complex scalars with $\lambda_S = |\lambda_f|^2$.

The large number of free parameters in the Standard Model poses another problem, which is no direct contradiction to observation but simply unsatisfying and a hint that there might be an underlying model. This is also incorporated in the standard model of cosmology, in which the fundamental forces are assumed to have been unified in the very early universe after the Big Bang, and separated with the cooling of the expanding universe to the ones observed today. It should be possible to formulate a theory in which the electroweak and strong force are described in a unified way. The energy dependence of the coupling constants of the electromagnetic, the weak and the strong force should therefore be such that the constants get the same value at some high energy scale², the so-called GUT scale at which this Grand Unified Theory comes into effect. In the Standard Model, the unification of coupling constants is not realized, while in Supersymmetry models it is possible, as illustrated in figure 2.1(b). The energy dependence of the coupling constants is caused by loop diagrams, therefore it is sensitive to the number of particles in the theory which contribute to these loops. In SUSY models, additional SUSY particles \tilde{X} affect the coupling constants above an energy of $Q^2 > M_{\tilde{X}}^2$. For $M_{\tilde{X}} \lesssim 1$ TeV, the couplings meet at 10^{16} GeV.

²While there is no reason to assume that these three couplings meet at the same energy scale, rather than two of them being unified first and building an intermediate coupling which is unified with the third one at an even higher energy scale, it is theoretically the simplest approach.

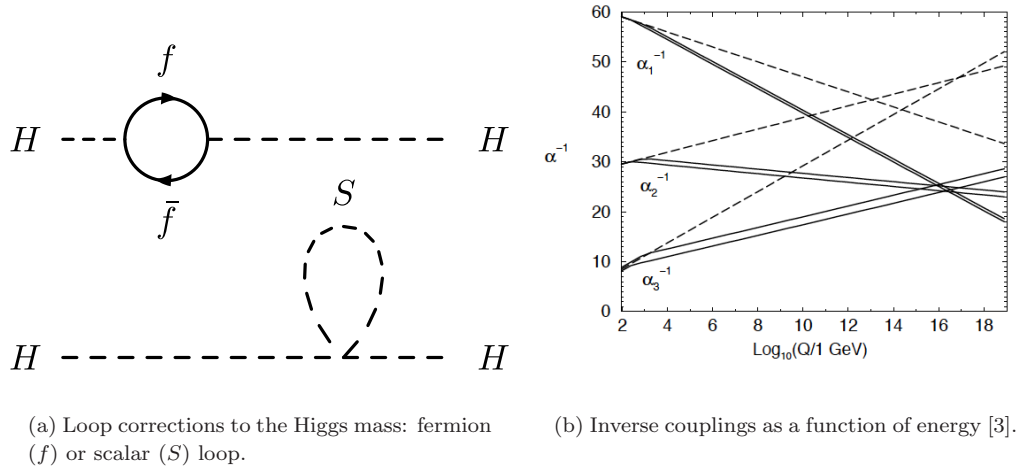


Figure 2.1. – Illustration of the hierarchy problem (a) and the unification of coupling constants (b): energy dependence of electromagnetic (α_1), weak (α_2) and strong (α_3) coupling in the Standard Model (dashed) compared to the MSSM (solid), up to two-loop effects. Two sparticle mass thresholds $M_{\tilde{X}}$ are shown: 250 GeV and 1 TeV.

The existence of at least one elementary particle yet unknown is made obvious by the so-called Dark Matter problem, a term which describes the fact that baryonic matter described by the Standard Model only accounts for $(4.58 \pm 0.16)\%$ of the total energy density of the universe, known from the cosmic microwave background measured by WMAP [10]. While SUSY cannot account for the $(72.5 \pm 1.6)\%$ assigned to Dark Energy, it is able to furnish a candidate for the $(22.9 \pm 1.5)\%$ Dark Matter in models with a well motivated mechanism for keeping the lightest supersymmetric particle (LSP) stable. Measurements with gravitational lensing and structure formation processes give constraints on the relic density of the Dark Matter, and therefore bounds on the mass and couplings of the LSP which have to be addressed when constructing a SUSY model.

The excess of baryonic matter itself is another fact the Standard Model lacks an explanation for: in order to get an excess in matter above antimatter to avoid total annihilation in the early universe, CP violation is one necessary (yet not sufficient) condition. The only source of such a matter-antimatter asymmetry in the Standard Model, the CP violating phase of the CKM matrix, is too small to explain the amount of matter observed today. Supersymmetry contains additional CP violating phases.

Furthermore, the Standard Model cannot be the most fundamental theory since it fails to include gravity, which is not necessary at low energy scales as the gravitational force there is much weaker than the other forces and can safely be ignored. On the Planck scale, however, gravitational effects are not negligible and hence necessitate a theory of quantum gravity. Requiring SUSY to be a local symmetry naturally introduces gravity [11]. Moreover, Supersymmetry is part of superstring theory, which also includes a quantum theory of gravity.

In summary, Supersymmetry is a well motivated extension of the Standard Model that might yield the best description of physics processes observable today. It does not constitute the most fundamental theory possible, since it also leaves unanswered questions like the reason for the observed number of particle families or the great amount of free parameters not determined by the theory, but it provides one step forward: the extension to the TeV scale which is going to be probed by the LHC experiments.

2.2. Supersymmetric extension of the Standard Model

The instability of the Higgs boson mass is caused by quadratically divergent terms with different sign for fermion and boson loops, therefore an ansatz to solve the hierarchy problem that presents itself is to assume a symmetry that relates fermions and bosons such that every fermionic term is cancelled by a bosonic term. Supersymmetry describes transformations from boson states into fermion states and vice versa: $Q|\text{fermion}\rangle \propto |\text{boson}\rangle$ and $Q|\text{boson}\rangle \propto |\text{fermion}\rangle$. Fermions and bosons related in this way are called superpartners. The supersymmetric generators Q have to be of half-integral spin and can be described by two-component spinors which satisfy

$$\{Q, \bar{Q}\} = -2\gamma_\mu P^\mu \quad (2.11)$$

$$\{Q, Q\} = \{\bar{Q}, \bar{Q}\} = [Q, P^\mu] = 0, \quad (2.12)$$

where \bar{Q} is the hermitian conjugate of Q , P^μ the four-momentum generator of spacetime translations and γ_μ are Dirac matrices. Principally, more than one SUSY generator Q is mathematically possible, but such “extended” supersymmetry theories are not capable of describing observations without introducing extra dimensions [3], so they are not considered here.

The irreducible representation of the SUSY algebra are so-called supermultiplets with equal numbers of bosonic and fermionic degrees of freedom. Therefore, Standard Model fermions have two SUSY partner particles, one for each spin degree of freedom, which are called left- and right-handed $\tilde{f}_{L,R}$ despite their scalar nature according to the chirality of the Standard Model particle. An exception are third generation particles, which have a large left-right-mixing due to their large Yukawa couplings, so their mass eigenstates can be significantly different from their gauge eigenstates and are called $\tilde{f}_{1,2}$, with the subscript 1 denoting the lower mass. A supermultiplet consisting of one two-component Weyl fermion and a complex scalar field is called *chiral* supermultiplet, while a combination of a gauge boson with its spin-1/2 superpartner is called *gauge* supermultiplet. In unbroken SUSY, particles of the same multiplet must have the same mass since Q, \bar{Q} commute with P^2 . Since the SUSY generators also commute with those of the gauge transformations, superpartners must also have the same electrical charge, weak isospin and color. The spin thus remains the only characteristic in which superpartners differ.

Superpartners of fermions are called sfermions, so e.g. the partner of an electron e is a scalar called selectron \tilde{e} , while superpartners of bosons are denoted with the suffix “-ino”, so e.g. the SUSY partner of a gluon is a gluino \tilde{g} . Partners of spin-1 bosons carry spin $\frac{1}{2}$.

particles		spin 0	spin $\frac{1}{2}$	$SU(3)_C, SU(2)_L, U(1)_Y$	mass eigenstates
(s)quarks	Q	$(\tilde{u}_L \ \tilde{d}_L)$	$(u_L \ d_L)$	$(\mathbf{3}, \mathbf{2}, \frac{1}{6})$	$u, \tilde{u}_{L,R}, d, \tilde{d}_{R,L}$
	\bar{u}	\tilde{u}_R^*	u_R^\dagger	$(\bar{\mathbf{3}}, \mathbf{1}, -\frac{2}{3})$	$c, \tilde{c}_{L,R}, s, \tilde{s}_{R,L}$
	\bar{d}	\tilde{d}_R^*	d_R^\dagger	$(\bar{\mathbf{3}}, \mathbf{1}, \frac{1}{3})$	$t, \tilde{t}_{1,2}, b, \tilde{b}_{1,2}$
(s)leptons	L	$(\tilde{\nu} \ \tilde{e}_L)$	$(\nu \ e_L)$	$(\mathbf{1}, \mathbf{2}, -\frac{1}{2})$	$e, \tilde{e}_{L,R}, \mu, \tilde{\mu}_{R,L}, \nu_{e,\mu}$
	\bar{e}	\tilde{e}_R^*	e_R^\dagger	$(\mathbf{1}, \mathbf{1}, \mathbf{1})$	$\tau, \tilde{\tau}_{1,2}, \nu_\tau, \tilde{\nu}_\tau, \tilde{\nu}_{e,\mu}$
higgs(inos)	H_u	$(H_u^+ \ H_u^0)$	$(\tilde{H}_u^+ \ \tilde{H}_u^0)$	$(\mathbf{1}, \mathbf{2}, \frac{1}{2})$	h, H, H^\pm, A
	H_d	$(H_d^0 \ H_d^-)$	$(\tilde{H}_d^0 \ \tilde{H}_d^-)$	$(\mathbf{1}, \mathbf{2}, -\frac{1}{2})$	
winos, W bosons		$\tilde{W}^\pm \ \tilde{W}^0$	$W^\pm \ W^0$	$(\mathbf{1}, \mathbf{3}, \mathbf{0})$	$\tilde{\chi}_{1,2}^\pm, \tilde{\chi}_{1,2,3,4}^0$ W^\pm, Z, γ
bino, B boson		\tilde{B}^0	B^0	$(\mathbf{1}, \mathbf{1}, \mathbf{0})$	
gluon, gluino		\tilde{g}	g	$(\mathbf{8}, \mathbf{1}, \mathbf{0})$	g, \tilde{g}

Table 2.2. – Chiral and gauge supermultiplets of the MSSM. Only the first family of (s)quarks and (s)leptons is shown but for the mass eigenstates. Right-handed (s)quarks and (s)leptons appear as conjugates due to the convention of defining chiral supermultiplets in terms of left-handed Weyl spinors.

2.2.1. Minimal Supersymmetric Standard Model (MSSM)

The minimal supersymmetric extension of the Standard Model (MSSM) is constructed such that a minimal number of additional fields is introduced, but omitting terms which violate lepton number L or baryon number B . The superpotential of the MSSM hence reads [3]

$$W_{MSSM} = \mathbf{y}_u \bar{u} Q H_u - \mathbf{y}_d \bar{d} Q H_d - \mathbf{y}_e \bar{e} L H_d + \mu H_u H_d, \quad (2.13)$$

where Q , \bar{u} , \bar{d} , L , \bar{e} , H_u and H_d are each chiral superfields that contain Standard Model particles and their superpartners (see table 2.2), and the Yukawa coupling parameters $\mathbf{y}_{u,d,e}$ are 3×3 matrices in family space. The first term includes e.g. a $t_R^\dagger t_L H_u^0$ term and a $t_R^\dagger \tilde{t}_L \tilde{H}_u^0$ term with the same top quark yukawa coupling strength y_t . The superpotential enters the Lagrangian in the form

$$\mathcal{L}_{int} = - \left(\frac{1}{2} W^{ij} \Psi_i \Psi_j + W^i W_i^* \right) + c.c. \quad (2.14)$$

with

$$W^i = \frac{\partial W}{\partial \phi_i} \text{ and } W^{ij} = \frac{\partial^2 W}{\partial \phi_i \partial \phi_j}$$

to describe interactions between members of the chiral supermultiplets, where Ψ_i and ϕ_i are fermion and scalar fields, respectively, with the index i running over all gauge and flavour degrees of freedom.

The Superpotential also enters the description of free chiral supermultiplets, where a non-propagating complex auxiliary field F_i has to be introduced in order to make the SUSY algebra close off-shell, adding a so-called ‘‘F-term’’ $F^{*i} F_i$ to the Lagrangian. Using the classical equations of motions, this field can be identified as $F_i = -W_i^*$ and $F^{*i} = -W^i$.

Expression 2.14 is the most general form of an interaction Lagrangian under the conditions of renormalizability and invariance under both gauge and supersymmetry transformations. The latter condition leads to the requirement that W^{ij} must be analytic in the complex scalar fields ϕ_i , which becomes important when considering electroweak symmetry breaking in the MSSM.

The Yukawa couplings from the superpotential and the last term of 2.13 combine in the second term of \mathcal{L}_{int} to form (scalar)³ couplings. Terms containing $\mu^* y_u \tilde{u}_R^* \tilde{u}_L H_d^{0*}$, $\mu^* y_d \tilde{d}_R^* \tilde{d}_L H_u^{0*}$ and $\mu^* y_e \tilde{e}_R^* \tilde{e}_L H_u^{0*}$ arise, which correspond to left-right mixing when H_d^0 , H_u^0 get vacuum expectation values (VEVs). This mixing is proportional to the Yukawa coupling strength known from the Standard Model, which is largest for third generation quarks and leptons and so leads to largest left-right-mixing for third generation SUSY partners, while the mixing in the first two generations is negligible. This is the reason why taus play a special role in SUSY searches in models with large mixing.

Unlike the Standard Model, where B- or L-violating terms would make the theory non-renormalizable, in a SUSY theory such terms are in principle possible:

$$W_{RPV} = \frac{1}{2} \lambda^{ijk} L_i L_j \bar{e}_k + \lambda'^{ijk} L_i Q_j \bar{d}_k + \mu'^i L_i H_u + \frac{1}{2} \lambda''^{ijk} \bar{u}_i \bar{d}_j \bar{d}_k. \quad (2.15)$$

Here, $i, j, k = 1, 2, 3$ are family indices. The first three terms violate lepton number, the last term violates baryon number. Due to vertices shown in figures 2.2(a) and 2.2(b) from the couplings of the second and fourth term, the proton could decay via $p^+ \rightarrow e^+ \pi^0$ diagrams as shown in figure 2.2(c), which implies that either λ' or λ'' or both have to vanish.

Since no B or L violating processes have been observed in nature, these terms are eliminated from the MSSM Lagrangian by a new symmetry, R-parity³, involving a conserved multiplicative quantum number $R = (-1)^{3(B-L)+2s}$. While R-parity conservation (RPC) is closely related to baryon and lepton number conservation, it is noteworthy that R is still conserved if B and L are separately violated, as long as $(B - L)$ is conserved. Standard Model particles have an

³The discrete R-parity might be a remnant of a continuous $U(1)_{B-L}$ R-invariance, which is broken in order to allow for gluino masses [12].

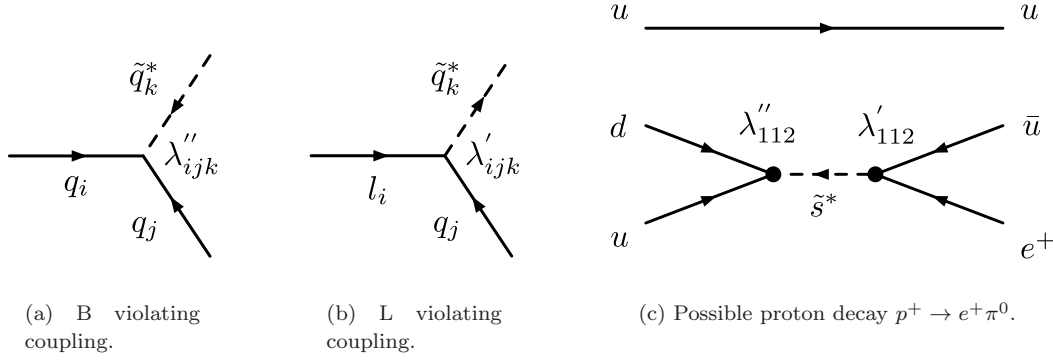


Figure 2.2. – Baryon and lepton number violating couplings possible in the MSSM superpotential and consequential proton decay example.

R-parity of +1, while their SUSY partners are R-odd. Hence R-parity conservation forbids a direct exchange of sfermions between Standard Model fermions, and thus stabilizes the proton. As a further consequence, SUSY particles can only be produced in pairs and only decay in R-parity odd states, which in turn requires the lightest supersymmetric particle (LSP) to be stable. RPC SUSY theories thus naturally contain a candidate for (cold) Dark Matter, solving another basic problem of the Standard Model. It should however be noted that R-parity is not necessarily needed to keep the proton stable, demanding *B* or *L* conservation suffices since $p^+ \rightarrow e^+ \pi^0$ is violating both. The theoretically best motivated alternative is baryon triality [13], which effectively conserves *B* and violates *L*. In R-parity violating SUSY (RPV) theories, an independent solution to the Dark Matter problem is needed. If the now non-stable LSP decays within the detector or is charged, the phenomenology at collider experiments is drastically different, therefore this thesis limits itself to RPC SUSY.

In the MSSM, two separate Higgs doublets are needed to give mass to the up- and down-type quarks: the superpotential must be analytic in the chiral superfields in order to get a Lagrangian that is invariant under supersymmetric transformations, therefore the hermitian conjugate of one Higgs superfield cannot be used (as is the case in the Standard Model). Another argument for two Higgs doublets arises from gauge anomalies associated with fermion triangle diagrams, which are introduced by a single Higgsino doublet and must be cancelled by a second one with opposite hypercharge [14]. From the eight degrees of freedom introduced by two complex doublets, three become longitudinal states of the Z and W^\pm bosons after electroweak symmetry breaking, therefore five physical Higgs bosons remain: two charged scalars H^\pm , two neutral scalars H , h and a neutral pseudoscalar A . The SUSY partner particles of these mix with the SUSY partners of the electroweak Standard Model gauge bosons to form four neutral *neutralinos* $\tilde{\chi}_{1,2,3,4}^0$ and four charged *charginos* $\tilde{\chi}_{1,2}^\pm$ ⁴.

The particle content of the MSSM is summarized in table 2.2.

A second auxiliary field similar to F_i that becomes important in further considerations is necessary: Gauge supermultiplets contain massless gauge boson fields A_μ^a and two-component Weyl fermion gauginos λ^a , where the index a runs over the generators of the gauge groups. Since the fermionic and bosonic degrees of freedom of λ^a and A_μ^a do not match off-shell, a real bosonic auxiliary field D^a has to be introduced, adding so-called “D-terms” $D^a D^a$ to the Lagrangian. This field can be expressed as $D^a = -g(\phi^* T^a \phi)$, where T^a are the generators of the corresponding gauge group with coupling g . The complete scalar potential contained in the Lagrangian is

$$V(\psi, \psi^*) = F^{*i} F_i + \frac{1}{2} \sum_a D^a D^a = W_i^* W^i + \frac{1}{2} \sum_a g_a^2 (\phi^* T^a \phi)^2. \quad (2.16)$$

⁴If SUSY was unbroken, \tilde{B}^0 and \tilde{W}^0 would mix to mass eigenstates \tilde{Z} and $\tilde{\gamma}$, analogously to their SM partners.

Spontaneous SUSY breaking mechanisms are classified in D-term and F-term SUSY breaking, depending on which kind of field receives a non-vanishing vacuum expectation value. In the MSSM, an F-term breaking mechanism is pursued without assumption of its origin.

Soft SUSY breaking

Obviously, the known particles of the Standard Model alone do not form superpartners, therefore every Standard Model particle must have a superpartner that is not yet discovered. A solution to this problem is to assume that superpartners of the Standard Model particles are too heavy to have been observed in particle physics experiments so far, thereby violating the newly introduced symmetry. If SUSY is broken in the low-energy regime, the SUSY breaking scale has to be small enough to still solve the hierarchy problem. For the same reason, SUSY breaking terms have to be introduced such that dependencies on the cut-off Λ are at most logarithmic. SUSY breaking without introduction of new quadratic divergences is called *soft* SUSY breaking.

Soft SUSY breaking terms must then give corrections to the Higgs squared mass of the form $\Delta m_H^2 = m_{soft}^2 \left(\frac{\lambda}{16\pi^2} \ln \frac{\Lambda}{m_{soft}} + \dots \right)$ [3], where λ is a Yukawa coupling constant and m_{soft} is the largest mass scale associated with the soft SUSY breaking terms. The mass difference between Standard Model particles and their SUSY partners cannot be too large, otherwise a new fine-tuning problem arises. If $\lambda \sim 1$ and $\Lambda \sim m_{planck}$, SUSY particles are expected to be at the order of 1 TeV, i.e. well in reach of the LHC experiments.

While SUSY is thought to be spontaneously broken, the MSSM is formulated without assumption of a specific breaking mechanism by introducing soft SUSY breaking terms by hand into the Lagrangian [3]:

$$\begin{aligned} \mathcal{L}_{soft}^{MSSM} = & -\frac{1}{2}(M_3\tilde{g}\tilde{g} + M_2\tilde{W}\tilde{W} + M_1\tilde{B}\tilde{B} + c.c.) \\ & -(\tilde{u}\mathbf{a}_u\tilde{Q}H_u - \tilde{d}\mathbf{a}_d\tilde{Q}H_d - \tilde{e}\mathbf{a}_e\tilde{L}H_d + c.c.) \\ & -\tilde{Q}^\dagger\mathbf{m}_Q^2\tilde{Q} - \tilde{L}^\dagger\mathbf{m}_L^2\tilde{L} - \tilde{u}\mathbf{m}_{\tilde{u}}^2\tilde{u}^\dagger - \tilde{d}\mathbf{m}_{\tilde{d}}^2\tilde{d}^\dagger - \tilde{e}\mathbf{m}_{\tilde{e}}^2\tilde{e}^\dagger \\ & -m_{H_u}^2H_u^*H_u - m_{H_d}^2H_d^*H_d - (bH_uH_d + c.c.) , \end{aligned} \quad (2.17)$$

where $M_{1,2,3}$ are bino, wino and gluino mass terms, $\mathbf{a}_{u,d,e}$ are complex 3x3 matrices in family space corresponding to the Yukawa couplings in the superpotential 2.13 and describing (scalar)³ couplings, $\mathbf{m}_{\tilde{Q},\tilde{u},\tilde{d},\tilde{L},\tilde{e}}^2$ are complex hermitian 3x3 matrices in family space representing squark and slepton mass terms, and the last line finally contains mass terms of the Higgs fields. The Lagrangian $\mathcal{L}_{soft}^{MSSM}$ is the most general formulation of soft SUSY breaking under the conditions of gauge invariance and R-parity conservation.

The MSSM now contains 105 free parameters in addition to those of the Standard Model. Besides indicating a non-fundamental nature of the theory, this large number of free parameters leads to difficulties concerning concrete predictions. There are, however, constraints from low energy observations concerning flavour changing neutral currents (FCNCs) and CP violation which allow to reduce these 105 free parameters significantly [3, 4]:

Processes with FCNCs, which are forbidden in the Standard Model at tree level, occur at loop level via box diagrams such as the first diagram shown in figure 2.3(a). In the MSSM, additional contributions to the kaon mass difference $\Delta m(K_L, K_S)$ exist, an example of which is shown in the second diagram of figure 2.3(a). These are caused by possibly large off-diagonal elements in the squared squark mass matrix, which also lead to flavour violating decays like $b \rightarrow s\gamma$. Similarly, corresponding diagrams in the (s)lepton sector lead e.g. to the muon decay $\mu \rightarrow e\gamma$, as shown in figure 2.3(b). This is called the *SUSY flavour problem*.

Parameters of soft SUSY breaking terms can generally be complex, introducing CP violating phases which are constrained e.g. by measurements of the electric dipole moment of the electron and the neutron, or by measurements of the CP violating decay $K_L \rightarrow \pi\pi$. Low energy measurements lead to the conclusion that CP violating phases introduced by SUSY breaking have to be very small, which is known as the *SUSY CP problem*.

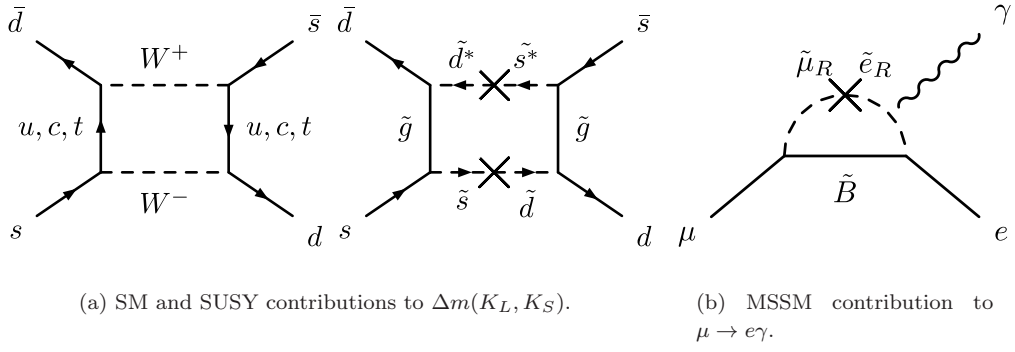


Figure 2.3. – Examples of flavour changing neutral currents in the MSSM.

The SUSY flavour and CP problems can be avoided by assuming the squark and slepton squared mass matrices to be real, flavour-blind and diagonal:

$$\mathbf{m}_X^2 = m_X^2 \mathbf{1} \text{ with } X = Q, \bar{u}, \bar{d}, L, \bar{e}.$$

Then squarks and sleptons with the same electroweak quantum number are mass degenerate, so mixing angles can be rotated away. Cubic scalar terms are set proportional to their corresponding Yukawa coupling matrices

$$\mathbf{a}_x = A_x \mathbf{y}_x \text{ with } x = u, d, e,$$

so only third generation particles have large trilinear couplings. Large CP violation can further be avoided by removing complex phases:

$$M_{1,2,3}, A_{u,d,e} \in \mathbb{R}.$$

These conditions are known as soft SUSY breaking *universality*.

2.2.2. Minimal Supergravity (mSUGRA)

While in the MSSM the soft SUSY breaking terms have been inserted by hand into the Lagrangian, leading to the necessity of universality requirements introduced rather arbitrarily, the form of SUSY breaking terms can also be assumed to be the result of a specific breaking mechanism.

A global SUSY breaking mechanism is difficult to describe at tree level without leading to contradictions with observation, therefore many models assume the SUSY breaking to happen indirectly or radiatively in a so-called “hidden sector”, caused by particles with no direct couplings to those of the MSSM. The phenomenologically important question is how the SUSY breaking is then mediated to the “visible sector” of the MSSM. If this is done via a flavour-blind interaction, the universality conditions will hold automatically. The two main candidates for this mediating interaction are gravity and gauge interactions.

In the first case, known as *supergravity*, SUSY is a local symmetry. In unbroken SUSY, the graviton (spin 2) and its SUSY partner the gravitino (spin $\frac{3}{2}$) are both massless. Since the SUSY generators Q are fermionic, the Nambu-Goldstone state emerging from a spontaneous breaking is a massless neutral Weyl fermion, which is called goldstino. The goldstino is absorbed by the gravitino which thereby acquires a mass $m_{3/2}$. In analogy to electroweak symmetry breaking, this is called the *super-Higgs* mechanism. Supergravity models naturally lead to SUSY breaking terms of the form 2.17 as present in the MSSM, with $m_{soft} \sim \frac{\langle F \rangle}{m_{Planck}}$ at the order of a few hundred GeV [3], $\langle F \rangle$ being the vacuum expectation value of the corresponding SUSY breaking auxiliary field.

The number of free parameters can be reduced by choosing a flat Kähler metric in the limit $m_{Planck} \rightarrow \infty$ which leads to common scalar masses at the GUT scale [4]. Further assumed are common gaugino masses. The soft terms in 2.17 can then be described with four parameters and a sign:

$m_0^2 = m_{H_u}^2 = m_{H_d}^2$ and $m_0^2 \mathbf{1} = \mathbf{m}_{\mathbf{Q}, \bar{\mathbf{u}}, \bar{\mathbf{d}}, \mathbf{L}, \bar{\mathbf{e}}}^2$ the common scalar mass at the GUT scale

$m_{1/2} = M_{3,2,1}$ the common gaugino mass at the GUT scale

$A_0 = A_{u,d,e}$ the common trilinear coupling at the GUT scale

$\tan \beta = \frac{v_u}{v_d}$ the ratio of the Higgs VEVs at the electroweak scale

$\text{sgn}(\mu)$ the sign of the higgsino mixing parameter.

This is called the *minimal supergravity* (mSUGRA) model.

The mSUGRA parameter space

The parameter space spanned by these four continuous parameters and one sign still involves a large variety of phenomenological possibilities. Some regions, however, are in contradiction to observation and can thus be excluded. Necessary requirements on possible mSUGRA parameter points arise from the following arguments:

Since the LSP is stable if R-parity is conserved, it must be neutral and colorless, i.e. a weakly interacting massive particle (WIMP). This requirement excludes regions of small m_0 and at the same time large $m_{1/2}$, in which the $\tilde{\tau}_1$ is the LSP. Furthermore, the relic density of the LSP is constrained by the measured amount of cold Dark Matter: the contribution of an mSUGRA LSP tends to be too large if annihilation effects are not amplified. These requirements already constrain the allowed parameter regions to thin lines in the m_0 - $m_{1/2}$ -plane for fixed $\tan \beta$.

Sparticle masses should be around the TeV scale due to the arguments concerning the SUSY breaking scale given above. They have to additionally meet lower bounds from direct searches at LEP and Tevatron. Since mSUGRA predicts a Standard Model like light neutral Higgs boson, searches aiming at the Standard Model Higgs can be interpreted in the mSUGRA context to give parameter limits. Particularly invisible Higgs searches combined with selectron searches at LEP exclude regions with low $m_{1/2}$ [17].

Tevatron experiments additionally give an upper bound on $\tan \beta$ as a function of m_A , and exclude substantial areas of the MSSM parameter space for pseudoscalar Higgs boson masses up to 300 GeV [18]. Searches for charged Higgs bosons further exclude regions of the $m_{H^+} - \tan \beta$ -plane [19]. Bounds on m_0 and $m_{1/2}$ are obtained by searches for associated chargino and neutralino production, and chargino masses up to 130 GeV can be excluded for $\tan \beta$ up to 9.6 at 95 % CL [20] or up to 164 GeV for $\tan \beta = 3$, $A_0 = 0$ GeV, $m_0 = 60$ GeV and $\mu > 0$ [21]. Squark production searches with tau final states yield limits on the squark mass of 410 GeV (95 % CL) in mSUGRA regions with $\tan \beta = 15$, $A_0 = -2m_0$ and $\mu < 0$ [22]. Jet final states interpreted in mSUGRA for $\tan \beta = 3$, $A_0 = 0$ GeV and $\mu < 0$ exclude squark masses up to 379 GeV and gluino masses up to 308 GeV [23], or for $\tan \beta = 5$ and $m_{\tilde{q}} = m_{\tilde{g}}$ degenerate squark and gluino masses up to 392 GeV [24].

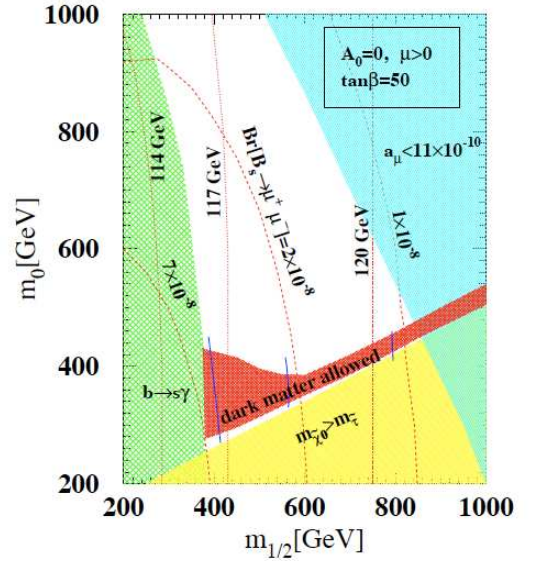


Figure 2.4. – m_0 - $m_{1/2}$ plain for $\tan \beta = 50$, $A_0 = 0$ and $\mu > 0$. Shaded areas are excluded by $b \rightarrow s\gamma$, stau LSP or a_μ . Dotted red lines are exclusion lines for limits on $BR(B_s \rightarrow \mu\mu)$, the current best limit is $5.8 \cdot 10^{-8}$ (CDF [15]). Vertical dotted lines label Higgs masses. From [16].

The branching fraction of $b \rightarrow s\gamma$, measured at CLEO, Belle and BABAR to give an average of $3.55 \cdot 10^{-4}$ [25], further excludes regions with small $m_{1/2}$ dependent on $\tan\beta$, where $\mu < 0$ scenarios are stronger constrained than $\mu > 0$ regions [4]. The latter are therefore more widely studied, and the benchmark points studied in this thesis also assume $\mu > 0$.

The branching fraction of $B_s \rightarrow \mu\mu$ gets enlarged by neutral SUSY Higgs bosons depending on $\tan\beta$ [26], disfavouring regions with large $\tan\beta$ and small $m_0, m_{1/2}$.

The anomalous magnetic moment of the muon a_μ is sensitive to chargino-sneutrino- and neutralino-smuon-loops, and thus gives further constraints on the masses of the particles involved in these loops.

Figure 2.4 shows the m_0 - $m_{1/2}$ plain for $\tan\beta = 50$, $A_0 = 0$ GeV and $\mu > 0$. Shaded regions are excluded due to measurements of a_μ , $b \rightarrow s\gamma$ or a cosmologically forbidden $\tilde{\tau}_1$ LSP. Vertical dotted lines represent the mass of the SM-like Higgs, curved dotted lines are exclusion lines reachable with certain precision of the $B_s \rightarrow \mu\mu$ branching fraction, with the current best limit from CDF II at 90 % CL being $5.8 \cdot 10^{-8}$ [15].

First results from SUSY searches in the ATLAS experiment at the LHC, using 35 pb^{-1} of data taken in 2010 with $\sqrt{s} = 7$ TeV, exceed the limits obtained in the Tevatron experiments. Interpreted in mSUGRA, results from searches with one lepton, jets and missing transverse energy exclude gluino masses below 700 GeV with 95 % CL [27] for equal squark and gluino masses, $A_0 = 0$ GeV, $\tan\beta = 3$ and $\mu > 0$. Similar searches with zero leptons exclude equal squark and gluino masses below 775 GeV in a mSUGRA/CMSSM scenario or below 870 GeV in models which contain only squarks of the first two generations, a gluino octet and a massless neutralino [28].

A combination of these searches with one or zero leptons exceeds the limit on equal squark and gluino masses to 815 GeV [29].

Benchmark points The constraints described above leave a limited number of regions in the parameter space, wherein certain benchmark points are defined which represent one region of phenomenologically similar points of the parameter space. Benchmark points defined in ATLAS are chosen such that they are within reach of the LHC program. Those important for this thesis are:

SU3 The *bulk region* is one of the most studied regions due to small m_0 and $m_{1/2}$ leading to small SUSY masses. Other than in the *low mass region* described below, $m_{1/2} > m_0$ and so $m(\tilde{\chi}_2^0) > m(\tilde{\tau}_1)$, which leads to a possible decay $\tilde{\chi}_2^0 \rightarrow \tilde{\tau}_1 \tau \rightarrow \tilde{\chi}_1^0 \tau \tau$ ideal for tau studies.

SU4 This point in the *low mass region* has the smallest m_0 and $m_{1/2}$ combination and thus the highest cross section of all ATLAS benchmark points. It directly continues the region covered by Tevatron Run II searches. Gluino and squark masses are nearly degenerate with 400 GeV, and the gluino predominantly decays via stops and sbottoms in third generation quarks, leading to b -jet enriched signatures.

SU11 This is a point specifically chosen for tau studies: a high $\tan\beta$ of 50 ensures large third generation mixing and thus enhancement of tau final states, while reasonably low m_0 and $m_{1/2}$ keep the SUSY masses small and thereby the total production cross section large enough to make tau final states a promising discovery channel.

SU3 is the point of interest for the first part of the analysis, which deals with pp collisions at $\sqrt{s} = 14$ TeV and $\sqrt{s} = 10$ TeV. Although SU3 has been ruled out by Dark Matter constraints, its collider phenomenology is representative for a large region of mSUGRA parameter space which is still allowed. The cross-section of 28 pb in 14 TeV collisions is large enough to allow for an early discovery and an endpoint measurement of $m_{\tau\tau}$ for tau leptons emerging from $\tilde{\chi}_2^0 \rightarrow \tilde{\tau}_1 \tau \rightarrow \tilde{\chi}_1^0 \tau \tau$. The branching fraction for this decay is about ten times the ones for the respective decays to

	SU3	SU4	SU11
m_0 [GeV]	100	200	270
$m_{1/2}$ [GeV]	300	160	205
$\tan\beta$	6	10	50
A_0 [GeV]	-300	-400	0
$\text{sgn}(\mu)$	+	+	+

(a) mSUGRA parameters.

	SU3	SU4	SU11
$\sqrt{s} = 14$ TeV	27.7	400	95
$\sqrt{s} = 10$ TeV	8.2	160	25
$\sqrt{s} = 7$ TeV	2.1	60	9

(b) NLO cross sections in pb.

	SU3	SU4	SU11
$m(\tilde{g})$	717.46	413.37	519.28
$m(\tilde{t}_1)$	424.12	206.04	374.87
$m(\tilde{\chi}_4^0)$	480.59	327.76	297.01
$m(\tilde{\chi}_3^0)$	463.99	308.94	275.36
$m(\tilde{\chi}_2^0)$	218.60	113.48	144.06
$m(\tilde{\chi}_1^0)$	117.91	59.84	79.47
$m(\tilde{\tau}_2)$	232.17	236.04	293.79
$m(\tilde{\tau}_1)$	149.99	200.50	161.05

(c) Masses in GeV.

Table 2.3. – Parameter values, cross sections and most important masses of the three benchmark points of interest. Cross section are calculated by **Prospino2** [30–35], mass spectra by **ISAJET** [36].

muons or electrons, which makes tau final states an important contribution to SUSY searches in this part of the parameter space. In 7 TeV collisions, however, the cross-section is reduced to 2 pb and thus too small to permit a measurement with the $1\text{--}3\text{ fb}^{-1}$ expected to be recorded with this centre of mass energy.

The second part of this thesis focuses on pure discovery prospects in the ditau and missing transverse energy channel with 7 TeV data, and takes SU11 as the main benchmark point. In addition, SU4 is studied for easier comparison with other search channels since SU11 is only used for tau related searches. Compared to SU3, SU11 has a much larger cross section, and due to its large $\tan\beta$ tau final states are enhanced. Both SU11 and SU4 have $m(\tilde{\tau}_1) > m(\tilde{\chi}_2^0)$, so the signal decay chain of the first part of the analysis is closed. The main source for tau leptons in SU11 is the corresponding 3-body decay $\tilde{\chi}_2^0 \rightarrow \tau^+ \tau^- \tilde{\chi}_1^0$. Though SU11 is excluded by low energy precision measurements, as is obvious in figure 2.4, it is representative for the region in which tau final states might provide a better sensitivity than other search channels.

The low mass point SU4 is not ideal for tau studies because less taus on average are accompanied by many jets, in particular b -jets, which tend to fake tau leptons. This leads to an environment with poor performance of the tau identification algorithms. The SU4 point is nevertheless studied besides SU11 since tau independent SUSY searches mostly focus on this benchmark scenario due to the very high cross section, and have indeed excluded it with the ATLAS data recorded in 2010 [28].

A list of important masses, branching fractions and total cross sections of these three benchmark points is given in table 2.3.

Another region that will be mentioned is

SU1: In the *co-annihilation region*, the $\tilde{\chi}_1^0$ -LSP and $\tilde{\tau}_1$ are nearly mass degenerate and keep the LSP relic density small due to $\tilde{\chi}_1^0 \tilde{\tau}_1 \rightarrow \tau \gamma$ annihilation. This point yields experimentally very challenging tau signatures: caused by this small mass difference, taus from $\tilde{\tau}_1 \rightarrow \tau \tilde{\chi}_1^0$ decays are so soft they can hardly be reconstructed. The cross section is too small (6 pb at 14 TeV) to make a discovery study in the tau channel feasible.

Alternative SUSY breaking models: GMSB and AMSB

Gravity is not the only possibility to mediate SUSY breaking to the visible sector, although it is the most widely studied. The second most studied model is the beforementioned gauge mediated (GMSB) scenario, where SUSY breaking is mediated by a $SU(3)_C \otimes SU(2)_L \otimes U(1)_Y$ gauge interaction. Supersymmetry remains unbroken in leading order, and the breaking that happens in loop corrections is mediated by coupling to so-called *messenger particles*, the mass scale M_m of which is one of six free parameters of the model. The LSP is a very light gravitino \tilde{G} , while in mSUGRA models it is the lightest neutralino $\tilde{\chi}_1^0$. The phenomenology is strongly dominated by the nature of the next to lightest SUSY particle (NLSP), the lifetime of which, another free parameter of the model⁵, can vary significantly. Other parameters defining the GMSB parameter space are the SUSY breaking scale Λ , the number of messenger fields N_5 as well as $\tan\beta$ and $sgn(\mu)$. In regions with large $\tan\beta$, the NLSP is the lightest stau which decays as $\tilde{\tau}_1 \rightarrow \tau\tilde{G}$, leading to similar tau enhanced signatures like in the according mSUGRA parameter regions if the $\tilde{\tau}$ lifetime is small. Therefore this kind of GMSB scenario will be included in the SUSY search study of chapter 6 by the benchmark point

GMSB6: The parameters defining this GMSB benchmark point are $\tan\beta = 30$, $M_m = 250$ TeV, $\Lambda = 40$ TeV, $N_5 = 3$, $C_{grav} = 1$ and $sgn(\mu) > 0$. The NLSP is the $\tilde{\tau}_1$, leading to a phenomenology which is rich in tau leptons.

In any model where SUSY breaking happens in a hidden sector, there are loop-level contributions from gravitational interactions which become dominant if no other mechanism to communicate SUSY breaking to the visible sector is present. This effect is called anomaly-mediated SUSY breaking (AMSB). Such models predict a wino-like LSP with a nearly mass degenerate chargino, leading to a chargino lifetime that may be large enough to allow a direct detection. This kind of scenario will not be investigated in this thesis.

2.3. mSUGRA phenomenology

As mentioned above, SUSY particles can only be produced in pairs from pp collisions due to R-parity conservation. The dominant production processes at the LHC are $\tilde{g}\tilde{g}$, $\tilde{g}\tilde{q}$ and $\tilde{q}\tilde{q}$ pair production from gg , gq or qq collisions, examples of which are shown in figure 2.5, assuming the squark and gluino masses are light enough to be produced at the LHC. Compared to the Tevatron, processes with $q\bar{q}$ initial states are less important. In the mSUGRA benchmark points considered in the analysis, squark-gluino production is dominant⁶.

After SUSY pair production, successive decays to the lightest SUSY particle lead to a characteristic SUSY signature of many, spherically distributed jets and leptons, accompanied by large missing energy from the two undetectable LSPs. Possible or dominant decay modes depend on the SUSY mass hierarchy and on the couplings which hinge on the admixture of wino, bino and higgsino components in the neutralinos and charginos. Mostly a chain of 2-body decays is assumed, like those shown in figure 2.6, where the intermediate SUSY particles are produced on-shell. The typical lifetime of SUSY particles is too small to show secondary vertices, therefore all Standard Model particles from both decay chains of a SUSY event seem to emerge from one single vertex.

The missing energy carried away by the two LSPs in each SUSY event cannot be fully determined because the initial state of the colliding partons is unknown, but the transverse component which is zero in the initial state of the head-on parton collisions can be used. Missing transverse energy \cancel{E}_T is the most characteristic feature of R-parity conserving SUSY events. However, it is noteworthy that although R-parity conservation leads to \cancel{E}_T , the reverse conclusion does not hold since in RPV models the LSPs might decay outside the detector. RPV couplings are

⁵An equivalent parameter which determines the lifetime is C_{grav} . The NLSP decay length scales with C_{grav}^2 .

⁶Production cross-section of separate processes taken from **Prospino2** [30–35].

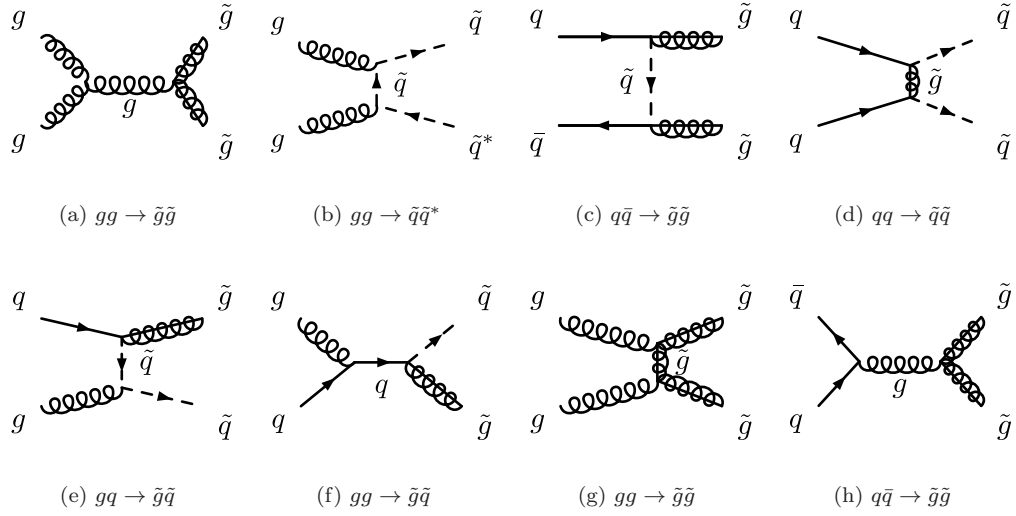


Figure 2.5. – Example diagrams for gluino-gluino, gluino-squark and squark-squark production.

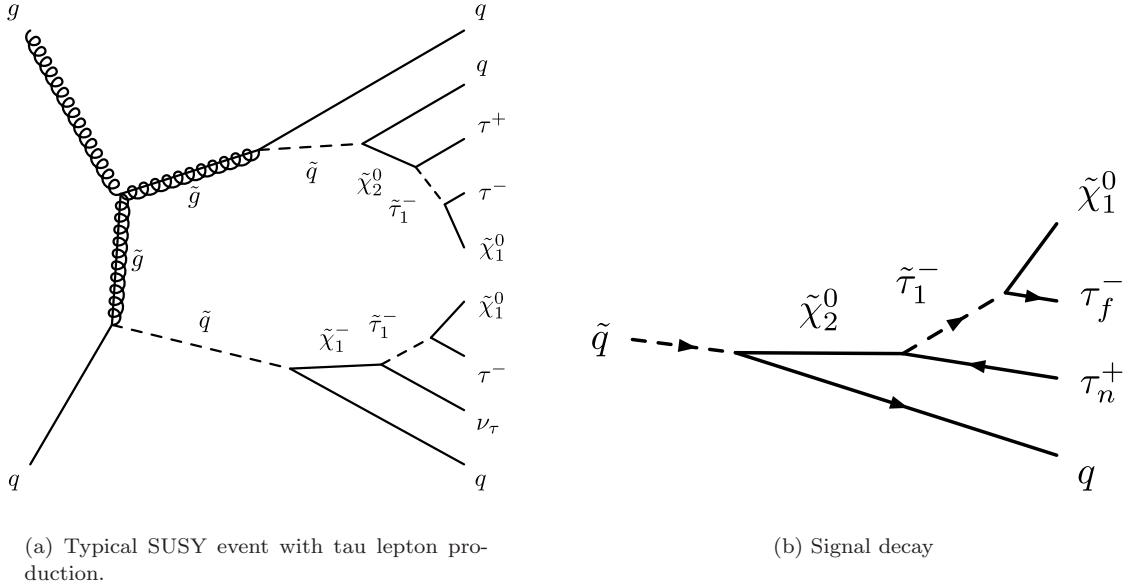


Figure 2.6. – Signal decay and SUSY event containing both signal and background example.

constrained to be smaller than the gauge couplings, therefore according decays are not dominant but reveal themselves mainly in the decay of the LSP. Signatures of RPV models with a long LSP lifetime thus might be indistinguishable from RPC models at the LHC.

After an excess of some signal over the Standard Model background compatible with a SUSY hypothesis is found, attributes of the newly discovered particles have to be measured in order to strengthen or disprove specific SUSY models. Programs are under development [37, 38] that calculate model parameters e.g. of mSUGRA at the GUT scale based on observables like endpoints and topological cross sections measured at experimentally accessible energy scales.

Two undetected LSPs per SUSY event prohibit reconstruction of mass peaks, but an estimation of the SUSY mass scale can be obtained by the so-called effective mass $M_{eff} = \sum_{i=1}^{N_{jet}} p_T^{jet,i} + \sum_{i=1}^{N_{lep}} p_T^{lep,i} + \cancel{E}_T$, where the sums run over all selected objects (jets and leptons) depending on the search channel.

Although masses of SUSY particles cannot be measured directly in RPC scenarios at the LHC, they are accessible via endpoints of invariant mass spectra [39, 40]: mass distributions of particles emerging from SUSY decay cascades show kinematic edges which are dependent on the intermediate SUSY particles. The two taus from the target signal decay $\tilde{\chi}_2^0 \rightarrow \tilde{\tau}_1 \tau \rightarrow \tilde{\chi}_1^0 \tau \tau$, for example, have an endpoint depending on $m(\tilde{\chi}_2^0)$, $m(\tilde{\tau}_1)$ and $m(\tilde{\chi}_1^0)$:

In the $\tilde{\chi}_2^0$ rest frame, energy-momentum conservation demands $m_{\tilde{\chi}_2^0} = E_{\tilde{\tau}} + E_{\tau}$ and $\vec{p}_{\tau} = -\vec{p}_{\tilde{\tau}}$ in the $\tilde{\chi}_2^0$ decay. The tau lepton emerging from this first part of the chain is also called the *near* tau τ_N . The mass of the tau lepton is negligible compared to the masses of SUSY particles, therefore

$$\begin{aligned} p_{\tilde{\tau}}^2 &= E_{\tilde{\tau}}^2 - m_{\tilde{\tau}}^2 = (m_{\tilde{\chi}_2^0} - E_{\tau})^2 - m_{\tilde{\tau}}^2 = (m_{\tilde{\chi}_2^0} - |\vec{p}_{\tau}|)^2 - m_{\tilde{\tau}}^2 \\ &\Leftrightarrow 2m_{\tilde{\chi}_2^0}|\vec{p}_{\tau}| = m_{\tilde{\chi}_2^0}^2 - m_{\tilde{\tau}}^2 \\ &\Leftrightarrow E_{\tau,N} = |\vec{p}_{\tau,N}| = \frac{m_{\tilde{\chi}_2^0}^2 - m_{\tilde{\tau}}^2}{2m_{\tilde{\chi}_2^0}}, \end{aligned}$$

and analogously for the tau lepton emerging from the $\tilde{\tau}$ decay (also called the *far* tau τ_F)

$$E_{\tau,F} = |\vec{p}_{\tau,F}| = \frac{m_{\tilde{\tau}}^2 - m_{\tilde{\chi}_1^0}^2}{2m_{\tilde{\tau}}}.$$

It follows that the invariant mass is given as

$$m_{\tau\tau}^2 = (E_{\tau,N} + E_{\tau,F})^2 - (\vec{p}_{\tau,N} + \vec{p}_{\tau,F})^2 = 2|\vec{p}_{\tau,N}||\vec{p}_{\tau,F}| - 2\vec{p}_{\tau,N}\vec{p}_{\tau,F} = 2|\vec{p}_{\tau,N}||\vec{p}_{\tau,F}|(1 - \cos\theta),$$

which has a maximal value at $\cos\theta = -1$ of⁷

$$m_{\tau\tau}^{max} = \sqrt{\frac{(m_{\tilde{\chi}_2^0}^2 - m_{\tilde{\tau}}^2)(m_{\tilde{\tau}}^2 - m_{\tilde{\chi}_1^0}^2)}{m_{\tilde{\tau}}^2}}. \quad (2.18)$$

A sufficiently long decay cascade yields as many such endpoints as SUSY particles involved, thus allowing reconstruction of the SUSY masses. If a decay chain includes n SUSY particles, $(2^{n-1} - n)$ endpoints can be extracted [39].

To measure such endpoints experimentally, ideally the shape of the invariant mass spectrum would be calculated, folded with detector effects and the resulting function related to the value of the endpoint. This is usually only done in the region around the edge of the distribution because of background contamination or object reconstruction turn-on effects dominating in the low mass regions. The shape of the $m_{\tau\tau}$ invariant mass spectrum would be a triangular distribution [39] if the four-momenta of the two taus could be fully reconstructed, i.e. rising linearly until cut off at the maximal value. Invariant mass spectra of electrons and muons emerging from an equivalent decay chain show this behaviour, so their endpoints can be determined by a linear fit to the edge of the distributions. For taus, however, the neutrinos present among their decay products lead to the invariant mass spectrum being depleted at the high edge since the maximal value can now only be achieved if the whole energy of the tau is passed on to the visible decay products alone. More on techniques to extract the endpoint position in such spectra can be found in chapter 5.

Since there are always two SUSY decay chains present in any SUSY event, it is not unlikely that further leptons produced in the second chain lead to combinatorial background in the reconstructed invariant mass spectrum. This background is reducible due to the charge correlation of the two taus from the signal decay. Further SUSY background is caused by chargino decays, as shown in the lower part of figure 2.6(a), if present in both cascades. The charge correlation between the two taus from chargino decays depends on whether the primary SUSY production is dominated by $\tilde{q}\tilde{q}^{(*)}$, $\tilde{g}\tilde{g}^{(*)}$ or $\tilde{g}\tilde{g}$. As mentioned above, in SU3, SU4 and SU11, $\tilde{g}\tilde{g}$ is the dominant production process, so due to the Majorana nature of the gluino, there is no charge correlation between leptons emerging from the two different SUSY decay branches.

⁷Note that expression 2.18 is Lorentz-invariant although the two tau energies have been taken in different rest frames.

2.3.1. Tau final states

In the considerations above, SUSY decays involving tau leptons have been used for good reasons as an example: though experimentally challenging, tau leptons take on a special position in SUSY processes.

The decay chain $\tilde{q} \rightarrow \tilde{\chi}_2^0 q \rightarrow \tilde{l}^\pm l^\mp q \rightarrow \tilde{\chi}_1^0 l^+ l^- q$ is present in a wide region of the mSUGRA parameter space and thus promising for SUSY mass measurements. The decay to tau leptons might be favoured because their SUSY partners can be significantly lighter than selectrons and smuons. This is the effect of large Yukawa and trilinear couplings in the renormalization group (RG) equations which describe the energy dependence of the SUSY masses from the GUT scale to the electroweak scale, and thus their evolution in time during the expansion of the universe. A second reason for the difference in the third generation is the left-right-mixing mentioned in section 2.2.1: The gauge eigenstates $\tilde{\tau}_{L,R}$ are mixed into two mass eigenstates $\tilde{\tau}_{1,2}$ which can be significantly different, while the two slepton and smuon gauge eigenstates remain approximately unmixed and yield two nearly degenerate mass eigenstates. Furthermore, the $\tilde{\tau}_L$ component in $\tilde{\tau}_1$ is larger than the left-handed component of \tilde{e}_1 , $\tilde{\mu}_1$. This enhances the coupling to $\tilde{\chi}_2^0$ and $\tilde{\chi}_1^\pm$, which are dominantly wino in mSUGRA. The squared mass matrix in the gauge-eigenstate basis reads [3]

$$m_{\tilde{\tau}}^2 = \begin{pmatrix} m_{L_3}^2 + \Delta_{\tilde{e}_L} + m_{\tilde{\tau}}^2 & v(a_{\tilde{\tau}}^* \cos \beta - \mu y_{\tilde{\tau}} \sin \beta) \\ v(a_{\tilde{\tau}} \cos \beta - \mu^* y_{\tilde{\tau}} \sin \beta) & m_{\tilde{\tau}_R}^2 + \Delta_{\tilde{e}_R} + m_{\tilde{\tau}}^2 \end{pmatrix}, \quad (2.19)$$

and similar for all squarks and sleptons, with sine and cosine interchanged for up-type sfermions. Contributions of the form $va_{\tilde{\tau}} \cos \beta$ come from the trilinear terms $\tilde{e} \mathbf{a}_e \tilde{L} H_d$ of the soft SUSY breaking Lagrangian 2.17, and $m_{L_3}, m_{\tilde{\tau}_R}$ are the soft breaking stau mass terms of 2.17. $\Delta_{\tilde{e}_{L,R}} = (T_{3\phi} - Q_{\phi} \sin^2 \theta_W) \cos 2\beta m_Z^2$ terms are coming from the D-term contribution in the scalar potential 2.16, with the third component of the weak isospin $T_{3\phi}$ and electric charge Q_{ϕ} of the field ϕ . The F-terms in the scalar potential yield contributions of the form $-\mu v y_{\tilde{\tau}} \sin \beta$, and such equal to $m_{\tilde{\tau}}^2$ (which are negligible for all particles but the top quark).

Matrix 2.19 can be diagonalized by a unitary matrix to give mass eigenstates

$$\begin{pmatrix} \tilde{\tau}_1 \\ \tilde{\tau}_2 \end{pmatrix} = \begin{pmatrix} \cos \theta_{\tilde{\tau}} & \sin \theta_{\tilde{\tau}} \\ -\sin \theta_{\tilde{\tau}} & \cos \theta_{\tilde{\tau}} \end{pmatrix} \begin{pmatrix} \tilde{\tau}_L \\ \tilde{\tau}_R \end{pmatrix} \quad (2.20)$$

with the stau mixing angle $\theta_{\tilde{\tau}}$.

The magnitude of the mixing thus depends on the Yukawa couplings and $\tan \beta$, and is therefore large for third generation particles in mSUGRA regions with large $\tan \beta$. This leads to a $\tilde{\tau}_1$ mass that can be significantly smaller than $m(\tilde{\tau}_2)$ and the degenerate selectron and smuon masses $m(\tilde{e}_R) \simeq (\tilde{\mu}_R)$ (and $m(\tilde{e}_L) \simeq m(\tilde{\mu}_L)$), making $\tilde{\tau}_1$ the lightest slepton (and \tilde{t}_1 the lightest squark). These effects of left-right-mixing in the third generation are not singular to mSUGRA, but are also present in other SUSY models. The methods developed in chapters 5 and 6 to discover SUSY with tau lepton final states and to measure the di-tau invariant mass endpoint are therefore applicable to all SUSY models with such enhanced tau lepton production and with a mass hierarchy that allows the signal or a similar decay chain to be open.

3. The ATLAS detector at the LHC

The design of the Large Hadron Collider is geared to proton-proton and heavy ion collisions which enable studies of particle physics under conditions similar to states realized in the early universe. This purpose requires unprecedented high energy, as well as a high luminosity in order to be able to produce heavy new particles at a high rate. The design luminosity of the LHC collisions is about two orders of magnitude higher and the center-of-mass energy a factor of seven larger than in the proton-antiproton collisions of the Tevatron [41] at Fermi National Accelerator Laboratory (FNAL) [42]. Such conditions put strong demands on accelerator technology and detector performance, as well as data distribution and storage.

This chapter gives an overview of the experimental setup, focussing on the ATLAS detector and its performance with regard to the tau lepton enhanced SUSY signature examined in the previous chapter. The first part describes the LHC including beam parameters important for pp collision data, before the design of the ATLAS detector is explained in the second part of this chapter.

3.1. The Large Hadron Collider

The Large Hadron Collider (LHC) [43, 44] is built at the European Organization for Nuclear Research (CERN¹) in a tunnel of 27 km circumference about 100 m underground beneath the french-swiss border near Geneva (Switzerland). It will provide collisions of protons in bunches of $1.15 \cdot 10^{11}$ particles, at a design luminosity of $10^{34} \text{ cm}^{-2} \text{ s}^{-1}$ and a center-of-mass energy of $\sqrt{s} = 14 \text{ TeV}$. It will also collide lead ions with 5.5 TeV per nucleon pair at a design luminosity of $10^{27} \text{ cm}^{-2} \text{ s}^{-1}$.

Two proton beams counterrotate in the LHC, each by design containing 2808 proton bunches. These are brought to collision at four interaction points (IPs) inside the four large LHC experiments ATLAS² [45], CMS³ [46], ALICE⁴ [47] and LHCb⁵ [48]. Former two are multi-purpose experiments, the physics intent of which range from precision measurements of Standard Model parameters to discovery of the Higgs boson and new physics processes like the one investigated in this thesis. ALICE aims at exploring quark-gluon plasma formed with lead ion collisions, while LHCb is dedicated to physics of B mesons involving CP violation.

Two smaller experiments, LHCf⁶ and TOTEM⁷, are located further away from the interaction points of ATLAS and CMS, respectively, and are dedicated to forward physics, but can also contribute to luminosity measurements for the two multipurpose detectors.

Figure 3.1(a) shows the chain of proton acceleration, starting with the extraction by hydrogen ionization and continuing with successive acceleration in the LINAC2 to 50 MeV, the Proton Synchrotron Booster (PSB) to 1.4 GeV, the Proton Synchrotron (PS) to 26 GeV and the Super Proton Synchrotron (SPS) to 450 GeV, before the protons get injected in the LHC and are accelerated to the final energy of 7 TeV. The protons are packed in bunches of 10^{11} particles with a longitudinal spread of 7.5 cm, separated by a distance of 7.5 m which corresponds to a time interval of 25 ns between bunch crossings.

¹Conseil Européen pour la Recherche Nucleaire

²A toroidal LHC apparatus

³Compact muon solenoid

⁴A large ion collider experiment

⁵Large Hadron Collider beauty

⁶Large Hadron Collider forward

⁷Total elastic and diffractive cross section measurement

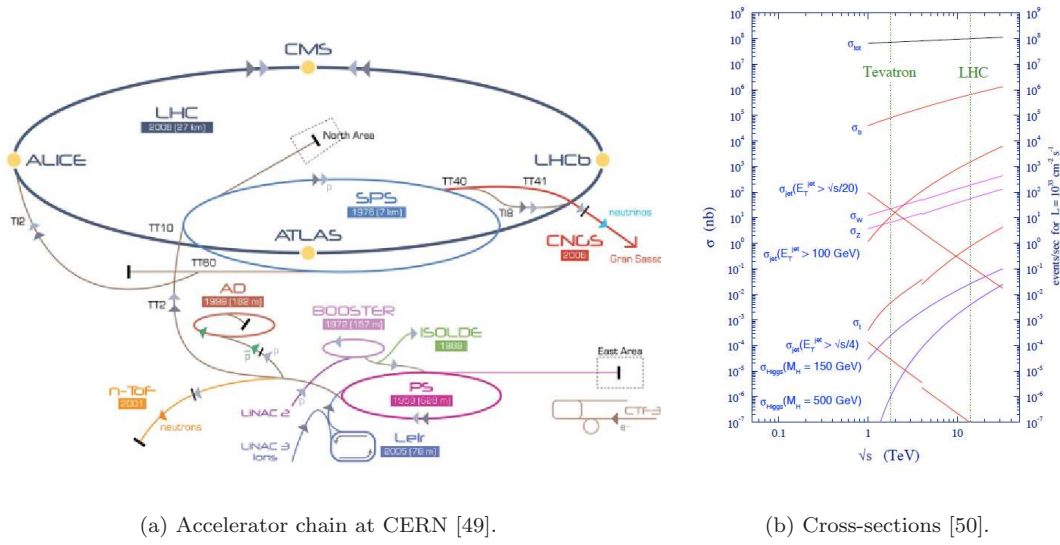


Figure 3.1. – Particle acceleration at CERN and QCD prediction for production cross-sections of processes in proton-(anti)proton collisions at LHC and Tevatron.

This high collision rate is necessary to produce rare physics processes which include particles of interest such as the Higgs boson with sufficient rates, the production cross-sections of which is predicted to be orders of magnitudes smaller than those of well-know SM processes, as illustrated in figure 3.1(b). The total production cross-section of typical SUSY processes such as those introduced in section 2.2.2 with e.g. $\sigma_{\text{SUSY}} \simeq 30 \text{ pb}^{-1}$ are comparable to that of the SM Higgs boson with $\sigma_H \simeq 10 \text{ pb}^{-1}$ for pp collisions with $\sqrt{s} = 14 \text{ TeV}$. Figure 3.1(b) also shows the different dependence of subprocesses on the center-of-mass energy, which leads to a significantly improved initial signal to background ratio at the LHC compared to the Tevatron and according gain in the prospects for discovery of new physics. This behaviour also indicates the disadvantage for new physics searches of running at half the design energy in the first few years of LHC operation.

The instantaneous luminosity is determined by the number of particles per bunch N_p , the number of circulating bunches N_B , the effective collision area $A_{\text{eff}} = 4\pi\sigma_x\sigma_y$ defined by the RMS of the transverse particle distribution in the beam $\sigma_{x,y}$, and the beam revolution frequency f_{rev} :

$$L = f_{\text{rev}} \frac{N_p^2 N_B}{A_{\text{eff}}} . \quad (3.1)$$

To avoid unwanted additional collisions near the interaction points, the beams are brought to collision under a crossing-angle of $\Phi_C \simeq 200 \text{ prad}$. This leads to an increased effective collision area and thus a reduction of the instantaneous luminosity by a factor F , which is about 0.9 for the LHC [43]. In terms of beam parameters, the luminosity can now be expressed as

$$L = f_{\text{rev}} \frac{N_p^2 N_B \gamma_r}{4\pi\epsilon_n \beta^*} F , \quad (3.2)$$

with the normalized emittance ϵ_n , the beta-function at the interaction point β^* and the relativistic gamma factor γ_r [44].

The most important technical parameters are summarized in table 3.1, comparing design values with those realized in the time period in which the data used in chapter 6 has been recorded.

parameter		design	realized (2010)
Peak Luminosity (proton collisions) [$\text{cm}^{-2}\text{s}^{-1}$]	L	$1.0 \cdot 10^{34}$	$2.07 \cdot 10^{32}$
Peak Luminosity (lead ion collisions) [$\text{cm}^{-2}\text{s}^{-1}$]	L_{Pb}	$1.0 \cdot 10^{27}$	$30.4 \cdot 10^{24}$
Number of bunches	N_B	2808	348
Protons per bunch	N_P	$1.15 \cdot 10^{11}$	$1.15 \cdot 10^{11}$
Proton energy [GeV]	E_P	7	3.5
Bunch spacing [ns]		25	150
Transverse normalized emittance [$\mu\text{m rad}$]	ϵ_n	3.75	~ 2.1
Beta function at ATLAS interaction point [m]	β^*	0.55	3.5
Full crossing angle [μrad]	Φ_C	285	200

Table 3.1. – LHC beam parameters: design values [44] and extrema realized in 2010 [51, 52].

Operational history

In its first year of operation, the LHC delivered 48.1 pb^{-1} of pp-collisions with $\sqrt{s}=7 \text{ TeV}$ at a maximal instantaneous luminosity of $2.1 \cdot 10^{32} \text{ cm}^{-2} \text{ s}^{-1}$ in IP1 where the ATLAS experiment is located, as well as 9.69 pb^{-1} of heavy ion collisions with $\sqrt{s}=2.76 \text{ TeV}$ per nucleon with a peak luminosity of $30.4 \cdot 10^{24} \text{ cm}^{-2} \text{ s}^{-1}$. The reason for running at half the design energy in the first years of operation is an incident which occurred on September 19th 2008, when nine days after proton beams had been circulated in the LHC for the first time, a faulty electrical connection between two superconducting magnets induced a resistive zone, which in turn lead to an electrical arc puncturing the helium enclosure. The mechanical damage caused by the escaping helium resulted in one year of repairs as well as preparatory work to prevent a similar incident during further operation. When it became obvious that a center-of-mass energy of 14 TeV could not be realized without an even longer delay, $\sqrt{s}=10 \text{ TeV}$ collisions were assumed to be within reach, causing the greater part of the analysis described in chapter 5 to be aimed at this energy. Weighting the risk to further damage the accelerator against the gain of potential for early discoveries finally lead to the decision to operate at $\sqrt{s}=7 \text{ TeV}$ until at least $\int L dt = 1 \text{ fb}^{-1}$ has been delivered to the experiments. The LHC re-started circulating proton beams on November 20th 2009, shortly followed by collisions with $\sqrt{s}=0.9 \text{ TeV}$. First collision data with $\sqrt{s}=7 \text{ TeV}$ was delivered to ATLAS on March 30th 2010, followed by one year of data-taking at this center-of-mass energy. At the time of writing, it is planned to continue $\sqrt{s}=7 \text{ TeV}$ collisions throughout the year 2011, followed by another year of operation. A shutdown of approximately two years⁸ thereafter is foreseen to enable $\sqrt{s}=14 \text{ TeV}$ collisions by the year 2015.

3.1.1. Event topology of proton-proton collisions

Since protons are composite particles, the center-of-mass energy of the interacting partons in pp-collisions is smaller than the collision energy. Detailed understanding of the proton structure is required to draw sensible conclusions from pp-collisions at the LHC. While a description of the hard interaction involving large energy transfer can employ perturbation theory due to the asymptotic freedom in the strong force, the initial state of the partons has to be described by nonperturbative parton distribution functions (PDFs) obtained by experiments. The momentum fraction x carried by quarks and gluons within the proton has been measured in electron-proton collisions at HERA, the result of which is shown in figure 3.2(a) for a momentum transfer of $Q^2 = 10 \text{ GeV}^2$. In addition to the PDFs, their uncertainties are important to know precisely, since they can contribute significantly to final results obtained at the LHC experiments. Several experimental data including the HERA results can be combined in global fits using different parameterizations, an example of which shown in figure 3.2(a) is the CTEQ6 [54] parameterization that is used for SUSY analysis in ATLAS. First measurements of the muon charge asymmetry

⁸A 15 to 19 months lasting shutdown between beams can be anticipated to result in about two years without physics runs [53].

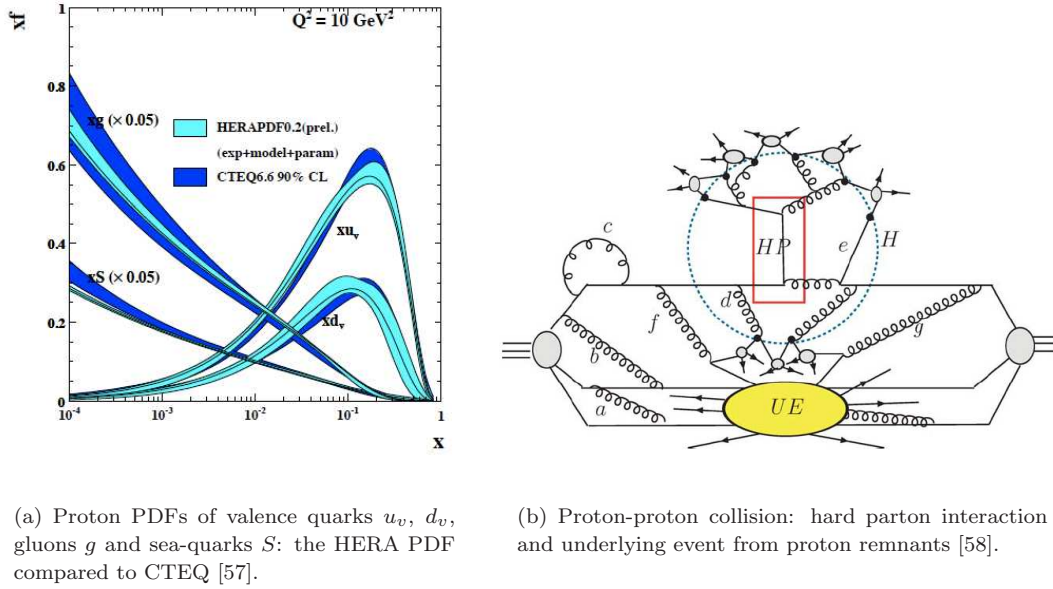


Figure 3.2. – Parton distribution functions (PDFs) and schematic pp-collision.

in W decays at $\sqrt{s} = 7$ TeV with ATLAS [55] and CMS [56] using 31 pb^{-1} and 36 pb^{-1} of data, respectively, will be used as input for the next generation PDF fits and reduce corresponding uncertainties in future studies.

As depicted in figure 3.2(b), the hard process (HP) of quasi-free partons is accompanied by multiple low-energy processes, the so-called underlying event (UE). Interactions of the proton remnants as well as their color-connection to the partons of the hard scattering lead to many additional particles which pollute the interesting part of the event. Furthermore, more than one pp-interaction can take place in one bunch-crossing, depending on the beam configuration. In the collisions realized in 2010, on average two interactions per bunch-crossing occurred. Most of these interactions do not contain a hard process of interest, but are soft scattering events called *Minimum Bias* events. The overlap of several events is called *pile-up*.

Both this high particle multiplicity per event as well as the high frequency of the bunch-crossings put stringent demands to the LHC detectors. The dedicated design of the ATLAS detector is described in the following section. More detailed information about the ATLAS detector and its expected performance can be found in [40, 45]. Design parameter values quoted in this chapter are also taken from these references if not stated otherwise.

3.2. The ATLAS Experiment

The conditions at the LHC as described above require radiation hard, fast detectors with high granularity to be able to process the expected particle fluxes. At the same time, precise particle position measurements as well as high energy resolution in almost full solid angle coverage are necessary for the analysis at hand. The phenomenology described in the previous chapter in particular demands an excellent tau lepton reconstruction as well as missing transverse energy resolution.

To meet these requirements, the ATLAS detector consists of several subdetectors arranged in cylinder-shaped layers around the interaction point, as shown in figure 3.3. Closest to the interaction point is the inner detector, a combination of semiconductor and drift tube tracking devices within a 2 T solenoidal magnetic field, responsible for momentum and vertex measurements. It

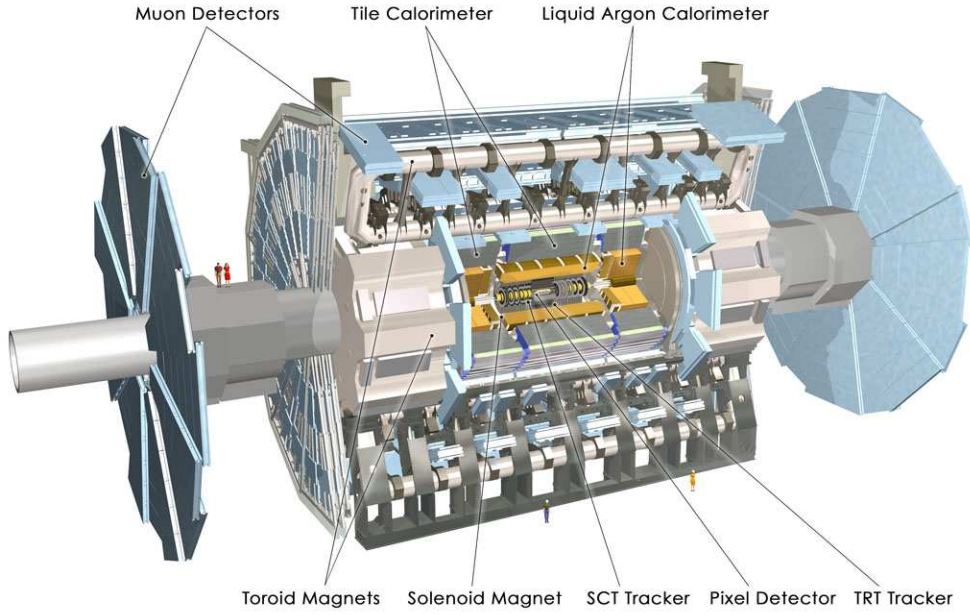


Figure 3.3. – Schematic drawing of the ATLAS detector: overall geometry. [45]

is surrounded by high granularity electromagnetic and hadronic sampling calorimeters providing energy and position measurements. The outermost part of the ATLAS detector consists of a muon spectrometer in a toroidal magnetic field.

Each subdetector is divided into a cylindrically formed barrel covering the central region, and two endcaps perpendicular to the beam line covering the forward regions.

The remainder of this chapter describes the ATLAS detector in more detail, starting with the magnet system and continuing with the individual subdetectors, moving outwards from the interaction point. The coordinate system used thereby is centered at the nominal interaction point, with the beam direction defining the z -axis. The positive x -axis is pointing to the center of the LHC ring, the positive y -axis is pointing upwards. Rather than the polar angle θ from the beam axis, the pseudorapidity $\eta = -\ln(\tan \frac{\theta}{2})$ is used to describe particle positions and detector coverage, together with the azimuthal angle ϕ around the z -axis. To describe particle separation or detector resolution power, the distance in the pseudorapidity-azimuthal angle plane $\Delta R = \sqrt{\Delta\phi^2 + \Delta\eta^2}$ is commonly used. Transverse momentum $p_T = \sqrt{p_x^2 + p_y^2}$ and (missing) transverse energy $E_T^{(miss)}$ are defined in the x - y -plane.

3.2.1. Magnet System

The magnet system of the ATLAS detector consists of four superconducting magnets: one solenoid as well as one barrel and two endcap toroids.

The solenoid is aligned along the beampipe and placed between the inner detector and the barrel electromagnetic calorimeter. It provides a 2 T magnetic field parallel to the z -axis. The single layer coil of niobium-titanium (NbTi) conductor is optimized to achieve a high field with minimal radiative thickness. It ranges from 1.23 m to 1.28 m in radial direction, with an axial length of 5.8 m. Together with a 12 mm thick aluminum supporting structure, the whole assembly contributes only about 0.66 radiation lengths at normal incidence, which results from dedicated optimization of material thickness to assure minimal degradation of calorimeter performance.

The toroid magnets provide a magnetic field of 0.5 T and 1 T for the muon spectrometer in the barrel and end-cap regions, respectively. The barrel toroid spans 25.3 m along the z -axis,

and consists of eight coils inside racetrack-shaped vacuum vessels. The two end-cap toroids have an axial length of 5 m, each consisting of a single, rigid structure containing eight square coils.

3.2.2. The Inner Detector

The inner detector (ID) is inside the 2 T solenoid magnetic field, and is the part of ATLAS closest to the beam pipe. 7 m long and with a radius of 1.15 m, it covers a pseudorapidity range of $|\eta| < 2.5$, in which approximately 1000 particles per 25 ns will emerge from the interaction point. This constitutes challenging conditions in terms of required radiation hardness, as well as granularity to resolve very high track densities.

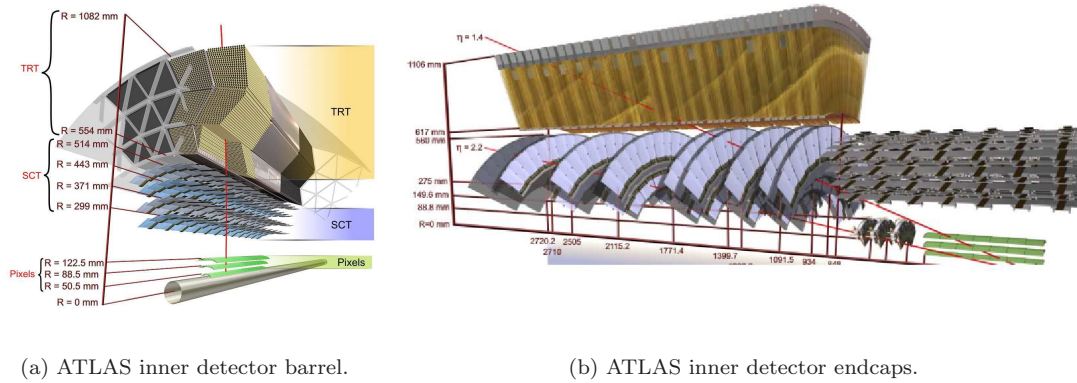
The ID consists of three subdetectors schematically shown in figure 3.4, the granularity of which decreases from the innermost silicon pixels (Pixels) over pairs of silicon strips in the semiconductor tracker (SCT) to the outermost gaseous straw tubes of the transition radiation tracker (TRT).

The Pixel Detector

Closest to the interaction point are three cylindrical layers of silicon pixels in the barrel region, and two times three silicon pixel end-cap discs. Ionizing particles passing through the semiconductor material give rise to electron-hole pairs which are channeled by an electric field to create a detectable current. With a size of $50 \times 400 \mu\text{m}^2$ per pixel, an intrinsic measurement accuracy of $10 \mu\text{m}$ in $R\text{-}\phi$ and $115 \mu\text{m}$ in z (barrel) or radial direction (end-caps) is reached. The innermost pixel layer, being only 5 cm away from the beam axis, has to withstand the highest radiation exposure, and will have to be replaced after approximately three years of operation. This layer is important for (secondary) vertex reconstruction and impact parameter measurements, which are input to tau lepton identification. Silicon pixels require a complex readout system containing a large amount of channels to enable the high granularity, which is only needed at the innermost layers with highest particle densities. At larger radii, coarser silicon strips are more cost efficient.

The Semiconductor Tracker

The silicon strips of the SCT consist of two 6.4 cm long daisy-chained modules with a strip pitch of $80 \mu\text{m}$, which are arranged in $40 \mu\text{rad}$ inclined double-layers to enable measurement of the z coordinate. There are four double-layers in the barrel region, in which the strips are aligned parallel to the z -axis, and two times nine end-cap discs, in which the strips are radially aligned.



(a) ATLAS inner detector barrel.

(b) ATLAS inner detector endcaps.

Figure 3.4. – Schematic drawing of the ATLAS inner detector barrel (left) and endcaps (right), traversed by charged particles (red lines) [45].

The intrinsic measurement accuracy reached is $17\text{ }\mu\text{m}$ in $R\text{-}\phi$ and $580\text{ }\mu\text{m}$ in z (barrel) or radial direction (end-cap region).

The Transition Radiation Tracker

Unlike these silicon parts of the inner detector, the TRT enveloping the SCT provides no three-dimensional space-point measurement, but gives $R\text{-}\phi$ information only. In the barrel region, 144 cm long drift tubes are aligned parallel to the z -axis, while the 37 cm long end-cap tubes are aligned radially in wheels. The intrinsic accuracy is $130\text{ }\mu\text{m}$ per straw. The TRT covers $|\eta| < 2.0$ compared to the $|\eta| < 2.5$ range of the former two subdetector parts, but provides a much larger number of typically 36 hits per track compared to 3 pixel and 4 SCT hits in the barrel region. It is made of 4 mm diameter polyamide tubes coated with aluminum and filled with a gas mixture of 70 % Xe, 27 % CO_2 and 3 % O_2 around a $31\text{ }\mu\text{m}$ diameter tungsten wire plated with gold. A voltage of 1.5 kV is held between the aluminum cathode and the golden anode. Charged particles traversing the TRT ionize its gas molecules, giving rise to electrons and ions which in turn drift to the electrodes, amplifying the signal by further ionization.

The polyamid between the drift tubes introduces a dielectric transition boundary for particles traversing the tubes, leading to transition radiation roughly proportional to the particle's energy. Two independent thresholds allow to distinguish between transition radiation and ionization effects, thereby contributing to particle identification by separating electron from pion signals. The ratio of high threshold to low threshold hits in the TRT is also used in tau identification to veto electrons which might fake hadronic tau decays.

The distance of a particle's trajectory to the anode wire is determined by the drift time measured in a testbeam before installation in the detector. The remaining left-right ambiguity can only be resolved by a combination of several measured hits. Though the resolution of this gaseous detector is inferior to that achieved with semiconductor technology, it contains much less material that can lead to multiple scattering and furthermore degrade the energy measurement in the calorimeters. In addition, the large amount of hits enables robust track reconstruction.

The amount of material in terms of radiation lengths X_0 averaged over Φ and integrated from the interaction point to the outer end of the TRT is estimated to be $0.469\text{ }X_0$ at $\eta=0$ and $1.126\text{ }X_0$ at $|\eta|=1.8$.

Exact knowledge of the position of all detector layers is crucial for the tracking performance. The material distribution of the inner detector has been measured with 2010 collision data at $\sqrt{s}=7\text{ TeV}$ by reconstruction of secondary vertices originating from hadronic interactions of primary particles [59]. While the overall material estimation in MC is found to be in good agreement with this measurement apart from a slight overestimation of material in the pixel detector, the profile of the vertex yield along the Φ axis shows the necessity of corrections to the center of the first and second pixel layers of $(-0.36\pm0.03)\text{ mm}$ in x -direction and $(-0.51\pm0.03)\text{ mm}$ in y -direction, and a smaller shift of the third pixel layer [59]. Furthermore, the center of the beampipe is found to be z -dependent, with a mean shift of $(-0.22\pm0.04)\text{ mm}$ and $(-2.0\pm0.04)\text{ mm}$ in x - and y -direction, respectively [59].

3.2.3. Calorimetry

The electromagnetic (EM) and hadronic (HCAL) calorimeters are located outside the solenoid, as depicted in figure 3.5(a). The former is finer in granularity to provide precision measurements of electrons and photons, while the latter is optimized for hadronic jet reconstruction and hermetic coverage for missing transverse energy.

Apart from energy measurements, good reconstruction of the jet shape contributes to particle identification: one essential tool in differentiating hadronically decayed tau leptons from QCD jets is the narrowness of the former compared to the latter. Another important capacity,

especially for studies of R-parity conserving Supersymmetry, is the missing transverse energy measurement, which ideally requires hermetically sealed calorimetry. The EM covers a pseudo-rapidity range of $|\eta| < 3.2$, the forward calorimeters of the HCAL provide electromagnetic as well as hadronic energy measurement up to $|\eta| < 4.9$. The whole calorimeter system is built as sampling calorimeter, alternating absorber material for shower initiation with active material for detection and readout. Liquid argon (LAr) technology is used for the latter in both the EM calorimeter and the HCAL end-caps, which has been chosen because of its intrinsic radiation hardness, linear behaviour and stability of response over time. Lead absorber plates alternate with LAr regions to initiate showering and to reduce the volume needed.

Electromagnetically interacting particles are brought to shower by the absorber material inducing bremsstrahlung, Compton scattering and conversion of photons to e^+e^- pairs. These shower particles ionize the LAr in the active regions, which is placed in a high-voltage field in order to collect the ionization charges.

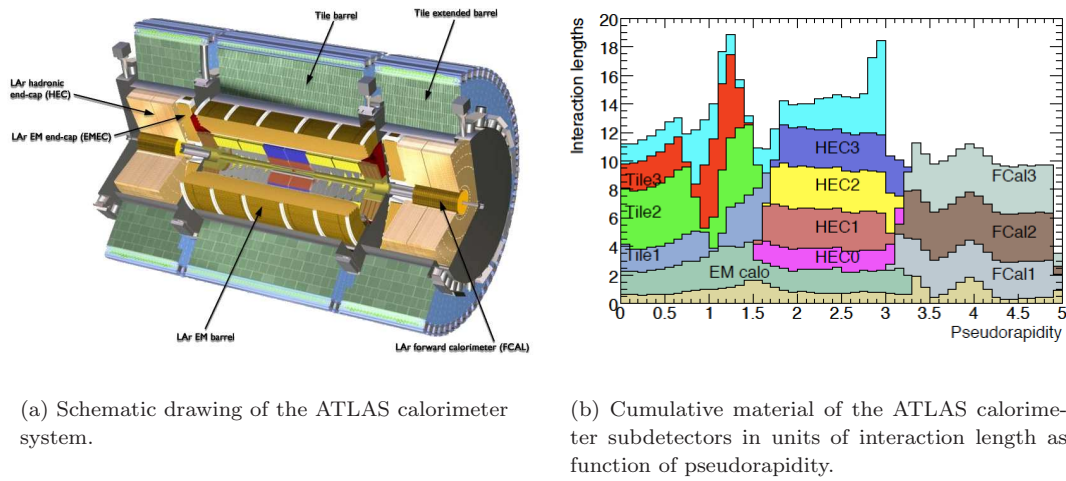


Figure 3.5. – The ATLAS Calorimeter System [45].

The Electromagnetic Calorimeter

The EM calorimeter is a LAr sampling calorimeter with zigzag-shaped kapton electrodes and lead absorber plates, divided into a barrel part of $|\eta| < 1.475$ with a mean granularity of $0.025 \times 0.025 \Delta\eta \times \Delta\Phi$, and two end-caps covering $1.375 < |\eta| < 3.2$. The novel accordion shape in radial direction allows particles to cross the same layer several times, and read-out at the front and rear ends of the plates enables a hermetic azimuthal coverage.

In the pseudorapidity region $|\eta| < 2.5$, which is optimized for precision physics, the EM calorimeter is segmented into three layers, while in the regions of higher $|\eta|$, two layers suffice. The innermost layer of the precision region offers the highest granularity in η , making it possible to distinguish between π^0 s and photons with an energy as expected from $H \rightarrow \gamma\gamma$ decays. The second layer collects the largest energy fraction, while the third collects only the tail of an electromagnetic shower. The total thickness of the EM calorimeter is > 22 radiation lengths X_0 in the barrel region and $> 24 X_0$ in the end-caps. In $|\eta| < 1.8$, a thin⁹ layer of active liquid argon inside the barrel cryostat, the so-called Presampler, provides measurement of the energy lost in dead material (e.g. cryostat walls) upstream of the EM calorimeter.

⁹The radial extension of the presampler measures 1.1 cm in the barrel region and 0.5 cm in the end-caps.

The Hadronic Calorimeter

The hadronic calorimeter consists of three parts: a central tile calorimeter, hadronic endcaps (HEC) in the higher $|\eta|$ region and a forward calorimeter (FCal) very close to the beam pipe. The hadronic tile calorimeter in $|\eta| < 1.7$, the active material of which is made of scintillator tiles between steel absorbers, is segmented in three layers and extends radially from 2.28 m to an outer radius of 4.25 m. It is further divided into a barrel region of $|\eta| < 1.0$ and two extended barrels at $0.8 < |\eta| < 1.7$. Strongly interacting particles initiate showers by interaction with the atomic nuclei of the absorber material. The shower particles then excite the scintillator atoms, which in turn produce scintillation light detected by photomultipliers when re-emitting the absorbed energy. Since the plastic scintillator tiles cannot withstand high radiation exposure, LAr technology is employed in the two more forward regions. The Hadronic End-cap Calorimeter uses copper as passive material and consists of two wheels per end-cap, each consisting of two longitudinal sections, extending the HCAL out to $|\eta| < 3.2$. Further extension to $|\eta| < 4.9$ is provided by the Forward Calorimeter, which is a LAr detector composed of three layers, the first of which is optimized for electromagnetic showers and uses copper as passive material, while the outer two use tungsten in order to provide hadronic shower measurement. To prevent problems caused by the high particle flux in these large $|\eta|$ regions, the liquid argon gaps had to be built smaller in the FCal than in the EM barrel calorimeter to provide highest possible density and prevent ion build-up problems.

The cumulative amount of material in front of the different calorimeter parts is shown in figure 3.5(b) in units of interaction lengths and as function of pseudorapidity.

The energy resolution in both the EM and HCAL can be parameterized as

$$\frac{\sigma_E}{E} = \frac{S}{\sqrt{E}} \oplus \frac{N}{E} \oplus C, \quad (3.3)$$

where the first term describes the stochastic nature of the showering, N parameterizes noise and pile-up, and the constant term represents systematic effects like leakage or non-uniform behaviour.

The constant term of the energy resolution of the EM calorimeter and FCal has been measured with $Z \rightarrow ee$ events using 39 pb^{-1} of 2010 data, and found to be between 1.2 % and 3.3 % in the different detector regions [60]. The stochastic term is seen to be described by the MC simulation within 5 %, which is investigated by the observed agreement in the J/Ψ peak. The non-uniformity of the calorimeter response in Φ has been measured to be less than 1 %, and the linearity is found to be at the order of 1 % (barrel) to 2 % (forward regions) [60].

3.2.4. Muon System

Outside the calorimeters, the muon spectrometer is installed, the conceptual layout of which is shown in figure 3.6. It is designed to measure the momentum of charged particles escaping the calorimeters, i.e. muons or long-lived charged particles predicted by some extensions of the Standard Model, like a long-lived $\tilde{\tau}_1$ decaying outside the detector. Muon detection based on ionization and drift time measurement is carried out by Monitored Drift Tubes (MDTs) and Cathode Strip Chambers (CSCs), while Resistive Plate Chambers (RPCs) and Thin Gap Chambers (TGCs) are part of the trigger system and are also employed to assign measured signals to certain bunch crossings. The magnetic field required to bend the muon trajectory along the z direction is created by the barrel toroid in $|\eta| < 1.4$ and by the end-cap toroids in $1.6 < |\eta| < 2.7$, while in the so-called transition region a combination of those fields provides the muon deflection. To gain a transverse momentum resolution of 10 % for 1 TeV tracks, a sagitta of 500 μm along the z -axis has to be measured with a resolution of $\leq 50 \mu\text{m}$. Muon momenta can be measured with the muon spectrometer stand-alone, or in combination with the inner detector measurement.

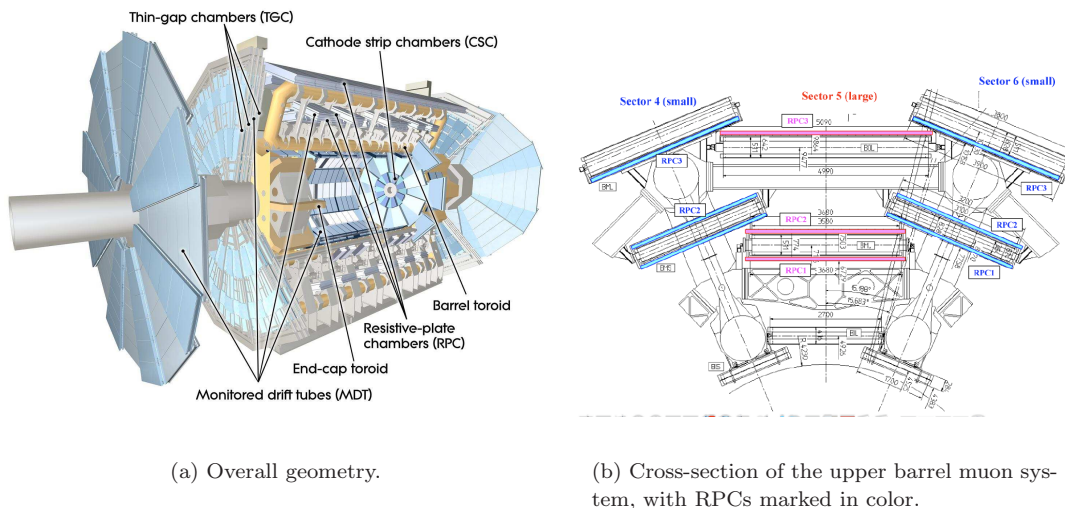


Figure 3.6. – Schematic drawing of the ATLAS muon spectrometer [45].

In the barrel region, three layers of muon chambers are cylindrically arranged, the outermost about 10 m away from the beam axis, while in the transition and end-cap regions, two times four wheels perpendicular to the beam axis are installed up to a maximal distance of 21.5 m away from the interaction point. At $|\eta| \approx 0$, a gap had to be left open for services to the detector parts and solenoid magnet inside, therefore a high momentum muon could escape without detection if its track is within $|\eta| < 0.08$.

Monitored Drift Tubes provide momentum measurement in $|\eta| < 2.7$, with an average precision of 80 μm per tube and 35 μm per chamber. In order to achieve the necessary resolution in the sagitta measurement, the positions of MDT wires have to be known up to 30 μm . To this end, an optical alignment system supplements precision mechanical assembly techniques to fulfill the alignment requirement. First measurements of the alignment in the bulk of the MDT endcap region ($1.4 < |\eta| < 2.0$) using cosmic and collision data recorded in 2009 and 2010, respectively, show no contradiction to the assumption that the achieved precision is at the order of 45 μm , although more data is required to prove this assumption [61].

Cathode-Strip Chambers are multiwire proportional chambers with higher time resolution and rate capability than MDTs, and are therefore used in the innermost layer of the forward region ($2.0 < |\eta| < 2.7$). The cathode plates of the CSCs are segmented into orthogonal strips allowing both coordinates to be measured with a precision of 40 μm in the bending plane and 5 mm in the transverse plane per chamber.

The possibility to trigger on muons and tag the bunch-crossing requires track information to be more accurate than the bunch spacing time of 25 ns. RPCs and TGCs are installed for that purpose in $|\eta| < 1.05$ and $1.05 < |\eta| < 2.4$, respectively. These trigger chambers measure the particle's position in two coordinates, the bending and the non-bending plane.

The luminosity weighted relative fraction of good data delivered during the $\sqrt{s} = 7$ TeV collisions in 2010 by the subdetectors described so far is listed in table 3.2, obtained with an integrated luminosity of 45 pb^{-1} of recorded data. The largest inefficiencies occurred in the LAr calorimeter systems and are mainly due to noise bursts and high voltage trips.

3.2.5. Forward Detectors

Besides interest in forward physics itself which is not the subject of this work, it is of great importance for any analysis to know the luminosity of collisions in a certain run, therefore the

	Inner Detector			Calorimeters				Muon Chambers			
subdetetcor	pixel	SCT	TRT	EM	Tile	HEC	FCal	MDT	CSC	RPC	TGC
uptime [%]	99.1	99.9	100	90.7	100	96.6	97.8	99.9	96.2	99.8	99.8

Table 3.2. – Fraction of good data delivered by subdetectors in 2010, luminosity weighted [51].

experiments have dedicated forward detector systems to measure this quantity independently of the machine. The main luminosity monitor, the Luminosity Cerenkov Integrating Detector (LUCID), is 17 m away from the ATLAS interaction point, and determines the luminosity delivered to ATLAS by measuring the proton remnants in the forward direction. A second detector 240 m away in z-direction, the so-called Absolute Luminosity for ATLAS (ALFA) detector, consists of Roman Pots up to 1 mm away from the beam pipe. Additionally, a Zero-Degree Calorimeter (ZDC) between LUCID and ALFA at $z = \pm 140$ m where the beam pipe separates into two tubes, can measure neutral particles at $|\eta| \geq 8.2$ in between the two beam pipes and determine the centrality of heavy-ion collisions.

Besides forward physics and luminosity measurement, these forward detectors can also be used to trigger on collision events.

3.2.6. Trigger System

When running at design luminosity, a data flux of about 1 PB/s is expected, read-out, storage and analysis of which is neither possible nor desired as most of it will be low-energy processes. Therefore a trigger system has been developed that selects events interesting for analyses in three steps: a fully hardware-based Level 1 (L1) trigger reduces the initial event rate of 40 MHz to 75 kHz within less than 25 μ s, its decision based on the muon trigger chambers and calorimeter information with reduced calorimeter granularity. If an interesting object such as a high p_T particle is found, its η - Φ -coordinates are passed to the next trigger level as so-called Regions-of-Interest (RoIs) for further investigation. The following Level 2 (L2) trigger uses the full detector information inside the RoIs, which accounts for approximately 2% of the full event information, and employs dedicated software to further reduce the event rate to 3.5 kHz within 40 ms on average. The third trigger level called Event Filter (EF) uses full detector information and offline analysis algorithms to reduce the rate within another 4 s to the final roughly 200 Hz, which accounts for a data flux of about 260 MB/s. The combination of L2 and EF is also called High Level Trigger (HLT).

Trigger items used in offline analyses are named after the thresholds on EF level, yet represent a trigger chain with different requirements at each trigger stage. If the rate of a trigger item gets too high with increasing luminosity, either the trigger threshold can be raised or the trigger is assigned a so-called prescale, which is a random selection of a subset of triggered events. A prescale of 1000 means that only one event of every 1000 which fire the trigger is written to disk. Such prescaled triggers are clearly not usable for searches of new physics like the one in this thesis, but are valuable for performance analyses. Events passing certain trigger items are written in streams which are collections of similar trigger chains, thus ordering datasets appropriate for certain analyses. The analysis presented in chapter 6 uses the *JetTauEtmiss* stream which includes trigger items as indicated by its name, while events triggered by light lepton triggers are collected in the *Egamma* and *Muon* streams. The *MinBias* stream collects events passing basic requirements so as to minimize the selection bias on the recorded sample. Though dominated by soft QCD events, the *MinBias* stream is in principle sensitive to new physics not thought of yet and which might not be selected by dedicated high energy triggers. Data of different streams contain partly the same events in order to allow most analyses to use one stream alone, thus causing potential overlap if triggers of different streams are combined in one analysis.

4. Event simulation and reconstruction

Probing physics theories at collider experiments involves comparison of theoretical expectations to data. In order to discover new physics and measure masses, cross sections and branching fractions, a detailed understanding of both the physics processes as well as of the interaction of the produced particles with the detector material is necessary to interpret observations. Hits in the inner detector and muon spectrometer as well as energy deposits in the calorimeters have to be sensibly combined and interpreted as physics objects from which to draw conclusions about the final state particles they originated from, before these in turn can be related to possible physics processes. To test what kind of signal to expect if a certain theory is realized in Nature, all scattering processes possible within this theory have to be modelled in the *event generation*, including all well known Standard Model processes. These have to be combined with a relative occurrence according to their cross-sections. Interactions of the final state particles produced in these collisions with detector material are then modelled in the *detector simulation* to obtain signals in the same format as produced by the ATLAS detector in real collision events. These signals are then processed in the *reconstruction* to build physics objects such as electrons, tau leptons and jets, which are input to the final *physics analysis*. In addition to the prediction of a detailed detector response for certain physics processes, simulation tools are used to investigate instrumental effects on real collision signals, as well as to develop and validate object reconstruction.

This chapter describes the event generation and detector simulation employed in samples used in this thesis. A more detailed description can be found in [62]. The same object reconstruction is applied to these simulated events and real collision data, and is explained in the last section of this chapter.

The whole chain of event generation, detector simulation and object reconstruction can be performed within the ATLAS software framework **athena** [63].

4.1. Event generation

Physics processes possible in pp collisions at the LHC are generated independent of the detector environment by *Monte Carlo generators* [64]. The typical event topology consisting of a hard process accompanied by the underlying event has already been explained in chapter 3.1.1. The Monte Carlo generation of such an event consists of the following steps:

Hard interaction: Partons within the colliding protons are selected to take part in the hard scattering with probabilities and energies according to the parton distribution functions, and the matrix element of the chosen interaction to be generated is calculated. The decay of short-lived resonances like W and Z bosons is also part of this hard process. The calculation is possible only up to a certain precision, mostly leading or next-to-leading order (NLO), and needs to employ approximations for non-perturbative processes originating from QCD confinement.

Radiation processes: Higher order processes like initial- or final-state radiation (ISR or FSR) of gluons or photons are usually not included in the matrix element calculation, but treated separately by different approximation schemes depending on the generator. In the *parton shower* approximation, complex $2 \rightarrow n$ processes are factorized into simpler sub-processes where particles are sequentially split as $q \rightarrow qg$ and $g \rightarrow q\bar{q}$ (in case of strong interacting

particles). Decreasing momentum transfer per radiation process enables to determine an end of the showering by a minimal particle momentum. In angular-ordered showers, the angle between the two particles produced in a single showering step decreases successively.

Hadronization: In the hadronization step, colored particles are combined into color-neutral states by phenomenologically obtained approximations.

Particle Decays: Short-lived hadrons generated in the previous step decay to the observable final state particles. Tau lepton decays are separately described by a dedicated program.

Underlying event: In addition to the hard process, interactions of the proton remnants have to be considered, both with each other as well as with the partons participating in the hard scattering.

Pile-up: Multiple pp-interactions between different protons within the same bunch crossing are considered by an overlay of the event of interest with several separately generated minimum bias events. Additionally, effects of cavern background, beam halo and beam gas interactions can be overlayed.

A schematic overview of the steps involved in event generation is shown in figure 4.1(a). This principle structure is common to all generators, yet differences arise in the implementation, making different generators suited for different purposes. A standardized interface following the *Les Houches accord* [66] allows the combination of different programs executing different parts of the event generation, as well as implementation of SUSY processes [67]. Tau leptons are treated as stable particles by the generators described below, all of which are interfaced to *Tauola* [68, 69] to separately generate tau lepton decays including spin correlations.

4.1.1. QCD dijets: PYTHIA

One of the most common generators is *Pythia* [70], which calculates the hard process in leading order in QCD and adds radiated particles iteratively according to the parton shower approximation described above. Hadronization is treated following the *Lund String* model illustrated schematically in figure 4.1(b): diverging colored particles are connected by a string containing energy proportional to the particle's distance according to linear QCD confinement. The string can break up to create a $q\bar{q}$ -pair when enough energy is contained, leading to two smaller strings

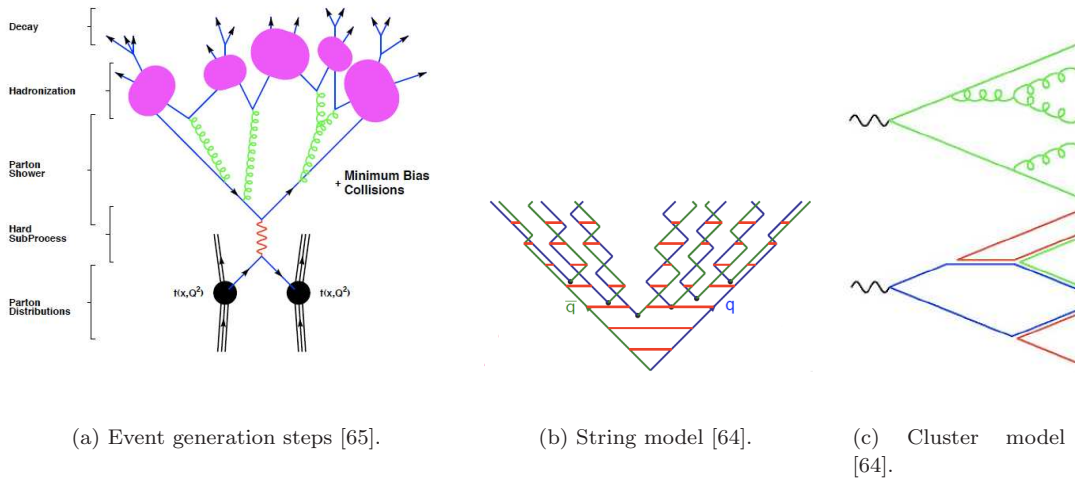


Figure 4.1. – Event generation (left) and schematic drawing of two hadronization models.

between the two initial and the two new particles, representing two color neutral states moving apart. This process is repeated until the energy of the outgoing quark-antiquark-pairs is no longer sufficient to build new particles. If several partons are emerging from one point, the string picture gets more complicated, but is still applicable. Gluons accompanying a quark pair lead to energy-momentum-carrying kinks on the string.

Pythia provides all SM processes as well as some additional models beyond the SM, but is only used for QCD dijet production in this thesis.

4.1.2. SUSY signal events: HERWIG

Supersymmetric processes are usually generated with *Herwig* [71–73], which is a leading-order generator similar to *Pythia*. It includes modelling of ISR and FSR, angular-ordered parton shower, hadronization and underlying event. The parton shower treatment accounts for azimuthal correlations due to spin effects. In difference to *Pythia*, hadronization is treated following the *cluster fragmentation* model based on pre-confinement due to the color structure in parton showers illustrated in figure 4.1(c). Adjacent partons can thus build color-neutral $q\bar{q}$ -pairs forming clusters with mesonic quantum numbers and small invariant masses that are independent of the hard scattering process. These excited mesons then decay into the observed final state particles. The underlying event can be generated by the external package *Jimmy* [74], which uses a multiple scattering model. *Herwig* includes a Les Houches accord interface to allow usage of external PDFs as well as implementation of new processes. An interface to *ISAJET* [36] provides SUSY spectrum and decay rate calculations for the most common SUSY models, including mSUGRA as well as MSSM and RPV scenarios.

All signal samples used in this thesis are generated with *Herwig+Jimmy*.

4.1.3. W and Z bosons: ALPGEN

Alpgen [75] is designed for SM processes in hadronic collisions with large jet multiplicities in the final states, therefore it is used in this thesis for $Z + jets$, $W + jets$ and partly for QCD multijets modelling. It calculates the exact leading order matrix elements for W and Z processes with up to 5 additional jets, and combines these with a parton shower generation by interfaces to *Herwig* or *Pythia*. High energetic jets are thus generated with the matrix element calculation, while additional soft jets are generated by the parton shower, with a jet p_T threshold configuring the transition between these methods. A dedicated matching algorithm prevents double-counting.

4.1.4. Top quark pair production: MC@NLO

MC@NLO [76, 77] is used for generation of $t\bar{t}$ processes in ATLAS because it gives a better description of the transverse momentum distribution of the produced top quarks than *Pythia* or *Herwig* [78]. It provides a full next-to-leading-order calculation of the hard process in QCD perturbation theory, and is interfaced to *Herwig* for generation of the hadronization. Matching of NLO computations with parton shower follows the subtraction method to avoid double-counting, leading to negative event weights.

4.2. Detector simulation

The output of the event generation is a set of stable¹ final state particles with their four-momenta. The detector simulation then calculates the trajectories of these particles through the detector volume and their interaction with the detector material they traverse thereby. The output of the detector simulation is transformed into signals in the format identical to real collision data, which is used as input to the event reconstruction. In this *digitalization* step, the hard scattering

¹Particles are considered stable by the event generators if $c\tau > 10$ mm.

event can be overlaid with minimum bias², beam halo, beam gas and cavern background events. Furthermore, detector noise can be added at this stage, and the hardware-based first trigger level is simulated in *pass-through* mode, i.e. the trigger decision is stored but no event is discarded at this stage.

4.2.1. Full detector simulation

The *full simulation* calculates every subdetector part having an impact on the state of the particle successively, based on **Geant4** [79]. The ATLAS geometry is provided in **athena** and has to be regularly updated to represent a realistic detector status including effects of misalignment or material distortions. Most of the samples used here are made with the full detector simulation. However, full detector simulation is a CPU-consuming effort limiting the amount of data possible to simulate in a reasonable time and with finite resources. Therefore two *fast simulation* programs called **Atlfast** are available.

4.2.2. Fast detector simulation

Atlfast-I

Atlfast-I [80, 81] approximates detector effects as a whole by smearing the four-momenta of the final state particles according to the detector resolution. No digitalization step is required, and the event reconstruction is replaced by directly altering the particle's four-momenta. Tau identification efficiency and fake rate are taken from the full simulation and parameterized in bins of transverse momentum and pseudorapidity. This fastest of all detector simulation options is employed in the part of the analysis described in chapter 5.3.2, where a large number of simulated events is necessary in order to obtain a calibration.

Atlfast-II

FastCaloSim [82] and **Fatras** [83] provide approximations of the calorimeters and of the inner and muon detectors, respectively, by using a simplified material distribution in the respective subdetectors. This approach has the advantage that information about e.g. single pixel hits or calorimeter energy depositions are available, thus the full reconstruction algorithms can be run and the approximation of one subdetector can be combined with full simulation of other subdetectors. $Z \rightarrow \nu\nu$ events of the analysis presented in chapter 5.4 are simulated with **FastCaloSim** in combination with a full simulation of the inner and muon detectors, also known as **Atlfast-II**. Rather than simulating detailed interactions of particles with the detector material, **FastCaloSim** approximates the calorimeter shower shape by parameterizing the longitudinal and lateral energy deposition profile under consideration of the material distribution. A combination of **FastCaloSim** and **Fatras** is called **Atlfast-IIF**, but is not used in this work.

4.3. Event reconstruction and definition of physics objects

For a possible combination of different SUSY search channels, a common object definition is required. This chapter briefly describes the object reconstruction and identification used in the ATLAS SUSY group, focussing on tau leptons and missing transverse energy \cancel{E}_T as they are the key signature of this analysis. It should be kept in mind that the algorithms described in this chapter are the ones used in this thesis, but alternative reconstruction methods are available within the ATLAS software for all objects.

Different identification methods have to be considered for the 10 TeV study which aims at a minimum of 1 fb^{-1} of collected data in order to perform a measurement of the endpoint of the

²Mostly inelastic scattering events with low transverse energy, as predominantly selected by the *MinBias* trigger.

di-tau invariant mass spectrum, and for the early data analysis which deals with the first 7 TeV data collected until the end of 2010. While this discrimination is motivated by the different levels of detector understanding expected at different times of data-taking influencing particularly the complexity of variables used in tau identification, further changes are due to different software releases used in the two analyses.

4.3.1. Inner Detector Tracks

Inner detector tracks are an important component of object reconstruction and will be used in all algorithms described below.

To reconstruct a track, the fine granularity of the pixel detector and first layer of SCT is exploited to build track seeds out of space-points from these four ID compartments. These seeds are then extended through the full SCT to form track candidates and fitted to reject fake tracks, before they are finally extrapolated into the TRT and refitted using the information of all ID components.

Secondary tracks, e.g. from long-lived particles or conversions, are then found by a method called back-tracking. This algorithm starts from track segments in the TRT which have not been used by the procedure described above, and extends them to the SCT and pixel detector.

4.3.2. Jets

Strongly interacting particles hadronize to form collimated bundles of objects called jets, which are part of almost every interaction at hadron colliders and of particular importance to many SUSY signatures due to the long decay chains starting with squark and gluino decays. They also pose the main background for hadronically decaying taus, where the huge production cross-section of SM QCD processes at hadron colliders makes an effective suppression of such jets mandatory in order to retain a clean tau signal.

Reconstruction of hadronic jets is based on topological clustering [84]: calorimeter cells with an energy signal above a certain threshold X , which is measured in units of cell resolution $\sigma_{\text{noise,cell}}$, are taken as seeds. Adjacent cells with an energy above noise $E_{\text{cell}}/\sigma_{\text{noise,cell}}$ exceeding a second threshold Y are then assigned to the seed cell, and in a third step neighbouring cells with a respective threshold Z are added and finalize the topocluster. Standard values for $X/Y/Z$ are $4/2/0$. The noise level σ_{noise} is defined as the quadratic sum of electronic noise and the pile-up contribution.

Topoclusters formed in this way are then grouped to jets by either a *cone* or an *anti- k_T algorithm*. The former is used in the analysis presented in chapter 5, but was superseded by the latter in the analysis of chapter 6 due to its infrared and collinear safety. A jet algorithm is infrared safe if the combination of objects into jets is independent of the presence of additional soft particles between them. Collinear safety is given if the jet reconstruction yields the same result whether a certain amount of transverse momentum is carried by one single object or by two collinear particles the original object splits into.

Cone jets All topoclusters with energy exceeding a certain seed threshold are regarded as jet seeds by the cone algorithm. The seed with highest transverse momentum is taken as starting point, and all clusters within a fixed radius R_{cone} in $\Delta R = \sqrt{\Delta\eta^2 + \Delta\Phi^2}$ to the jet axis are combined with the jet seed. The jet axis is recalculated using the four-momenta of all objects in the jet, and additional clusters are collected within the thus redefined cone. This procedure is iterated until the cone does not change anymore. All jet seeds are treated this way in the order of decreasing transverse momentum. Then a *split-and-merge* algorithm is applied to partly correct for the lack of infrared safety. If two jets share a certain component, the jets are merged or split depending on whether the transverse momentum of the shared constituent exceeds a

certain fraction f_{sm} of the less energetic jet or not. The free parameters of this cone algorithm are set to $f_{sm} = 0.5$, $R_{cone} = 0.4$ and a seed threshold of $p_T > 1$ GeV in ATLAS³.

Anti- k_T jets The infrared and collinear safe anti- k_T clustering algorithm [85] is default in ATLAS at the time of writing. For a cluster i , the minimal momentum weighted distance to other clusters j , $d_{ij} = \min(k_{Ti}^{2p}, k_{Tj}^{2p}) \frac{\Delta_{ij}^2}{R^2}$, is compared to its squared transverse momentum with respect to the beam, $d_{iB} = k_{Ti}^{2p}$, where $\Delta_{ij}^2 = (y_i - y_j)^2 + (\Phi_i - \Phi_j)^2$ and k_{Ti} , y_i and Φ_i are the transverse momentum, rapidity and azimuth angle, respectively. The parameter R governs the radius and is set to 0.4 by jet reconstruction methods used in this work⁴. The parameter p adjusts the relative power of energy versus geometric scales. If $d_{ij} < d_{iB}$, cluster j is allocated to cluster i and their combination is added as a new member to the list of objects to be combined, otherwise cluster i is regarded as a jet and removed from the list. This procedure is reiterated until all clusters are assigned to jets.

The standard inclusive k_T algorithm is reproduced by setting p to 1, thus the algorithm using the value $p = -1$ used here is called anti- k_T algorithm.

Jet energy calibration An exact reconstruction of the jet energy is crucial for SUSY analyses, since any mismeasurement leads to a false calculation of the missing transverse energy. Several calibration steps account for a correct jet energy measurement:

Calorimeter cells are calibrated at the electromagnetic (EM) scale, which is set in test beams such that the energy of electrons and photons is correctly reproduced. Thus jets built from these cells are naturally also calibrated at EM scale.

The first correction to this is to take detector effects like dead material, crack regions, noise, longitudinal leakage and out-of-cone corrections into account, as well as calorimeter non-compensation.

To calibrate these jets to hadronic scale, a H1-style [86] cell weighting procedure is applied: since hadronic showers are broader than electromagnetic ones, the energy density is smaller, therefore jets with low signal densities are considered hadronic jets and get a weight proportional to the electron to pion ratio, while jets with high signal densities do not need such a weight. This weighting mechanism is applied on single cell signals, the values of the weights depending on the cell signal density and its position. This procedure can be applied globally on the jet level (*global cell weighting GCW*), or locally on the topocluster level before jet building (*local cluster weighting LCW*).

In this calibration step, also physics effects like corrections for the underlying event, pile-up, and initial and final state radiation are considered.

Now the jets are calibrated at the particle level, meaning they should correctly reproduce the energy of all final state particles in the jet. To get to the energy at parton level, further calibration steps are necessary, which depend on the type of interaction and are for example different for quark and gluon jets.

In early data analysis, EM scale jets are calibrated to the hadronic scale with a simple η and p_T dependent correction factor which is currently still taken from MC, but validated with data [87] and will be measured from γ -jets or di-jet samples in further studies. Unlike the LCW and GCW calibration schemes, the cell energy density and topocluster properties are not taken into account. This correction is currently obtained by running the jet reconstruction algorithm of interest on simulated truth jets, i.e. jets composed of final state particles after hadronization before a detector simulation has been performed. Corrections for pile-up and the jet origin⁵ are also applied in this so-called *EM+JES* scale.

³Cone jets with $R_{cone} = 0.7$ are also available in the default ATLAS reconstruction output.

⁴Anti- k_T jets with a radius of $R = 0.6$ are also used in some ATLAS analyses.

⁵The jet origin correction leaves the jet energy unaffected, but improves the angular resolution and thereby the p_T -response by replacing the geometrical centre of ATLAS by the primary vertex as reference point for the jet reconstruction.

In SUSY analyses, only central ($|\eta| < 2.5$) jets with a transverse momentum of at least 20 GeV are considered.

Measured jet energy scale and resolution performance First measurements of the calorimeter response obtained with $866 \mu\text{b}^{-1}$ of $\sqrt{s} = 7$ TeV pp-collision data show a calorimeter uncertainty of 2-5 % on central isolated hadrons, which propagates to an uncertainty of 1-3 % on the final calorimeter jet energy scale for jets with $15 \text{ GeV} < p_T < 2.5 \text{ TeV}$ in $0 < |\eta| < 0.8$ [88]. Of greater importance to the analysis presented in chapter 6 is the overall jet energy scale (JES) uncertainty, which is not only affected by the response of the ATLAS calorimeters but also by uncertainties related to noise and the JES calibration method, as well as model uncertainties in the event generation used in the MC simulation. In pp-collisions with $\sqrt{s} = 7$ TeV, a JES uncertainty of less than 6.5 % has been measured for central jets in $|\eta| < 0.8$ and with $p_T < 60 \text{ GeV}$, improving with rising transverse momentum up to 4 % for jets with $p_T > 200 \text{ GeV}$ [89]. The uncertainty is larger in the endcaps ($0.8 < |\eta| < 3.2$) with 9 % improving to 4.5 % for jets with $p_T < 60 \text{ GeV}$ and $p_T > 200 \text{ GeV}$, respectively, and 15 % for jets with $p_T < 60 \text{ GeV}$ in the forward regions ($3.2 < |\eta| < 4.5$) [89]. These measurements are valid for jets with $p_T > 20 \text{ GeV}$ and do not include the uncertainty caused by multiple pp-interactions.

In addition to the jet energy scale, the jet energy resolution might contribute to the systematic uncertainty of physics results. The relative momentum resolution can be parameterized analogously to the energy resolution of the calorimeter in equation 3.3 as

$$\frac{\sigma_{p_T}}{p_T} = \frac{N}{p_T} \oplus \frac{S}{\sqrt{p_T}} \oplus C, \quad (4.1)$$

where the three independent terms N , S and C parameterize noise, stochastic fluctuations and constant systematic effects, respectively. A measurement with 35 pb^{-1} of pp-collisions with $\sqrt{s} = 7$ TeV shows an agreement of ATLAS data with MC simulation within 10 % for jets with $30 \text{ GeV} < p_T < 500 \text{ GeV}$ in the rapidity range $|y| < 2.8$ [90].

4.3.3. Tau leptons

With a decay length of $c\tau = 87 \mu\text{m}$, tau leptons decay within the ATLAS detector and have to be identified by their decay characteristics. Due to the difficulty of distinguishing primary leptons from electrons or muons which emerge from a leptonic tau decay, standard tau identification algorithms in ATLAS concentrate on the 64.8 % of taus that decay hadronically⁶. Therefore in the context of tau reconstruction, a tau lepton refers to a hadronically decayed tau lepton if not stated otherwise.

Hadronic tau decays take place predominantly via vector meson resonances, most importantly the a_1 and ρ , but finally end in pion production. Tau leptons are therefore regarded as narrow jets of charged (and neutral) pions. A challenge to tau lepton identification is posed by hadronic jets, which are produced with cross-sections orders of magnitudes higher than those producing isolated tau leptons of interest for analyses. Compared to such QCD jets, tau jets are more collimated, contain fewer and more isolated tracks, and deposit a larger fraction of their energy in the electromagnetic calorimeter than in the hadronic calorimeter. Furthermore, a secondary vertex can be reconstructed if the tau lepton decay products contain 3 charged pions (3-prong), or an impact parameter in case of 1 charged decay particle (1-prong).

The tau objects employed in offline analyses are first built from calorimeter and track information in the tau *reconstruction*, which defines tau candidates and calculates their properties without any discrimination between tau and QCD jets. Almost every QCD jet also creates a tau candidate. The separation of tau candidates emerging from true tau leptons or QCD jets is performed in the separate tau *identification*.

⁶A new independent tau reconstruction and identification package (**PanTau** [91, 92]) which includes tau lepton decays into muons is under development at the time of writing.

Tau candidates are calibrated using the GCW scheme, using all cells within $\Delta R < 0.4$ of the tau barycenter.

Tau leptons in early data analysis

Tau lepton reconstruction is done by a combination of two algorithms⁷, using as seed either a track with $p_T > 6$ GeV which satisfies certain quality criteria on impact parameter and silicon hits, or a calorimeter cluster, which is formed in three steps by the topocluster algorithm from cells that exceed noise by at least 4, 2 or 0 times σ_{noise} , respectively. The tau candidate is required to have a calibrated transverse momentum of $p_T > 10$ GeV. The anti- k_T algorithm described in the context of jet reconstruction is used to group topoclusters to tau jets, and tracks within $\Delta R < 0.3$ are associated to the tau candidate. If such a calorimeter-seeded tau candidate can be matched to a seed track in $\Delta R \leq 0.2$, it is classified as a so-called overlap candidate. The overlap occurrence is roughly 70 %. 25 % of the tau leptons have only a calorimeter seed, while 5 % are found by the track-seeded algorithm only.

Tau properties such as energy and position are calculated from the calorimeter information for calorimeter seeded candidates, while the tau lepton direction is calculated from tracking information and the energy calculation uses an energy flow approach for track-seeded tau lepton candidates. For overlap candidates, the position and track multiplicity of the tau is defined by the track-based algorithm, while its transverse energy is calculated by the calorimeter cell information.

When this reconstruction step is completed, the separation of tau leptons from QCD jets can be made by a likelihood discriminant (Llh), a boosted decision tree (BDT) [95] or a simple cut based discrimination (SC). Three selection criteria loose, medium and tight are predefined such that the tau lepton identification efficiency is approximately 70 %, 50 % and 30 %, respectively. In this context, the efficiency is defined with respect to all reconstructed tau lepton candidates.

Following the tau performance group recommendations, this analysis makes use of the BDT discriminant. While the predefined selection criteria are investigated as reference, the selection is optimized in chapter 6.3 to meet the demands of this analysis. This BDT classifier is based on seven discriminating variables:

R_{EM} , the *electromagnetic radius*, is the calorimeter shower width calculated from E_T weighted calorimeter clusters,

R_{track} is the average distance of the tracks from the jet axis, weighted by p_T ,

f_{core} the centrality fraction is the ratio of transverse energy in the calorimeter within $\Delta R < 0.1$ to that within $\Delta R < 0.4$,

m_{topo} is the invariant mass of all topoclusters within the tau candidate,

m_{track} is the invariant mass of all tracks associated to the tau candidate (only defined for multiprong taus),

f_{EM} the electromagnetic fraction is the fraction of the total energy which is reconstructed in the presampler and the first two EM calorimeter layers, and

f_{track1} is the transverse momentum fraction of the leading track with respect to the transverse momentum of the tau candidate.

The likelihood discriminant in the software version of this analysis also uses these variables but without f_{core} , the simple cut analysis uses only the uncorrelated variables R_{EM} , R_{track} and f_{track1} . Unlike the jets used in early data analysis which are calibrated at the EM+JES scale, tau jets are initially calibrated by global cell weighting and then corrected by hadronic tau calibration factors in a p_T and η dependent way.

⁷The track seeded **tau1p3p** [93] and the topocluster seeded **tauRec** [94] algorithm.

Tau leptons in the 10 TeV analysis

The studies performed for 10 TeV and 14 TeV centre-of-mass energies use an older software release than the 7 TeV analysis, therefore some differences in the tau lepton reconstruction and identification exist:

The two reconstruction algorithms described above are not merged yet, but have to be used separately. This work has chosen the calorimeter seeded approach since the overall performance of this algorithm proved to be better for the purpose of this analysis (see chapter 5.3.2).

The cone algorithm instead of the anti- k_T algorithm is used to group topoclusters, which is consistent with the jet reconstruction in the according analysis.

For tau lepton identification, a likelihood is the recommended discriminant, BDT and SC are not available⁸.

The likelihood discriminant [96] used in the 10 TeV analysis is defined as $d = \frac{L_S}{L_B + L_S}$ ⁹, where $L_{S,B}$ are the likelihoods of real and fake tau candidates, respectively. These likelihoods are products of probability density functions of the following variables (for calorimeter-seeded candidates):

$R_{EM}, R_{track}, m_{track}$ defined as in the BDT description above,

$E_T/p_T^{lead.track}$ is the ratio of tau energy to the momentum of the leading track in the transverse plane,

R_{HAD} is the hadronic radius defined analogously to R_{EM} ,

N_{strip} is the number of hits in the η strip layer, where hits count within $\Delta R < 0.4$ of the cluster axis if the energy deposit is above 200 MeV,

$\frac{d_0}{\sigma_{d_0}}$ is the transverse impact parameter of the leading track divided by its resolution (impact parameter significance),

f_{ET} is the ratio of transverse energy in the EM calorimeter within $0.1 < \Delta R < 0.2$ to that within $\Delta R < 0.4$,

Isolation fraction is the ratio of electromagnetic transverse energy within $0.1 < \Delta R < 0.2$ to that within $\Delta R < 0.4$,

$\Delta\eta$ is the width of the transverse energy deposited in the η strip layer, calculated as the E_T -weighted variance in η ,

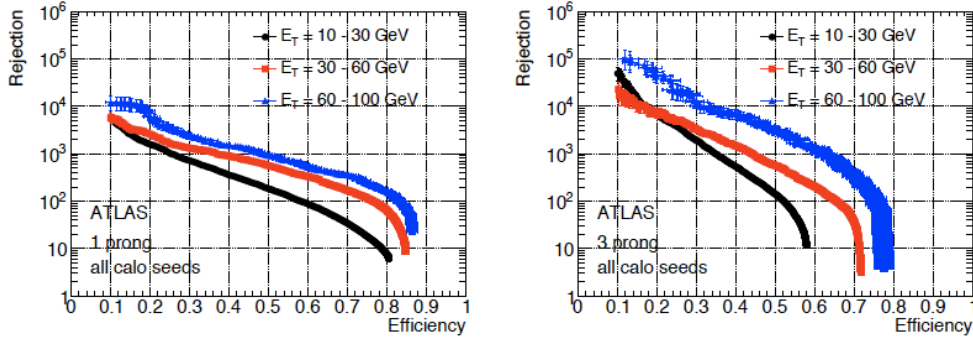
$L_{xy}/\sigma_{L_{xy}}$ is the transverse flight path significance, where the transverse displacement L_{xy} is defined with respect to the primary vertex.

Electron and muon rejection

In addition to this QCD suppression, a veto on electrons faking tau leptons is determined using the ratio of the electromagnetic transverse energy and the transverse momentum of the leading track, as well as the ratio of high threshold to low threshold hits in the TRT. This veto retains 95 % of tau leptons from $W \rightarrow \tau\nu$ events while suppressing electrons from $W \rightarrow e\nu$ by a factor of 60 [40]. Alternatively, a separate likelihood discriminant is available for separating electrons from tau leptons [97]. This electron suppression tool has been used in the 14 TeV and 10 TeV analyses, yet since it is not maintained in the newer software releases, the electron veto is used in the 7 TeV study. For a tau identification efficiency of 95 %, the electron background efficiency with the dedicated likelihood is about 4 % [97].

⁸Alternatives to the likelihood are a neural network or PDERS discriminant.

⁹Out of technical reasons, the transformed discriminant $d' = -\ln \frac{1}{d} - 1$ is used, which shows a gaussian-like spectrum.



(a) Performance of the tau likelihood discriminant used in the 10 TeV study [98].

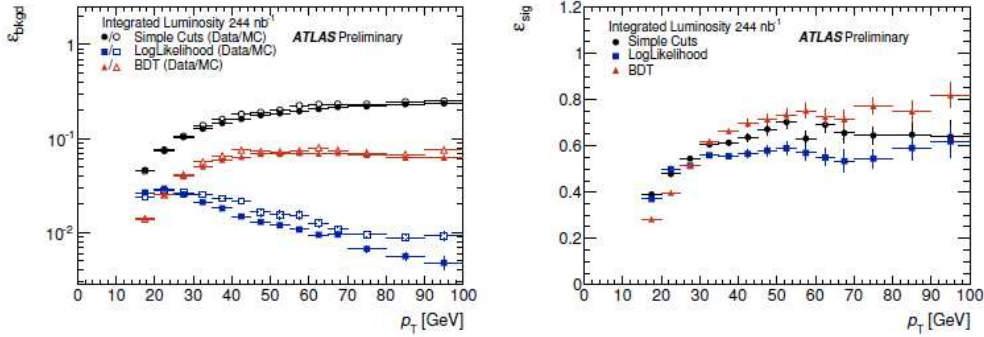
(b) Performance of the tau BDT discriminant used in the $\sqrt{s} = 7$ TeV early-data study [99].

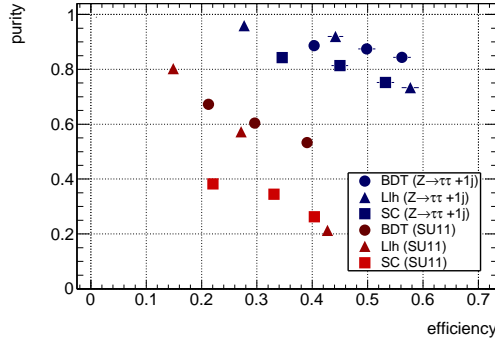
Figure 4.2. – (a) Rejection versus efficiency in three different p_T regions with the Llh used in the 10 TeV study, and (b) background and signal efficiency with the medium selection of SC, BDT and Llh identification in the early-data analysis software version.

In order to veto a muon track being misinterpreted as a leading track for building a tau lepton candidate, a minimal energy deposition of 5 GeV at EM scale is required around the track. Less than 1% of tau leptons are lost due to this requirement, while 3.3% of isolated muons are still misidentified as taus [40].

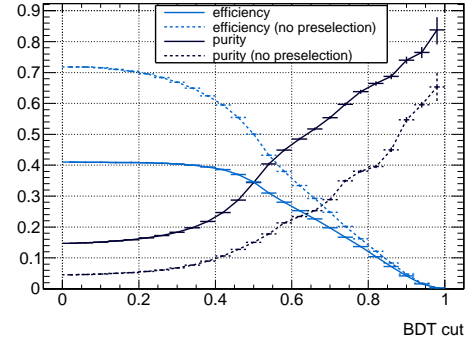
Tau identification performance

Figure 4.2(a) shows the rejection of QCD jets as a function of tau identification efficiency for three different energy ranges and separately for 1-prong and 3-prong tau leptons, with the likelihood version used in the $\sqrt{s} = 10$ TeV analysis. The background rejection is defined in terms of the background efficiency ϵ_{BG} as $r = \frac{1 - \epsilon_{BG}}{\epsilon_{BG}}$. For low- p_T tau leptons, QCD rejection is significantly worse in the high efficiency regions compared to harder tau leptons, both for 1-prong and 3-prong tau candidates. This p_T -dependence of the tau identification performance is more prominent for multiprong tau candidates.

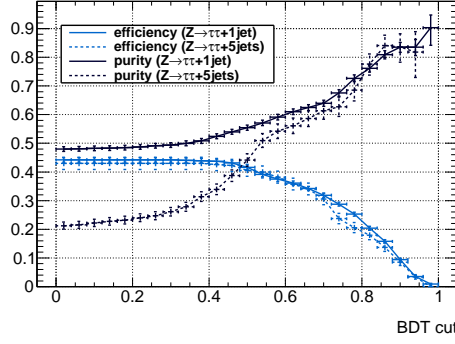
Figure 4.2(b) shows the p_T -dependent signal and background efficiencies for the medium BDT selection [99] in comparison with the Llh and SC identification of the tau identification version used in the $\sqrt{s} = 7$ TeV analysis. While the signal efficiency is only known from MC so far, background efficiencies are given both for MC and measured from data. Signal tau leptons are taken from $Z \rightarrow \tau\tau$, the MC background efficiency uses *Pythia* QCD dijets and the fake rate



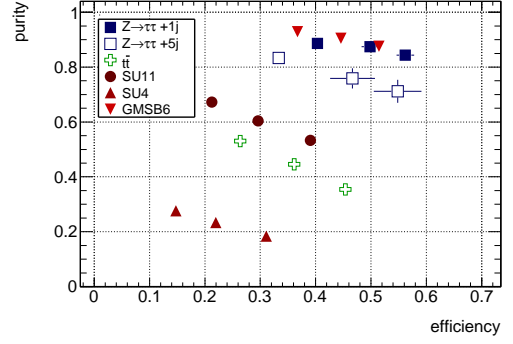
(a) Purity versus efficiency: comparison of BDT, Llh and SC discriminants. Loose, medium and tight selection for $Z \rightarrow \tau\tau + 1$ jet and SU11.



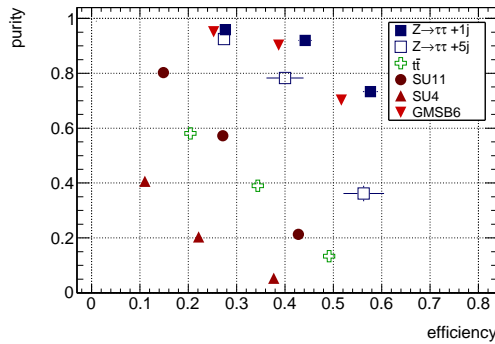
(b) Purity and efficiency as function of BDT cut in SU11 with and without tau preselection requirements.



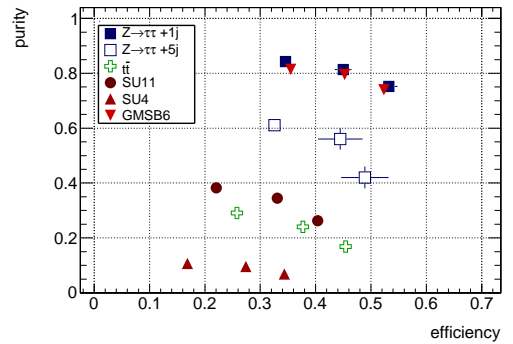
(c) Purity and efficiency as function of BDT cut in $Z \rightarrow \tau\tau$ with 1 or 5 additional jet(s).



(d) BDT performance in different event topologies (loose, medium and tight selection).



(e) Llh performance in different event topologies (loose, medium and tight selection).



(f) SC performance in different event topologies (loose, medium and tight selection).

Figure 4.3. – Performance of tau discriminants in the version as used in the $\sqrt{s} = 7$ TeV study.

measured from data uses QCD dijet enriched events with a tag-and-probe method. The BDT is shown to provide the best signal efficiency, while the BG efficiency is lower than for the SC but higher than for the Llh selection. However, data and MC show better agreement for the BDT than for the Llh.

Figure 4.3(a) compares the efficiency versus purity behaviour for loose, medium and tight selection of the three discriminants, both for an easy SM topology of $Z \rightarrow \tau\tau$ with only one additional jet as well as for the target SUSY scenario SU11. In both cases, the BDT outperforms the Llh and SC discriminants, with the Llh covering the broadest efficiency region and showing the steepest purity decrease with rising efficiency. Efficiency and purity are here defined as $\epsilon = \frac{N(\tau^{match})}{N(\tau^{true})}$ and $p = \frac{N(\tau^{match})}{N(\tau^{reco})}$, where τ^{reco} are reconstructed tau leptons that pass the appropriate identification criteria (loose/medium/tight) as well as additional preselection requirements. τ^{match} are reconstructed tau leptons matched to a true hadronic tau lepton in $\Delta R < 0.2$, and τ^{true} are truth taus in $|\eta| < 2.5$ that decayed hadronically, and the visible decay products of which satisfy $E_T^{vis} \geq 10$ GeV. Tau preselection cuts applied in this figure are electron and muon veto, exactly one or three tracks, a charge of ± 1 and a minimal transverse energy of $E_T > 15$ GeV. The effect of these requirements is illustrated in figure 4.3(b), where the efficiency and purity are shown as functions of the BDT selection cut with and without these additional criteria. For a loose BDT selection, the efficiency loss by applying these cuts is larger than the purity gain, yet for a BDT cut larger than 0.5 as applied in the analysis, the purity gain is comparable or even larger than the loss in efficiency.

The impact of more jets per event on the purity of the tau selection is large for loose BDT requirements and decreases with rising BDT cut, as shown in figure 4.3(c) by the comparison of $Z \rightarrow \tau\tau$ events with one or five additional jets. The effect of the additional jets on the tau reconstruction and identification efficiency is small and hardly depends on the BDT selection cut.

Tau lepton identification algorithms have been trained on $Z \rightarrow \tau\tau$, $W \rightarrow \tau\nu$ and $H/A \rightarrow \tau\tau$ processes, which are very clean compared to the average SUSY event, and have harder tau leptons than present in many SUSY points.

Depending on the exact SUSY model and parameters, the tau lepton identification performance can be very different, as made apparent in figure 4.3(d-f) where the tau lepton identification efficiency and purity after tau preselection cuts are shown for the SUSY points SU11, SU4 and GMSB6 in comparison to the SM processes $t\bar{t}$ and $Z \rightarrow \tau\tau$.

The relative performance of the three discriminants is very similar, with SU4 being the hardest scenario for tau reconstruction while SU11 and GMSB6 are similar to $t\bar{t}$ and $Z \rightarrow \tau\tau + 1\text{jet}$, respectively.

4.3.4. Electrons

The electron reconstruction algorithm `egamma` used in this thesis is optimized for isolated electrons, which are the electrons relevant for SUSY analyses. Algorithms dedicated to low p_T electrons and electrons within jets or to forward electrons are present in the ATLAS software framework, but will not be described here.

The electron reconstruction is seeded by a cluster in the EM calorimeter that is built with a sliding-window algorithm. These clusters thus have a rectangular shape with fixed size, positioned in a way as to maximize the energy in the cluster. Matching tracks not belonging to photon conversions are searched for in two steps, first using the position of the track origin, secondly an extrapolation of the track to the calorimeter. Tracks matched to a cluster are required to have a momentum consistent with the cluster energy within $E/p < 10$. Approximately 93% of true isolated electrons ($p_T > 20$ GeV, $|\eta| < 2.5$) are thus reconstructed as electron candidates [40].

Electron identification is based on calorimeter shower shapes, quality of the matching of track and cluster, as well as a large fraction of high threshold TRT hits.

Cut-based identification criteria define different levels of electron selection: loose, medium and tight¹⁰. An isolation flag based on the calorimeter energy fraction in a cone of $\Delta R = 0.2$ around the electron axis is also computed.

In this work, isolated medium electrons with $p_T > 10$ GeV and $|\eta| < 2.5$ are used.

For early data analysis, the isolation requirement is dropped, only electrons within an $|\eta| < 2.47$ are considered and the p_T -threshold is raised to 20 GeV. Furthermore, the medium electron identification is replaced by a so-called *robust* medium criterium, which corrects for differences in the shower shapes modelled in MC compared to data leading to a lower efficiency in data than MC simulation if the former electron identification is used. Electrons are rejected if they touch a calorimeter region with dead OTX¹¹ readout electronics, maps of which are taken in real collision data runs. The latest map from 2010 data taking is used for MC events.

These changes of electron identification criteria are in accordance with the egamma working group recommendations based on first data measurements with $W \rightarrow e\nu$ and $Z \rightarrow ee$ events [100].

In the transition region between the EM barrel and end-caps, $1.37 < |\eta| < 1.52$, electron identification performance is worse than average. Therefore, if a reconstructed electron passing the above selection is found in that so-called crack region, the event is rejected in the analysis.

4.3.5. Muons

In this work, so-called combined muons¹² are used, which are muons reconstructed in the muon chambers by a standalone algorithm¹³ matched to tracks in the inner detector.

The standalone algorithm first reconstructs track segments in each of the three layers of muon chambers and combines them into tracks. When these tracks are extrapolated to the interaction point, corrections for energy loss in the calorimeter is accounted for based on the material crossed by the track.

Tracks in the inner detector are built independently, as described in section 4.3.1.

Combined muons are then built by matching standalone muon-spectrometer tracks to ID tracks, which is done by a statistical combination of the independent tracks. The quality of the combination is characterized by the chi-square of the match, demands on which can be used in each analysis. The transverse momentum of the muon is also calculated by combining information of the two tracks, where the muon-spectrometer is performing better for high p_T muons, while the ID measurement is preferable at low p_T .

The 10 TeV analysis uses combined muons with $p_T > 10$ GeV, $|\eta| < 2.5$ and a χ^2 of the track matching between 0 and 100. Furthermore, the electromagnetic (hadronic) energy in a cone of $\Delta R = 0.2$ around the muon must not exceed 2 (10) GeV to assure proper isolation.

The early data analysis uses combined muons with $p_T > 20$ GeV, $|\eta| < 2.4$ and a $\chi^2 < 150$. In addition to combined muons, segment-tagged muons are also considered to recover efficiency at $|\eta| \sim 0$ and $|\eta| \sim 1.2$. These are muons reconstructed from inner detector tracks and matched to track segments in the muon chambers. The total calorimeter energy in a cone of $\Delta R = 0.2$ around the muon is required to be less than 1.8 GeV for the muons to be considered isolated. In order to reproduce the measured muon p_T resolution, muon momenta in MC events are smeared with factors measured from data.

¹⁰The loose identification only uses calorimeter information, the medium selection additionally cuts on tracking variables and the number of strips in the first EM layer, and the tight selection uses all available information, including vertexing and the ratio of low to high threshold hits in the TRT.

¹¹Calorimeter cell outputs are transmitted with optical transmitter modules (OTX), some of which are not working properly.

¹²Matched by the STACO algorithm.

¹³The Muonboy algorithm of the STACO family.

4.3.6. Overlap removal

The object identification methods described above are run separately on the detector signals, therefore a signature originating from the same object can be interpreted by several algorithms as part of the respective object they are designed to find. To avoid double counting, overlapping objects are removed in the 10 TeV analysis as follows¹⁴:

- If an electron and a jet are found within $\Delta R < 0.2$, the object is counted as an electron.
- If an electron is found in the vicinity of a jet within $0.2 < \Delta R < 0.4$, the electron is assumed to originate from a particle within the jet, and thus removed from the list of electrons.
- If a muon is found within $\Delta R < 0.4$ of a jet, it is removed with the same argument used for electrons in the previous point.
- If an electron and a muon overlap with $\Delta R < 0.2$, the object is counted as a muon.
- If a tau lepton and a muon overlap with $\Delta R < 0.2$, the object is counted as a tau lepton. This is a deviation from the standard selection, yet justified by the use of the muon veto within the tau lepton identification algorithm.
- If a tau lepton and an electron overlap with $\Delta R < 0.2$, the object is regarded a tau lepton, which is again non-standard as in the case of muons.
- If a tau lepton and a jet overlap with $\Delta R < 0.2$, the object is considered a tau lepton.

In the early data analysis, tau leptons are removed if they overlap with electrons and muons in order to be consistent with other tau search channels. For the same reason, no electron-muon overlap is corrected for. Both these changes give only minor modifications to the object selection.

4.3.7. Missing transverse energy

Missing transverse energy \cancel{E}_T is the key signature for every R-parity conserving supersymmetry model, but its exact reconstruction is also necessary for other studies like the Higgs mass measurement in $H \rightarrow \tau\tau$ or the reconstruction of the top quark mass in semileptonic $t\bar{t}$ decays. Challenges for the \cancel{E}_T reconstruction are dead channels or insensitive material in transition regions between subdetectors, as well as noise and fake \cancel{E}_T caused by mismeasured objects.

Missing transverse energy is reconstructed as an imbalance of the total transverse energy in an event. Energy deposited in calorimeter cells is weighted according to the cell position and energy density. Only cells which pass noise suppression criteria are taken into account. Corrections for energy loss in the cryostat and for muon energy are applied.

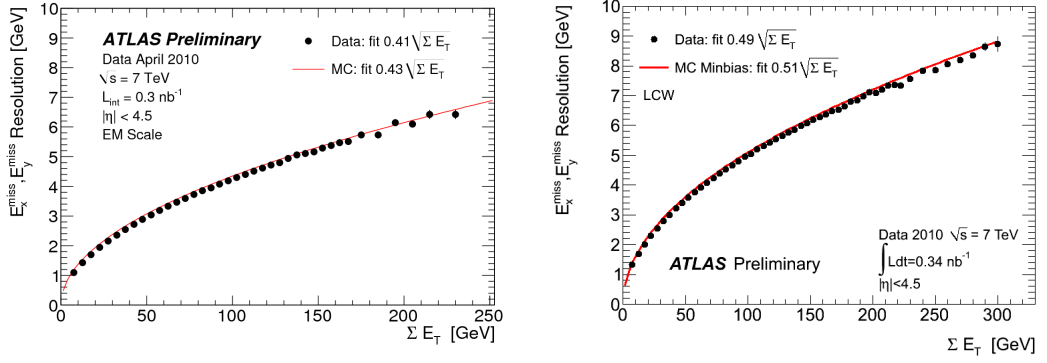
A slightly more sophisticated way to suppress noise is to use cells that are part of topoclusters¹⁵ rather than all cells above a certain noise threshold.

In the 10 TeV analysis, the so-called **Met.RefFinal** is used, where in a second calibration step, cell energies are weighted according to the reconstructed object they have been assigned to. This refinement does not use the overlap removal described above, which is suited for offline analysis, but assigns the reconstructed objects in the following order: electrons, photons, muons, hadronically decayed tau leptons, b-jets and light jets. The calibration of these objects is then used for the respective cells, without object reconstruction based corrections like out-of-cone energy, since this would lead to double counting in the context of \cancel{E}_T reconstruction. The x-y-components of the **RefFinal** missing transverse energy are thus given by

$$\begin{aligned} (E_{x,y}^{miss})^{\text{RefFinal,calib}} &= (E_{x,y}^{miss})^{\text{RefEle}} + (E_{x,y}^{miss})^{\text{RefGamma}} + (E_{x,y}^{miss})^{\text{RefTau}} + (E_{x,y}^{miss})^{\text{RefJet}} \\ &\quad + (E_{x,y}^{miss})^{\text{RefMuon}} + (E_{x,y}^{miss})^{\text{CellOut}} \end{aligned}$$

¹⁴Apart from the treatment of tau leptons, this procedure follows the standard of SUSY analyses in ATLAS.

¹⁵For a description of the topocluster algorithm see section 4.3.2.



(a) Cells calibrated on electromagnetic scale [101].

(b) Cells calibrated on hadronic scale with LCW [102]

Figure 4.4. – Missing transverse energy resolution in data compared to MC in minimum bias events.

with $(E_{x,y}^{miss})^{\text{CellOut}}$ computed from cells in topoclusters not assigned to any object. Each term is calculated as the negative sum of cell energies calibrated according to the assigned object. The \cancel{E}_T -term above corresponds to the missing transverse energy measured by calorimeter cells alone. In addition, energy loss in the cryostat as well as muons contribute to the final missing transverse energy calculation:

$$(E_{x,y}^{miss})^{\text{RefFinal}} = (E_{x,y}^{miss})^{\text{RefFinal,calib}} + (E_{x,y}^{miss})^{\text{Muon}} + (E_{x,y}^{miss})^{\text{cryo}}.$$

The expected \cancel{E}_T resolution achieved with this method is $\sigma = a \cdot \sqrt{\Sigma E_T}$, where a is between 0.53 and 0.57 depending on the total energy, and higher $\sqrt{\Sigma E_T}$ corresponds to larger values of a [40].

In the early data analysis, a simplified version of this refined \cancel{E}_T is used. Calorimeter cells associated with jets are calibrated at the hadronic jet energy scale (EM+JES) in accordance with the object definitions, and energy depositions in topoclusters not associated to any object are taken at the electromagnetic scale. No tau identification is used since the uncertainty introduced by the tau identification performance is larger than the error due to calibration differences between hadronic tau leptons and jets. Thus the **SimplifiedRefFinal** missing transverse energy is calculated from

$$(E_{x,y}^{miss})^{\text{SimplifiedRefFinal}} = (E_{x,y}^{miss})^{\text{RefEle}} + (E_{x,y}^{miss})^{\text{RefJet}} + (E_{x,y}^{miss})^{\text{RefMuon}} + (E_{x,y}^{miss})^{\text{CellOut}}.$$

Only jets with $p_T > 20$ GeV enter the \cancel{E}_T computation. Since the $(E_{x,y}^{miss})^{\text{RefMuon}}$ term contains some high- p_T non-isolated muons which lead to very high \cancel{E}_T , this term is replaced in the analysis by muons selected in the analysis but without the isolation criterium or overlap removal applied.

A reasonable agreement between the computed \cancel{E}_T in data and MC is obtained in the first $\sqrt{s} = 7$ TeV collisions, as shown in figure 4.4 for two different calibration levels.

4.3.8. Derived quantities

To characterize SUSY signals, multiplicity and kinematic properties of the objects described above are used in combination with derived quantities which are sometimes more suitable to exploit the distinctive physics features separating supersymmetric processes from SM events.

	$\sqrt{s} = 10/14$ TeV	early data ($\sqrt{s} = 7$ TeV)
<u>jets</u>		
jet building algorithm	cone	anti-k _T
jet energy calibration	LCW	EM+JES
<u>tau leptons</u>		
building algorithm	cone	anti-k _T
tau-jet separation	Lh	BDT
tau-electron separation	τ - e -Llh	electronVeto
\cancel{E}_T	RefFinal	SimplifiedRefFinal

Table 4.1. – Most important differences in object definitions of the 10 TeV (chapter 5) and early data (chapter 6) analysis.

The effective mass M_{eff} is defined as the sum of missing transverse energy and the transverse momenta of jets and leptons, and represents the total activity in an event. It is thus correlated to the mass of the originally produced pair of SUSY particles, and thereby to the SUSY mass scale. Different definitions use either all jets and leptons, only jets above a certain p_T -threshold or only the four hardest jets with or without leptons. The definition used in the 10 TeV analysis is $M_{\text{eff}} = \sum_{i=1}^4 p_T^{\text{jet},i} + \sum_{i=1}^{N_{\text{lep}}} p_T^{\text{lep},i} + \cancel{E}_T$, where lep includes electrons, muons and tau leptons. In the early data analysis, all jets satisfying $p_T > 40$ GeV and only tau leptons are used. A more powerful discriminant against SM processes than M_{eff} itself is its fraction of missing transverse energy $\frac{\cancel{E}_T}{M_{\text{eff}}}$.

H_T is defined similar to M_{eff} , without the \cancel{E}_T contribution, thus describing the total measurable energy in an event. Again, several definitions are possible; in this work, H_T is defined in analogy to M_{eff} such that $M_{\text{eff}} = H_T + \cancel{E}_T$ holds.

The \cancel{E}_T significance $S_{\cancel{E}_T}$ is the missing E_T divided by its expected uncertainty:

$$S_{\cancel{E}_T} = \frac{\cancel{E}_T}{0.5 \cdot \sqrt{\sum E_T}}.$$

The transverse mass M_T of a tau lepton $M_T = \sqrt{m_\tau^2 + m_\chi^2 + \vec{p}_T^\tau \cdot \vec{p}_T^{\text{miss}}}$, where p_T^{miss} is the \cancel{E}_T two-vector, and m_χ the mass of some invisible particle responsible for the \cancel{E}_T , and set to zero. This variable can be useful to suppress $W \rightarrow \tau \nu_\tau$, where the invisible particle is a neutrino, the mass of which can be safely neglected.

The most important differences between object definitions in the 10 TeV and the early data analysis are summarized in table 4.1.

5. Endpoint measurement of a $\tau\tau$ invariant mass spectrum

5.1. Introduction

When a new physics signal with features in line with supersymmetric events is observed, measuring the properties of new particles is crucial to strengthen or dismiss the SUSY hypothesis and to determine the parameters of the underlying SUSY model. Among the first accessible properties of new particles is the mass. While the undetectable LSPs prohibit direct mass peak reconstructions, as described in section 2.3, the maximal values of invariant mass spectra of particle combinations such as $m_{\tau\tau}$, $m_{q\tau}$ or $m_{q\tau\tau}$ from $\tilde{q} \rightarrow \tilde{\chi}_2^0 q \rightarrow \tilde{\tau}_1 \tau q \rightarrow \tilde{\chi}_1^0 \tau \tau q$ depend on the masses of the involved SUSY particles, thus allowing indirect measurements via a combination of endpoints [103]. This chapter therefore investigates the invariant mass spectrum of two tau leptons emerging from the signal decay $\tilde{\chi}_2^0 \rightarrow \tilde{\tau}_1 \tau \rightarrow \tilde{\chi}_1^0 \tau \tau$, depicted in figure 5.1(a), the endpoint of which is analytically calculable (see section 2.3) as

$$m_{\tau\tau}^{\max} = \sqrt{\frac{(m_{\tilde{\chi}_2^0}^2 - m_{\tilde{\tau}_1}^2)(m_{\tilde{\tau}_1}^2 - m_{\tilde{\chi}_1^0}^2)}{m_{\tilde{\tau}_1}^2}}. \quad (5.1)$$

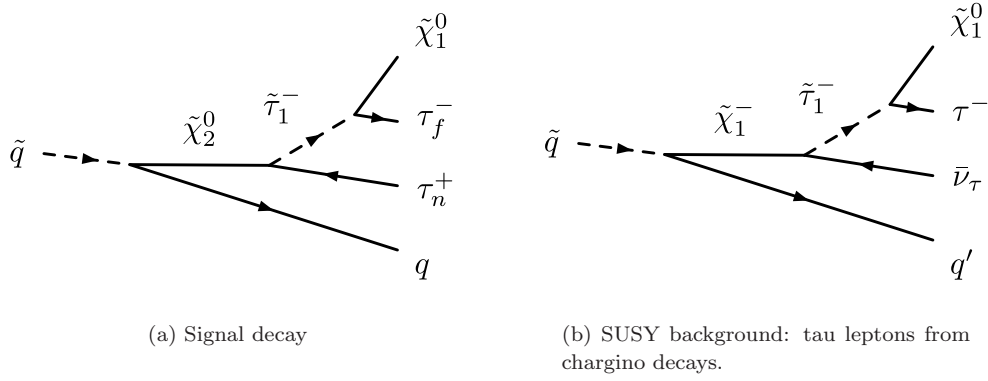
If the neutralino masses are known from other measurements, a determination of $m_{\tau\tau}^{\max}$ opens direct access to the $\tilde{\tau}_1$ mass. Furthermore, the tau lepton decay renders the potential to determine the tau lepton polarization, which carries information about the stau mixing angle, and thus about the couplings between stau and neutralinos. The impact of polarization effects on the study at hand is shortly discussed below, yet detailed analyses on this topic need amounts of data not accessible in the first few years of LHC operation and are therefore beyond the scope of this work.

This chapter evaluates the prospects of an endpoint measurement of the $\tau\tau$ invariant mass spectrum in proton-proton collisions with a center-of-mass energy of $\sqrt{s} = 10$ TeV and $\sqrt{s} = 14$ TeV. Although the original motivation to study $\sqrt{s} = 10$ TeV collisions, which was the expected start of LHC operation with beam energies of 5 GeV, did not come to pass, an intermediate step in center-of-mass energy between the 7 TeV collisions realized today and 14 TeV design energy is still possible. While the selection of a SUSY signal is more challenging with lower center-of-mass energy because its cross-section dependence is steeper than that of the SM background, the evaluated concepts are applicable to collisions with any center-of-mass energy.

A study focussing on discovery prospects with $\sqrt{s} = 7$ TeV and on understanding first ATLAS data in the tau lepton channel follows in the next chapter.

5.2. Di-tau SUSY signature at the LHC

As shown in chapter 2.3, SUSY particles are dominantly produced by strong interaction processes at the LHC and lead to signatures with many high energetic jets and leptons accompanied by large missing transverse energy. In this section, these features are exploited to select a given mSUGRA benchmark point suitable for an endpoint measurement, namely the bulk region point SU3 (see chapter 2.3 for an introduction of SUSY benchmark points).


Figure 5.1. – Tau sources in supersymmetric processes.

	NLO CS [pb]	decay	branching ratio
14 TeV	27.7	$\tilde{q}_L \rightarrow \tilde{\chi}_2^0 q$	0.32
10 TeV	8.2	$\tilde{\chi}_2^0 \rightarrow \tilde{\tau}_1^\pm \tau^\mp$	0.58
sparticle	mass [GeV]	$\tilde{\chi}_2^0 \rightarrow \tilde{\mu}_1^\pm \mu^\mp$	0.064
$\tilde{\chi}_2^0$	218.60	$\tilde{\chi}_2^0 \rightarrow \tilde{e}_1^\pm e^\mp$	0.063
$\tilde{\chi}_1^0$	117.91	$\tilde{\chi}_2^0 \rightarrow \tilde{\chi}_1^0 \tau^\pm \tau^\mp$	0.001
$\tilde{\tau}_2$	232.17	$\tilde{\chi}_1^\pm \rightarrow \tilde{\tau}_1^\pm \nu_\tau$	0.48
$\tilde{\tau}_1$	149.99	$\tilde{\tau}_1^\pm \rightarrow \tilde{\chi}_1^0 \tau^\pm$	1

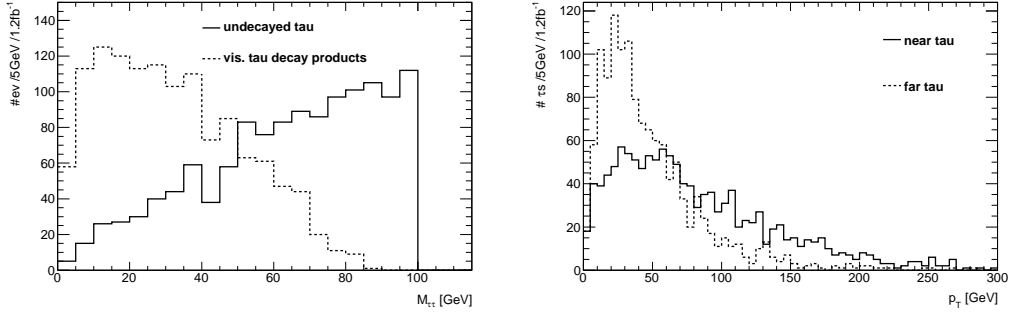
(a) Cross section and masses of SUSY particles (PROSPINO 2.0.6).

(b) Some branching ratios (Sphenov2.2.2).

Table 5.1. – SU3 characteristics

Figure 5.1 shows example Feynman graphs for the signal process, as well as another SUSY source of tau leptons that might yield a significant contribution. Characteristics of the benchmark point SU3 relevant to derive expectations about signal and SUSY background composition are given in table 5.1. SU3 is chosen as signal scenario to derive selection and measurement techniques because the reasonably high production cross-section, accompanied by an enhanced tau lepton production with $BR(\tilde{\chi}_2^0 \rightarrow \tilde{\tau}_1^\pm \tau^\mp) \gg BR(\tilde{\chi}_2^0 \rightarrow \tilde{\mu}_1^\pm \mu^\mp, \tilde{e}_1^\pm e^\mp)$, yields favourable statistics in the selected signal after SM background suppression to enable a measurement with an integrated luminosity of $\int L = 1 \text{ fb}^{-1}$. While SU4 and SU11 both offer higher cross-sections, the signal decay $\tilde{\chi}_2^0 \rightarrow \tilde{\tau}_1 \tau \rightarrow \tilde{\chi}_1^0 \tau \tau$ is closed because $m(\tilde{\chi}_2^0) < m(\tilde{\tau}_1)$, and the $m_{\tau\tau}$ endpoint of the corresponding 3-body decay $\tilde{\chi}_2^0 \rightarrow \tilde{\chi}_1^0 \tau^\pm \tau^\mp$ yields no information about $m(\tilde{\tau}_1)$. In SU3, the main source of $\tilde{\chi}_2^0$ s are squark decays: The relevant branching fractions for the SU3 point are $BR(\tilde{q}_L \rightarrow q \tilde{\chi}_2^0) = 0.32$, $BR(\tilde{\chi}_2^0 \rightarrow \tilde{\tau}_1^\pm \tau^\mp) = 0.58$ and $BR(\tilde{\tau}_1^\pm \rightarrow \tilde{\chi}_1^0 \tau^\pm) = 1.0$. Decays via $\tilde{\tau}_2$ are closed because $m(\tilde{\tau}_2) > m(\tilde{\chi}_2^0)$. The $\tilde{\chi}_2^0$ 3-body decay is negligible in SU3, but chargino decays have to be considered as competing sources of tau leptons.

Figure 5.2(a) depicts the invariant mass spectrum of two tau leptons coming from the signal decay $\tilde{\chi}_2^0 \rightarrow \tilde{\tau}_1 \tau \rightarrow \tilde{\chi}_1^0 \tau \tau$ as seen with a perfect detector. Due to neutrinos from the tau decays, the characteristic triangular shape of the invariant mass spectrum loses its sharp edge at the maximum value, and fades out smoothly instead. This makes a measurement of the spectrum's endpoint challenging, and demands special techniques to extract the endpoint position in a reliable way. While this problem is common to all SUSY scenarios, further intricacies may arise



(a) Invariant mass of undecayed tau leptons (solid line) and visible decay products (dotted line). The theoretical endpoint is $m_{\tau\tau}^{\max} = 98$ GeV.

(b) Transverse momenta of near (solid line) and far (dotted line) tau lepton.

Figure 5.2. – Invariant mass and transverse momenta of signal tau leptons without detector effects ($\sqrt{s} = 10$ TeV) in the SU3 benchmark point.

if the mass difference between the $\tilde{\tau}_1$ and either neutralino $\tilde{\chi}_{1,2}^0$ is small, leading to a very soft tau lepton difficult to reconstruct with common algorithms. Table 5.1(a) lists the respective masses and figure 5.2(b) shows the transverse momentum spectra of the two tau leptons from $\tilde{\chi}_2^0 \rightarrow \tilde{\tau}_1 \tau_n \rightarrow \tilde{\chi}_1^0 \tau_n \tau_f$, where τ_n (near tau lepton) denotes the tau lepton from the $\tilde{\chi}_2^0$ decay and τ_f (far tau lepton) the one from the $\tilde{\tau}_1$ decay. Due to the small mass gap between the stau and the lightest neutralino in the chosen point, the transverse momentum spectrum of the far tau lepton is very soft and peaks between 20 and 30 GeV, which has to be compared to a tau reconstruction threshold of 10 GeV and a reconstruction and identification efficiency significantly lower than average for taus with $p_T < 30$ GeV for the calorimeter-based τ reconstruction algorithm used in the studies presented in this chapter.

5.2.1. Standard Model background

While this chapter focuses on the measurement of the endpoint $m_{\tau\tau}^{\max}$ rather than on discovery, a necessary boundary condition is the separation of a clear SUSY signal from the relevant SM background.

Due to long decay chains of two pair-produced heavy SUSY particles, SUSY processes feature many high energy jets and leptons which are spherically distributed. The most prominent signature, however, is large missing transverse energy \cancel{E}_T from at least two undetected LSPs, sometimes accompanied by neutrinos.

The most similar SM process is $t\bar{t}$, where also two heavy particles are created which decay instantaneously to two b-jets and two W-bosons which in turn decay into up to four additional jets, or two visible leptons. In addition to the possibility of two real tau leptons from the W-decays there are therefore many jets which might mimic tau leptons, particularly b-jets, which form B-mesons during hadronization that can decay into real tau leptons. These are contained within the b-jet, overlap with other particles and are therefore regarded as fake in this context. $t\bar{t}$ decays also produce real \cancel{E}_T due to neutrinos from the W-decays and neutrinos in jets, but are also prone to fake \cancel{E}_T from jets which are mismeasured or lost. All these features make $t\bar{t}$ particularly difficult to distinguish from SUSY events, especially in cases where real tau leptons are present.

The second largest SM background is $W \rightarrow \tau\nu$, as it contains real missing energy accompanied by one real tau lepton. Similarly, $Z \rightarrow \tau\tau$ and $Z \rightarrow \nu\nu$ pose the third largest backgrounds, with

either two real tau leptons or large real \cancel{E}_T , though produced with a smaller cross-section than the W contribution. Jets falsely identified as tau leptons are reconstructed with an electrical charge largely uncorrelated to that of any other fake or true reconstructed tau lepton. While thus all backgrounds containing one or two fake tau lepton(s) can be suppressed by separating oppositely charged (OS) tau lepton-pairs from those carrying the same charge (SS), and subtracting the invariant mass distribution of the latter from the one of the former, $Z \rightarrow \tau\tau$ has to be controlled by event selection criteria such as high \cancel{E}_T or energetic jets. Decays of Z and W bosons to electrons and muons are also included in this study, yet shown to be of minor importance.

QCD dijet events seldomly satisfy selection criteria including two tau leptons and large \cancel{E}_T , yet their cross-sections are orders of magnitudes above those of all other processes. Therefore even rare events can spoil a SUSY selection if QCD is not efficiently rejected. In the di-tau invariant mass spectrum, the OS-SS method should suppress QCD contributions, which are composed purely of uncorrelated fake tau leptons.

In order to perform a measurement, additional background from SUSY processes not containing the targeted signal decay has to be taken into account. If there are more than two tau leptons in an event, the pair which is closest in ΔR is selected to enrich tau leptons from the signal decay $\tilde{\chi}_2^0 \rightarrow \tilde{\tau}_1\tau \rightarrow \tilde{\chi}_1^0\tau\tau$ in the invariant mass spectrum, with an additional requirement that $(\Delta R)_{min} < 2$ to avoid selecting two tau leptons from two different decay chains. Combinatorial background is further suppressed by the OS-SS subtraction described above. The effect on SUSY background depends on the dominant SUSY production process, since tau leptons from chargino decays are correlated w.r.t. electrical charge if the charginos emerge from $\tilde{q}\tilde{q}^*$ production, while they are uncorrelated if $\tilde{g}\tilde{g}$ or $\tilde{q}\tilde{q}$ production is dominant. The OS-SS method is further based on the assumption that the uncorrelated part of the OS spectrum can be measured by the SS spectrum, which is only valid for sufficiently large statistics.

The first part of the analysis presented in this chapter aims at collisions with 14 TeV design center-of-mass energy. The second and main part extends the $\tau\tau$ signal to leptonically decaying tau leptons. It has been performed with a 10 TeV center-of-mass energy setup, which was supposed to be the initial LHC energy after the incident which put 14 TeV out of reach, and before 7 TeV had been decided. Although the current LHC plan does not foresee a 10 TeV run, the conceptual gain from this part of the analysis is still valid. Furthermore, if the planned upgrade to 14 TeV should prove too challenging to incorporate, a center-of-mass energy closer to 10 TeV than to 14 TeV might be realized.

5.3. Invariant mass of two hadronic tau leptons in $\sqrt{s} = 14$ TeV collisions

5.3.1. Starting point: previous work

A method to select a SUSY signal with di-tau final states in 14 TeV collisions has already been presented in a feasibility study [104] based on the fast detector simulation [80]. The signal decay $\tilde{\chi}_2^0 \rightarrow \tilde{\tau}_1\tau \rightarrow \tilde{\chi}_1^0\tau\tau$ has been investigated in the bulk region point SU3, as well as in the co-annihilation point SU1. It has been shown that while both these mSUGRA points could be discovered with less than 1 fb^{-1} of integrated luminosity, only the SU3 signal proved large and clean enough to enable an endpoint measurement with 10 fb^{-1} [104]. Therefore, the measurement presented here also focuses on SU3.

The method to measure the endpoint of a ditau invariant mass spectrum that will be used in this thesis was also developed in [104], and is shortly summarized in the following:

Combinatorial background is suppressed by subtracting the spectrum of same-sign (SS) tau lepton pairs from that of opposite-sign (OS) tau lepton pairs, thus using $((\tau^\pm\tau^\mp) - (\tau^\pm\tau^\pm))$ (OS-SS). It has been shown that the trailing edge of this invariant mass distribution can be

described by a log-normal function

$$f(x; p_0, p_1, p_2) = \frac{p_0}{x} \cdot \exp\left(-\frac{1}{2p_2^2}(\ln(x) - p_1)^2\right), \quad (5.2)$$

with three free parameters $p_{0,1,2}$, where p_0 is a normalization factor while p_1 and p_2 describe the mean and width of the distribution, respectively.

This function approaches the x-axis asymptotically, and therefore does not provide an endpoint directly. The trailing edge can be characterized by its inflection point:

$$m_{\tau\tau}^{\text{IP}} = \exp\left(-\frac{1}{2}p_2^2\left(3 - \sqrt{1 + \frac{4}{p_2^2}}\right) + p_1\right).$$

This inflection point can be converted into the endpoint position by way of a calibration scheme derived from modified mass spectra, where either of the $\tilde{\chi}_2^0$, $\tilde{\tau}_1$ or $\tilde{\chi}_1^0$ masses have been varied to gain different endpoints, while all other masses of the SU3 spectrum have been kept at their nominal values. Thus fourteen spectra were fitted with function 5.2, and the relation of the measured inflection points to the maximum values of the invariant masses, calculated with equation 5.1, was found to be

$$m_{\tau\tau}^{\text{IP}} = (0.71 \pm 0.09)m_{\tau\tau}^{\text{max}} + (13 \pm 9) \text{ GeV}.$$

A test measurement with the unmodified SU3 signal then yields an endpoint of $m_{\tau\tau}^{\text{max}} = (97 \pm 9^{\text{stat}} \pm 6^{\text{syst}}) \text{ GeV}$ with 10 fb^{-1} of integrated luminosity, which is consistent with the theoretical expectation of 98 GeV. The given systematic uncertainty is caused by binning effects and fit range variation; for further details see [104].

Tau polarization effects

Another uncertainty on the endpoint measurement arises from the polarization of the tau leptons. By way of their dependence on the stau mixing angle $\theta_{\tilde{\tau}}^1$, such polarization effects can themselves unveil information about the SUSY couplings [40, 105, 106]:

The polarization of the two tau leptons emerging from the decay chain $\tilde{\chi}_2^0 \rightarrow \tilde{\tau}_1 \tau \rightarrow \tilde{\chi}_1^0 \tau \tau$ is a function of the couplings between the $\tilde{\chi}_2^0$, the $\tilde{\tau}$ and the $\tau_{R,L}$. Considering the decay of a single tau lepton, the fixed chirality of the neutrino ν_τ in combination with angular momentum and momentum conservation leads to a preferred boost of the visible tau lepton decay products parallel or antiparallel to the tau lepton momentum. The direction will depend on the polarization of the tau lepton and on the resonance over which the tau lepton is decaying. The invariant mass spectrum of the two taus is therefore distorted in a decay mode sensitive manner. The most dominant polarization effect on the spectrum can be described by the sum of the polarizations of the near and far tau $P_n + P_f$, which, if measurable, gives the stau mixing angle $\theta_{\tilde{\tau}}$ with a two-fold ambiguity². A measurement of the tau polarization sum, however, requires statistics on the order of 30 fb^{-1} . As a consequence, polarization can only be treated as an additional systematic uncertainty in this context. The maximal possible shift of the trailing edge of the di-tau invariant mass spectrum leads to a systematic uncertainty on the endpoint measurement of $\pm 7 \text{ GeV}$ in the analysis described in the previous section, which was targeted at 1 fb^{-1} of integrated luminosity. It is therefore the dominant systematic contribution, leading to a summarized final result of $m_{\tau\tau}^{\text{max}} = (102 \pm 17^{\text{stat}} \pm 5.5^{\text{fit}} \pm 7^{\text{pol}}) \text{ GeV}$ (1 fb^{-1})³.

¹The tau polarization also depends on the neutralino mixing matrix, which is supposed to be known from other measurements in order to extract information about $\theta_{\tilde{\tau}}$ from the di-tau invariant mass spectrum.

²Under the assumption that the neutralino sector is fully explored by the time such a measurement can be performed.

³Detailed information on polarization effects, a method to measure the polarization along with the endpoint and conclusions for $\theta_{\tilde{\tau}}$ can be found in [105, 106].

5.3.2. Further development of the analysis

While the method to measure the endpoint is adopted in this thesis, the calibration developed in [104] can not be used because the tau lepton identification algorithm in the software release used in [104], including its parameterization in the fast detector simulation, has significantly changed. Therefore, the calibration has to be amended with an updated release before further usage. The result is then validated with full detector simulation, and trigger effects are studied with respect to bias of the spectrum shape, a possible effect which is not modelled in the fast detector simulation and was therefore not investigated before.

In the analysis presented, **ALPGEN 2.06** [75] multijet samples have been employed which use matrix element calculations for three to five jets and are simulated in six p_T -bins to cover the whole spectrum. Both W and Z processes have also been simulated with **ALPGEN 2.06**, in subsamples where zero to five additional jets are modelled by matrix element calculations and further jets by parton showers. $t\bar{t}$ processes have been simulated with **MC@NLO** [76, 77], SU3 signal events with **Herwig 6.5** [71–73]. Fully simulated MC samples are summarized in table A.2 in appendix A.

New calibration

The calibration described in [104] was done in **athena 11.0.4** and is now revised with a newer software release (**athena 12**): the parameterization of the tau reconstruction and identification algorithm in the fast detector simulation [80, 81] has been revised between those versions, and a parameterization of the track-based algorithm (see chapter 4.3.3) has been added to that of the cluster-based algorithm, which was the only one available in the study described above. Therefore, above study is renewed with **athena 12.0.6**, under consideration of both the track-based and the calorimeter-based tau lepton reconstruction algorithm. SM background events are generated in **athena 12.0.64**, SU3 signal events in **athena 12.0.7**. In addition to the calorimeter-based tau reconstruction and identification algorithm used in [104], the parameterization for the track-based approach is investigated, yet found to give an overall worse performance for the analysis at hand than the cluster-based algorithm: although more low p_T tau leptons are reconstructed and identified, the background rejection is significantly worse, resulting in a ratio of SS to OS events which is a factor of two larger if the parameterization of the track-based tau lepton algorithm is used compared to results obtained with the calorimeter based approach. Consequently, a significantly lower OS-SS SU3 signal spectrum is obtained. For this reason, only the parameterization of the cluster-based algorithm is used in the study presented below.

Conceptually the very same analysis as the one described in the previous section, only the updated results will be given here: the signal is selected by requiring two tau leptons in the same hemisphere $\Delta R < 2$, a missing transverse energy of at least $\cancel{E}_T > 230$ GeV, and four jets with minimal transverse momenta of $p_T > 220, 50, 50$ and 40 GeV. These are the same selection criteria as used in [104], only the cut on the 4th jet is changed: in order to be consistent with an event filter used in the officially produced datasets, this cut has been augmented by 10 GeV. The calibration line is found to be

$$m_{\tau\tau}^{\text{IP}} = (0.47 \pm 0.02)m_{\tau\tau}^{\text{max}} + (15 \pm 2) \text{ GeV}, \quad (5.3)$$

with a covariance between slope b and axis intercept a of $\text{cov}(a, b) = -0.0342$. The fit from which this calibration line is obtained is shown in figure 5.3(a). Relation 5.3 shows a significantly smaller slope as compared to the calibration obtained in the preceding study, and will be used in the subsequent analysis. It is already documented in [107] and [40], and has by now also been applied in studies of other groups focussing on the SU1 mSUGRA point [40] or a GMSB scenario [108]. The SU3 test measurement for 10 fb^{-1} of 14 TeV data now yields $m_{\tau\tau}^{\text{max}} = (105 \pm 4^{\text{stat}} \pm 4.5^{\text{syst}}) \text{ GeV}$, where the systematic uncertainty again mainly arises from the fitting procedure. The impact of a systematically over- or underestimated jet energy scale (JES) is tested by changing the energy and transverse momentum of all jets in a correlated way

by 5 %. The result of the endpoint measurement then changes by 1 %, so this effect is negligible compared to the uncertainty introduced by the fitting procedure.

The calibration found in [104] with the old software release would yield an endpoint of (73 ± 13) GeV for the inflection point measured with the new software, which is clearly wrong and illustrates the extent of change made to tau reconstruction. The axis intercept of the new calibration line is furthermore determined with much better precision than in the old calibration, which in turn enables a more precise endpoint measurement.

All fits have been performed with MINUIT [109]; for further information on data samples or calibration fits see [107].

Verification with full detector simulation

While usage of the fast detector simulation is sensible for first feasibility studies as the one described in 5.3.1, or if many datasets with large statistics are needed as in the case of the calibration in 5.3.2, it has to be verified that the simplifications introduced thereby do not affect the obtained result. Comparing equation 5.3 with the result of the former study, a significant change in the slope of the calibration line is observed. A transition from fast to full detector simulation could involve even further changes, since validation of the fast detector simulation is done by comparing basic kinematic distributions of reconstructed objects, testing the overall resemblance when averaging over large statistics, which not necessarily ensures preservation of the spectrum shape of the di-tau invariant mass. Therefore, the method to measure the endpoint using the above calibration has been tested with a set of SU3 and SM data that have been processed through the full ATLAS detector simulation⁴.

Figure 5.3(b) shows the OS-SS $\tau\tau$ spectrum after the selection cuts as detailed in section 5.3.2 are applied. SM contributions are seen to be small and do not distort the spectrum shape of the SU3 signal. Only $t\bar{t}$, $W \rightarrow \tau\nu$, $Z \rightarrow \tau\tau$ and $Z \rightarrow \nu\nu$ contribute to the SM background.

With an integrated luminosity of 1 fb^{-1} , (337 ± 5) signal events (N_S) are expected. The total sum of (21 ± 2) SM background events (N_{BG}) then leads to a statistical significance of $N_S/\sqrt{N_B} = (74 \pm 7)$, thus enabling an early discovery. The endpoint measurement, however, suffers significantly with decreased amount of available data, as can be seen by the comparison of figures 5.3(c) and 5.3(d) where the log-normal fit to the trailing edge of the spectrum is shown for integrated luminosities of 10 fb^{-1} and 1 fb^{-1} , respectively. For 1 fb^{-1} , the precision of the measurement is significantly worse: while a fit at 10 fb^{-1} yields $m_{\tau\tau}^{\text{max}} = (103 \pm 5^{\text{stat}}) \text{ GeV}$, with a tenth of the statistics, the result $m_{\tau\tau}^{\text{max}} = (102 \pm 17^{\text{stat}}) \text{ GeV}$ is obtained in 5.3(d), which is consistent with an expected loss of precision of the order of $\sqrt{10}$. The statistical uncertainty thus rises from 5 % to 17 %, while the systematic uncertainty introduced by the fitting procedure is stable at $\pm 5.5^{\text{syst}} \text{ GeV}$ ⁵.

With both high and low statistics, a result close to the true value is obtained. The simplifications made in the fast detector simulation have not derogated the calibration.

Trigger strategy

At design luminosity of $10^{34} \text{ cm}^{-2}\text{s}^{-1}$, the ATLAS trigger system has to efficiently filter out interesting events, thus high trigger thresholds have to be expected for \cancel{E}_T and jet triggers in order to allow them to run unscaled, because these triggers can also be fired by QCD events. For the analysis at hand, combined jet and \cancel{E}_T triggers are the obvious choice in light of the offline selection cuts. Trigger menus are under constant revision, so the exact trigger thresholds to be expected for high luminosity runs have not been fixed at the time of writing. For \cancel{E}_T triggers, thresholds can be expected to be lower than the offline selection cut since there are not many SM processes leading to high \cancel{E}_T , therefore the rates are expected to be low. This is different for high energetic jets, which are copiously produced at the LHC. A way to use low jet

⁴In `athena 12.0.6`

⁵As in the previous study, the impact of the jet energy scale uncertainty is negligible.

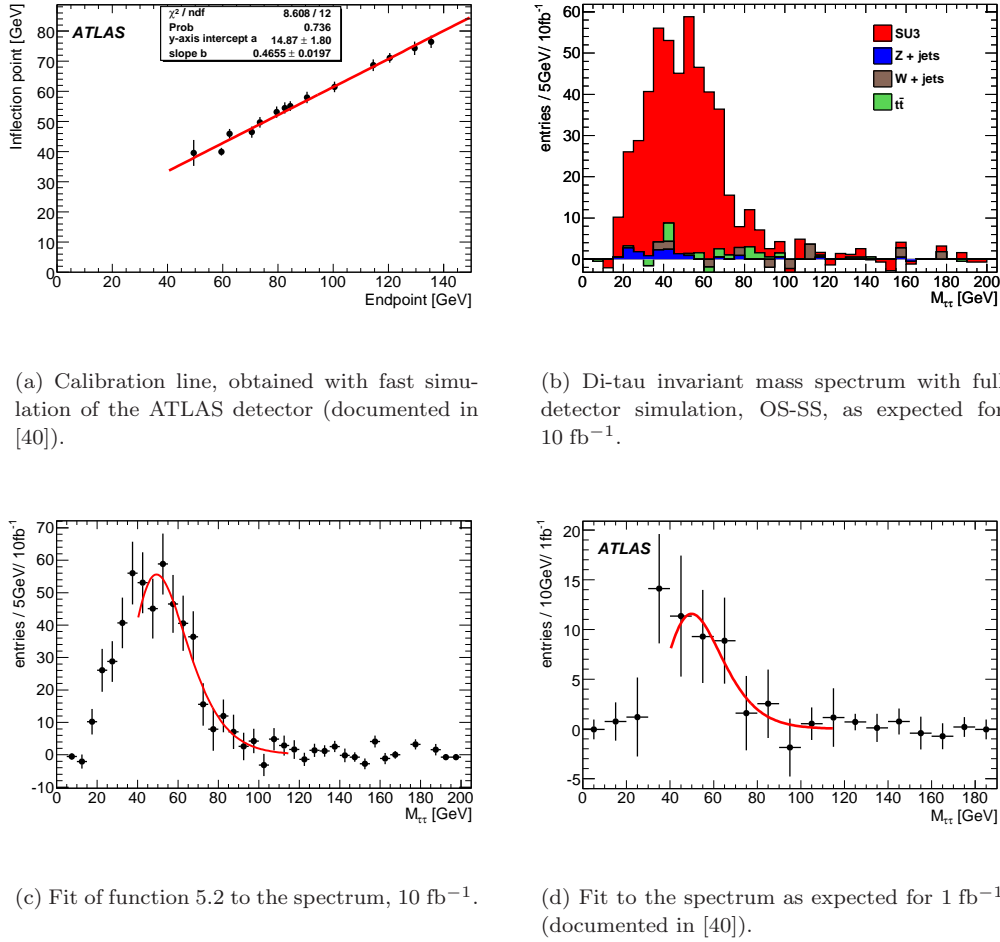


Figure 5.3. – Calibration line for the endpoint measurement of a di-tau invariant mass spectrum, validation with full detector simulation and transition to low statistics (1 fb^{-1}).

p_T thresholds anyway is to trigger on more than one jet at a time, or combine jet with \cancel{E}_T or lepton triggers. Unlike pure \cancel{E}_T triggers, it is not ensured that all signal events can be selected with jet triggers. The same is true for tau lepton triggers, which have comparable low efficiencies caused by slow turn-on curves limiting the overall performance ([40]) and thresholds too high for soft tau leptons as present in many SUSY scenarios. Furthermore, tau lepton triggers might introduce a bias in the di-tau invariant mass spectrum, a concern further investigated below.

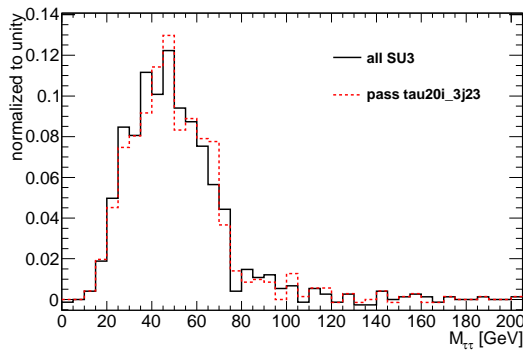
To evaluate possible alternatives to a pure \cancel{E}_T trigger, which provides an efficiency of about 100 %, table 5.4(a) lists examples for jet and combined tau-jet triggers⁶. The nomenclature here is such that j200 denotes one jet with $p_T > 200 \text{ GeV}$ and tau20i an isolated tau lepton with at least 20 GeV at event filter (EF) level.

Table 5.4(a) shows the trigger efficiency with respect to events passing the offline selection (ϵ_{sel}), as well as the efficiency with respect to the whole SU3 sample (ϵ_{all}). Even j200, the threshold of which is still below the value of the respective offline selection cut, yields not 100 % efficiency, so single jet triggers are shown to be not a good option. This efficiency loss near the trigger threshold is caused by turn-on effects, which have to be measured from data for every trigger and are difficult to model by MC alone. Depending on the rate evolution during LHC operation, this trigger might also get prescaled. All jet triggers requiring more than one jet have thresholds above the respective offline selection cuts. The second highest efficiency with respect

⁶The trigger menu used is part of **athena** 13.0.4.

trigger	ϵ_{all}	ϵ_{sel}
j200	0.83	0.99
j400	0.27	0.39
2j120	0.64	0.78
3j65	0.53	0.84
4j55	0.31	0.86
tau20i_j120	0.41	0.96
tau20i_2j70	0.40	0.95
tau20i_3j23	0.42	0.96

(a) Trigger efficiencies of possible backup-triggers.



(b) Invariant mass spectrum with and without combined tau lepton-jet trigger.

Figure 5.4. – Trigger efficiencies w.r.t. all SU3 events ϵ_{all} and w.r.t. offline selected events ϵ_{sel} , for different jet triggers and tau-jet trigger combinations. A possible bias in the endpoint measurement is disproved by comparison of the invariant mass spectrum with and without trigger.

to offline selected events show the combined tau-jet triggers. In case such a trigger will have to be used, the shape of the invariant mass spectrum might be distorted as the trigger imposes a cut on the p_T of the harder tau lepton. The possibility of thus introducing a bias in the di-tau invariant mass spectrum is tested by comparison of the spectrum with and without trigger requirement. Figure 5.4(b) shows the OS-SS invariant mass distribution for the tau20i_3j23 trigger, normalized to unity in order to compare the spectrum shape. No impact of this trigger on the spectrum shape is observed.

In conclusion, tau triggers pose a backup option to trigger on SUSY events with tau final states if combined jet and \cancel{E}_T triggers might not perform as expected for some period of data-taking. While this scenario leads to a decrease in efficiency and thus statistics available for the endpoint measurement, a bias in the shape of the spectrum is not observed. The result of an endpoint measurement can therefore be expected to be less precise due to a larger statistical uncertainty, but without dominant systematic effects introduced by the trigger.

5.4. Extension to leptonic tau lepton decays in $\sqrt{s} = 10$ TeV collisions

So far, only hadronically decaying tau leptons were taken into account because the tau lepton reconstruction and identification algorithms do not aim at leptonic tau decays. This is caused by the difficulty in distinguishing leptons emerging from a tau lepton decay from so-called prompt leptons coming from the hard interaction, the decay of a heavy SM particle or a particle proposed in some new-physics model such as SUSY. When considering di-tau final states, only 42 % of all $\tau\tau$ -pairs can be found by this selection. In 46 % of all cases one tau lepton decays leptonically, in 12 % both. In the context of SUSY searches this means that a signal can be observed with half the statistics if $\tau\tau$ -pairs can be selected where one of the tau leptons decayed leptonically (henceforth labelled hl) in addition to the fully hadronic channel (henceforth called hh). The fully leptonic channel (ll) is covered separately in lepton search modes, yet for a measurement of the di-tau endpoint, each of these three channels poses an independent signal spectrum, so each can improve the precision of the obtained result.

This section investigates a possible combination of hh, hl and ll channel for pp collisions with $\sqrt{s} = 10$ TeV. First a short review of a preceding study supplementing calibration lines

for the two additional channels (using fast detector simulation with $\sqrt{s}=14$ TeV) is given. A new signal selection is then developed in all three channels, to combat a worsened initial signal to background ratio due to the lower center-of-mass energy. An alternative fitting procedure is introduced, before the selection as well as the endpoint measurement are finally tested in a signal grid scanning the m_0 - $m_{1/2}$ -plane for $\tan\beta=10, 30$ and 50 .

Throughout this chapter, the term lepton refers to electrons, muons *and* tau leptons. If generally used or in the context of truth particles before detector effects, τ is used for all tau leptons regardless of the decay mode, while for reconstructed objects, τ denotes a tau-lepton identified by the according algorithm as a hadronically decayed tau-lepton.

5.4.1. Starting point: preceding work regarding (semi-)leptonic spectra

A first extension to leptonically decayed tau leptons based on fast detector simulation has been made in [92], where the same Monte Carlo samples as in section 5.3.2 have been used to perform analogous calibrations for spectra with one or two leptonically decayed taus. The method of leptonic tau selection and the additional calibrations from [92] will be used in this chapter, and are therefore shortly summarized in the following:

Since current tau reconstruction and identification algorithms in ATLAS are limited to hadronic tau decays, electrons and muons identified by their according algorithms (see object definitions in chapter 4.3) are used to access leptonically decayed taus. For the semileptonic channel, i.e. $e\tau$ and $\mu\tau$ pairs, it is likely that the e or μ emerged from a tau decay if no other leptons are present in the event (and the tau lepton is a real one). That is different in the fully leptonic channel, where the background for ee or $\mu\mu$ pairs is overwhelming without any selection to ensure that the source of an e or μ really is a τ decay. However, there are very few sources of mixed flavour pairs $e\mu$, so by constraining the analysis to these events, tau pairs should be the dominant source⁷.

Like in the fully hadronic channel, combinatorial background as well as contributions from fake tau leptons, muons or electrons are suppressed by the OS-SS subtraction and by requiring the leptons to be close in ΔR .

The background composition obviously changes if one or two taus are replaced by an electron or a muon, so different event selection cuts have to be applied. For $\sqrt{s}=14$ TeV collisions, appropriate cuts can be found in [92], while for $\sqrt{s}=10$ TeV, a new selection is developed in section 5.4.2.

Leptonic tau lepton decays $\tau \rightarrow e/\mu\nu_e/\mu\nu_\tau$ contain one more neutrino than hadronic tau lepton decays, so the peak of the di-tau invariant mass spectrum gets shifted towards smaller values while the endpoint stays the same. The calibration 5.3 is therefore not fit to describe these spectra. Analogous to the previous study on hadronically decayed taus, calibrations for the two additional signal channels (hl and ll) have been performed with the same modified SU3 spectra used in the hh-calibration, as well as a test measurement with the actual SU3 data. The results are summarized in table 5.2 together with those of the hh study.

signal channel: invariant mass of	calibration: $m_{\tau\tau}^{\text{IP}} = a \cdot m_{\tau\tau}^{\text{max}} + b$			measured $m_{\tau\tau}^{\text{max}}$ [GeV] (nominal: 98 GeV)
	$a \pm \Delta a$	$b \pm \Delta b$	cov(a,b)	
$\tau^\pm\tau^\mp - \tau^\pm\tau^\pm$	0.47 ± 0.02	(15 ± 2) GeV	-0.034	$(105 \pm 4^{\text{stat}} \pm 4.5^{\text{syst}})$
$(\tau^\pm\mu^\mp + \tau^\pm e^\mp) - (\tau^\pm\mu^\pm + \tau^\pm e^\pm)$	0.30 ± 0.01	(13 ± 1) GeV	-0.011	$(94 \pm 4^{\text{stat}} \pm 1^{\text{syst}})$
$\mu^\pm e^\mp - \mu^\pm e^\pm$	0.13 ± 0.01	(12 ± 1) GeV	-0.010	$(99 \pm 7^{\text{stat}} \pm 3^{\text{syst}})$

Table 5.2. – Results of the leptonic tau decay modes (from [92]) compared to the full hadronic mode (from section 5.3.2), for an integrated luminosity of 10 fb^{-1} and corresponding to $\sqrt{s}=14$ TeV. Exactly the same datasets have been used in both studies.

⁷The assumption that mixed flavour lepton pairs predominantly arise from tau lepton decays is made without proof in [92]. A performance study investigating this assumption is given in section 5.4.2.

All systematic uncertainties on the endpoint measurements given in table 5.2 are based on effects of the fitting procedure.

5.4.2. Event selection for $\sqrt{s} = 10$ TeV

With only 10 TeV center-of-mass energy, the signal to background ratio worsens making it more difficult to select a clean sample of tau pairs to measure the endpoint of the spectrum: for the SU3 signal point, the NLO cross-section drops from 27.7 pb^{-1} to 8.16 pb^{-1} . This reduction factor of 0.3 is much smaller than the reduction of the main SM background, $t\bar{t}$, by a factor of 0.5.

For event generation with $\sqrt{s} = 10$ TeV, **MC@NLO** [76, 77] is used for $t\bar{t}$, **Alpgen** [75] for $W + \text{Jets}$ and $Z + \text{Jets}$, and **Pythia** [70] for the generation of p_T -binned QCD dijets. The SUSY signal is again produced with **Herwig 6.5** [71–73]. Full simulation of the ATLAS detector in **athena 14.2.25.8**⁸ is used for all but one sample, $Z \rightarrow \nu\nu$, which is made with the fast detector simulation **Atlfast-II** [110]. Differently to the fast simulation used in the studies above, this revised version consists of a new fast simulation for the calorimeter (**FastCaloSim** [82]) combined with full simulation of the inner and muon detectors. All datasets used in this study are summarized in Appendix A.2⁹.

Tau lepton identification

The hadronic tau lepton identification is slightly changed compared to the 14 TeV study: the cut on the likelihood discriminant that distinguishes taus from QCD jets has been lowered from 4 to 2. The additional fakes gained thereby are controlled by requiring the tau candidate to have exactly one or three tracks and an electric charge of exactly plus or minus one. Additionally, instead of the ΔR based overlap removal with electrons, the dedicated likelihood discriminant for tau-electron-separation [97] is used with a cut value of -2.

With this selection, the average reconstruction and identification efficiency is found to be $\epsilon_\tau^{SU3} = (55.5 \pm 0.8) \%$ in SU3 events, with a purity of $p_\tau^{SU3} = (69.9 \pm 0.9) \%$, where efficiency and purity are defined as

$$\begin{aligned} \epsilon_\tau &= \frac{N_\tau^{match}}{N_\tau^{true}} \\ p_\tau &= \frac{N_\tau^{match}}{N_\tau^{sel}} , \end{aligned}$$

with N_τ^{true} being the number of true hadronically decayed tau leptons with visible transverse momentum larger than 10 GeV and within $|\eta| < 2.5$, N_τ^{sel} the number of reconstructed taus passing above identification criteria, and N_τ^{match} the subset of selected taus that is matched ($\Delta R < 0.2$) to a true tau.

The according performance in $Z \rightarrow \tau\tau$ events is $\epsilon_\tau^{Z \rightarrow \tau\tau} = (62.4 \pm 0.2) \%$ $[(58.7 \pm 0.8) \%]$ and $p_\tau^{Z \rightarrow \tau\tau} = (97.5 \pm 0.1) \%$ $[(83.9 \pm 0.7) \%]$ for $Z \rightarrow \tau\tau + 0$ jets [+5 jets].

Jet and electron background rejection are defined via the according background efficiencies ϵ_{BG} : $r = \frac{1 - \epsilon_{BG}}{\epsilon_{BG}}$. In SU3 events, jet (electron) rejection is at the order of 100 (2000), while QCD jet rejection is between 100 (J2) and 280 (J6), and electrons from $Z \rightarrow ee$ events are rejected with a factor of 3300.

For leptonic tau lepton decays, purities p_e^{SU3} (p_μ^{SU3}) can analogously be defined as the fraction of selected electrons (muons) matched to a true electron (muon) which originated from a tau lepton decay. The selection of leptonic tau lepton decays via τ - e , τ - μ and μ - e combinations is found to perform only moderately well, with purities of $p_e^{SU3} = (31 \pm 1) \%$ and $p_\mu^{SU3} = (37 \pm 1) \%$,

⁸Reprocessing tag **r635-t53**

⁹Diboson (WW , WZ and ZZ) events (generated with **MC@NLO**) have also been investigated, but found not to contribute and are therefore not explicitly listed.

and efficiencies of $\epsilon_e^{SU3} = (68 \pm 2) \%$ and $\epsilon_\mu^{SU3} = (71 \pm 2) \%$. The purities can be somewhat augmented by an additional requirement on the maximal distance of the τ - e/μ pair (see below), but stay around 0.5.

Cut optimization

Event selection cuts have been optimized by maximizing the statistical significance $N_S/\sqrt{N_B}$ (S: signal, B: background) for events which contain at least one lepton pair satisfying $\Delta R < 2.8$. In order not to reject any SUSY signal at this first selection stage, the ΔR requirement is softened compared to the 14 TeV analysis. Figure 5.5 shows the ΔR between two tau leptons in the hh-channel and between the tau lepton and electron or muon in the hl-spectrum, respectively, for tau leptons emerging from a signal decay compared to tau leptons from other sources. Only SU3 events are investigated, and contributions from chargino pairs are displayed separately from other backgrounds. Fig. 5.5(a) and 5.5(b) are normalized to unity to demonstrate shape differences before detector simulation, τ_h here denoting the visible part of the true hadronic tau lepton decay. In fig. 5.5(a), all possible tau lepton-pair combinations are included, while in 5.5(b) only events with exactly one τ - e - or τ - μ -pair are taken into account. It is obvious that beyond the cut value of 2.8, the ΔR spectra are dominated by background sources.

Fig. 5.5(c) and 5.5(d) show the respective distributions after detector simulation for an integrated luminosity of 1.1 fb^{-1} , for reconstructed objects matched ($\Delta R(l_{\text{reco}}, l_{\text{true}}) < 0.2$) to a true lepton and passing the offline lepton-pair selection. If more than two tau leptons are present in an event, the $\tau\tau$ -pair with the least ΔR is chosen. For the semileptonic and fully leptonic

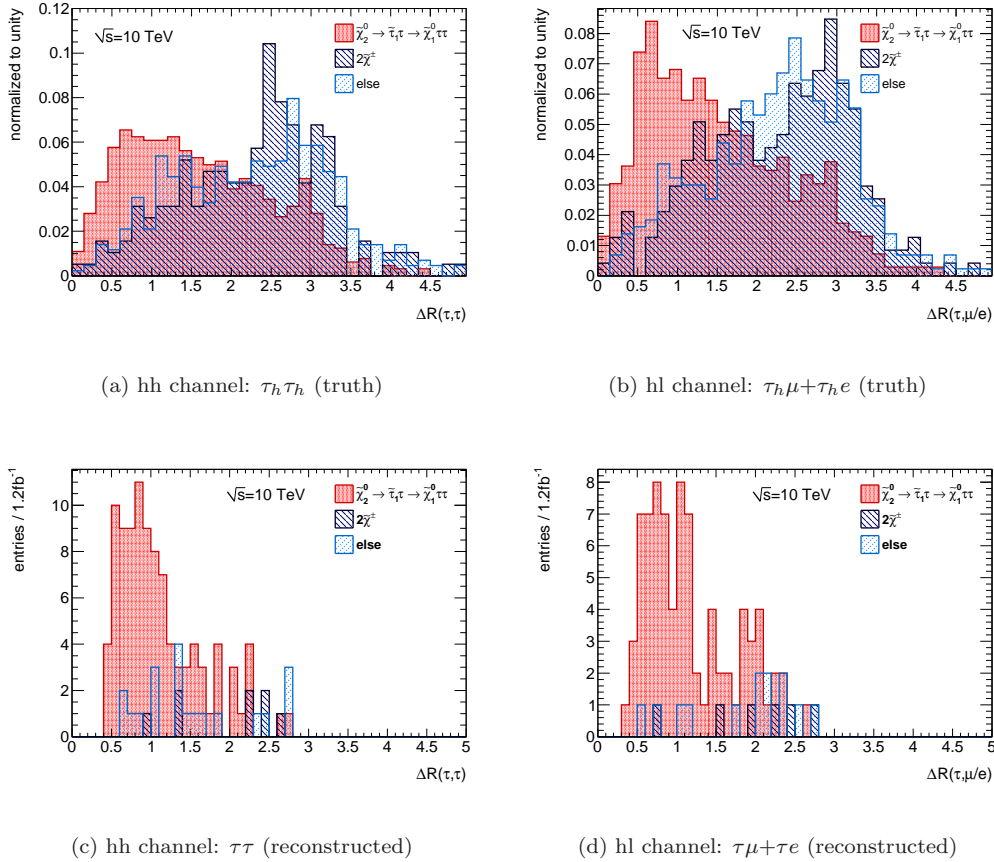


Figure 5.5. – ΔR of $\tau\tau$ -pairs (left) and $\tau(\mu/e)$ -pairs (right) in SU3, before detector simulation (up) and selected reconstructed lepton pairs (down).

channel, however, this procedure cannot be applied because only events with exactly two opposite flavour leptons are taken into account. A comparison of true and reconstructed spectrum, figures 5.5(a) and 5.5(c), confirms that choosing the tau lepton-pair closest in ΔR gives the right tau lepton-combination in most of the cases. The chargino contribution is further depleted by the tau lepton reconstruction: Since $\tilde{\chi}_1^\pm \rightarrow \tilde{\tau}_1 \nu$, those tau lepton-pairs consist of two very soft tau leptons emerging from a $\tilde{\tau}_1$ decay, therefore it is less likely that both tau leptons get reconstructed. The loosened ΔR requirement is thus shown to be sufficient.

For semileptonic tau lepton pairs, the $\Delta R < 2.8$ cut hightens the purity of selected electrons and muons coming from a tau lepton decay to $p_e^{SU3} = (46 \pm 4) \%$ and $p_\mu^{SU3} = (52 \pm 3) \%$, to be compared with overall purities of $(31 \pm 1) \%$ and $(37 \pm 1) \%$ before that cut.

Selection cuts to suppress SM background can now be obtained by maximizing the statistical significance $N_S/\sqrt{N_B}$ after the lepton pair selection. Instead of requiring a certain hardness of single leading jets as in the study with 14 TeV center-of-mass energy presented before, cutting on $H_T = \sum_{i=1}^{N_{jet}} p_T^{\text{jet}_i}$, $p_T^{\text{jet}_i} > 20$ GeV (see chapter 4.3) now performs better. To protect against events with either many low- p_T jets or a single very high- p_T jet, either of which are not very well understood, an additional safety cut requiring at least two jets with transverse momentum above 40 GeV is kept, although this cut does not increase the significance further after the other cuts have been applied. The most efficient discriminating variable remains the missing transverse energy, which is the only characteristic cut upon besides H_T . In order to avoid large fake \cancel{E}_T from mismeasured jets, the separation between \cancel{E}_T and the leading jet is required to be greater than 0.2 in $\Delta\Phi$. This cut is also regarded as a safety cut to strengthen the \cancel{E}_T predication. Figure 5.6 shows the \cancel{E}_T and H_T distributions in all three selection channels hh, hl and ll after all other cuts are applied (including the trigger EF_j70_xe30, see below). The cut values given in the captions maximize $N_S/\sqrt{N_B}$.

Events selected in this manner can best be triggered by jet plus \cancel{E}_T triggers. Trigger efficiencies with respect to SU3 events selected in the three signal channels are compared for various triggers in figure 5.7. Note that pure jet triggers are denoted with capital J, which means their performance is evaluated at Level 1 and its HLT selection is left in pass-through mode in the trigger menu used in the available datasets. While jet triggers look promising, those showing 100 % efficiency w.r.t. offline selection cannot be assumed to stay in HLT pass-through mode and unscaled but for the lowest luminosity runs. Therefore a combined jet- \cancel{E}_T -trigger, EF_j70_xe30, has been chosen for the further analysis. Although EF_2j42_xe30 is more similar to the offline selection cuts, it yields exactly the same efficiency w.r.t. offline selected events, but lower efficiency w.r.t. all SU3 events. Tau-triggers have lower efficiencies in all selection channels, shown in fig. 5.7(b).

The trigger selection will have to be reviewed when the trigger menu for a given data taking run is finalized, and offline selection cuts adjusted where necessary to secure being in the plateau of the efficiency curve of the chosen trigger.

Discovery potential of a bulk region SUSY point

The complete selection criteria for each channel and their performance in terms of SM background suppression are listed in table 5.3, a graphical display of the cut flows is given in figure 5.8. In the cut flows, the requirement of two jets with $p_T > 40$ GeV is included in the step with the H_T cut, while the $\Delta\Phi$ requirement is included in the \cancel{E}_T cut¹⁰.

The errors given in the last step of the cut flows are purely statistical, and only take subsamples into account which contribute with more than 0 events. While this is principally dangerous for QCD, where an insufficient amount of MC data leads to huge scaling factors, the expectation of zero QCD events in the final selection is strengthened by the fact that QCD is not removed by the final cut, but already by the \cancel{E}_T requirement.

¹⁰More detailed cut flow tables including the safety cuts separately as well as statistical errors on every selection step can be found in table B.1 in appendix B.

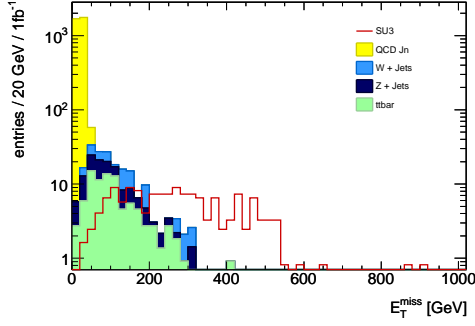
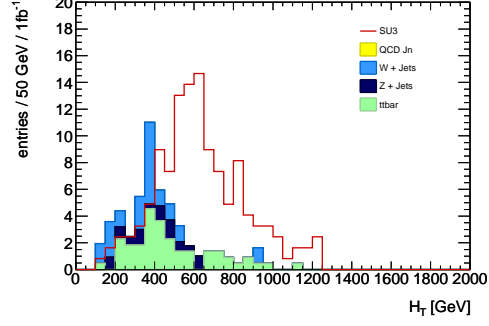
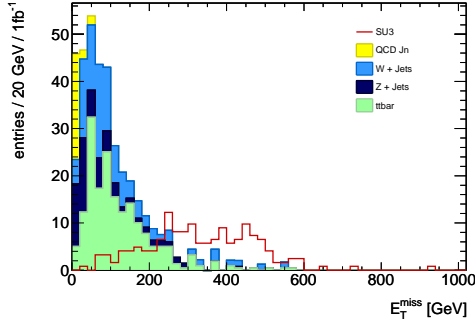
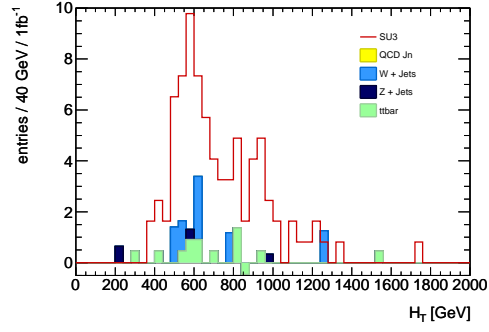
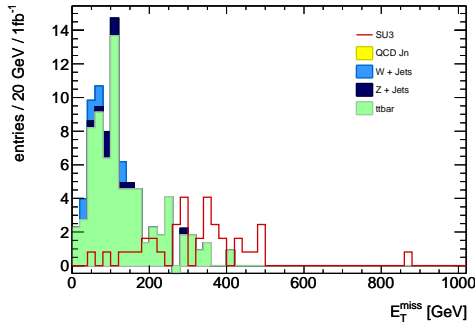
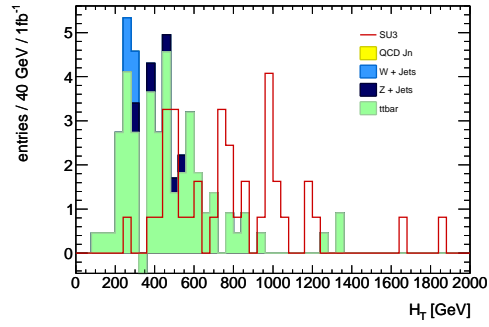

 (a) hh: E_T^{miss} (cut: 200 GeV)

 (b) hh: H_T (cut: 450 GeV)

 (c) hl: E_T^{miss} (cut: 340 GeV)

 (d) hl: H_T (cut: 500 GeV)

 (e) ll: E_T^{miss} (cut: 240 GeV)

 (f) ll: H_T (cut: 500 GeV)

Figure 5.6. – E_T and H_T distributions for SM background (stacked) and signal after all other cuts are applied, normalized to $\int L dt = 1 \text{ fb}^{-1}$.

signal channel	event selection					
	# leptons	$\Delta R(l_1, l_2)$	$\Delta\Phi(j_1, \cancel{E}_T)$	\cancel{E}_T [GeV]	p_T^{jet2} [GeV]	H_T [GeV]
hh	$\geq 2 \tau$	< 2.8	> 0.2	> 200	> 40	> 450
hl	$1 \tau + 1 (e/\mu)$	< 2.8	> 0.2	> 340	> 40	> 500
ll	$1 e + 1 \mu$	< 2.8	> 0.2	> 240	> 40	> 500

(a) Event selection for 10 TeV collisions in the three channels hh, hl and ll.

process	selection step			
	ΔR	EF	\cancel{E}_T	H_T
SU3	49	45	27	19.6 ± 1.8
$t\bar{t}$	725	239	5.8	2.3 ± 0.6
W+jets	9916	569	10	0.7 ± 0.4
Z+jets	5259	281	1.9	0.7 ± 0.2
QCD	$1.2 \cdot 10^7$	2346	0	0
ΣBG	$1.2 \cdot 10^7$	3435	18	3.7 ± 0.7

(b) cut flow: hh

process	selection step			
	ΔR	EF	\cancel{E}_T	H_T
SU3	11	9.1	6.0	4.6 ± 0.9
$t\bar{t}$	799	354	3.3	2.1 ± 0.5
W+jets	1120	69	0.2	0
Z+jets	436	44	0.3	0.1 ± 0.1
QCD	$3 \cdot 10^{-6}$	$3 \cdot 10^{-6}$	0	0
ΣBG	2355	467	3.9	2.2 ± 0.5

(c) cut flow: ll

process	selection step			
	ΔR	EF	\cancel{E}_T	H_T
SU3	53	47	17.1	14.3 ± 1.5
$t\bar{t}$	1794	756	1.2	0.9 ± 0.3
W+jets	36366	2096	1.8	1.5 ± 0.6
Z+jets	8418	526	0.3	0.14 ± 0.10
QCD	$1.5 \cdot 10^5$	10	0	0
ΣBG	$2.0 \cdot 10^5$	3387	3.2	2.6 ± 0.7

(d) cut flow: hl

channel	significance	Z_n	$\int L$ for $Z_n > 5$
	$\frac{N_S}{\sqrt{N_B}}$		
hh	10.2	4.6	250 pb^{-1}
hl	9.0	4.2	300 pb^{-1}
ll	3.1	1.6	$> 10 \text{ fb}^{-1}$
hh+hl+ll	13.9	6.5	100 pb^{-1}
hh+hl	13.6	6.3	110 pb^{-1}

(e) Significances.

Table 5.3. – Event selection, cut flows and significances for the 10 TeV selections in the hh-, hl- and ll-channel. Event numbers are normalized to 200 pb^{-1} . The H_T cut in the cut flows contains $N_{\text{jet}}(p_T > 40 \text{ GeV}) \geq 2$. EF denotes the trigger chain EF-j70_xe30. Z_n is evaluated with 50 % systematic background uncertainty (details see text).

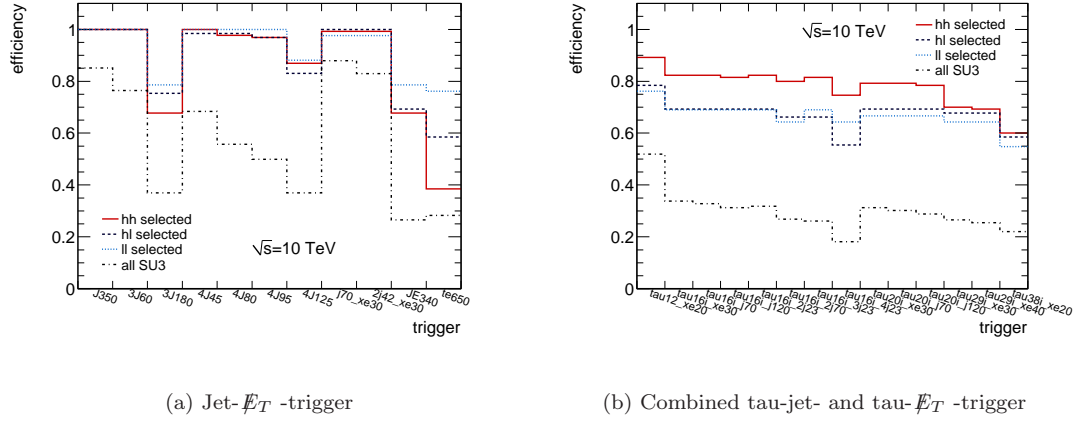


Figure 5.7. – Trigger efficiencies of various triggers. Efficiencies are w.r.t. selected events in the different channels and w.r.t. all SU3.

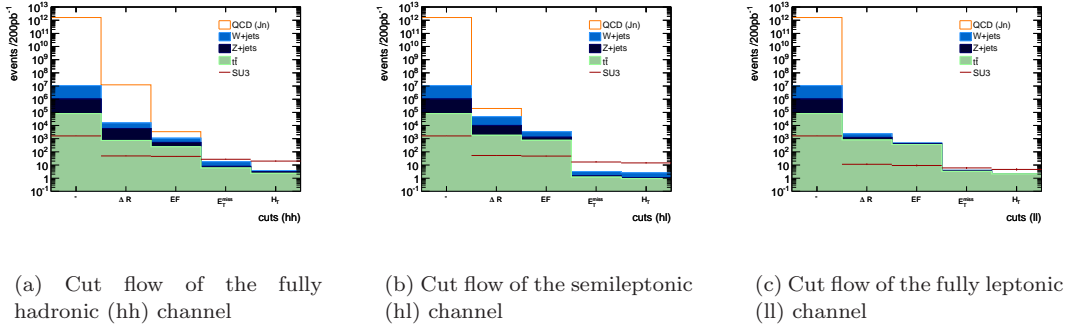


Figure 5.8. – Number of expected events with 200 pb^{-1} at the different selection stages: stacked SM background overlayed with SU3.

Since $N_S/\sqrt{N_B}$ is only a good measure of significance in the limit $N_S \ll N_B$ and for large statistics, which is given during cut optimization but not after final selection, the performance is additionally characterized by the significance Z_n [111], which is a more appropriate quantity to describe the probability of an observed signal being caused by background fluctuations in terms of standard deviations:

$$Z_n = \sqrt{2} \cdot \text{erf}^{-1}(1 - 2p) ,$$

where

$$p = A \int_0^\infty db G(N_B, \delta N_B) \sum_{i=N_{\text{data}}}^\infty \frac{e^{-b} b^i}{i!}$$

is the p-value describing the probability of measuring $N_{\text{data}} \geq N_S + N_B$ events if no signal is present (null-hypothesis). The background probability density function is here assumed to be a Poisson probability for the background fluctuating to the observed value, convoluted with a Gaussian $G(N_B, \delta N_B)$ with width δN_B and mean N_B , and normalized by a factor A .

Table 5.3(e) shows that with an integrated luminosity of $\int L dt = 200 \text{ pb}^{-1}$, $Z_n > 5$ can only be reached with a combination of both hh and hl channel, not with one signal channel alone. It is further obvious that the fully leptonic channel ll does not contribute much to the discovery potential. The combined significance Z_n can be calculated as the median significance from an Asimov test statistic $q = -2 \ln \frac{L_{S+B}}{L_B}$, where L_{S+B} is the likelihood of the signal model and L_B of the background-only hypothesis. The likelihood ratio factorizes into a product of the ratios of

the three channels [112]. Since the median discovery significance can be approximated as $Z = \sqrt{q}$ [112], it follows $Z = \sqrt{-2 \sum_i \ln \frac{L_{S+B}}{L_B}} = \sqrt{\sum_i q_i}$, thus significances of the single channels can be added in quadrature to obtain an estimation of the combined significance. The combined significance $N_S/\sqrt{N_B}$ is calculated analogously.

The minimal amount of pp collisions necessary for a 5σ discovery with these settings corresponds to $\int Ldt = 100 \text{ pb}^{-1}$ in the combination hh+hl+ll. For a proper treatment of systematic uncertainties it is favourable to consider channels separately first; 5σ can then be expected with $\int Ldt \geq 250 \text{ pb}^{-1}$, and first be observed in the hh channel.

Signal selection efficiency and purity If only lepton pairs emerging from the signal decay chain are regarded as signal rather than all SU3 events, the signal selection efficiencies within SU3 events are $\epsilon_{hh}^{sel} = (7.3 \pm 0.8) \%$, $\epsilon_{hl}^{sel} = (6 \pm 4) \%$ and $\epsilon_{ll}^{sel} = (6 \pm 9) \%$. It is noteworthy that in the semileptonic channel, the selection efficiency for $\tau\mu$ -pairs is $\epsilon_{\tau\mu}^{sel} = (8 \pm 2) \%$ and thus much better than for τe -pairs with $\epsilon_{\tau e}^{sel} = (3 \pm 2) \%$.

If no fake leptons are taken into account, $(87 \pm 4) \%$ of selected $\tau\tau$ -pairs originate from the signal decay, as well as $(91 \pm 6) \%$ of semileptonic tau lepton-pairs. In this context only chargino pairs, wrong tau lepton combinations and other SU3 sources of lepton pairs are regarded as background, and seen to be well under control.

If fake leptons within SU3 processes are also taken into account, where real electrons and muons not originating from a leptonic tau lepton decay are also regarded as fakes, this real signal purity falls to $(64 \pm 5) \%$ in the hh channel and $(26 \pm 5) \%$ in the hl channel. Fake sources of hadronic and leptonic tau lepton decays thus contribute significantly to the amount of selected SUSY events. The next section investigates to what extent an endpoint measurement under these conditions is feasible.

5.4.3. Endpoint measurement

The low signal purity ascertained above makes a fake suppression technique necessary in order to perform a sensible measurement. This is usually done by the OS-SS method, the effect of which is first tested here in SM scenarios to avoid SUSY model dependent contributions from complicated lepton correlations: the ratio $\frac{N_{SS}}{N_{OS}}$ of same-sign lepton pairs to opposite-sign pairs for $Z \rightarrow \tau\tau$, $W \rightarrow \tau\nu_\tau$ and QCD dijets are given in table 5.4(a), where the cross-section weighted mean over all subsamples (of additional jets) is taken. Events are separated into two fake tau leptons, one fake and one true tau lepton as well as one fake tau lepton and one true muon or electron. Events with fake electrons or muons do not yield enough statistics to perform this test. Only dijets with transverse momenta of at least 140 GeV (J4-J8) have been taken into account since processes composed of less energetic jets are unlikely to pass a SUSY selection. To preserve reasonable statistics, the only event selection applied is the lepton pair requirement according to the respective signal channel.

Combinations of two fake tau leptons obviously satisfy the assumption that SS pairs can, at least in amount, describe fake OS pairs. For lepton pairs composed of one true lepton and one fake tau lepton, however, this is no longer true for $W \rightarrow \tau\nu$ processes, a fact which is due to the dominant W boson production at LHC being $qg \rightarrow Wq'$, leading to a quark q' accompanying the W which is oppositely charged by sign. If the jet formed during hadronization conserves the sign of the quark charge, a resulting fake tau lepton will be oppositely charged to the lepton emerging from the decay of the W boson, thus making OS lepton pairs more likely than SS pairs. This explanation is strengthened by the fact that the excess of OS pairs decreases with the number of jets produced along with the W boson, a tendency shown in table 5.4(b) for $\tau_{\text{fake}}\tau_{\text{true}}$ pairs. For $Z \rightarrow \tau\tau$, the ratio of SS to OS tau lepton pairs shows the expected behaviour for combinations with one fake tau lepton as well as for combination of two fake tau leptons. It is therefore concluded that the OS-SS procedure yields the desired background suppression but for an irreducible fraction of W+jets events.

	hh		hl	
	$\tau_f\tau_f$	$\tau_f\tau_t$	$\tau_f\mu_t$	$\tau_f e_t$
QCD dijets	0.9 ± 0.3	-	-	-
$Z \rightarrow \tau\tau$	1.0 ± 0.3	0.90 ± 0.05	0.9 ± 0.1	0.9 ± 0.1
$W \rightarrow \tau\nu$	1.1 ± 0.2	0.39 ± 0.03	0.42 ± 0.05	0.41 ± 0.05

 (a) Ratio $\frac{N_{SS}}{N_{OS}}$. Indices f and t denote fake and true leptons, respectively.

Number of additional jets					
0	1	2	3	4	5
0.49 ± 0.05	0.30 ± 0.02	0.38 ± 0.02	0.41 ± 0.02	0.51 ± 0.03	0.57 ± 0.06

 (b) Ratio $\frac{N_{SS}}{N_{OS}}$ for $W \rightarrow \tau\nu$ subsamples, one true and one fake tau lepton.

Table 5.4. – Accuracy of modelling fake background contribution with same sign lepton pairs.

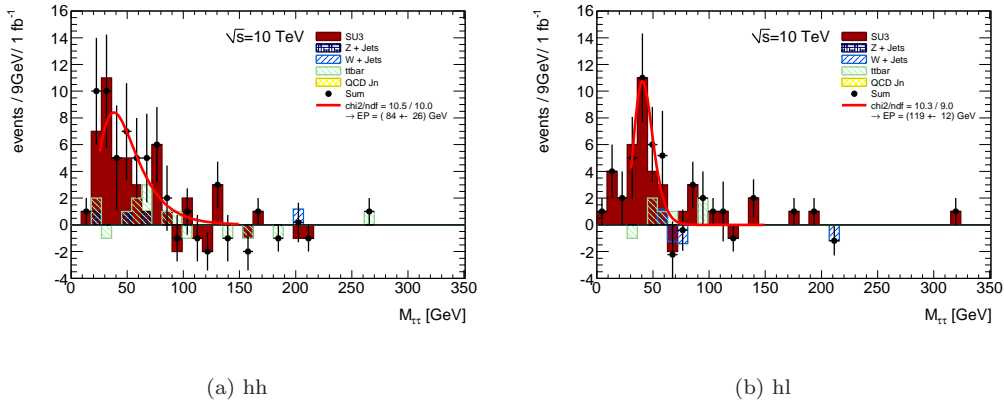
Fit results

With 1 fb^{-1} , 98 signal events can be expected in the hh channel, and 72 in the hl channel. Since roughly one third (fifth) of these events are same-sign tau lepton pairs in the hh (hl) distribution, even less events remain to show the $m_{\tau\tau}$ spectrum shape. These low statistics make an endpoint measurement challenging, and will lead to an according uncertainty on the result.

As before, fits have been done with MINUIT [109]. $m_{\tau\tau}$ distributions showing the signal and background contribution in the resulting spectra after event selection for 1 fb^{-1} are given in figure 5.9. Endpoint fits yield $m_{\tau\tau}^{max,hh} = (84 \pm 26) \text{ GeV}$ (hh) and $m_{\tau\tau}^{max,hl} = (119 \pm 12) \text{ GeV}$ (hl), which can be combined to the weighted mean

$$m_{\tau\tau}^{max} = (113 \pm 15) \text{ GeV} . \quad (5.4)$$

This result matches the theoretical value of 98 GeV well.


Figure 5.9. – Log-normal fits to hh and hl spectrum after 10 TeV event selection, normalized to $\int Ldt = 1 \text{ fb}^{-1}$, with endpoint (EP) result.

5.4.4. Systematic uncertainties

This section describes systematic uncertainties on the event selection performance and the endpoint measurement. Events passing all selection cuts of the hh, hl or ll channel under conditions modified as described below are summarized in figure 5.10 (a-c). The resulting integrated luminosity needed for a $Z_n > 5$ discovery under the assumption that the systematics under investigation do not evolve throughout data-taking and with 50 % additional systematic uncertainty on the SM background are listed in table 5.5. Endpoint measurements given in that same table have been performed with loosened cuts on the signal sample to avoid missing distortions of the invariant mass spectrum due to a lack of statistics; to this end, the cut values on \cancel{E}_T and H_T have been halved¹¹. Modifications on jets, taus, muons or electrons can influence other particle selections due to the overlap removal procedure, and have been propagated accordingly.

Fitting procedure

In the former study ($\sqrt{s} = 14$ TeV), the most dominant source of systematic uncertainties was the fitting procedure, which consists of a χ^2 minimization performed with MINUIT [109] on histograms with very little statistics. With $\sqrt{s} = 10$ TeV, due to considerably less statistics, less variation of the fitting setup is possible without MINUIT running into problems. Main source of uncertainty caused by the fitting procedure is the choice of the lower border of the fit range.

Effects of the histogram binning should be reflected in the uncertainties given on the fitted parameters by MINUIT, and thus be included in the result already. This has been verified by variation of the histogram binning, which yields endpoint results not more than 0.6 (0.5) σ away from the best fit in the hh (hl) channel.

Impact of fit range variation has been tested likewise. In the fully hadronic channel, all results are within 1 σ of the best fit, with a difference between the two most extreme results of 21 GeV. In the semileptonic channel, constraints arising from the possibility of performing a sensible fit lead to a maximum variation in results of only ± 1 GeV.

Jet and tau lepton energy scale

Another source of systematic errors is the uncertainty of the jet energy scale (JES), which is assumed to be known up to 5 % by the time 1 fb⁻¹ of data has been gathered. Effects of an over- or underestimation of the jet energy to this extent have been studied, including recalculation of \cancel{E}_T . Taus have been treated as jets here, and modified in the same way. How event selection and endpoint measurement are affected is shown in figure 5.10 and table 5.5: signal to background composition, and thus the discovery potential, are hardly influenced but for the case of a lowered jet energy scale in the semileptonic and leptonic channel, where the signal is significantly reduced while the SM background is nearly stable. This is caused by the reduced \cancel{E}_T , the cut on which is very high in the hl selection. In all channels, the \cancel{E}_T -cut is placed at the high end of the spectrum where the SM background is steeply falling, while the signal spectrum is in the plateau or just before the peak. Therefore, an underestimated \cancel{E}_T due to mismeasured jet energies, which is equivalent to a higher \cancel{E}_T -cut, results in a great loss of signal events accompanied by very little loss of background. If the JES is lowered by 5 %, the signal to background ratio in the hl channel is decreased such that a significance Z_n of 5 needed for discovery cannot be reached with default cuts and less than 10 fb⁻¹, while the fully hadronic channel shows a stable discovery potential. If the JES is measured 5 % too high, 1.5 times the data is needed for a discovery in the hh channel, while the hl signal can be observed even sooner than with accurate measurement of the jet energy.

¹¹Note that default values of endpoint results given in table 5.5 slightly differ from results stated before due to changed selection cuts.

Results of the endpoint measurement are seen to be well within 1σ in both the hh and the hl channel, even in the case where the signal to background ratio is too low for discovery. The maximal variations are $+7$ GeV (hh) and -14 GeV (hl).

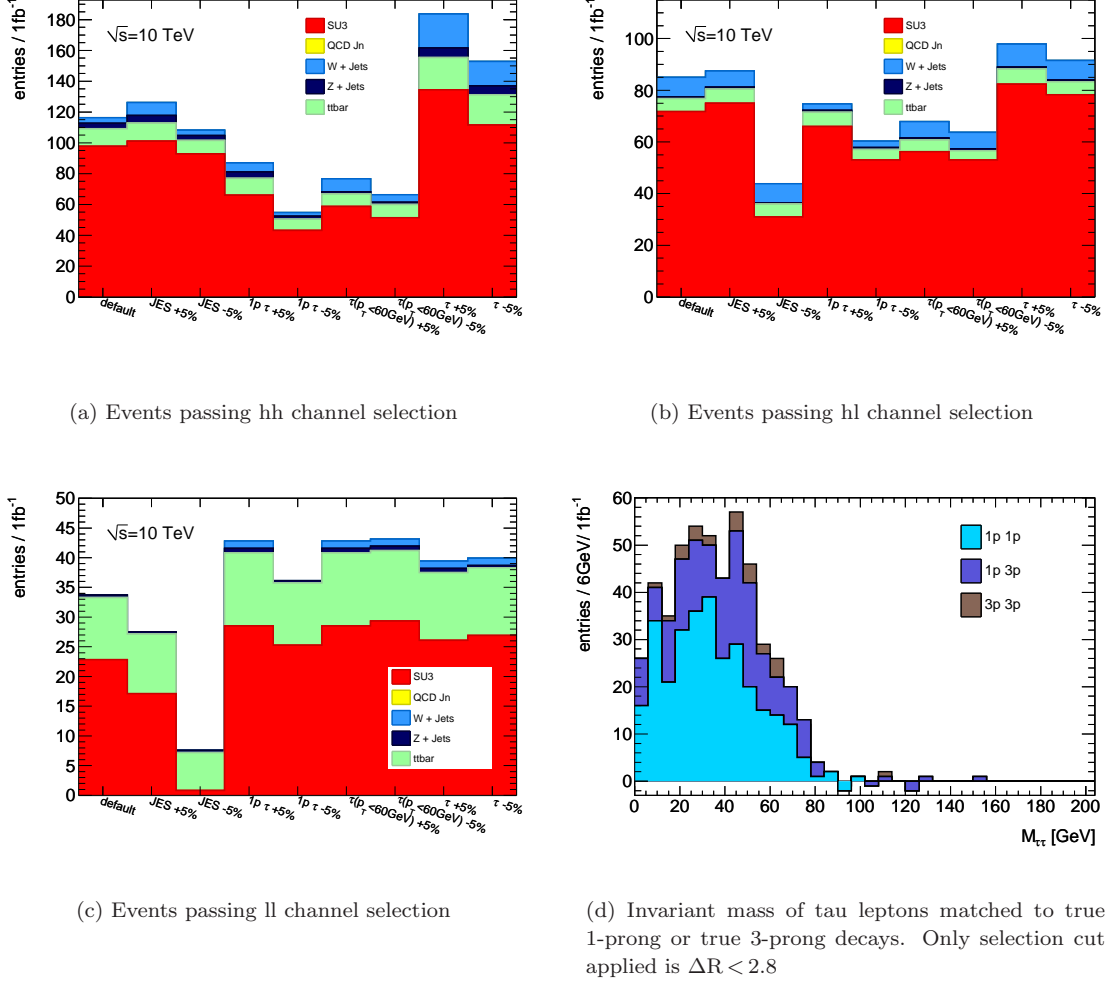


Figure 5.10. – Effect of different systematic uncertainties (a-c), and invariant mass of tau leptons matched to true 1-prong or true 3-prong decays to illustrate possible distortions from an asymmetric efficiency.

Tau identification efficiency

While a modification of the tau lepton reconstruction and identification efficiency will influence the statistics available in the invariant mass spectrum and the signal to background ratio, the spectrum shape can also be distorted if certain classes of tau leptons alone are reconstructed less or more efficiently than other classes of tau decays. This is most likely to happen between 1- and 3-prong tau leptons, since most τ identification algorithms train separate discriminants (likelihood, BDT or set of cuts) for them, or for tau leptons of different p_T regimes. The effects of a modified tau lepton identification efficiency is therefore tested by performing the event selection and endpoint measurement with $\pm 5\%$ identification efficiency of all tau leptons, 1-prong tau leptons or tau leptons with $p_T < 60$ GeV. To this end, the spectrum of the likelihood discriminant of according tau leptons has been integrated from the original cut value of 2 such

that $\int_{x,low}^2 dL = \int_2^{x,high} dL = 0.05 \cdot \int_2^\infty dL$, with x_{high} , x_{low} then giving the cut on the likelihood discriminant to obtain 5 % less or more identified tau leptons, respectively.

The fully hadronic channel is naturally more vulnerable to an uncertainty in the tau lepton efficiency than the semileptonic channel. Varying the overall tau lepton efficiency ϵ_τ by ± 5 % both leads to an increasing amount of signal and background events passing all selection cuts in the hh and hl channels: if more tau leptons are identified this development is straight forward, a decreased ϵ_τ leads to lost tau leptons being considered as jets, thus contributing to H_T and increasing the probability of an event to pass the cut threshold. Since these mechanisms operate on signal and background alike, the signal to background ratio worsens such that the discovery potential is significantly reduced in the fully hadronic channel. The extent of this effect is however highly model dependent, since it will change with the average amount of real tau leptons and jets present in the realized SUSY scenario, and also on the preferred type of jets since b -jets are more prone to fake tau leptons than jets originating from light quarks, which in turn mimic tau leptons more often than gluon jets.

An overall uncertainty of the tau lepton identification efficiency does not, however, affect the accuracy of an endpoint measurement since reduced statistics of real tau leptons will reflect back into the statistical error, and additional fakes are controlled by the OS-SS subtraction. This is confirmed in table 5.5.

If only tau leptons reconstructed as 1-prong are identified more or less efficiently, figure 5.10(d) suggests that for lower efficiency of 1-prong tau leptons ϵ_τ^{1p} , the invariant mass spectrum should be distorted to higher values, while an excess of 1p tau leptons should favour low invariant masses and thus lead to an underestimation of the endpoint. Similarly, if only low p_T tau leptons are identified with higher or lower efficiency ϵ_τ^{pT} in data than modelled in MC while the efficiency of high p_T tau leptons behaves as expected, the invariant mass spectrum should give higher or lower endpoint values as fit results. The according measurements, however, show endpoint values significantly too low for both variations of ϵ_τ^{1p} and of ϵ_τ^{pT} compared to the default result in the hh channel, with only the relative endpoint values between over- and underestimation of the efficiencies meeting the expectation. This shift to low invariant masses is (with the given precision) not observed in the semileptonic channel. A possible explanation might be that if the lower part of the spectrum gets depleted, more of the rising edge of the spectrum is taken into account and the fit function is pulled to lower values, thus producing lower inflection point and endpoint. Nevertheless it must be concluded that if the relative efficiency of 1p to 3p tau leptons is not precisely known, as well as if the relative efficiency of low p_T to high p_T tau leptons involves considerable uncertainty, a measurement in the fully hadronic channel suffers from an additional systematic uncertainty of up to 50 % for ± 5 % uncertainty in either of the investigated efficiencies.

Evidence of wrongly modelled tau lepton efficiencies can be obtained by the ratio of data in the different signal channels, assuming a high signal cross-section resulting in large statistics. Before the tau identification performance in a SUSY environment can be measured in such a way, the efficiency can be tested in well understood SM processes like $Z \rightarrow \tau\tau$, $W \rightarrow \tau\nu$ and $t\bar{t} \rightarrow W^+W^-b\bar{b} \rightarrow \tau\nu_\tau l\nu_l b\bar{b}$, where $l = e, \mu$.

The same procedure as above has been done with the likelihood dedicated to tau-electron separation, modifying the default cut at -2 to alter the overall efficiency ϵ_τ^e by ± 5 %. All endpoint measurements obtained in this way are compatible within 1σ with the unmodified measurement.

Electron and muon energy scale

The energy measurement of electrons and muons is more accurately known than for tau leptons. Nevertheless a systematic over- or underestimation of the muon or electron energy could affect the semileptonic invariant mass spectrum. Therefore energy shifts of the order of ± 2 % have been tested, including the respective \cancel{E}_T contribution. The impact on both selection efficiencies and endpoint results are negligible compared to the other uncertainties.

	$\int dtL$ for $Z_n > 5$ [pb $^{-1}$]		$m_{\tau\tau}^{max}$ [GeV]	
	hh	hl	hh	hl
default	240	350	111 \pm 10	104 \pm 18
JES +5%	360	270	118	111
JES -5%	220	-	106	90
ϵ_τ +5%	2070	300	111	109
ϵ_τ -5%	2890	260	111	98
ϵ_τ^{1P} +5%	1190	160	61	110
ϵ_τ^{1P} -5%	1520	300	78	104
ϵ_τ^{PT} +5%	1270	500	69	90
ϵ_τ^{PT} -5%	1150	550	81	89
ϵ_τ^e +5%	240	240	102	89
ϵ_τ^e -5%	150	210	117	83

Table 5.5. – Impact of dominant systematics on discovery potential and endpoint result.

Endpoint ambiguity

A different kind of systematic error on the endpoint measurement is caused by the assumption that the invariant mass spectrum that can be described by a log-normal function is caused by the signal decay $\tilde{\chi}_2^0 \rightarrow \tilde{\tau}_1 \tau \rightarrow \tilde{\chi}_1^0 \tau \tau$. However, depending on the SUSY model, other sources might lead to a similar spectrum. If the signal decay is kinematically closed, an observed spectrum can be dominated by similar decay chains $\tilde{\chi}_A^0 \rightarrow \tilde{\tau}_B \tau \rightarrow \tilde{\chi}_C^0 \tau \tau$ with any of the four $\tilde{\chi}^0$ and the two $\tilde{\tau}$ involved. An observed ditau spectrum could also have emerged from a 3-body decay instead of successive 2-body decays.

Figure 5.11 shows the hh invariant mass spectrum of reconstructed tau leptons matched to true tau leptons, ordered by the origin of the truth tau lepton, in the mSUGRA points SU3 and SU11. Both spectra can be fitted with a log-normal function, yet the obtained endpoint of SU11 does not satisfy equation 5.1, but does not depend on the $\tilde{\tau}_1$ mass at all because the measured spectrum is dominated by tau lepton-pairs from the 3-body decay $\tilde{\chi}_2^0 \rightarrow \tilde{\chi}_1^0 \tau \tau$.

A distinction between 2- and 3-body decays can easily be made in muon- or electron-spectra

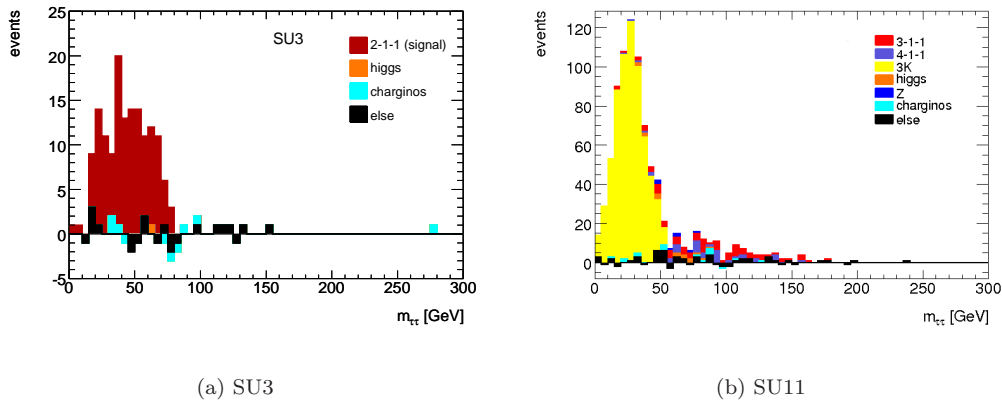


Figure 5.11. – Origin of tau leptons in the hh invariant mass spectrum in SU3 and SU11 ($\sqrt{s} = 10$ TeV): possible signals $\tilde{\chi}_A^0 \rightarrow \tilde{\tau}_B \tau \rightarrow \tilde{\chi}_C^0 \tau \tau$ are denoted A-B-C, with 2-1-1 being the main signal targeted. 3K means the 3-body-decay $\tilde{\chi}_2^0 \rightarrow \tilde{\chi}_1^0 \tau \tau$.

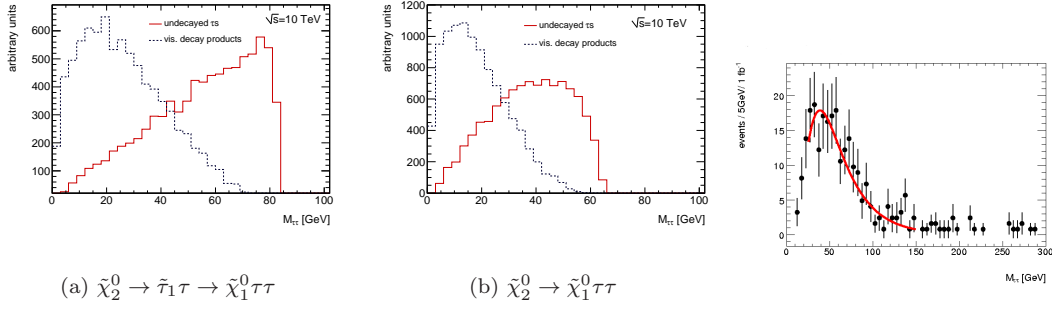


Figure 5.12. – Shape difference of invariant mass spectra of two tau leptons (before detector effects) emerging from a $\tilde{\chi}_2^0$ by 3-body-decay or successive 2-body-decays, with true endpoints at 65 GeV and 83 GeV, respectively.

Figure 5.13. – Fit of log-normal function to OS+SS spectrum: $\chi^2/ndf = 13.5/16$.

because the triangular shape characteristic for a signal-like decay chain is not present in case of a 3-body decay. Figure 5.12 illustrates invariant mass spectra for both 3- and 2-body decays before simulation of detector effects, for undecayed tau leptons as well as for the visible decay products of the tau leptons. While the spectra of undecayed tau leptons are easy to distinguish by their shape, the tau lepton decay smears out these differences.

5.4.5. Alternative fit method: unbinned maximum likelihood fit

One problem of the above measurement is the very poor statistics available, which causes large fluctuations in the obtained result depending on the chosen histogram binning in the fit. While the uncertainty generated thereby is reflected in the fit parameter's uncertainties, it is nevertheless desirable to obtain a more robust way of fitting the presumed shape to data in order to be able to perform a measurement as soon as possible. If the number of events for a measurement is small (or the number of observables large), the classical method of choice is a maximum likelihood fit. This section evaluates the viability of such an approach.

The Likelihood function

The probability density function (pdf) of the invariant mass spectrum is a log-normal function as given in equation 5.2. The corresponding likelihood function is therefore

$$L(\vec{x}; \vec{p}) = \prod_i \frac{p_0}{x_i} \cdot \exp\left(-\frac{1}{2p_2^2}(\ln(x_i) - p_1)^2\right) \equiv \prod_i f(x_i, \vec{p}),$$

where $p_0 = \frac{1}{\sqrt{2\pi}p_2}$ is the normalization and p_1, p_2 are the mean and width to be determined by the fit. Since in MC simulation the data consist of various subsamples of signal and SM background, single events i contribute with a weight factor w_i :

$$L(\vec{x}; \vec{p}) = \prod_i (f(x_i, \vec{p}))^{w_i}.$$

The best fit can now principally be found by maximizing L , or more conveniently minimizing $-\ln(L)$. However, the pdf used in the likelihood describes the OS-SS spectrum, while this likelihood function takes single measurements $x_i = m_{\tau\tau,i}$ as input. This problem can not be avoided by fitting the OS and SS spectrum separately and subtracting the resulting functions afterwards, because even if the OS and SS spectra can separately be described by log-normal

functions, the difference of two log-normal functions is not itself an analytically calculable log-normal function anymore¹².

Figure 5.13 shows that the sum OS+SS can be reasonably well described by a log-normal distribution. The following approach has therefore been taken¹³: define two log-normal functions $u \equiv f_{OS} + f_{SS}$ and $v \equiv f_{OS} - f_{SS}$, with $f_{OS,SS}$ being the probability density functions of the OS and SS spectrum, respectively. Then $f_{OS} = \frac{1}{2}(u + v)$ and $f_{SS} = \frac{1}{2}(u - v)$, and the likelihood function of all invariant mass values (OS and SS) can be written as

$$\begin{aligned} L(\vec{x}; \vec{p}, \vec{q}) &= \prod_i f_{OS}(x_i, \vec{p}, \vec{q}) \cdot \prod_j f_{SS}(x_j, \vec{p}, \vec{q}) \\ &= \prod_{OS} \frac{1}{2}(u + v) \cdot \prod_{SS} \frac{1}{2}(u - v), \end{aligned} \quad (5.5)$$

with $u = u(\vec{q})$, $v = v(\vec{p})$ being two separate log-normal functions describing the OS+SS and the OS-SS spectra. Since u and v are both normalized, the ratio of OS to SS events is introduced by multiplicative factors $r_{1,2} = N_{OS} \pm N_{SS}$.

The probability distribution L is not straight-forward to normalize, therefore an extended maximum likelihood method [114] is used:

$$\sum_i \ln f(x_i; \vec{p}, \vec{q}) \rightarrow \sum_i \ln (N \cdot f(x_i; \vec{p}, \vec{q})) - N.$$

In data, the factor N should reflect the total number of events, while in MC, $N = \sum_i w_i$.

The function to be minimized is therefore finalized to

$$- \left(\sum_i^{N_{OS}} \left(w_i \ln \frac{N}{2} (r_1 u(x_i, \vec{q}) + r_2 v(x_i, \vec{p})) \right) + \sum_j^{N_{SS}} \left(w_j \ln \frac{N}{2} (r_1 u(x_j, \vec{q}) - r_2 v(x_j, \vec{p})) \right) - N \right). \quad (5.6)$$

This method has the disadvantage of introducing nuisance parameters \vec{q} , and of requiring $(r_1 u - r_2 v)$ to stay positive throughout the fitting procedure to assure that the logarithm of the likelihood describing the SS events is defined.

Result

Fits have been performed with MINUIT [109]. First, a binned histogram fit is made both to the OS-SS and the OS+SS spectra, and the parameter values for u and v gained thereby are taken as starting points for \vec{p} and \vec{q} . Results of the endpoint measurement obtained with both methods, the binned χ^2 minimization and the unbinned extended maximum likelihood (EML) method for the usual SU3 selection with SM background and with a statistics of $\int L dt = 1 \text{ fb}^{-1}$ are:

$$\begin{aligned} m_{\tau\tau}^{\max}(hh) &= (84 \pm 26) \text{ GeV } (\chi^2) \\ &= (92 \pm 12) \text{ GeV (EML)} \\ m_{\tau\tau}^{\max}(hl) &= (119 \pm 12) \text{ GeV } (\chi^2) \\ &= (97 \pm 5) \text{ GeV (EML)}. \end{aligned} \quad (5.7)$$

¹²The Fenton-Wilkinson (FW) approximation [113], which describes a sum of log-normal functions with a third log-normal function, and which is supposed to work well in the right tail of the spectrum, has been tested by comparing the approximated mean and width parameter with the fit result of the OS+SS spectrum.

The obtained parameter values are significantly different, therefore it is concluded that the spectrum region important for the measurement is not fully included in the region where the FW approximation is valid.

¹³The helpful suggestions of G. Cowan are gratefully acknowledged

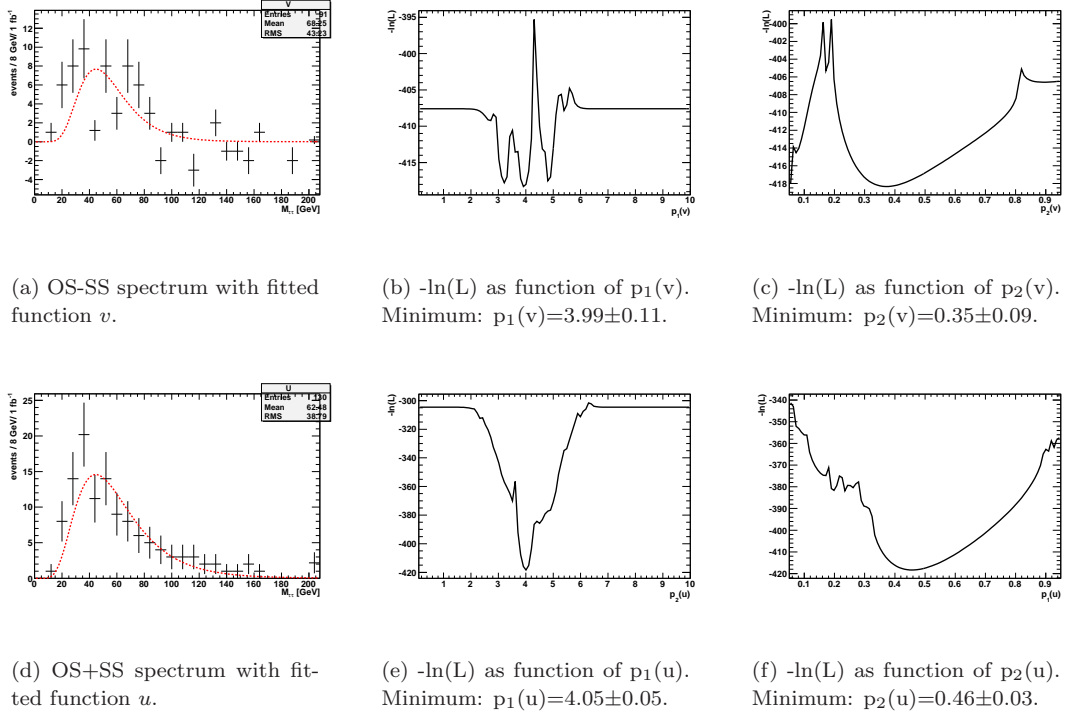


Figure 5.14. – Result of an unbinned maximum likelihood fit for the hh channel: fitted log-normal functions u , v and the negative log likelihood as function of the fit parameters, with all other parameters fixed at their fitted value.

Combining the hh and hl channel yields

$$\begin{aligned} m_{\tau\tau}^{\max}(hh) &= (113 \pm 15) \text{GeV } (\chi^2) \\ &= (96 \pm 7) \text{GeV } (\text{EML}). \end{aligned} \quad (5.8)$$

The endpoint values are consistent and the statistical error on the result seems to be smaller in the EML case than for the χ^2 fits. These errors, however, are sometimes profoundly underestimated, as is illustrated in figure 5.14 for the hh channel: Along with the fitted log-normal functions, $-\ln L$ is shown as a function of the nuisance parameters $p_{1,2}(u)$ and of the parameters of interest $p_{1,2}(v)$, which are used to calculate the endpoint. All respective other parameters are fixed at their fitted value. Parameter errors are calculated by MINUIT as the difference of the values they take as the likelihood rises by $+0.5$ left and right of the minimum to the values acquired in the minimum. If the likelihood is not a smooth function, however, this is not a sensible method. While the likelihood curve for parameters $p_2(u,v)$ is sufficiently smooth in the vicinity of the minimum, this is sometimes not the case for parameters $p_1(u,v)$. In case of the SU3 hh fit, $p_1(v)$ even has two local minima nearly as deep as the global one, which suggests an uncertainty of the order of the distance between the minima rather than the one given by the fit. This behaviour is caused by the ambiguity introduced by a subtraction of two functions with independent mean and width parameters such that a fit minimum can possibly be obtained by more than one combination. This hypothesis has been verified by forcing the nuisance mean parameter $p_1(u)$ to be equal to the target mean parameter of the OS-SS distribution $p_1(v)$, leading to a smooth likelihood function $-\ln L(p_1(v))$ with no secondary minima.

In order to test the reliability of such fit results and estimate an appropriate uncertainty, 500 sets of data points have been randomly generated following a combination of two log-normal

distributions u' , v' to represent opposite-sign (OS) and same-sign (SS) spectra: $OS = u' + v'$ and $SS = u' - v'$. The ratio of OS to SS events has been taken from the 14 TeV measurement with 10 fb^{-1} to get a realistic OS-SS expectation with minimal effects of statistical fluctuations, the absolute amount of data points represents the expected events for the hh channel at 10 TeV and 1 fb^{-1} . Both measures include selection cuts and SM background. The accuracy of results obtained with the unbinned likelihood procedure described above can now be tested by performing all 500 fits: the parameter results should be Gaussians with the mean representing the most likely fit value and the width the 1σ uncertainty on the result. The input parameters have been $p_2(v') = 0.32$ and $p_1(v') = 3.92$, which give an endpoint of 96 GeV.

The fitting is performed in $25 \cdot 8 = 200$ different ways for every one of the 500 datasets, with 8 different starting values of the fit parameters $p_2(v')$ and $p_1(v')$ combined with 5 different lower and upper fit range thresholds. The best fit is chosen such that a Kolmogorov test of the function v' to the OS-SS spectrum yields the best result.

This method to estimate the accuracy of the fit result differs in two aspects from the fitting procedure to be investigated, which have to be kept in mind when interpreting the fit results. Since the dicing procedure lacks a function to describe the OS and SS spectrum shapes, it includes addition and subtraction of two log-normal functions to simulate the OS and SS distribution, which then in turn are described by an additional combination of two log-normal functions in the fitting procedure. However, only the tails of the functions thus obtained are fit to describe a real measurement. Doubling this summation and subtraction in the Toy MC compared to the real measurement might result in a limitation of the range in which these spectra feature the expected properties.

A further difference might arise by the choice of the fit range. In a real measurement, the fit is performed such that it describes the trailing edge of the distribution best without major contribution from the rising edge of the spectrum. By scanning the fit range in an automatic way for all datasets from the Toy MC, the fits potentially take more of the spectrum's rising shoulder into account than the calibration is designed for. In order to minimize this effect, only data points with invariant masses greater than the median value are taken into account in the Kolmogorov test to choose the best fit out of the 200 performed per dataset, thus preventing a dominant contribution of the rising edge to the obtained result.

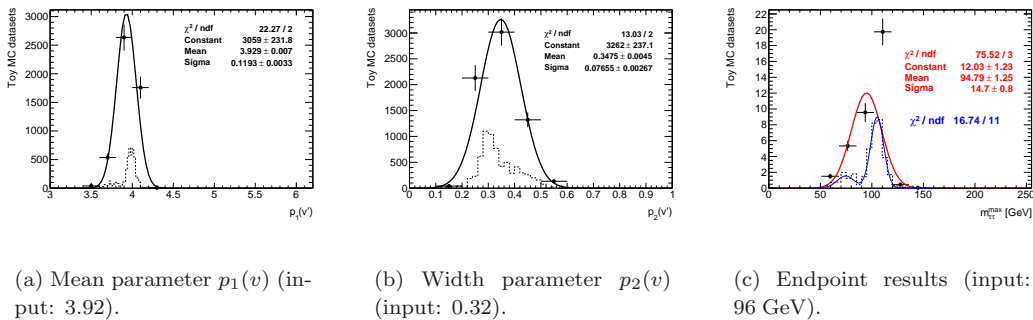


Figure 5.15. – Toy Monte-Carlo: results of 500 fits.

The measured parameter values and endpoints obtained in this manner are shown in figure 5.15. In order to take the different quality of the fits into account, the resulting parameters are filled in these histograms with a weight equal to the inverse of their uncertainties as given by the fits.

The χ^2 / ndf of Gaussian fits imply that the fitted parameters as well as the resulting endpoint measurements of each fit do not follow the expected Gaussian behaviour. This is caused by the ambiguity introduced with the minus-sign as mentioned above, which leads to a double-peak structure in the parameters describing the log-normal function v' , shown by the dotted lines in

figure 5.15. The nuisance parameters describing the function u' show no such substructure. The Gaussian behaviour in the two separate fit minima is tested by fitting a sum of two Gaussian functions to the spectrum of endpoint results in figure 5.15(c), which yield reasonable agreement. In order to estimate the uncertainty of the fit results besides this artefact of the Toy MC, a Gaussian fit is performed to spectra with such coarse binning that the substructure is washed out. This results in rather broad distributions with a mean endpoint result of (95 ± 1) GeV in agreement with the input variables, but spread around that mean value with (15 ± 1) GeV.

Comparison of this spread with the uncertainty of the result 5.7 given by the fit shows that the uncertainty is about one third larger than claimed by `Minuit`. However, a result obtained with the unbinned maximum likelihood fit is still more precise than the binned χ^2 fit, which is expected from the information loss involved in the binning procedure.

It must be concluded that the fitting method presented in this section is not suited to replace the binned histogram fit, because the error on the fit parameters are sometimes underestimated, and cannot always be determined without special effort. The likelihood function has to be checked to estimate the reliability of the errors given by the fit.

Nonetheless, the EML method is a valuable cross-check, especially in cases where endpoint measurements in the different channels hh and hl do not yield the same results. Examples of this can be found in the next section, where the analysis is tested on different mSUGRA points.

5.4.6. Scan of mSUGRA parameter space

The signal selection and endpoint measurement techniques described above have been developed for the mSUGRA bulk region point SU3, yet should be applicable in every scenario with similar mass hierarchy that allows for the signal chain to be open. In terms of selection efficiency, it is sufficient if tau lepton production is enhanced and a stable LSP provides more missing transverse energy than typically found in SM processes. This section evaluates the performance of the above selection in different points of the mSUGRA parameter space. To this end, a scan of the m_0 - $m_{1/2}$ -plane is performed for 7 different $\tan\beta$ and A_0 values, while $\text{sgn}(\mu)$ is kept positive. Most points have been generated for $\tan\beta=10$, $A_0=0$ GeV. For $\tan\beta=30$ and 50, simulated points are divided into 3 subplanes $A_0=0, \pm 400$ GeV. The mSUGRA grid used in this part of the study has been generated centrally as part of the official production by the ATLAS SUSY group. A full list of all investigated mSUGRA points including the relevant stau and neutralino masses can be found in appendix A.2.2.

The integrated luminosity necessary to observe a 5σ deviation from the SM background expectation with the selection cuts developed in section 5.4.2 and a systematic background uncertainty fixed to 30 % is shown in figure 5.16. Since the subgrids are not fine enough to determine discovery contours, data points are classified into four ranges of integrated luminosity with which $Z_n \geq 5$ can be achieved. For $\tan\beta=10$ and $A_0=0$ GeV, the significance Z_n is also shown in figure 5.16(a) for $\int Ldt = 1 \text{ fb}^{-1}$, as well as $N_S/\sqrt{N_B}$ in 5.16(b) for comparison¹⁴. If $N_S \gg N_B$, the probability p of the observed amount of events being caused by a background fluctuation is approximately zero, and thus the inverse error function $\text{erf}^{-1}(1-2p)$ and therefore Z_n approaches infinity. In this case, Z_n has been set to 100 in figures 5.16(b) and 5.17(b) to adjust the scale of Z_n to that of $N_S/\sqrt{N_B}$ for comparison.

The mSUGRA region with approximately $m_0 \leq 500$ GeV and $m_{1/2} \leq 200$ GeV can be discovered with up to $\int Ldt = 1 \text{ fb}^{-1}$ in all investigated scenarios, except for a few points where the signal decay is closed because $m_0 > m_{1/2}$ and so $m_{\tilde{\tau}_1} > m_{\tilde{\chi}_2^0}$, and simultaneously the branching fraction of the corresponding 3-body decay is too small to yield a sizable signal. Since few points have been generated in these interesting regions of parameter space, corresponding discovery thresholds given in this section are intended as order-of-magnitude benchmarks. They also serve to determine the region important for early searches with 7 TeV, for which a finer grid is used

¹⁴Exact values of Z_n including 30 % and 50 % systematic uncertainty on the background expectation and for an integrated luminosity of $\int Ldt = 1 \text{ fb}^{-1}$ for all subgrids are given in figures B.1 and B.2 in appendix B.

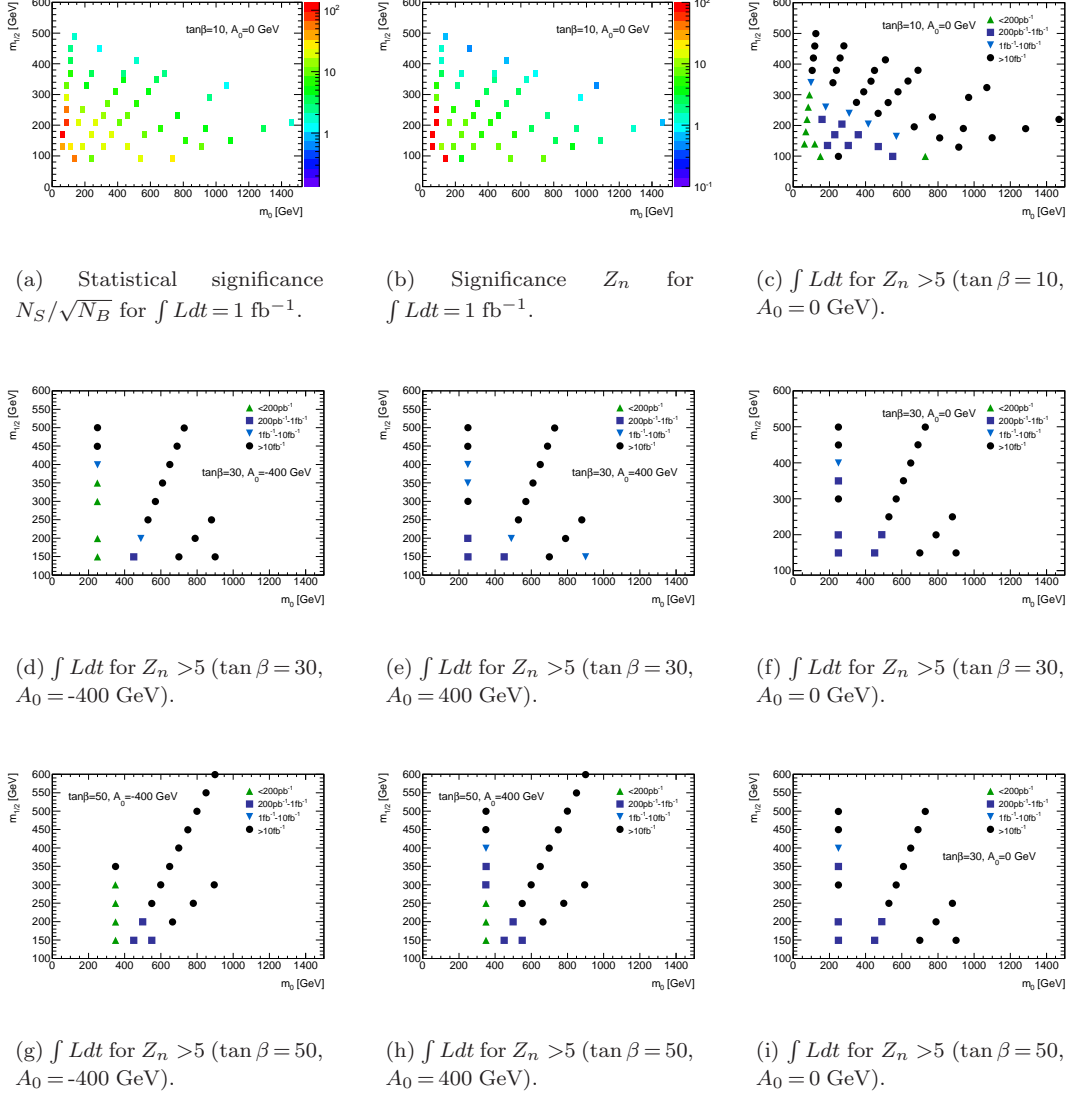


Figure 5.16. – Integrated luminosity necessary for 5σ as function of m_0 and $m_{1/2}$ for different $\tan\beta$ and A_0 ($\text{sgn}(\mu) > 0$), assuming a constant systematic background uncertainty of 30%. For $\tan\beta = 10, A_0 = 0 \text{ GeV}$, the distributions of actual Z_n and $N_S/\sqrt{N_B}$ values are also shown for fixed $\int Ldt = 1 \text{ fb}^{-1}$.

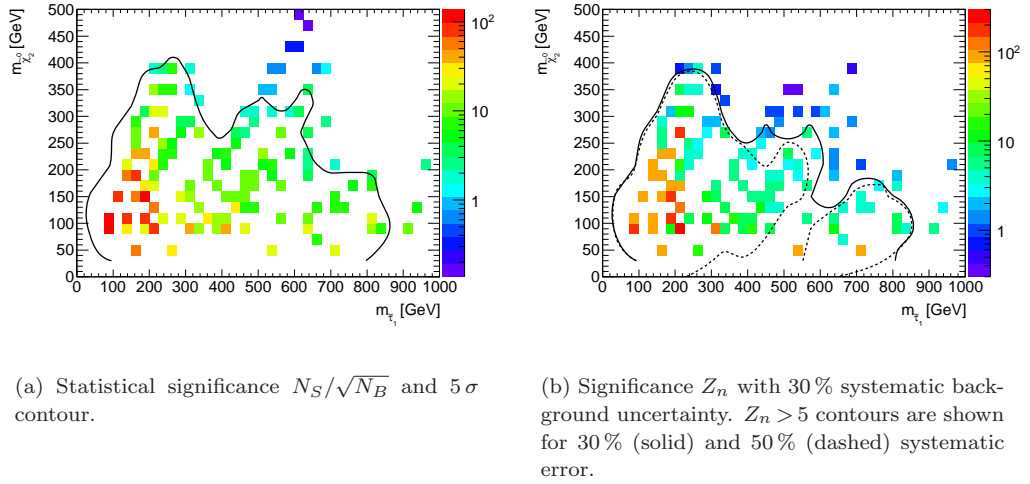


Figure 5.17. – Significance with and without systematic uncertainty for $\int L dt = 1 \text{ fb}^{-1}$ and 5σ discovery reach in $m_{\tilde{\tau}_1} - m_{\tilde{\chi}_2^0}$ -plane.

in the next chapter. For $A_0 = 0 \text{ GeV}$, the 1 fb^{-1} discovery reach is comparable for $\tan\beta$ 10, 30 and 50, while the 5σ region for 200 pb^{-1} is enlarged for $\tan\beta = 50$. This dependence on $\tan\beta$ is expected due to the enlarged mixing in the third generation with rising $\tan\beta$.

Figure 5.17 shows the significance for all investigated mSUGRA points in the $m_{\tilde{\tau}_1} - m_{\tilde{\chi}_2^0}$ -plane for 1 fb^{-1} , as well as the corresponding 5σ contour line.

If $m_{\tilde{\tau}_1} \leq 400 \text{ GeV}$ and $m_{\tilde{\chi}_2^0} \leq 200 \text{ GeV}$ or vice versa, a 5σ signal can be expected even with up to 50 % background uncertainty. Higher $\tilde{\tau}_1$ masses are however only accessible if the systematics are well under control.

In those parameter points that can be discovered first, the signal selection efficiency times production cross section can be expected to be large enough to allow an early endpoint measurement. Thus the measurement methodology can be tested in these different mSUGRA scenarios, and the unbinned EML fitting method described in the previous section can be tested against the standard χ^2 histogram fit. To these ends, according fits are performed with data corresponding to an integrated luminosity of 1 fb^{-1} , and compared to the theoretical value. Points thus investigated are listed in table 5.6¹⁵, and the results displayed in table 5.7. The errors given for the EML fit are calculated from the parameter uncertainties given by MINUIT and might thus be underestimated.

While the unbinned likelihood method is sometimes able to perform a fit of the hl spectrum in cases where the χ^2 procedure does not converge, the accuracy of obtained results is on average comparable. It is, however, a valuable cross-check to perform both fits, especially if only the hh spectrum yields a result: in points 2 and 3, for example, wrong endpoint results are obtained with the χ^2 fit, yet the incompatible EML measurement indicates a problem with this spectrum that is not yet understood.

If only spectra dominated by the signal decay are considered, in about half the cases (points 1, 2, 3 and 15) a bad fit result is exposed by a contradicting result of the second method: in three of these four points, the single EML result is within 1σ of the true value, while the χ^2 is farther off. In points where both methods yield compatible results (4, 9, 12 and 23), the endpoint is measured correctly within the statistical uncertainty. Only one point (22) gives consistent results in both measurements with a true endpoint slightly more than 1σ away.

¹⁵Some points principally among the first to be visible could not be investigated in this manner due to a lack of generated statistics.

5. Endpoint measurement of a $\tau\tau$ invariant mass spectrum

mSUGRA point						mSUGRA point					
	$\tan\beta$	A_0 (GeV)	m_0 (GeV)	$m_{1/2}$ (GeV)	$\int Ldt$ (pb $^{-1}$)		$\tan\beta$	A_0 (GeV)	m_0 (GeV)	$m_{1/2}$ (GeV)	$\int Ldt$ (pb $^{-1}$)
1	10	0	91	300	500	13	50	0	190	135	30
2	10	0	77	220	20	14	50	-400	350	150	150
3	10	0	70	180	10	15	50	400	350	350	450
4	10	0	84	260	50	16	50	0	230	170	30
5	10	0	120	140	280	17	50	0	270	205	40
6	10	0	160	220	1530	18	50	0	310	240	160
7	30	0	250	150	980	19	50	400	350	250	330
8	30	-400	250	150	210	20	50	400	350	300	650
9	30	-400	250	300	90	21	50	-400	350	200	10
10	30	0	250	200	1530	22	50	-400	350	250	30
11	30	-400	250	200	110	23	50	-400	350	300	80
12	30	-400	250	350	500						

Table 5.6. – mSUGRA points with selection efficiency and number of generated events sufficient for an endpoint measurement. Parameter values and integrated luminosity necessary for $Z_n > 5$. $sgn(\mu) > 0$ in all points.

Examining the spectra dominated by tau leptons from a $\tilde{\chi}_2^0$ 3-body decay shows that while in most cases the two fitting methods give incompatible results, even if the obtained endpoints are consistent they do not reflect the true value. This is to be expected since the kinematics and therefore the spectrum shape of a 3-body decay is different and therefore the calibration used in obtaining the endpoint is not appropriate.

Another aspect clearly visible in table 5.7 is that endpoint measurements below about 50 GeV are generally not successful, since the part of the corresponding invariant mass distributions

mSUGRA point	endpoint results (GeV)						endpoint (GeV)	process
	χ^2 fit			EML fit				
	hh	hl	mean	hh	hl	mean	truth	
1	109±18	136±20	121±19	89±13	125±43	92±18	94	2-1-1
2	45±7	-		74±26	-		69	2-1-1
3	41±4	-		25±4	-		50	2-1-1
4	90±12	59±17	80±14	89±13	96±99	90±18	83	2-1-1
5	22±15	-		20±7	-		38	3-body
6	72±11	-		-	-		69	3-body
7	34±13	-		21±5	-		42	3-body
8	32±10	-		23±5	-		50	3-body
9	61±30	119±24	96±27	107±20	122±40	110±25	92	2-1-1
10	46±27	-		21±5	-		62	3-body
11	43±9	-		65±15	-		69	3-body
12	121±21	-		135±25	138±48	136±31	127	2-1-1
13	22±4	-		13±6	57±32	14±8	37	3-body
14	31±11	28±38	31±15	15±4	19±10	16±5	50	3-body
15	70±29	-		115±34	131±31	124±32	115	2-1-1
16	34±6	-		48±12	-		50	3-body
	174±48	-		177±29	107±81	169±37	169	3-1-1
17	39±10	72±13	51±11	41±20	49±10	47±13	65	3-body
18	107±7	80±22	105±9	-	69±20		79	3-body
19	87±4	93±23	87±6	109±20	84±25	99±22	79	3-body
20	61±44	-		-	-		54	2-1-1
21	51±8	81±40	52±11	47±3	63±13	48±4	69	3-body
22	69±22	114±17	97±19	82±10	124±26	87±13	73	2-1-1
23	103±11	-		102±12	129±21	109±15	107	2-1-1

Table 5.7. – Fit results of χ^2 -fit and extended maximum likelihood (EML), compared to the theoretical endpoint. The last column gives the dominant source of tau leptons in the invariant mass spectrum.

important for a measurement then ranges into the region of inefficient tau lepton reconstruction and identification. In such cases, an endpoint measurement via the inflection point is not feasible without further adaptations.

5.5. Summary and conclusions

This chapter has investigated di-tau final states in terms of discovery potential and invariant mass measurement in pp-collisions with center-of-mass energies of 10 TeV and 14 TeV. It has been shown that including semi-leptonic decays improves both discovery prospects as well as accuracy of the endpoint measurement significantly, while fully leptonic decays do not contribute significantly in $\int L dt = 1 \text{ fb}^{-1}$ of $\sqrt{s} = 10 \text{ TeV}$ collision data.

Dominant systematic effects arise from tau identification efficiency uncertainties which potentially prohibit an early discovery, or bias the endpoint result if the difference of 1-prong to 3-prong tau leptons or of low p_T to high p_T tau leptons is not sufficiently well understood.

Assuming 1 fb^{-1} of $\sqrt{s} = 10 \text{ TeV}$ data and a systematic uncertainty on the SM background of 50 %, mSUGRA points with $m_{\tilde{\tau}_1} \leq 400 \text{ GeV}$ and $m_{\tilde{\chi}_2^0} \leq 200 \text{ GeV}$ or vice versa can be discovered using the di-tau search.

In addition to the χ^2 -fit employed in analyses preceding this one, valuable cross-checks have been shown to be gained by an unbinned likelihood maximization in SUSY points with challenging invariant mass spectra. The combination of these two fitting methods yields either the correct endpoint result or a contradiction indicating a wrong measurement.

6. Search for Supersymmetry with $\sqrt{s} = 7$ TeV collisions

6.1. Introduction

Tau lepton final states are not only important for model constraining measurements, but might also contribute significantly to SUSY searches if $\tan\beta$ is large. This chapter evaluates the discovery prospects of SUSY with the $\sqrt{s} = 7$ TeV collisions realized in the first LHC run period, which started in March 2010 and is planned to continue until late 2012. The ATLAS data available at the time this analysis was performed corresponds to an integrated luminosity of $(35 \pm 4) \text{ pb}^{-1}$.

The search for SUSY with tau lepton final states and missing transverse energy in ATLAS is independently conducted in three sub-channels: The *1-tau inclusive* search aims at any SUSY scenario leading to enhanced tau production, while the *di-tau* search described here is motivated by SUSY cascades such as those investigated in the previous chapter. The third SUSY search channel with tau leptons aims at di-tau events where one of the tau leptons decays leptonically, and hence selects events containing exactly one hadronic tau lepton and exactly one electron or muon. The possible contribution of this *semileptonic* channel in terms of discovery potential as well as endpoint measurement precision has been demonstrated in the previous chapter.

Since the 1-tau search requires any non-zero number of tau leptons, di-tau events could in principle be fully included in this search channel. However, in order to assure dominance of real tau leptons in the selected events, the tau identification has to be tight if only one tau lepton is required. A looser tau identification in the di-tau channel can recover events lost due to this stringent demands on the quality of selected tau leptons, and adds sensitivity to slightly different SUSY events.

A pre-study comparing SUSY events selected in the di-tau search with those events passing the 1-tau event selection using cuts developed for the $\sqrt{s} = 14$ TeV scenario¹ shows that about two third of the events selected by the di-tau channel do not overlap with the 1-tau selection. A separate search focussing on di-tau final states can thus be assumed to give a valuable, independent contribution to SUSY searches with tau lepton final states.

In the second part of this chapter, the ATLAS data and MC simulated datasets used in this analysis are described. The third part specifies details of the tau identification before the signal selection is developed in the fourth section. The QCD background is estimated using a data-driven technique in section 6.5, followed by an evaluation of systematic uncertainties in section 6.6. Finally, the results are interpreted in section 6.8.

6.2. Data and Monte Carlo simulated samples

6.2.1. ATLAS data 2010

The data used in this analysis has been taken between June 24th and October 29th 2010 in ATLAS data periods *D* to *I*, which correspond to an integrated luminosity of $\int L dt = (45 \pm 5) \text{ pb}^{-1}$. Data quality requirements defined by the SUSY working group for all SUSY analyses in common, summarized in a so-called good runs list (GRL), ensure that only data which was recorded with

¹Selection cuts of the 1-tau channel are taken from [40], the di-tau selection is performed as in chapter 5.3.2.

all ATLAS subdetectors operating at the expected performance is used. These data quality requirements reduce the data to an integrated luminosity of $\int L dt = 35 \text{ pb}^{-1}$ available for analysis, known with an uncertainty of 11% [115]. Data streams considered are the L1Calo stream for period D and the JetTauEtmisss stream for periods E-I. Data periods A-C are omitted because the trigger menu in these initial run periods did not contain the trigger used in the analysis. While a similar trigger could in principle be used, these periods would only contribute a total integrated luminosity of 16 nb^{-1} , and are therefore neglected.

The data has been reconstructed in **athena** release 15 and processed by the **SUSYD3PDMaker** version 00-07-11.

Data Stream	Data Period	Run numbers	$\int \mathcal{L} dt \text{ [pb}^{-1}\text{]}$	
			before GRL	after GRL
L1Calo	D	158045–159224	0.3	0.3
JetTauEtmisss	E	160387–161948	1.1	0.9
JetTauEtmisss	F	162347–162882	2.0	1.7
JetTauEtmisss	G	165591–166383	9.1	5.7
JetTauEtmisss	H	166466–166964	9.3	7.0
JetTauEtmisss	I	167575–167844	23	19

Table 6.1. – Data-taking periods with corresponding integrated luminosities before and after data quality requirements are applied.

6.2.2. Monte Carlo simulation

SUSY signal samples and Standard Model background expectation have been simulated by the same generators as in the 10 TeV study of the previous chapter², with the collision energy modified to $\sqrt{s}=7$ TeV. The underlying event and minimum bias description makes use of the ATLAS 2009 tune [116], and a full detector simulation based on **GEANT4** [79] is applied in the same release version as used for data reconstruction. A summary of all used MC samples can be found in appendix A.3.

6.3. Tau identification

Details on the tau reconstruction and identification software are given in chapter 4.3.3. Out of the three different discriminants provided by the tau identification software, the boosted decision tree (BDT) is found to give the best performance, as shown in table 6.2 where the efficiency and purity measured in SU11 di-tau events are given.

Efficiency $\epsilon_{2\tau}$ and purity $p_{2\tau}$ in this context are defined as

$$\begin{aligned} \epsilon_{2\tau} &= \left[\frac{N_{\tau}^{match}}{N_{\tau}^{true}} \right]_{\text{events with } \geq 2 \text{ true } \tau} \\ p_{2\tau} &= \left[\frac{N_{\tau}^{match}}{N_{\tau}^{sel}} \right]_{\text{events with } \geq 2 \text{ selected } \tau} , \end{aligned}$$

with N_{τ}^{true} being the number of true hadronically decayed tau leptons with visible transverse momentum larger than 10 GeV and within $|\eta| < 2.5$. N_{τ}^{sel} is the number of selected taus, i.e. tau candidates passing all identification criteria including overlap removal with other objects, and N_{τ}^{match} is the subset of selected taus that is matched ($\Delta R < 0.2$) to a true tau.

²QCD has been generated by **PYTHIA**, $t\bar{t}$ by **MC@NLO**, W and Z bosons production by **Alpgen** and SUSY signal samples by **HERWIG** and **JIMMY**.

ID	BDT			Llh			SC		
	$\epsilon_{2\tau}$	$p_{2\tau}$	$\epsilon_{2\tau} \cdot p_{2\tau}^2$	$\epsilon_{2\tau}$	$p_{2\tau}$	$\epsilon_{2\tau} \cdot p_{2\tau}^2$	$\epsilon_{2\tau}$	$p_{2\tau}$	$\epsilon_{2\tau} \cdot p_{2\tau}^2$
medium, 20 GeV	0.25	0.66	0.111 ± 0.005	0.23	0.66	0.099 ± 0.005	0.25	0.46	0.053 ± 0.002
tight, 10 GeV	0.20	0.73	0.106 ± 0.006	0.16	0.87	0.118 ± 0.006	0.18	0.64	0.074 ± 0.004
optimized	0.34	0.75	0.194 ± 0.006	0.26	0.79	0.161 ± 0.006	0.16	0.64	0.066 ± 0.004

Table 6.2. – Tau identification performance of log-likelihood (Llh), boosted decision tree (BDT) and simple cuts (SC) discriminants in SU11.

Apart from different cuts on the three available discriminants, different p_T -thresholds are tested, as well the tightness of the electron veto, to optimize the performance in the SU11 signal. As optimization figure of merit, $\epsilon_{2\tau} \cdot p_{2\tau}^2$ is chosen to balance a high signal selection efficiency with a high purity, slightly favouring the latter to ensure the presence of real tau leptons in the di-tau search channel. The performance of the tau identification strongly depends on the event topology (see chapter 4.3.3). As the analysis presented in the previous chapter has shown, the SM QCD background can be well controlled by event selection cuts, therefore an optimization of the tau identification performance assuming a SUSY event topology is sensible, and the SU11 benchmark point is used for this purpose.

The lowest possible p_T -threshold for tau leptons is 10 GeV. Since tau leptons from SUSY decays are generally very soft, a tighter p_T -cut results in a loss of signal tau leptons which dominates over the loss of background. The optimal selection using either BDT or Llh therefore uses tau leptons with $p_T > 10$ GeV.

In case of the likelihood discriminant, the best performance is obtained with a cut value of $Llh > 2.7$. The figure of merit shows a maximal value of 0.16, which is lower than the best performance achievable with the BDT, yielding a maximal $\epsilon_{2\tau} \cdot p_{2\tau}^2$ of 0.19.

The BDT cut has been optimized separately for 1-prong and 3-prong tau leptons because the initial probability of a 1-prong tau candidate to come from a real tau is higher than the probability of a 3-prong tau candidate, allowing for a looser BDT requirement for 1-prong taus compared to 3-prongs. The optimal cut values are found to be 0.55 (1-prong) and 0.76 (3-prong). Tau leptons with two tracks are treated as 3-prongs in this selection.

Table 6.2 shows that the simple cut selection (SC) is not competitive with the multivariate techniques. Cuts on the respective variables are therefore not optimized, the third row in table 6.2 gives performance of the tightest selection (SC tight, 20 GeV) instead, showing that the highest achievable purity is 65%. This behaviour is expected as the SC selection is constrained to so-called *safe variables*³.

The optimal tau identification is thus found to be the BDT selection with $BDT > 0.55$ (0.76) for 1-prong (3-prong) tau leptons. For the following analysis of the first 35 pb^{-1} of data, however, the selection is slightly modified for technical reasons: dedicated studies of systematic uncertainties performed by the combined performance group use certain benchmark tau selections, which do not include tau leptons with transverse momenta less than 15 GeV. Although these studies are done in a later software release⁴ than that used here and are therefore not directly applicable to this analysis, a comparison of their results with the ones obtained in the di-tau SUSY analysis can be useful. For reasons of consistency with these studies, the tau lepton identification applied here raises the p_T -threshold to 15 GeV and lowers the BDT cuts to 0.5 (0.7) for 1-prong (3-prong) tau leptons.

In summary, identified tau leptons are defined as passing the following selection:

- a charge of ± 1 ,
- 1-3 reconstructed tracks,

³For further details on safe variables, see chapter 4.3.3

⁴*athena* release 16

- $|\eta| \leq 2.5$,
- $E_T \geq 15$ GeV,
- muonVeto and electronVetoMedium,
- $\text{BDT} > 0.5$ (1-prong) or $\text{BDT} > 0.7$ (3-prong).

With these identification criteria, the efficiency and purity achieved in ditau events of the SU11 signal samples are $\epsilon_{2\tau} = (37 \pm 1)\%$ and $p_{2\tau} = (64 \pm 1)\%$.

Figure 6.1(a) shows the BDT output for reconstructed tau leptons that pass all identification criteria without the BDT cut, normalized to unity and separately for true (black line) and fake (red line) taus. True tau leptons predominantly get BDT values larger than 0.5, whereas jets emerging from quark and gluon hadronization obtain smaller BDT values. While this behaviour is common to 1-prong and 3-prong tau leptons, the ratio of true to fake tau leptons in the signal sample SU11 before applying the BDT cut is 0.25 for 1-prong and 0.19 for 3-prong tau leptons, motivating the different BDT cut values.

The number of true and fake tau leptons in SU11 di-tau events passing the final event selection (which is derived in the next section) is shown in figure 6.1(b). The numbers are given for all di-tau events as well as ordered by the relative sign of the two taus. Event numbers are normalized to $\int L dt = 35 \text{ pb}^{-1}$. Most τ -pairs consist of two real tau leptons, the second largest fraction of τ -pairs contains one true tau in combination with one jet mimicking a tau, and only a small fraction consists of two fake taus. When more statistics becomes available, this composition can be altered in favour of true tau leptons if the two taus are required to be of opposite sign.

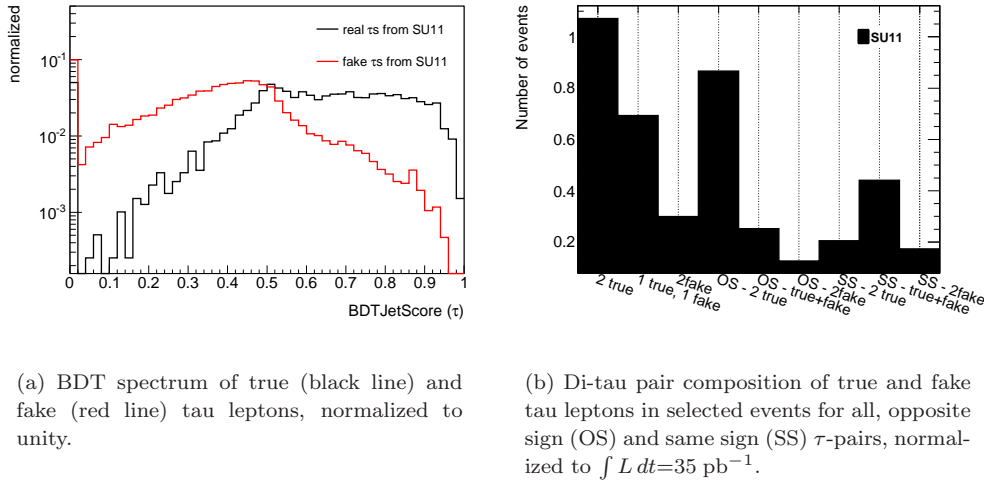


Figure 6.1. – BDT spectrum (a) and performance in selected events (b) for tau leptons in SU11.

So far, the performance of the tau selection has only been investigated for the SUSY benchmark point SU11; the performance for several MC data samples representing different event topologies is summarized in table 6.3. Di-tau efficiency and purity are given in events with at least two reconstructed and identified tau leptons, without any additional cuts but event cleaning to maintain large statistics. For the SUSY signal samples, the composition of identified tau leptons in di-tau events passing preselection cuts are also given, where the preselection consists of $N_\tau \geq 2$, a trigger and the according \cancel{E}_T and leading jet p_T requirements (see below).

Both efficiency and purity are largest in the GMSB6 benchmark point which features comparatively high energetic tau leptons, and has the largest value of $\tan \beta$ and hence large branching fractions for decays into tau leptons. SU4, by contrast, is not a tau enhanced point, featuring

sample	2 τ -events					τ composition after preselection			
	$\epsilon_{2\tau}$	$p_{2\tau}$	ϵ_{jet}	ϵ_e	ϵ_μ	τ	jet	e	μ
SU11	0.37	0.64	0.10	0.06	0.07	0.66	0.31	0.02	0.009
SU4	0.28	0.23	0.18	0.14	0.12	0.23	0.71	0.04	0.019
GMSB6	0.50	0.90	0.04	0.04	0.02	0.88	0.09	0.02	0.004

(a) Tau ID performance in SUSY environments.

sample	2 τ efficiency		sample	BG efficiency		
	$\epsilon_{2\tau}$	$p_{2\tau}$		ϵ_{jet}	ϵ_e	ϵ_μ
$Z \rightarrow \tau\tau + 1 \text{ jet}$	0.53	0.83	$Z \rightarrow \mu\mu + 3 \text{ jets}$	0.027	-	0.024
$Z \rightarrow \tau\tau + 3 \text{ jets}$	0.55	0.74	$Z \rightarrow ee + 3 \text{ jets}$	0.025	0.018	-
$Z \rightarrow \tau\tau + 5 \text{ jets}$	0.56	0.66	J4	0.016	-	-
$t\bar{t}$	0.38	0.37	$t\bar{t}$	0.024	0.014	0.013

(b) Tau ID performance in SM background samples.

Table 6.3. – Tau identification performance. Uncertainties are at the order of the last given digit or smaller.

many jets and hence a disadvantageous initial ratio of true tau leptons to possible sources of fake taus, leading to a very low purity.

The identification efficiency of background objects $\epsilon_{jet,e,\mu}$ are shown for representative background samples, where the probabilities of jets, muons or electrons to pass the tau identification criteria are evaluated without the $N_\tau \geq 2$ requirement due to lack of statistics otherwise. Background efficiencies are calculated as the number of background objects passing tau identification divided by the number of background objects reconstructed as a tau candidate.

The effect of additional jets in an event can best be seen by comparison of $Z \rightarrow \tau\tau$ events with 1, 3 or 5 additional jets. Every two extra jets lead to a purity loss of roughly 10 %.

6.4. Event selection

With this optimized tau identification, di-tau events from SUSY processes can be selected with kinematic cuts. However, necessary selection criteria partly independent of the SUSY event topology have to be applied before such cuts can be optimized. These include data quality criteria as well as choice of a suitable trigger.

6.4.1. Trigger

Since SUSY characteristics apart from tau leptons are \cancel{E}_T and energetic jets, a jet- \cancel{E}_T -trigger is employed in this analysis. EF_j75_jetNoEF_EFxe25_noMu is the lowest unrescaled combined jet- \cancel{E}_T -trigger. It is also used in other SUSY search channels which do not require light leptons and thus cannot use electron or muon triggers. The trigger chain corresponding to this trigger item is L1_J55 \rightarrow L2_j70_EFxe25_noMu \rightarrow EF_j75_jetNoEF_EFxe25_noMu⁵, so this trigger is not a classical combined jet- \cancel{E}_T -trigger but a pure jet-trigger on L1 and L2 combined with a pure \cancel{E}_T trigger at EF.

⁵A jet with transverse momentum of at least 55 GeV (70 GeV) is required on L1 (L2) and a missing transverse energy of at least 25 GeV on EF level.

In MC events and in some single data runs, this trigger is not present. In these datasets, the trigger is emulated by requiring L1_J55 to have fired, an L2 jet object with at least 70 GeV transverse momentum and a \cancel{E}_T computed at EF level of at least 25 GeV.

The performance of this trigger, as well as of related trigger items, is shown in figure 6.2. Event cleaning cuts are applied, and only events with at least one selected tau lepton are taken into account.

Figure 6.2(a) shows the trigger efficiency of the lowest unprescaled \cancel{E}_T trigger EF_xe40_noMu⁶ as a function of offline computed \cancel{E}_T separately for each trigger step. This trigger item represents the chain L1_XE25 \rightarrow L2_xe30_noMu \rightarrow EF_xe40_noMu. Efficiencies are taken with respect to the previous trigger level, so EF/L2 and L2/L1, and L1 is taken w.r.t. all events in the JetTauEtmis stream. The largest efficiency loss is obviously introduced by the L1 trigger, which reaches the plateau of the efficiency distribution (also known as *turn-on curve*) at about 150 GeV. This slow turn-on of the \cancel{E}_T trigger, which is mainly caused by the online \cancel{E}_T being uncalibrated, is the reason a jet- \cancel{E}_T -combination as in EF_j75_jetNoEF_EFxe25_noMu has been added to the trigger

⁶The suffix noMu implies that muons are not taken into account in the trigger- \cancel{E}_T definition.

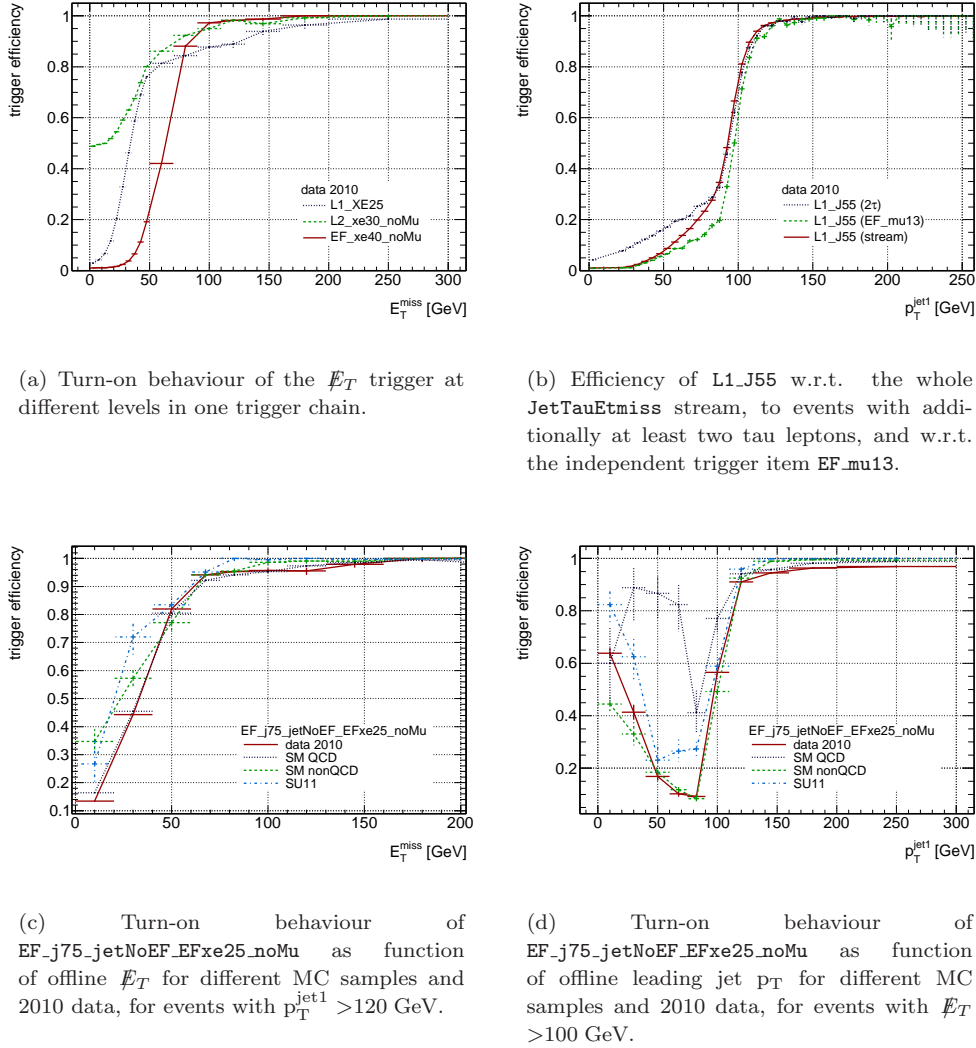


Figure 6.2. – Trigger turn-on curves for events passing event cleaning cuts and contain at least 1 tau lepton.

menu. A further advantage of triggering on \cancel{E}_T on EF level only is the high rate at L1 and L2, which necessitates higher thresholds for a certain instantaneous luminosity than with the jet-seeded approach. Furthermore, a slightly different trigger response has been found for events with real \cancel{E}_T compared to events with fake \cancel{E}_T , which is also mostly caused by the L1 and L2 part of the \cancel{E}_T trigger [117].

In figure 6.2(b), the efficiency of L1_J55 is displayed as a function of leading jet transverse momentum with respect to the JetTauEtmiss stream in comparison to an additional preselection requiring either the independent muon trigger EF_mu13 to have fired or the presence of at least two selected tau leptons. No significant deviation is seen above a leading jet p_T of 100 GeV, and the plateau of the trigger turn-on is reached at a threshold of about $p_T^{\text{jet1}} > 120$ GeV. The corresponding efficiency has been measured in the zero lepton SUSY search to be 98 % [117].

Figure 6.2 (c) and (d) show the trigger efficiency of EF_j75_jetNoEF_EFxe25_noMu as a function of \cancel{E}_T (6.2(c)) and leading jet p_T (6.2(d)) for data compared to MC simulated events. Since \cancel{E}_T and leading jet p_T are correlated, trigger turn-on effects have to be disentangled by appropriate preselection cuts, therefore $p_T^{\text{jet1}} > 120$ GeV or $\cancel{E}_T > 100$ GeV are required in figures 6.2(c) or 6.2(d), respectively. Due to a lack of statistics after this \cancel{E}_T -cut, the $N_\tau \geq 1$ requirement is dropped in figure 6.2(d).

The difference between data and MC is seen to be small, and the efficiency is stable for $\cancel{E}_T > 100$ GeV and $p_T^{\text{jet1}} > 120$ GeV. These cuts are therefore always applied along with the trigger requirement.

6.4.2. Event cleaning

Real collision data has to pass the GRL described in section 6.2.1. In addition, fake \cancel{E}_T caused by badly measured jets is eliminated by rejecting events that contain so-called *bad jets*. These are reconstructed jets which are believed to arise either solely from detector effects, or from any physical object not originating from the collision. Jets are classified as bad if they have a transverse momentum of at least 20 GeV and satisfy any of the following criteria:

- $f_{EM} < 0.1$, to protect against cosmics and beam background that show a very small electromagnetic energy fraction f_{EM} ,
- $f_{max} > 0.95$ and $|\eta| < 2$, applied against cosmics and beam background with the maximum energy fraction in one calorimeter layer f_{max} indicating a dominant energy contribution from a single calorimeter layer,
- $|t| > 25$ ns also indicates a non-collision source by the large jet time t (computed as the energy squared cells mean time),
- $f_{HEC} > 1 - |Q|$, where f_{HEC} is the energy fraction measured in the hadronic endcap calorimeter and the jet quality Q is the fraction of cells in the LAr which have a cell Q-factor of more than 4000, which in turn is a measure for the difference of the predicted and the measured pulse shape used to reconstruct the cell energy. $|Q|$ is normalized such that a value of 0 (1) corresponds to a high (low) quality jet. This cut protects against spikes in the HEC.
- $f_{HEC} > 0.8$ and $n_{90} \leq 5$ aims again at combating HEC spikes, with n_{90} being the minimum number of cells which contain at least 90 % of the total energy of the jet.
- $f_{HEC} < 0.3$ and $|Q| > 0.3$, also applied against HEC spikes.
- $f_{EM} > 0.9$ and $|Q| > 0.6$, similarly protecting against coherent noise in the EM calorimeter.

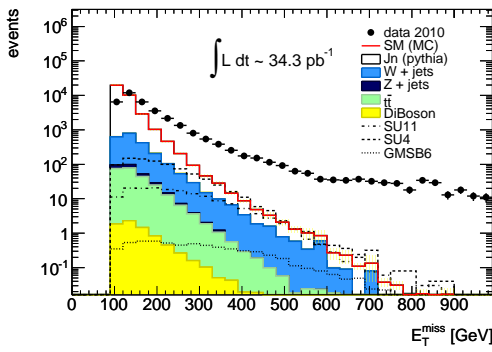
These jet cleaning cuts are only applied to real collision events. The efficiency of these cuts in data, found to be $(97.32 \pm 0.07) \%$ for the dataset used in this analysis, is applied as an additional scaling factor to MC events.

ATLAS data as well as simulated MC events are further rejected if an electron is reconstructed in the crack region $1.37 < |\eta| < 1.52$, as this region is known to be problematic for electron reconstruction and identification.

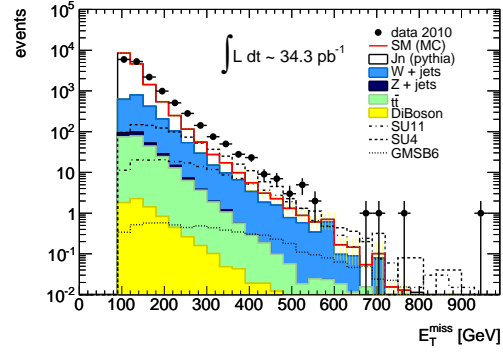
In order to further protect against non-collision background, a reconstructed primary vertex with at least 5 associated tracks is required, otherwise the event is rejected.

Figure 6.3 shows the data-MC agreement in the \cancel{E}_T spectrum with and without these cleaning cuts. Figures (a) and (b) compare the \cancel{E}_T spectrum of events passing the trigger and respective selection cuts, figures (c) and (d) show events containing additionally at least one selected tau lepton.

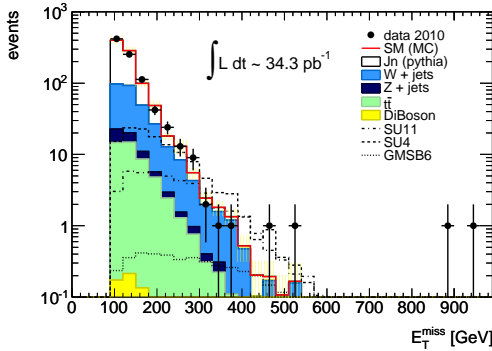
Without the tau lepton requirement, a long tail of unphysical large- \cancel{E}_T events is rejected by the event cleaning. Remaining differences of data compared to MC are caused by the QCD normalization being taken as the LO MC prediction at this stage of the analysis. With the requirement of at least one tau lepton, most of the statistics in the \cancel{E}_T tail is lost, but there are still single high \cancel{E}_T events rejected by the event cleaning procedure.



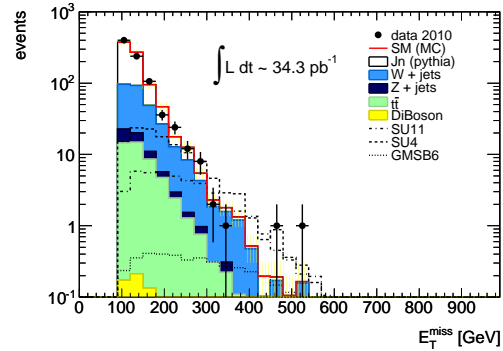
(a) \cancel{E}_T without event cleaning.



(b) \cancel{E}_T with event cleaning.



(c) \cancel{E}_T without event cleaning, events with at least 1 tau lepton.



(d) \cancel{E}_T with event cleaning, events with at least 1 tau lepton.

Figure 6.3. – \cancel{E}_T distribution with and without event cleaning cuts.

6.4.3. SUSY event selection

Starting point for the event selection are events containing at least two tau leptons identified as explained above, which pass the event cleaning criteria as well as the jet- \cancel{E}_T -trigger with

according requirements on \cancel{E}_T and leading jet p_T to be in the plateau of the trigger turn-on curve. In the following, this first step is called preselection:

- event cleaning, trigger, $\cancel{E}_T > 100$ GeV and leading jet $p_T > 120$ GeV,
- 2 selected tau leptons

Event selection cuts have then been optimized with respect to SU11, maximizing the significance $\frac{S}{\sqrt{B}}$ (S = signal, B = background events) while trying to minimize the loss in signal events:

- $H_T > 450$ GeV, where H_T is defined as the scalar sum of transverse momenta of all jets with $p_T > 40$ GeV and all selected tau leptons, and
- $\cancel{E}_T > 200$ GeV.

Other variables have also been investigated, yet these two have shown the best separation power with least signal loss at the respective selection step. In comparison, a cut on \cancel{E}_T / M_{eff} leading to a similar signal efficiency results in a significance of 24 % less than obtained with the H_T selection cut. By using M_{eff} instead of H_T as discriminating variable, a comparable (but not better) performance can be achieved in combination with the \cancel{E}_T -cut. As M_{eff} and \cancel{E}_T are highly correlated, H_T is considered better suited for the selection.

The H_T and \cancel{E}_T spectra at the selection stage right before cutting on the variable are shown in figure 6.4, as well as the significance $\frac{S}{\sqrt{B}}$ for the three SUSY signal samples as a function of possible cut values. The spectra show the SM background stacked, with the red line representing its sum and the yellow band the uncertainty of the MC prediction. This error band includes the statistical uncertainty taking the generated MC statistics into account, quadratically added to a systematic cross-section uncertainty on the W and Z backgrounds of 5 % and on the $t\bar{t}$ background of 6 %.

The optimal H_T -cut in terms of significance is slightly different for SU4 and SU11, while an optimization for GMSB6 requires dramatically higher H_T due to the many hard tau leptons in this SUSY point. Since the target signal region for this early data analysis is represented by SU11, a minimal H_T of 450 GeV is chosen as selection requirement. After this cut is applied, the significance evolution with increasing \cancel{E}_T -requirement shows two maxima. Out of these, the first is selected because in the global significance maximum only (0.99 ± 0.01) expected signal events remain with an integrated luminosity of 35 pb^{-1} due to the steep signal efficiency decrease with rising \cancel{E}_T -cut, compared to (3.2 ± 0.2) expected SU11 events in the local maximum. The second reason for not choosing the second peak of the significance distribution is the lack of MC statistics in this part of the phase space, which is clearly visible by the sudden jump in the S/\sqrt{B} distribution and the following bumpy behaviour, as well as in the respective part in the \cancel{E}_T spectrum. The optimal \cancel{E}_T -cut is thus found to be 200 GeV.

In order to be able to combine the di-tau selection with the one-tau and the semileptonic channel, overlap has to be eliminated. Due to the different tau identification criteria, a separation according to the number of tau leptons per event is not possible, therefore separate vetos are applied:

- Veto events which pass the 1-tau selection.
- Veto events which pass the semileptonic selection.

Tau identification and event selection cuts employed in the 1-tau and in the semileptonic di-tau channel are given in appendix D.

These vetos reduce the significance, and are only applied to enable a combination of the three channels. The first veto rejects around one third of the SU11 signal while keeping most of the SM background, the impact of the second veto is negligible.

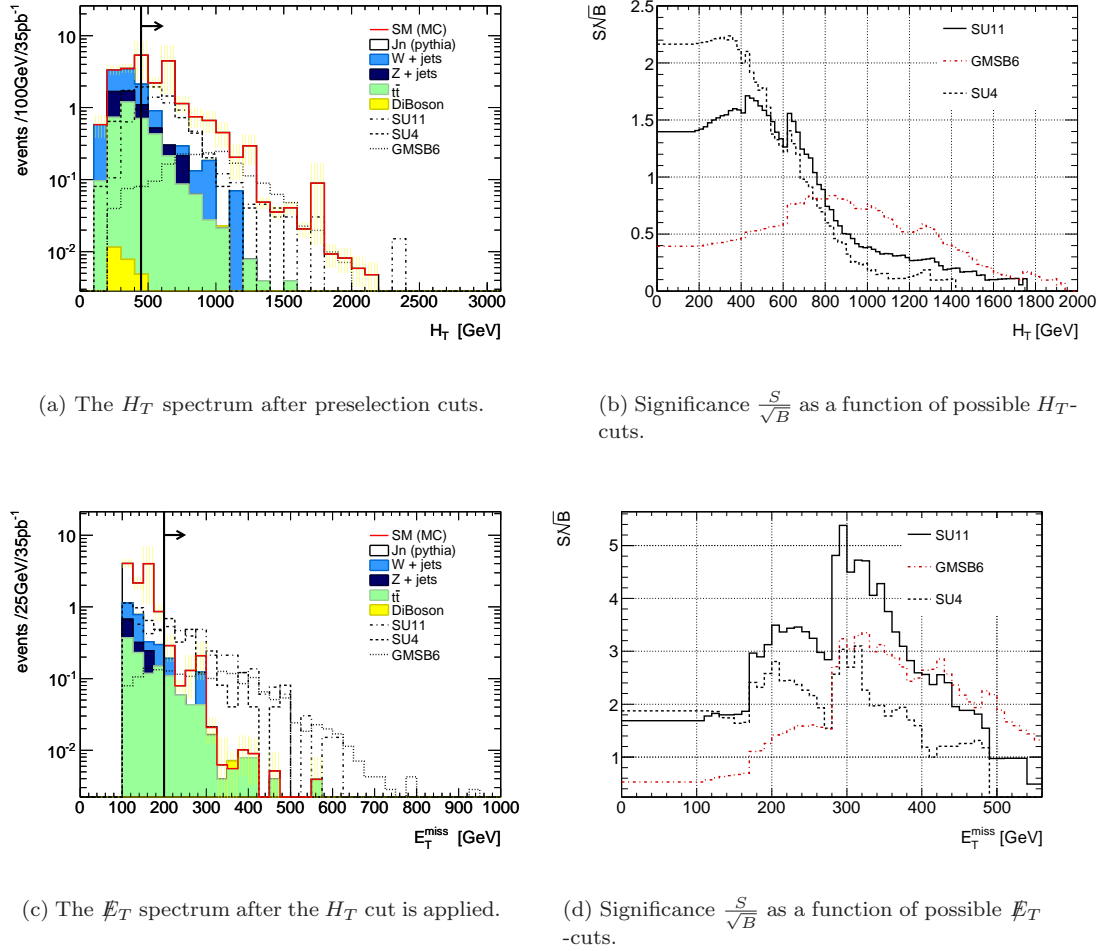


Figure 6.4. – Event selection cuts.

The number of events expected at each selection step with 35 pb⁻¹ of integrated luminosity are listed in table 6.4. Only semileptonic and leptonic $t\bar{t}$ events and only dijet events containing jets with $p_{T>70}$ GeV (J3-J7) are taken into account, since lower energetic jets and fully hadronic $t\bar{t}$ decays only contribute in the beginning of the cut-flow⁷.

Impact on tau composition The event selection cuts hardly bias the composition of tau leptons in selected events, as can be seen in figure 6.5 which shows the origin of tau leptons in events passing different selection steps. The fraction of tau leptons emerging from different mother particles is shown in figures 6.5(a-c) for tau leptons in events with at least two selected taus (a), in events passing the preselection (b) and passing all di-tau selection cuts (c) without the 1-tau and semileptonic vetos to retain statistics. In this context, leptonically decaying taus are also regarded as true tau leptons. The last column called *other fakes* denotes reconstructed tau leptons that could not be matched to any truth object. To reveal which type of tau leptons contribute to the different samples, events are normalized to unity separately for each dataset. With more stringent event selection cuts, the relative contribution from light jets mimicking hadronic tau leptons gets slightly more dominant, which is mainly due to Z and diboson events with real tau leptons getting cut away more efficiently than events of these samples containing fake taus. Figure 6.5(d) shows the number of tau leptons for events expected to be selected with

⁷A table containing these events, as well as statistical errors on all selection steps, can be found in appendix B (table B.3).

the low mass SUSY point is dominantly selected by light jets faking hadronic tau leptons. Since in SU11 and SU4 the decay $\tilde{\chi}_2^0 \rightarrow \tilde{\tau}_1 \tau \rightarrow \tilde{\chi}_1^0 \tau \tau$ is kinematically forbidden, the main real tau lepton sources in these samples are seen to be neutralinos and charginos, while in GMSB6 where the similar decay $\tilde{\chi}_{1,2}^0 \rightarrow \tilde{\tau}_{1,2} \tau \rightarrow \tilde{G} \tau \tau$ is open, the main origin of real tau leptons is a $\tilde{\tau}$, followed by neutralino sources.

6.5. MC validation with data

The MC predictions for the SM background contain various uncertainties and have to be validated against data. Particularly the QCD background, the simulation of which cannot be done with sufficient statistics and uses leading order (LO) calculations, thus involving a large uncertainty on the production cross-section, has to be estimated from data. With the amount of ATLAS data available, the QCD contribution to the selected events can be corrected according to data in dedicated sidebands, while a measurement of the W , $t\bar{t}$ and Z background requires larger statistics. The descriptions of these backgrounds by the MC simulation is therefore only validated in one non-QCD dominated phase-space region at this stage of the analysis.

Before the event selection developed above can be applied to data, the accuracy of the MC description has to be verified. To this end, the shape of variables used in tau identification are first compared between MC and data. Only event cleaning cuts, the trigger including corresponding \cancel{E}_T and leading jet p_T cuts as well as the requirement of at least two identified tau leptons are applied. The QCD contribution to the SM background is still dominant at this selection stage, and the shapes of the variables are compared by scaling the QCD MC to data.

Figures 6.6 and 6.7 show variables used for tau lepton identification (see chapter 4.3.3 for details) for all tau candidates in events passing the preselection cuts. While the yellow error band in the pure MC distributions shown above include only the statistical uncertainty and cross-section uncertainties on W , Z and $t\bar{t}$, in comparison with data an additional systematic contribution arises from the luminosity uncertainty, measured by ATLAS to be 11 % [115]. Since the QCD contribution is scaled to data, this uncertainty is only applied to $t\bar{t}$, W , Z and diboson background. A QCD scaling uncertainty is derived along with the scaling factor from statistical error propagation.

All variables important for tau lepton identification seem to be well modelled in MC compared to data within the statistical fluctuations. Note that the ratio of data to MC simulated events is only drawn in bins with more than 0 data events, therefore single data events in the tail of a distribution, where the MC expectation per bin is less than 1 event, lead to a seemingly systematic data excess with a ratio larger than one for all points in the tail. This is an artefact of the bins with 0 data events not being drawn as an undershoot.

6.5.1. QCD background estimation

QCD multijet processes constitute the SM BG most difficult to predict by MC simulation due to the high cross-sections rendering a sufficient amount of simulated data impossible, the large uncertainties of this cross-sections as well as the missing transverse energy in these events arising mainly from badly measured jets. A control region dominated by QCD events with large instrumental \cancel{E}_T can be defined by requiring the \cancel{E}_T -vector to point in the direction of one of the leading jets. In order to be distinct from the signal region, the \cancel{E}_T -cut is inverted: $100 \text{ GeV} < \cancel{E}_T < 200 \text{ GeV}$. The smaller threshold is kept to avoid trigger turn-on effects. The two vetos on events selected by either the 1-tau or the semileptonic di-tau search are also applied, as well as the H_T -cut, in order to be similar to the signal region. The angular distance between the two leading jets and the \cancel{E}_T in events satisfying these criteria are shown in figure 6.8 for the stacked SM BG overlaid with the three different SUSY points and with ATLAS data. The QCD MC is scaled to the number of data events with the non-QCD BG subtracted. The shape of these two $\Delta\Phi$ -distributions is seen to be well described in MC, and as expected the $\Delta\Phi < 0.5$ regions

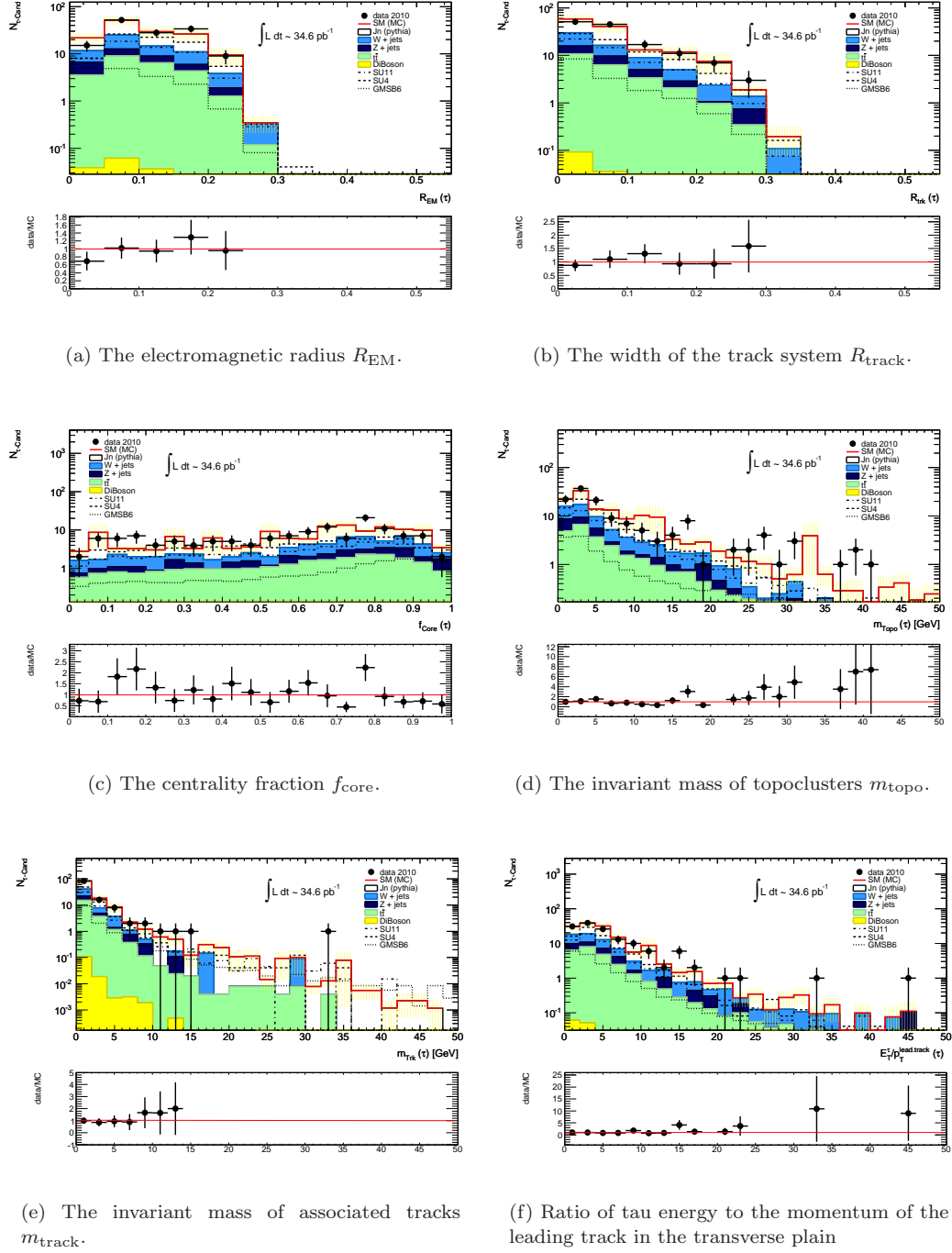
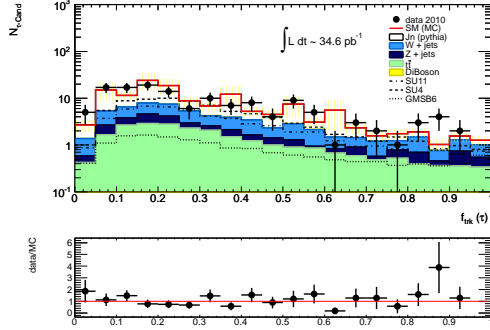
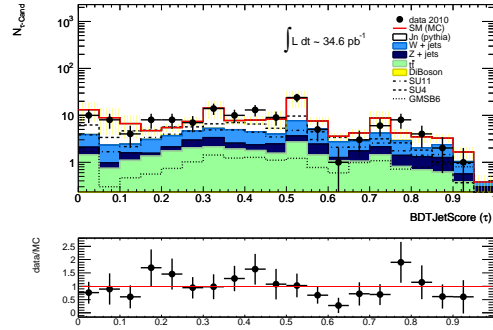


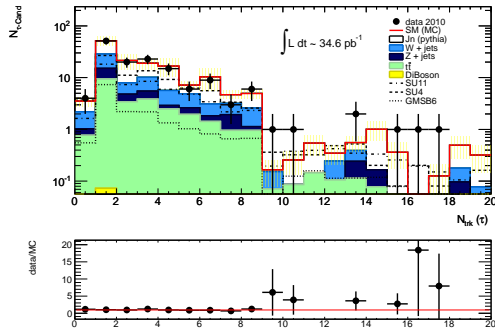
Figure 6.6. – Variables used for tau lepton identification within the BDT discriminant, for all tau candidates in events passing preselection criteria.



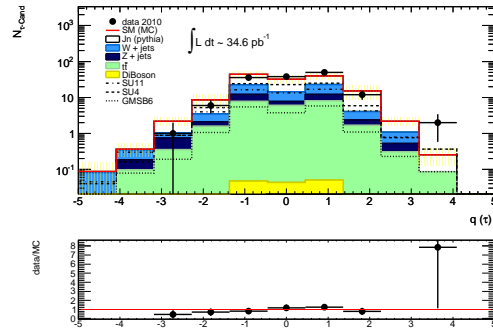
(a) The transverse momentum fraction of the leading track f_{track1} .



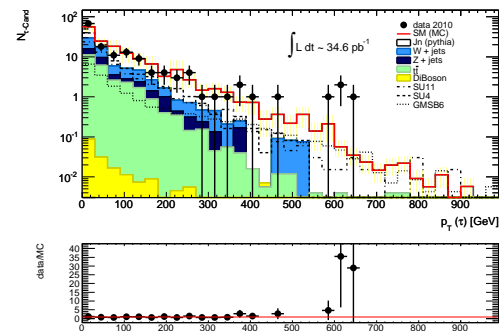
(b) BDT discriminant.



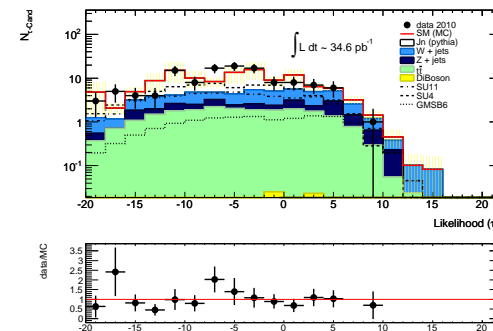
(c) Number of tracks.



(d) Charge.



(e) Transverse momentum spectrum.



(f) Likelihood discriminant.

Figure 6.7. – Variables used for tau lepton identification, for all tau candidates in events passing preselection criteria.

are dominated by QCD. Therefore in the following, *QCD-sideband* refers to events passing at least one of the conditions $\Delta\Phi(E_T^{miss}, \text{jet1}) < 0.5$ or $\Delta\Phi(E_T^{miss}, \text{jet2}) < 0.5$, as well as the cuts mentioned above.

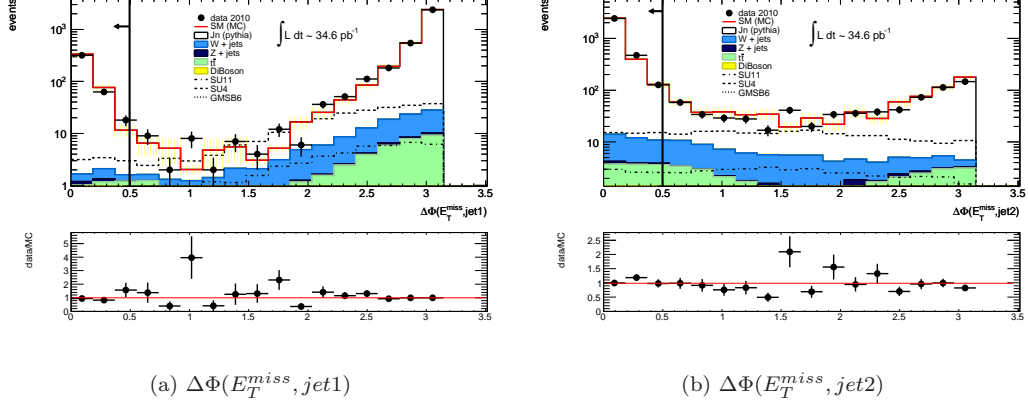


Figure 6.8. – Definition of QCD dominated regions.

In order to measure the difference between the tau fake rate in MC and data, this QCD-region is further split into sidebands with 0, 1 and 2 tau leptons. A QCD cross-section correction factor w_0 can then be obtained in the 0-tau sideband for the overall QCD scale:

$$w_0 = \frac{N_{0\tau}^{data} - N_{0\tau}^{nonQCD}}{N_{0\tau}^{QCD}} , \quad (6.1)$$

where $N_{0\tau}^{data}$ denotes the number of data events in the 0-tau-sideband and $N_{0\tau}^{nonQCD}$ ($N_{0\tau}^{QCD}$) the respective number of MC events for non-QCD (QCD) background. Similarly, a fake rate correction factor f can be obtained from the 1-tau sideband by

$$f = \frac{w_1}{w_0} = \frac{N_{1\tau}^{data} - N_{1\tau}^{nonQCD}}{w_0 \cdot N_{1\tau}^{QCD}} . \quad (6.2)$$

This factor corresponds to the difference of the fake rate in MC compared to data. It follows the QCD scale in the 2-tau region:

$$w_2 = w_0 \cdot f^2 . \quad (6.3)$$

While w_0 is phase-space dependent and hence cannot directly be used in the signal region, the fake rate correction factor f only depends on the tau lepton identification, and will be used to estimate the number of QCD events in the signal region. However, the fake rate correction factor obtained with this method is averaged over the number of jets that can create a possible fake tau, as well as over the transverse momentum of the tau candidates. Since the tau identification performance depends on both these variables, this constitutes a simplification that might corrupt the applicability of f to tau leptons in the signal region events. When more data is available, these effects have to be taken into account by a measurement of f as a function of the p_T and of the number of tau candidates $N_{\tau-Cand}$.

As a rough estimate of the mean fake rate, the ratio of identified tau leptons to the mean number of tau candidates per event can be taken, assuming that the contribution from real tau leptons is negligible in the QCD sideband. If only the 1τ region is taken into account, the fake rate measured from data is 16 %, compared to an 18 % fake rate in QCD MC. The ratio of these reproduces the factor f obtained by the method above. The 1τ region is, however, not suitable to estimate the overall fake rate since it is biased towards events with fake taus. Therefore the 0τ ,

	w_0	f	w_2^{est}	w_2^*
QCD-region	1.32 ± 0.04	0.89 ± 0.13	1.06 ± 0.21	2.3 ± 1.1
loose tau region	1.28 ± 0.04	1.07 ± 0.09	1.47 ± 0.17	1.9 ± 0.4

(a) Validation of QCD estimation method.

	w_0	f	w_2^{est}
signal-like	1.70 ± 0.16	0.8 ± 0.3	1.1 ± 0.7
signal			1.4 ± 0.3

(b) Results.

Table 6.5. – Data-driven QCD estimation: method test (a) and result (b).

1 τ and 2 τ region are combined with weights according to the relative number of events in these regions, yielding overall fake rates of 1.2 % (1.5 %) in data (QCD MC) events. This is lower than the approximate 5 % of the medium BDT selection in figure 4.2(b) [99] from the fake rate study of the tau performance working group⁸, but the tendency of a slightly lower fake rate in data compared to MC simulation is consistent. The medium BDT selection used in the cited study uses a harder BDT cut for 1-prong and a looser BDT cut for 3-prong tau candidates compared to the study at hand. The selection cuts defining the QCD sideband as well as the cuts used in the cited study lead to a domination of 3-prong tau candidates, hence the overall effect of the different tau selections is a smaller fake rate in the di-tau study.

Validation of the procedure

The accuracy of relation 6.3 can be tested within the QCD-sideband by comparison of w_2 with the ratio of non-QCD subtracted data events to MC simulated QCD events in that region, i.e. with $w_2^* = \frac{N_{2\tau}^{\text{data}} - N_{2\tau}^{\text{nonQCD}}}{N_{2\tau}^{\text{QCD}}}$ in the QCD sideband. If the simplifications contained in f are negligible, $w_2 = w_2^*$ within the precision of the measurements. The first row of table 6.5(a) shows the scaling factors obtained in the QCD sidebands, where w_2^{est} is the QCD scale estimated with relation 6.3. It is seen to agree with w_2^* within 1.3σ . Due to small statistics in the 2 τ -sideband, the statistical uncertainty on w_2^* is quite large, therefore an additional QCD-dominated region is defined with looser tau identification criteria and without the 1-tau and semileptonic veto, but otherwise identical selection. The only change in the tau identification is the BDT requirement, which is loosened to $\text{BDT} > 0.3$ (0.5) for 1-prong (3-prong) candidates. The scaling factors obtained in this *loose tau* region are shown in the second row of table 6.5(a). The relative statistical uncertainty of w_2^* is significantly smaller than in the QCD-region using the nominal tau identification, and the estimated QCD scaling factor is still consistent with the direct scaling factor within 1.3σ . Figure 6.9 shows the M_{eff} distribution in these six control regions. The QCD background in the 2-tau regions is estimated by the scaling factor obtained from the respective 0- and 1-tau regions.

⁸A different study [118] performed by the tau performance working group using a similar working point, with a tight BDT cut for 3-prong taus, a medium BDT cut for 1-prong taus and a medium electron veto, but with a newer BDT version (**athena** release 16) finds a fake rate of about a factor 10 smaller than in reference [99] (depending on the number of vertices and on the η region).

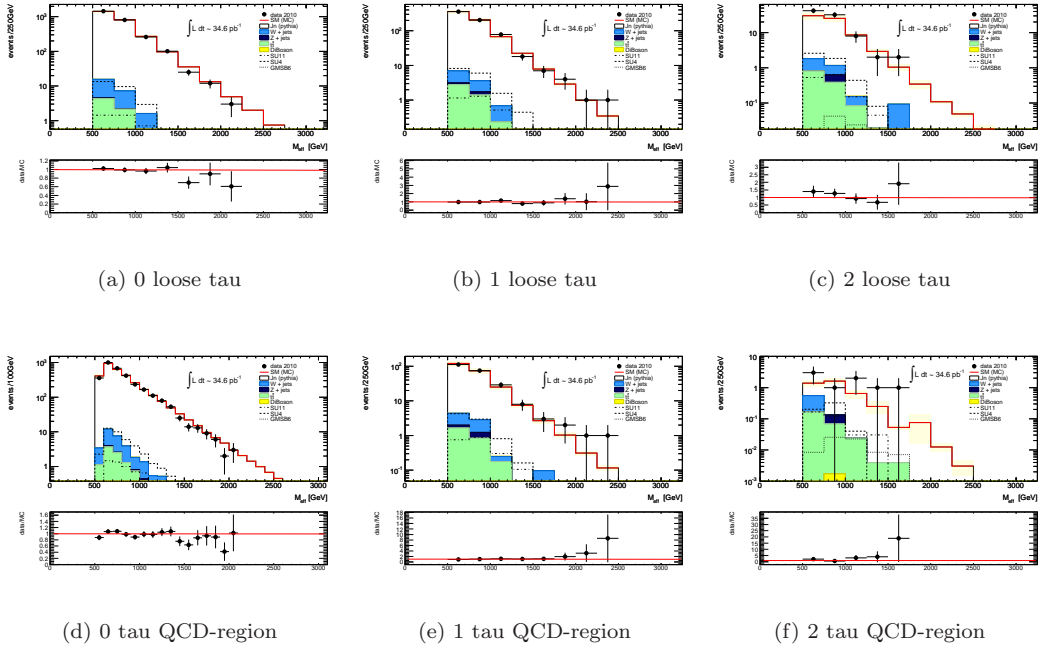


Figure 6.9. – QCD control regions: with loose tau identification (a-c) and with nominal tau identification (d-f). QCD in 2-tau sidebands scaled according to factors from 0- and 1-tau sidebands.

Result of QCD estimation

Events passing all selection cuts but the N_τ -requirement are referred to as *signal-like* regions if N_τ equals 0 or 1, and *signal-region* if N_τ equals 2 (or more). The number of expected QCD events in the signal region could in principle be estimated from the signal-like regions with 0 and 1 tau leptons; the respective scale factors are given in table 6.5(b). Due to the large uncertainty in $f = (0.8 \pm 0.3)$ arising from small statistics in the signal-like 1-tau region, $f = (0.89 \pm 0.13)$ is taken from the QCD-region which uses the same tau identification and thus yields the adequate fake rate correction factor, assuming the tau identification performance is sufficiently independent of the missing transverse energy in the events. Another advantage of taking f from the QCD sideband is that a possible bias arising from an inadequate MC description of the non-QCD background is negligible. The overall scaling factor w_0 in contrast has to be taken from the signal-like region directly since it is phase-space dependent. Note that unlike the six QCD dominated regions investigated above, a possible SUSY signal contamination in the signal-like regions could result in an overestimation of w_0 . However, the effect of the largest contribution from the example SUSY points is still seen to be smaller than the uncertainty of the SM expectation in the signal-like 0-tau region.

An overall good MC description of the M_{eff} spectra in the signal-like 0 and 1 tau regions is shown in figure 6.10.

The resulting QCD-scale in the signal region is extracted from the 1-tau sideband of the QCD-dominated region combined with the 0-tau sideband from the signal-like region. It yields an estimated amount of $N_{QCD}^{est} = (0.23 \pm 0.12)$ QCD events.

Figures 6.11, 6.12, 6.13 and 6.14 show the \cancel{E}_T , H_T , \cancel{E}_T / M_{eff} and $S_{\cancel{E}_T}$ (\cancel{E}_T significance) distributions in these 8 sidebands and in a non-QCD dominated sideband defined in the following section. The three SUSY signal points are separately overlayed with the SM background in all control regions. As before, the QCD contribution in (c) and (f) is scaled according to the factors obtained in the respective 0- and 1-tau regions. The data mostly agrees with the MC expectation within the given uncertainties. In the 0τ QCD and 0 loose tau regions, a small shape difference

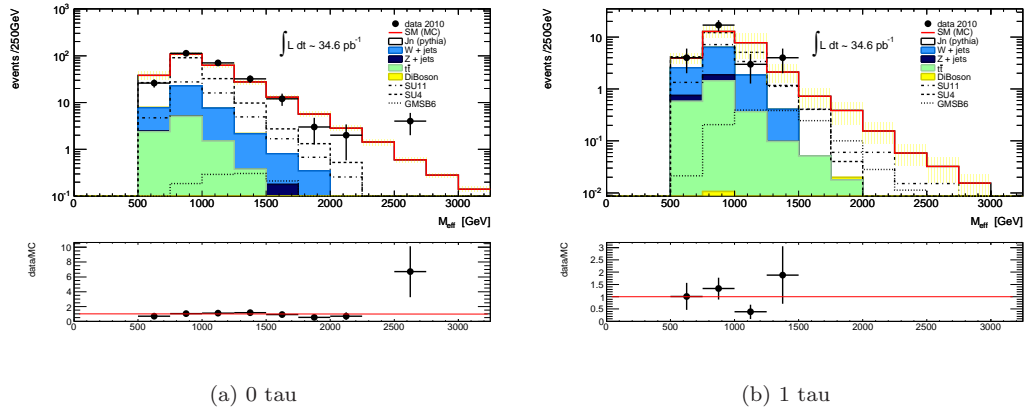


Figure 6.10. – M_{eff} in signal-like regions with 0 and 1 tau lepton, including all other event selection cuts.

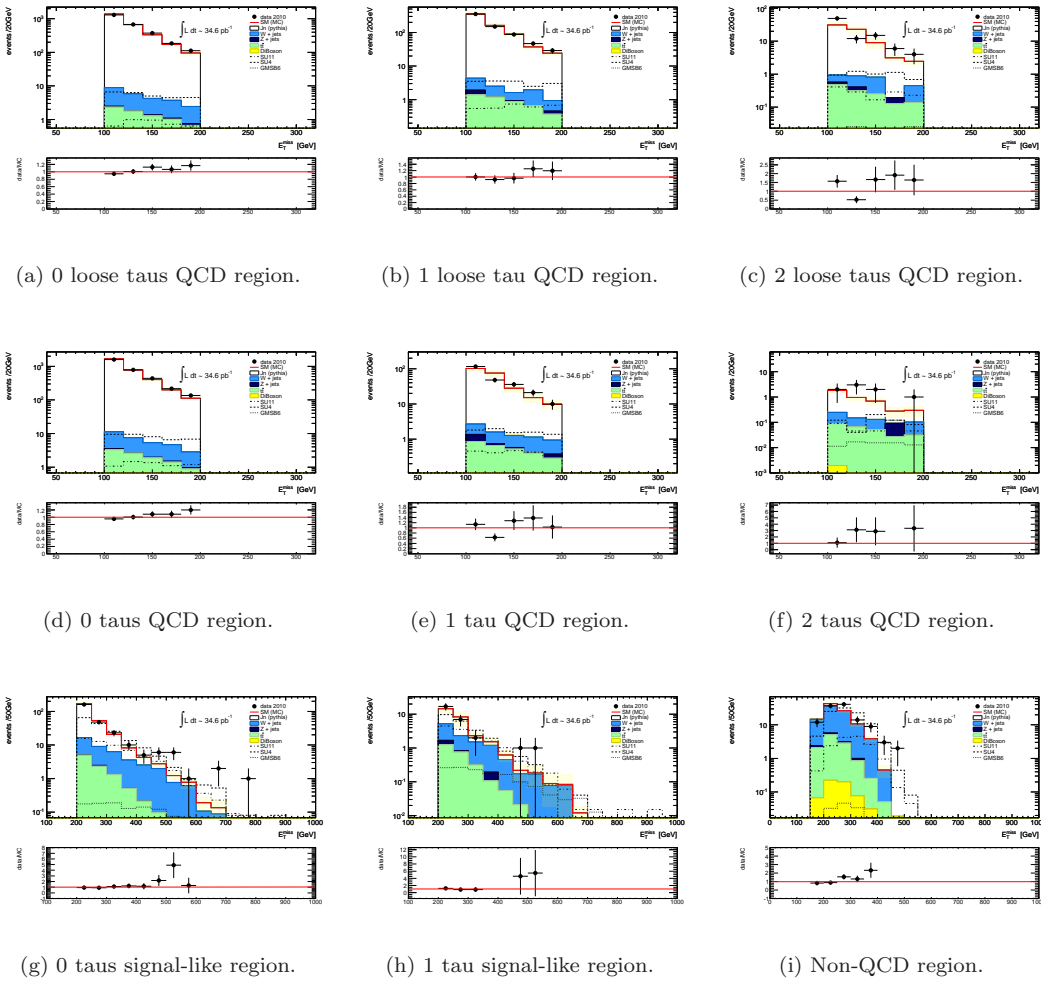


Figure 6.11. – E_T^{miss} spectra in control regions: loose tau region, QCD region and signal-like region in 1st, 2nd and 3rd row, with 0, 1 or 2 tau leptons (left, middle, right) and the non-QCD in (i).

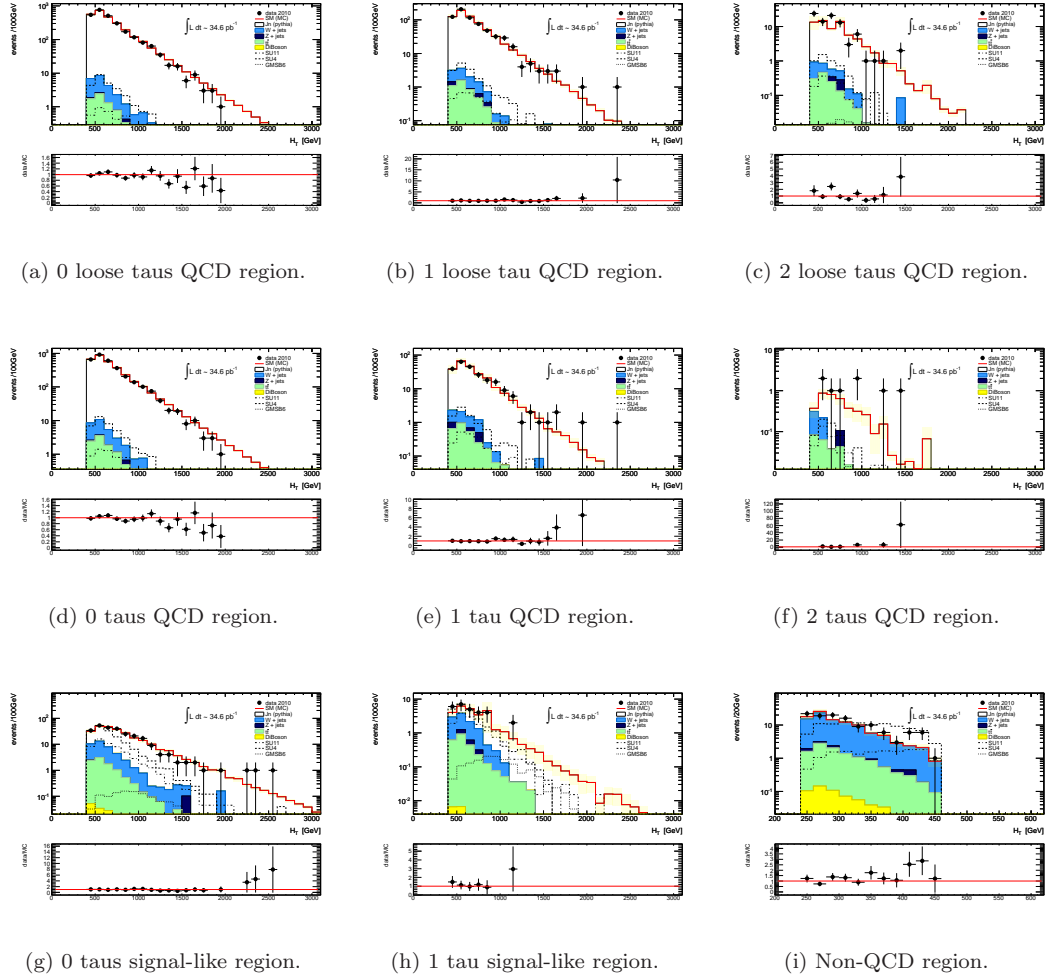


Figure 6.12. – H_T spectra in control regions: loose tau region, QCD region and signal-like region in 1st, 2nd and 3rd row, with 0, 1 or 2 tau leptons (left, middle, right) and the non-QCD in (i).

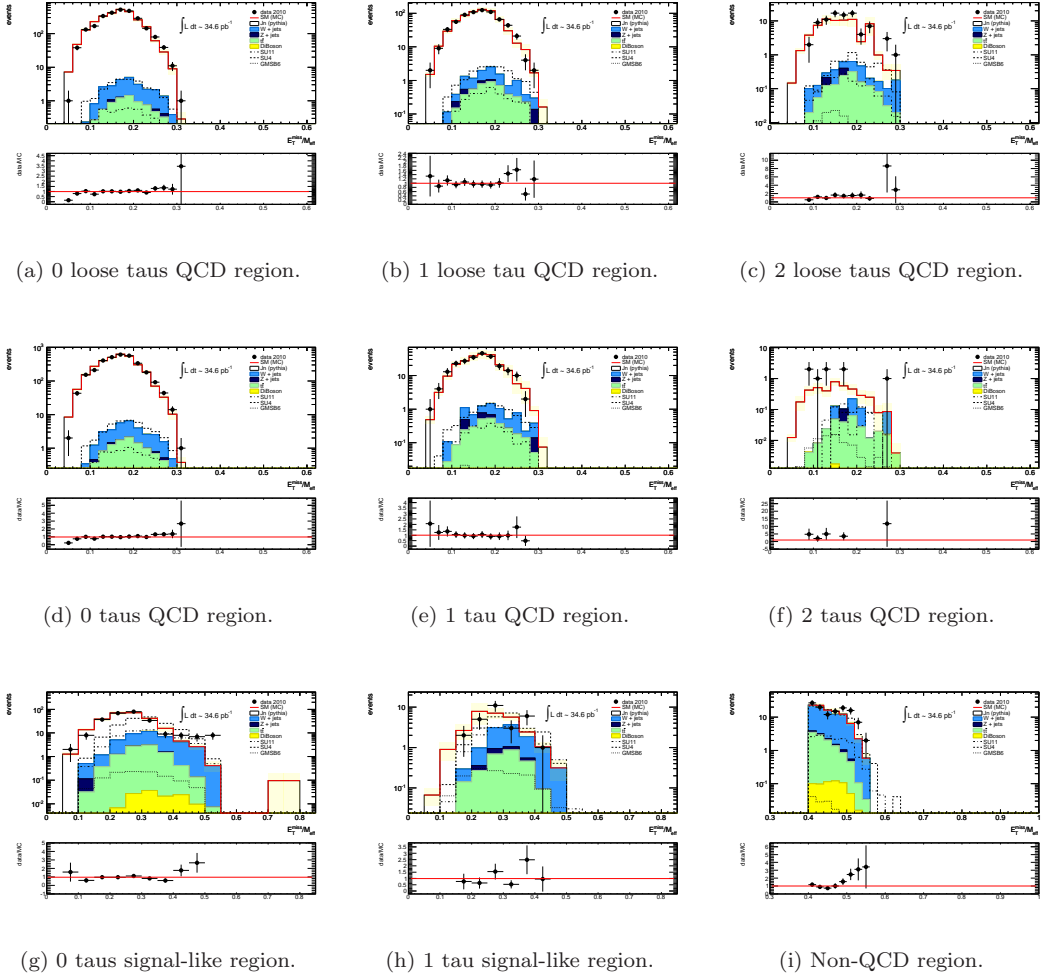


Figure 6.13. – E_T / M_{eff} spectra in control regions: loose tau region, QCD region and signal-like region in 1st, 2nd and 3rd row, with 0, 1 or 2 tau leptons (left, middle, right) and the non-QCD in (i).

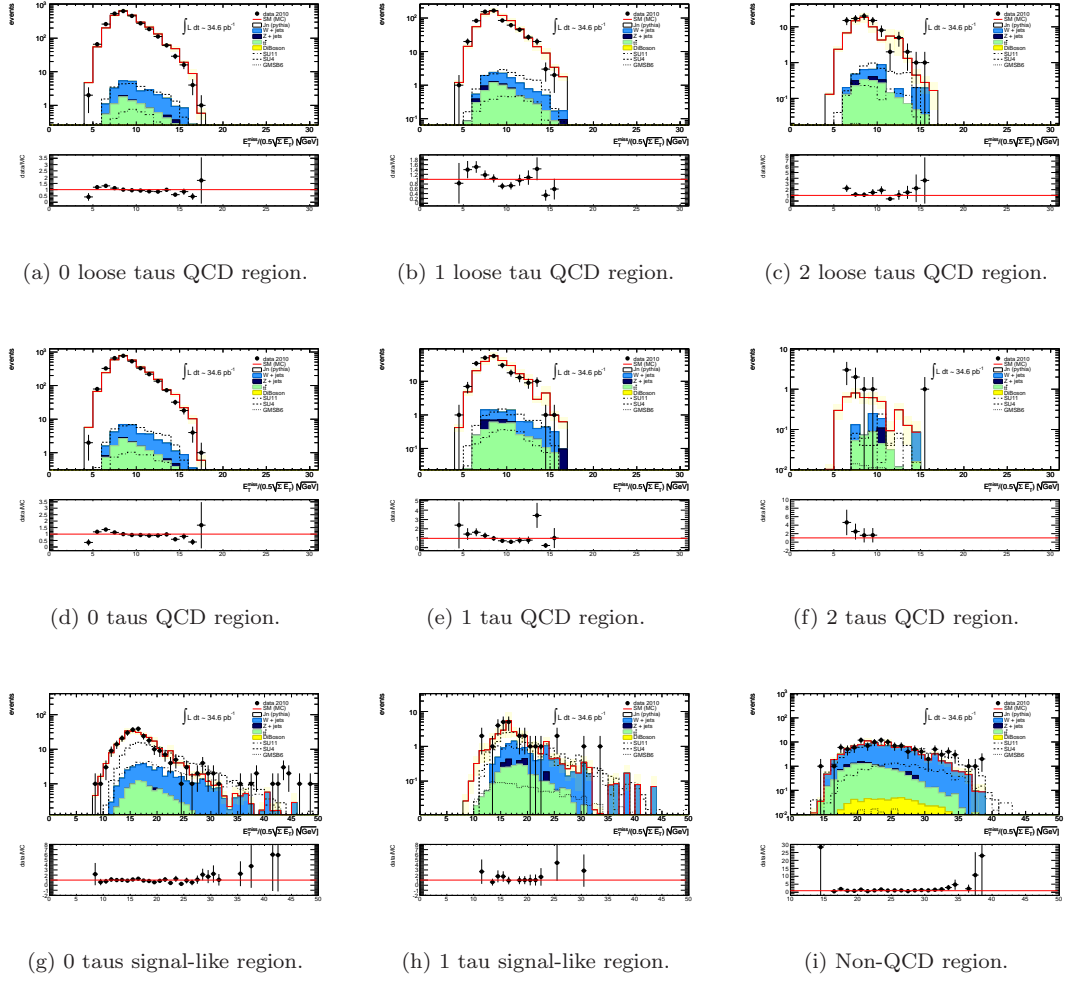


Figure 6.14. – \mathcal{E}_T significance in control regions: loose tau region, QCD region and signal-like region in 1st, 2nd and 3rd row, with 0, 1 or 2 tau leptons (left, middle, right) and the non-QCD in (i).

in the \mathcal{E}_T and, more prominently, in the \mathcal{E}_T / M_{eff} spectrum is observed: the distribution of data points is slightly shifted towards higher values. The \mathcal{E}_T significance shows no such shift. Since this effect is only visible in the 0τ sidebands and only in QCD dominated regions, a possible overestimation of QCD in the high- \mathcal{E}_T region could occur if the absolute QCD scale was propagated from the low- \mathcal{E}_T to the signal region. However, the signal-like 0τ region from which w_0 is determined is in the same \mathcal{E}_T regime as the signal region, and the fake rate estimated from the QCD sidebands is determined by a ratio of 0τ and 1τ region, thus \mathcal{E}_T dependent scale differences do not affect the QCD estimation in the signal region.

When more data is available, it is desirable to measure the QCD shape from QCD dominated sidebands like the 2τ QCD region. If the observed shape difference is significant also has to be determined with larger statistics.

6.5.2. Non-QCD BG validation

The most dominant SM background to the di-tau selection apart from *QCD* is $t\bar{t}$ followed by $W + jets$. While it is desirable to correct the MC expectation for these backgrounds separately in dedicated control regions, with the amount of data available at the time of writing it is only

possible to validate the overall non-QCD contribution by a data-MC comparison in a non-QCD dominated sideband, which in turn is effectively dominated by $W + jets$ due to its comparably large cross-section. Figure 6.15 shows the \cancel{E}_T contribution to the effective mass for events which do not satisfy the $\Delta\Phi$ requirements that define the QCD region, but pass the 1-tau and semileptonic veto as well as the preselection cuts without an N_τ -requirement. Instead of the inverted \cancel{E}_T -cut of the QCD dominated regions, non-QCD contributions are selected in an H_T sideband of (250-450) GeV. The region $\frac{E_T^{miss}}{M_{eff}} > 0.4$ is shown to be approximately free of QCD events, and is in the following taken as a non-QCD background validation region.

The contribution of different MC background samples in the various control regions is summarized in the table of figure 6.16. In the non-QCD region, the W background dominates at about 80 %, with a 10 % $t\bar{t}$ contribution and a QCD contamination expected to be approximately 6 %. The ratio of observed data events with subtracted QCD MC to the number of non-QCD MC predicted events in the non-QCD region is

$$\frac{N_{\text{data}} - N_{\text{QCD}}}{N_{\text{nonQCD}}} = 1.22 \pm 0.12^{\text{stat}} . \quad (6.4)$$

Considering an additional 11 % luminosity uncertainty, the non-QCD MC shows reasonable agreement with the observed data.

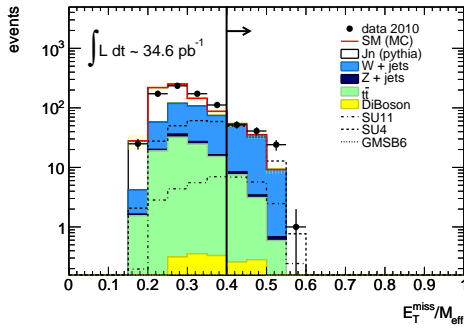


Figure 6.15. – Definition of non-QCD region.

region		QCD	W	Z	$t\bar{t}$
QCD	0 τ	98.8 %	0.8 %	0.02 %	0.3 %
	loose tau	97.7 %	1.3 %	0.15 %	0.9 %
	2 τ	93.1 %	3.5 %	0.6 %	2.7 %
QCD	0 τ	98.7 %	0.9 %	0.02 %	0.4 %
	1 τ	96.1 %	2.1 %	0.4 %	1.4 %
	2 τ	80.1 %	9.8 %	3.2 %	6.8 %
signal-like	0 τ	76.7 %	18.6 %	0.16 %	5.5 %
	1 τ	52.2 %	34.4 %	2.5 %	10.8 %
non-QCD		5.9 %	81.4 %	1.4 %	10.8 %

Figure 6.16. – Standard Model background composition in the different control regions.

Figure 6.17 shows spectra of variables important for the di-tau analysis (and not already included in figures 6.11, 6.12, 6.13 and 6.14), comparing data to the MC expectation within this non-QCD region. The QCD contribution is scaled according to the 0 τ QCD sideband factor since no requirement on the number of tau leptons is applied and thus the 0 τ events can be expected to dominate. The overall scale of the non-QCD MC is well reproducing the data within the given uncertainty, and also the shape of most distributions is seen to be modelled correctly in MC, including angular correlations. As before in the 0 τ QCD regions, the \cancel{E}_T spectrum seems to be slightly shifted towards higher values in data compared to the MC expectation (see figure 6.11(i)). This shift could result from an overestimated W cross-section accompanied by a sizable signal contamination. It is, however, not significant and has to be investigated when more data is available. The measured number of jets and tau leptons as well as their p_T spectra are in good agreement with the MC expectation, as well as the H_T spectrum following therefrom.

Unlike the QCD dominated regions defined in the previous chapter, presence of a SUSY signal could potentially influence the conclusions drawn from this control region. An SU4-like mSUGRA point would significantly alter the M_{eff} spectrum as well as the number of selected jets and observed tau candidates, while an SU11-like point would lead to an overestimation of non-QCD background. A SUSY scenario similar to GMSB6 is still not distinguishable from the SM expectation due to its comparably small cross-section.

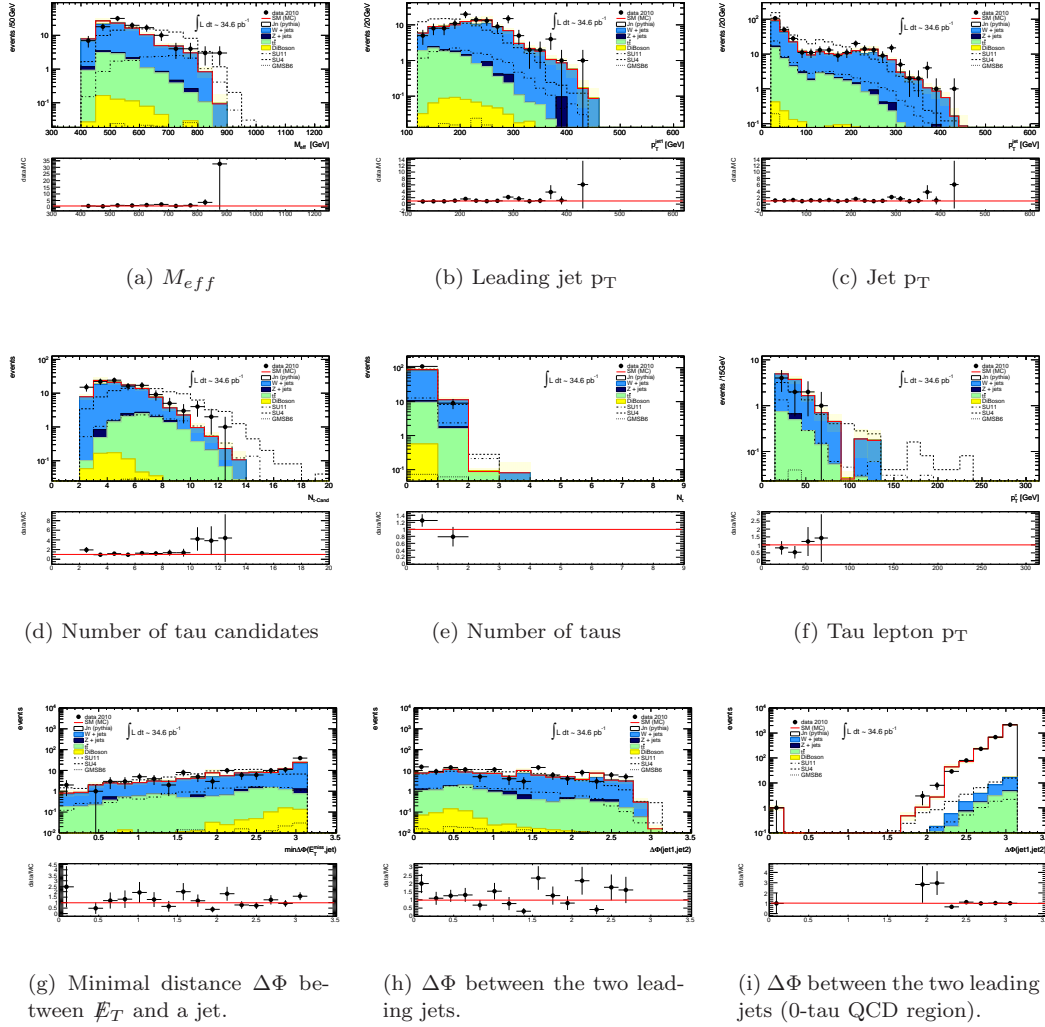


Figure 6.17. – MC description versus data in non-QCD dominated phase space region (a-h). Figure (i) shows the same spectrum as (h) in a QCD dominated region for comparison.

6.6. Systematic uncertainties

The number of expected SM background events in the signal region is either directly taken from MC (non-QCD background) or estimated with data-driven techniques using the MC prediction (QCD background). The systematic uncertainty on this MC based prediction is composed of several contributions, the sources of which are described in the following.

Due to the vetos of the 1-tau and the semileptonic channel, effects of different systematic uncertainties are not straight-forward to anticipate, but partly cancel. Therefore the uncertainty on selected events is given for both the final selection as well as for the pure di-tau selection without the vetos. As indicated by the statistical uncertainties, the MC statistics in these last event selection steps is rather small for some background contributions, therefore the discussion of the systematic effects concentrates on the combination of all non-QCD SM backgrounds.

For all non-QCD BG samples as well as for the SUSY signals, the effect on the selected number of events is obtained by performing the selection under varying conditions. Since the QCD contribution in the signal region is estimated by the data-driven method described in section 6.5.1, systematic effects on the QCD background are obtained by repeating both the event selection as well as the weighting procedure under conditions varied as explained in the following.

6.6.1. Jet energy scale

The energy of jets is calibrated to the hadronic scale by correction factors taken from MC simulation. This simulation has been validated by the ATLAS Jet-Etmiss performance group with 2010 data, and the jet energy scale (JES) uncertainty has been determined by comparison of the relative jet response in different η regions between data and MC simulation, and furthermore by comparison of different MC simulations using alternative detector configurations as well as different hadronic shower and physics models [119]. The results of these measurements are implemented in the tool `JESUncertaintyProvider`, which gives the relative JES uncertainty for jets as a function of their p_T and η . The relative uncertainty for jets in the SU11 sample is shown in figure 6.18(a), the mean uncertainty of which is about 5%. The p_T -dependence is illustrated in figure 6.18(b) by comparing jets in different Jn samples, corresponding to different p_T ranges. Soft jets are assigned a higher relative uncertainty than hard jets, but the difference in mean is at the order of per mil only. This JES uncertainty has been measured for well isolated jets. To account for the expected performance degradation in dense environments, an additional uncertainty of 5% is added for jets in the vicinity ($\Delta R < 0.6$) of which other jets are present. The energy of all jets is shifted by the thus obtained uncertainty in a correlated way, and the difference propagated to the missing transverse energy by

$$E_{x,y}^{\text{miss,new}} = E_{x,y}^{\text{miss,old}} + \sum_{\text{jets}} p_{x,y}^{\text{old}} - \sum_{\text{jets}} p_{x,y}^{\text{new}}. \quad (6.5)$$

Note that all jets are modified before applying any jet selection or overlap removal.

The effect of the JES uncertainty on the non-QCD BG selection is the largest of all systematic contributions (see table 6.8) if the jets are scaled up, i.e. if the jet energy is overestimated, while the effect of underestimated jet energies is comparably small. This effect is caused by the jet selection threshold of 20 GeV, which can be passed by many additional low-energetic jets if their true energy is overestimated. These jets contribute to the \cancel{E}_T correction, leading to more events passing the \cancel{E}_T requirement in the cut-flow. Similarly, more jets passing the $p_T > 40$ GeV threshold enter the H_T calculation, amplifying the effect.

An underestimation of the jet energy scale, on the other hand, has a much smaller impact on the final selection, since only events with a leading jet p_T , H_T or \cancel{E}_T slightly above the cut thresholds are affected in a selection altering way. Since the jet p_T -spectra are strongly peaked at low momentum values, an upward fluctuation of low- p_T jets leading to a migration above a

certain threshold is more likely than a downward migration, even though the shift scales with p_T .

The 1-tau selection requires a second jet with $p_T > 30$ GeV and also uses \cancel{E}_T , therefore it is affected in the same way as the di-tau selection, and the overall effect on the non-QCD BG is reduced if the vetos are applied.

The impact of the JES uncertainty in absolute number of selected events is shown in table 6.6. The systematic uncertainty on the QCD estimation is of the same order of magnitude as for the non-QCD background.

Out of the SUSY signal samples, SU4 is most affected by jet energy scale uncertainties since it has the most jets. The difference between a pure di-tau selection and the whole selection including the vetos is small.

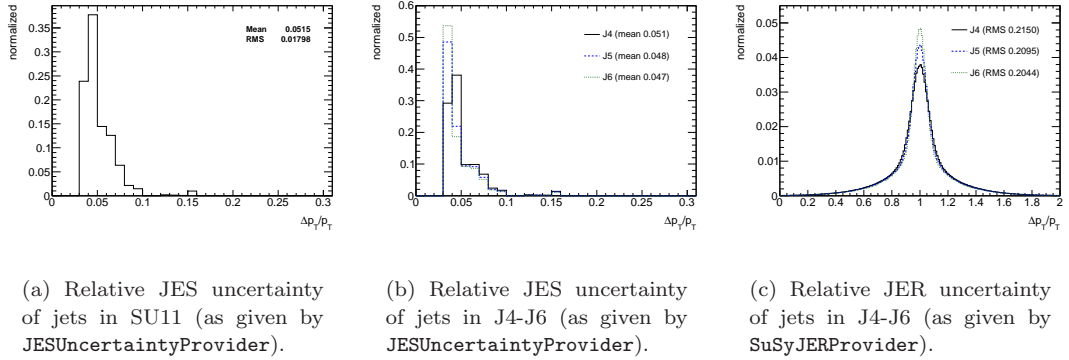


Figure 6.18. – Relative jet energy uncertainties due to energy scale and resolution.

6.6.2. Jet energy resolution

The agreement between the MC simulated jet energy resolution (JER) and the one in data has been measured with $\sqrt{s} = 7$ TeV data [120, 121], and the resulting relative jet energy uncertainty is provided in the `SuSyJERProvider` tool as a function of the jet p_T . The resolution is thereby parameterized as in equation 4.1, with a noise parameter N of 4.6 GeV, a stochastic term with $S = 0.846$ GeV and a constant C of 0.064. These terms describing the relative momentum resolution are added in quadrature and the resulting uncertainty is multiplied with a factor of 0.55 according to the observed discrepancy of data and MC simulation. The relative uncertainty obtained in this way is shown in figure 6.18(c) for QCD dijets in three different p_T ranges. To estimate the effect of this uncertainty on the final result, all jets are smeared with a Gaussian of width equal to this JER uncertainty before the analysis is performed. Jet energy differences are propagated to \cancel{E}_T as described above in equation 6.5. The effect on the non-QCD estimation is in between those of a systematic over- or underestimation of the jet energy scale, which is understandable if only events with an overall upward correction yield a sizable contribution.

The systematic uncertainty on the QCD estimation is again of the same order of magnitude for the non-QCD background, as shown in table 6.6.

6.6.3. Tau energy scale and resolution

The impact of the tau energy scale and resolution uncertainty are determined in analogy to the jet energy scale and resolution, using the same tools:

Every tau lepton that produces a reconstructed tau candidate is also reconstructed as a jet. The tau energy calibration applied in samples used in this analysis uses the EM scale jet energy and multiplies it with factors based on the properties of the tau candidate to calibrate the object

sample		JES +	JES -	JER	TES +	TES -	TER
SU11	sel.	+0.25	-0.46	+0.02	+0.13	-0.14	+0.05
	+vetos	+0.20	-0.32	+0.06	+0.08	-0.09	+0.06
SU4	sel.	+0.63	-0.59	+0.13	+0.13	-0.29	-0.08
	+vetos	+0.42	-0.34	± 0	+0.08	-0.25	± 0
GMSB6	sel.	+0.06	-0.07	+0.007	+0.018	-0.019	-0.01
	+vetos	+0.05	-0.05	+0.001	+0.009	-0.013	-0.02
ttbar	sel.	+0.09	-0.11	-0.02	+0.03	-0.008	+0.012
	+vetos	+0.08	-0.09	-0.012	+0.02	-0.008	+0.008
W+jets	sel.	+0.17	+0.08	+0.16	± 0	± 0	± 0
	+vetos	+0.17	+0.08	+0.16	± 0	± 0	± 0
Z+jets	sel.	+0.08	± 0	+0.08	± 0	± 0	+0.08
	+vetos	± 0	± 0	± 0	± 0	± 0	± 0
Di-boson	sel.	+0.003	± 0	± 0	+0.002	± 0	± 0
	+vetos	+0.002	± 0	± 0	+0.002	± 0	± 0
Sum non-QCD	sel.	+0.35	-0.03	+0.22	+0.03	-0.008	+0.08
	+vetos	+0.25	-0.008	+0.14	+0.02	-0.008	+0.008
estimated QCD	sel.	+0.18	+0.04	+0.07	-0.04	-0.06	-0.03
	+vetos	+0.19	+0.03	+0.08	-0.03	-0.07	-0.02

Table 6.6. – Impact of jet and tau energy scale and resolution uncertainties on the absolute number of selected events with 35 pb^{-1} .

to the tau energy scale. Therefore, both jets and tau leptons use the same baseline calibration of the same object before applying correction factors f which take the difference between QCD jets and hadronic tau jets into account:

$$\begin{aligned}
E_{\text{jet}} &= E_{\text{jet}}^{\text{EMscale}} \cdot f_{\text{jet}} \\
E_{\tau} &= E_{\text{jet}}^{\text{EMscale}} \cdot f_{\tau} = E_{\text{jet}} \frac{f_{\tau}}{f_{\text{jet}}} .
\end{aligned}$$

The energy uncertainty of a tau lepton can therefore be calculated from the relative uncertainty of the respective jet $u_{\text{rel,jet}} = \frac{\Delta E_{\text{jet}}}{E_{\text{jet}}}$ by

$$\begin{aligned}
\Delta E_{\tau} &= \Delta E_{\text{jet}} \frac{f_{\tau}}{f_{\text{jet}}} = u_{\text{rel,jet}} E_{\text{jet}} \frac{f_{\tau}}{f_{\text{jet}}} \\
&= u_{\text{rel,jet}} E_{\tau} ,
\end{aligned} \tag{6.6}$$

assuming no uncertainty contribution from the scaling factors f_{τ} and f_{jet} . The tau energy uncertainty caused by the energy scale and resolution are thus estimated by the relative energy uncertainty of the jet matched to the tau (closest in ΔR). If no match is found within $\Delta R < 0.2$, which is the case in 0.07 % of all tau leptons in the SU11 sample, a conservative uncertainty of 10 % is assumed.

The impacts of these uncertainties are compared in table 6.6 to those of the according jet energy uncertainties. Unlike the jet energy, uncertainties of the tau energy measurement do not influence the \cancel{E}_T because the simplified \cancel{E}_T calculation does not make use of the tau identification (see section 4.3.7).

This and the fact that there are on average more jets than tau leptons in the events results in a smaller uncertainty on the number of selected events caused by the tau lepton energy uncertainty than the uncertainty caused by jet energy uncertainties.

6.6.4. Tau efficiency and fake rate

The hadronic tau lepton identification efficiency and fake rate are estimated here to have an uncertainty of 20 %⁹. The consequences of an efficiency or fake rate over- or underestimated

⁹This is a conservative assumption, made because no official uncertainty from the Tau Combined Performance working group is available for the tau identification version used in this analysis. Studies using a newer tau

by this value is tested by changing the BDT cut for either true or fake taus such that the number of additionally identified or lost taus is 20 % of the number of tau leptons which pass the identification with the nominal selection criterium:

$$\int_{\text{BDT}_{\text{new}}}^1 d\text{BDT} N_{\tau} = x \cdot \int_{\text{BDT}_{\text{old}}}^1 d\text{BDT} N_{\tau}$$

with x equals 1.2 (0.8) for higher (lower) efficiency or fake rate. The new cut values BDT_{new} for 1-prong and 3-prong taus in the di-tau selection as well as in the 1-tau and semileptonic selection are listed in table 6.7(a). They are determined in the SU11 sample since the goal of this study is to estimate the systematic uncertainty in the signal region, which should be dominated by SU11-like events. The different BDT cuts listed for the modified tau identification efficiency ϵ_{τ} are only applied to reconstructed tau leptons which are matched to a true tau within $\Delta R < 0.2$, while the modified fake rate f_{τ} is realized by different BDT cuts to reconstructed tau leptons without truth match only.

The impact on the number of selected events is given in table 6.7(b). Naturally, the fake rate uncertainty has a larger impact on the final selection than the uncertainty of the tau identification efficiency in samples dominated by jets, i.e. the SM background as well as the low-mass SUSY signal point SU4, while the SUSY points with enhanced tau lepton production are more affected by uncertainties in the tau identification efficiency.

A summary of relative systematic uncertainties caused by the effects explained so far is given in table 6.8, compared to the relative statistical uncertainty in the third column.

identification software (as present in **athena** release 16) at different BDT cut working points show a relative uncertainty of less than 20 % for all these tau identification possibilities, and less than 10 % for most of these working points [122]. Unfortunately, these working points cannot be directly compared to the tau identification used in this analysis since the BDT itself has changed, so cutting at the same BDT value cannot be expected to yield the same results.

	1tau / semileptonic	di-tau 1-prong	ditau 3-prong
nominal	0.7	0.5	0.7
$\epsilon_{\tau} + 20\%$	0.645	0.223	0.665
$\epsilon_{\tau} - 20\%$	0.752	0.579	0.743
$f_{\tau} + 20\%$	0.68	0.482	0.675
$f_{\tau} - 20\%$	0.723	0.519	0.728

(a) Modified BDT cut values.

sample		$\epsilon_{\tau} +$	$\epsilon_{\tau} -$	$f_{\tau} +$	$f_{\tau} -$
SU11	sel.	+0.52	-0.68	+0.32	-0.47
	+vetos	+0.41	-0.41	+0.25	-0.28
SU4	sel.	+0.13	-0.25	+0.76	-0.67
	+vetos	+0.13	-0.21	+0.46	-0.46
GMSB6	sel.	+0.14	-0.24	+0.02	-0.04
	+vetos	+0.13	-0.20	+0.02	-0.04
ttbar	sel.	+0.02	-0.03	+0.09	-0.09
	+vetos	+0.02	-0.03	+0.09	-0.07
W+jets	sel.	± 0	± 0	+0.15	-0.08
	+vetos	± 0	± 0	+0.15	-0.08
Z+jets	sel.	± 0	± 0	± 0	± 0
	+vetos	± 0	± 0	± 0	± 0
Di-boson	sel.	± 0	± 0	± 0	-0.002
	+vetos	± 0	± 0	± 0	-0.002
Sum non-QCD	sel.	+0.02	-0.03	+0.24	-0.18
	+vetos	+0.02	-0.03	+0.24	-0.15
estimated QCD	sel.	-0.002	+0.001	-0.05	-0.23
	+vetos	-0.001	+0.001	-0.03	-0.15

(b) Impact of tau identification efficiency and fake rate uncertainties on the absolute number of selected events with 35 pb^{-1} .

Table 6.7. – Evaluation of systematic uncertainties on the number of selected events with 35 pb^{-1} caused by tau identification and fake rate uncertainties.

sample		stat	JES +	JES -	JER	TES +	TES -	TER	ϵ_τ +	ϵ_τ -	f_τ +	f_τ -
SU11	sel.	7	8	15	0.5	4	5	1.5	17	22	10	15
	+vetos	9	10	15	3	4	5	3	20	20	12	14
SU4	sel.	13	27	25	5	5	12	4	5	11	32	29
	+vetos	17	29	24	0	6	18	0	9	15	32	32
GMSB6	sel.	3.3	4	5	5	1.3	1.4	0.8	10	17	1.5	3
	+vetos	3.7	4	5	0.1	0.8	1.2	1.9	12	18	1.6	4
ttbar	sel.	12	29	36	5	9	3	4	8	11	29	10
	+vetos	14	32	35	1.6	8	3	1.6	6	13	34	26
W+jets	sel.	71	100	49	50	0	0	0	0	0	92	50
	+vetos	71	100	49	50	0	0	0	0	0	92	50
Z+jets	sel.	0	∞	0	∞	0	0	∞	0	0	0	0
	+vetos	0	0	0	0	0	0	0	0	0	0	0
Di-boson	sel.	100	137	0	68	68	0	0	0	0	0	74
	+vetos	100	72	0	72	72	0	0	0	0	0	78
Sum non-QCD	sel.	26	73	5.9	32	6.3	1.7	16	5.1	6.8	51	37
	+vetos	29	59	1.8	19	5.2	1.9	1.0	3.9	7.7	57	36
QCD	sel.	25	57	13	22	14	20	10	0.6	0.4	15	76
	+vetos	27	84	13	36	14	29	9	0.6	0.4	13	67

Table 6.8. – Systematic uncertainties: relative difference in % before and after 1-tau and semileptonic vetos, for jet energy scale (JES), jet energy resolution (JER), tau energy scale (TES), tau energy resolution (TER), tau identification efficiency (ϵ_τ) and fake rate (f_τ).

6.6.5. Pile-up

The mean number of collisions per bunch-crossing in data recorded in 2010 is two, while the MC simulation samples used in this analysis do not include overlap of different events in the same bunch-crossing. Separate pile-up samples with 2 additional interactions per bunch-crossing are taken to estimate the systematic uncertainty caused by this difference between data and MC simulation. Such dedicated pile-up samples are only available for the $t\bar{t}$, W and Z backgrounds. Since the diboson contribution to the final selection is very small, its contribution to the systematic uncertainty caused by pile-up is neglected. For the QCD background, no centrally produced pile-up samples are available. The uncertainty on the estimated number of QCD events in the signal region caused by the difference in non-QCD background used in the QCD estimation procedure is less than 0.1%. The difference in non-QCD background events estimated from MC simulation is shown in the table of figure 6.20.

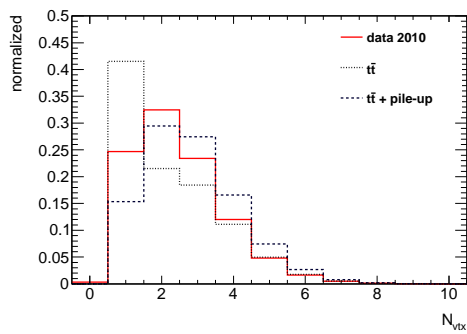


Figure 6.19. – Number of vertices with ≥ 3 tracks in data and $t\bar{t}$ MC simulation.

sample		absolute		%	
		stat	pile-up	stat	pile-up
ttbar	sel.	± 0.02	-0.03	8	10
	+vetos	± 0.02	-0.03	9	10
W+jets	sel.	± 0.12	+0.07	71	43
	+vetos	± 0.12	+0.07	71	43
Z+jets	sel.	± 0	± 0	0	0
	+vetos	± 0	± 0	0	0

Figure 6.20. – Impact of pile-up on number of selected events compared to statistical uncertainty: difference in number of selected events absolute with 35 pb^{-1} and relative in %.

6.6.6. Other sources of systematic uncertainties

The uncertainty on the luminosity measurement used in this analysis is 11 % [115]. Since the QCD scale is taken from data, this uncertainty only applies to the non-QCD background estimation. A theoretical uncertainty on the cross-section of 5 % is assumed for W and Z production [123] and 6 % for $t\bar{t}$ production [124].

Systematic effects arising from light lepton identification efficiency and fake rate, as well as from light lepton energy measurement uncertainties, are not taken into account. Light leptons enter this analysis only in the semileptonic and 1-tau selection vetos. While the semileptonic veto has no large effect on the final result, the 1-tau selection uses light leptons only in a veto and is thus hardly affected by their energy scale and resolution uncertainties. Therefore the overall impact of light lepton uncertainties on the di-tau selection result can be neglected.

The uncertainty caused by the MC modelling using approximations for the proton PDFs as well as for initial and final state radiation of soft gluons can in principle be estimated by usage of different MC generators. However, no such samples are available in the data reprocessing version used in this thesis ¹⁰. For the $t\bar{t}$ background estimation, according studies performed in other SUSY search channels show a 17 % uncertainty by comparison of MC@NLO to the POWHEG [125] generator, and an additional uncertainty of $^{+6\%}_{-25\%}$ by changing parameters of the initial and final state radiation modelling [126]. Similarly, uncertainties on the W and Z background estimation arising from the choice of **Alpgen** settings regarding factorization and renormalization scale or matching parameters lead to an uncertainty of $\pm 25\%$ [126].

It is further shown by other SUSY analyses using the same trigger that an inefficiency at $|\eta| \sim 1.5$ associated with the transition between barrel and endcap calorimeter leads to an additional systematic uncertainty of 2 % [126].

6.7. Results

6.7.1. Expectations in the signal region

Taking the systematic uncertainties evaluated in the last section into account, the expected number of SM background events in the signal region is

$$N_{\text{SM}} = 0.77 \pm 0.19^{\text{stat}} \pm 0.14^{\text{MC}} \pm 0.05^{\text{Lumi}} \pm 0.53^{\text{syst}}_{-0.30} \text{ (no vetos)}, \quad (6.7)$$

$$N_{\text{SM}} = 0.64 \pm 0.17^{\text{stat}} \pm 0.12^{\text{MC}} \pm 0.05^{\text{Lumi}} \pm 0.43^{\text{syst}}_{-0.23} \text{ (with vetos)}. \quad (6.8)$$

The MC denoted systematic uncertainty contribution here includes the cross-section uncertainties on the non-QCD background samples as well as uncertainties related to generator choices, which together account for 27 % uncertainty on the number of $t\bar{t}$, W and Z events. The luminosity uncertainty is given by the **Lumi** term, while the last term includes all other systematic uncertainties investigated in section 6.6. It is dominated by the jet energy scale and resolution, with the second largest contribution arising from the tau fake rate uncertainty.

As signal expectation, in addition to the three benchmark points SU11, SU4 and GMSB6, an mSUGRA m_0 - $m_{1/2}$ -plane with fixed $\tan\beta = 40$ and positive sign of higgsino mixing parameter is scanned for $A_0 = 0$ GeV and $A_0 = -500$ GeV. NLO cross-sections calculated with **Prospino** are used. The systematic uncertainties taken into account for these cross-section are induced by renormalization/factorization scale and PDF uncertainties.

Parameter points with same m_0 - $m_{1/2}$ values are more likely to be selected by the ditau search in the low A_0 grid because of the enhanced mixing due to the A_0 contribution in the off-diagonal elements of the stau mass matrix (see equation 2.19). This behaviour has already been observed in the $\sqrt{s} = 10$ TeV mSUGRA grids of chapter 5.4.6. Points in the low $m_{1/2}$

¹⁰Due to a bug in the tau identification in the full official dataset, an additional limited set of samples has been processed with a fix for tau identification to be used in the SUSY tau channel searches.

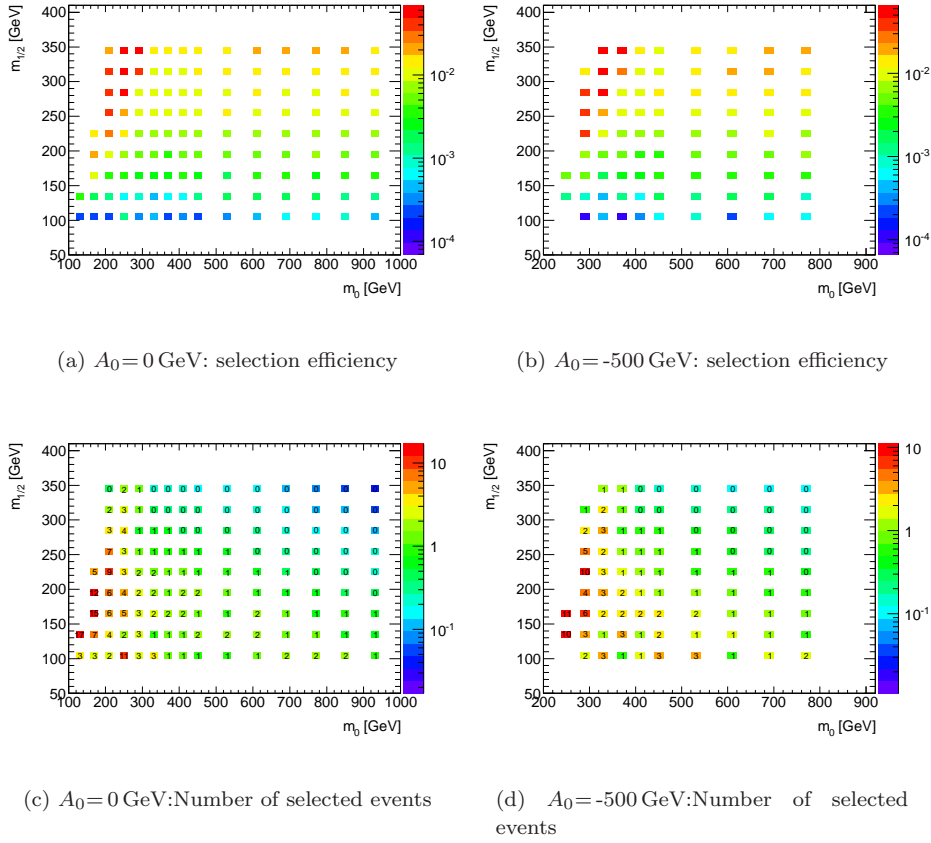


Figure 6.21. – Event selection in $\tan\beta = 40$ mSUGRA grids without 1-tau and semileptonic veto..

region are already excluded by $b \rightarrow s\gamma$ measurements (see section 2.2.2 and figure C.1(a) in appendix B), and $m_{1/2} < 160$ GeV (140 GeV) is also excluded by direct searches at LEP for $A_0 = 0$ GeV (-500 GeV). Points beyond the left-hand side border of the produced mSUGRA grids are theoretically excluded because they contain a stau LSP, which in combination with R-parity conservation leads to a stable massive charged particle in clear contradiction to observation.

The efficiencies of the ditau event selection cuts (without vetos) are shown for these mSUGRA points in figures 6.21 (a) and (b), the expected numbers of selected events with an integrated luminosity of 35 pb^{-1} are displayed in figures (c) and (d). For values of m_0 or $m_{1/2}$ of 300 GeV or higher, only one event or less is selected. The selection efficiency is worst in points with small $m_{1/2}$ and large m_0 , where the $\tilde{\tau}_1$ mass is so large that there are no stau particles produced at the LHC, and hence not many tau leptons. At the same time, the $\tilde{\chi}_1^0$ is so light that there is also not much missing transverse energy. Therefore the di-tau search has less sensitivity to this region than to mSUGRA points with $m_{1/2} > m_0$.

The effect of different systematic uncertainties on the number of selected events is displayed in figure 6.22 for the mSUGRA grid with $A_0 = 0 \text{ GeV}$ (a-e) and $A_0 = -500 \text{ GeV}$ (f-j). While the PDF uncertainty shows the largest impact in mSUGRA regions with large $m_{1/2}$ and large m_0 , the relative uncertainty on the number of selected events caused by the renormalization/factorization scale uncertainty shows a uniform behaviour throughout the mSUGRA regions investigated. The effects of the tau efficiency and fake rate uncertainties are diametrically opposed, with an accurate knowledge of the efficiency being most important in the region with small m_0 and large $m_{1/2}$. The jet energy scale uncertainty mostly affects points where both these parameters are small.

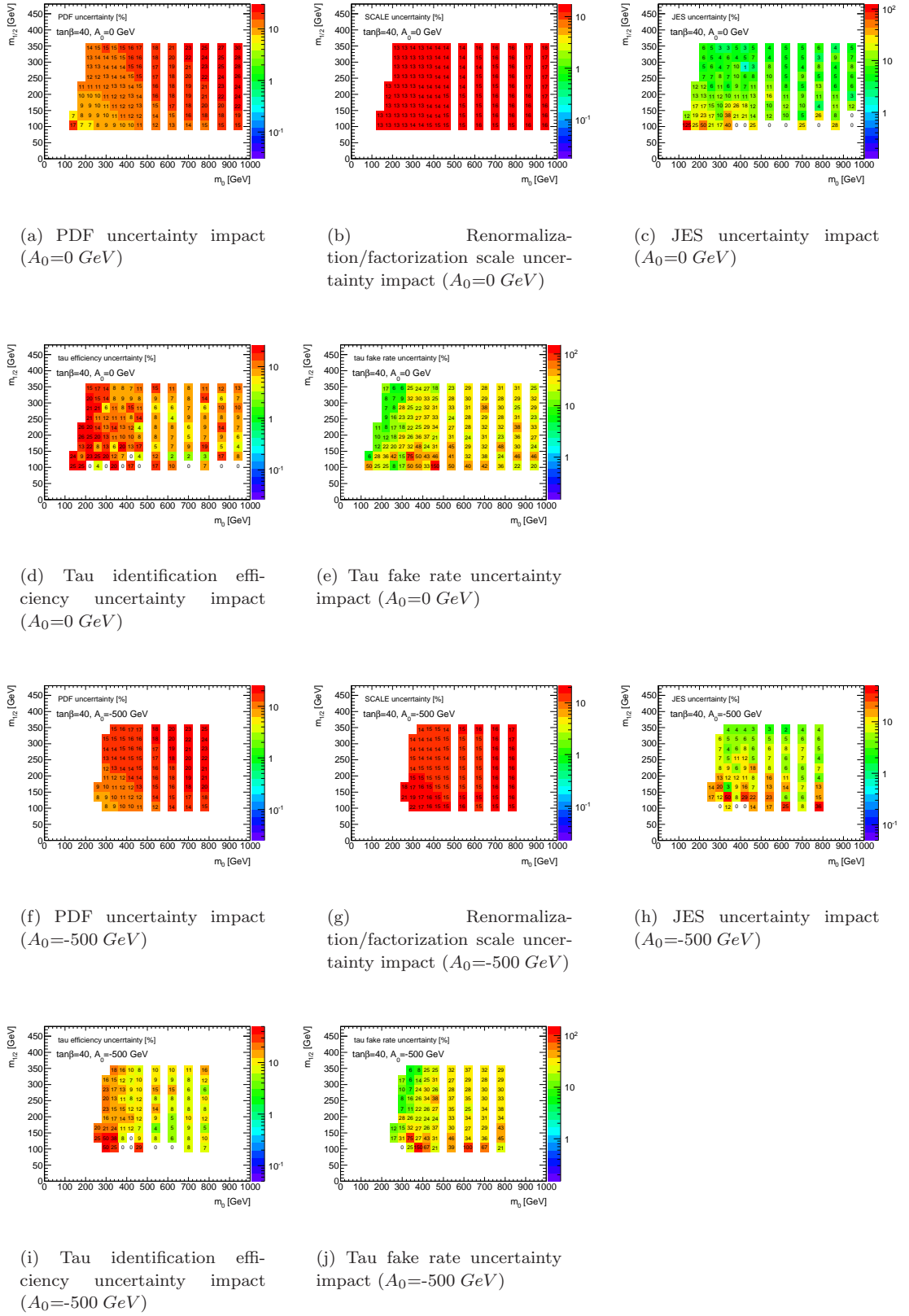


Figure 6.22. – Relative uncertainty in number of selected events with $\int L dt = 35 \text{ pb}^{-1}$ caused by different systematic uncertainties..

6.7.2. Observation

Table 6.9 shows the number of events from MC simulation compared to the number of events observed in data in different selection steps, beginning after the trigger and respective cuts on \cancel{E}_T and the leading jet p_T . Unlike in table 6.9, MC events are now scaled to 34.6 pb^{-1} and with the additional jet cleaning factor (see section 6.4.2) obtained from data applied. The QCD background is scaled with the signal-like 0-tau region factor and with the QCD region fake rate correction factor according to the number of tau leptons selected at each step.

cuts	Standard Model expectation						data 2010
	ttbar	W+jets	Z+jets	di-Boson	QCD	all SM	
preselection	239 \pm 1	1971 \pm 16	57 \pm 2	7.5 \pm 7.5	10947 \pm 1064	13220 \pm 1063	15586
$\geq 1 \tau$	47.5 \pm 0.5	232 \pm 5	18 \pm 1.2	0.7 \pm 0.7	840 \pm 150	1138 \pm 150	834
$\geq 2 \tau$	3.55 \pm 0.13	5.7 \pm 0.7	2.1 \pm 0.4	0.03 \pm 0.03	12 \pm 5	23 \pm 5	21
$H_T > 450 \text{ GeV}$	1.16 \pm 0.08	1.3 \pm 0.3	0.5 \pm 0.2	0.004 \pm 0.004	9 \pm 4	12 \pm 4	13
met > 200 GeV	0.30 \pm 0.04	0.17 \pm 0.11	0	0.002 \pm 0.002	0.31 \pm 0.15	0.77 \pm 0.19	2
veto 1-tau	0.25 \pm 0.03	0.17 \pm 0.11	0	0.002 \pm 0.002	0.23 \pm 0.12	0.64 \pm 0.17	2
veto lep-had	0.25 \pm 0.03	0.17 \pm 0.11	0	0.002 \pm 0.002	0.23 \pm 0.12	0.64 \pm 0.17	2

Table 6.9. – Cut-flow (events normalized to 34.6 pb^{-1}).

The agreement between expected and observed amount of data is very good but for the first two selection steps, which contain a phase space region slightly different from the sideband the QCD scale is taken from.

The expectation of SM events in the signal region, equation 6.7, is in agreement with 2 events observed in data. The properties of these events are listed in table 6.10, and figure 6.23 shows the selected events in the signal region in comparison with the MC expectation. In the spectra of \cancel{E}_T , H_T , M_{eff} and \cancel{E}_T / M_{eff} , both events are seen to have properties as expected from the SM background passing the event selection. Though also SUSY processes can produce such events, the observed events do not populate phase space regions dominated by signal.

Both events contain exactly two tau leptons and no light lepton. Although both events contain at least one tau that also passes the identification criteria applied in the 1-tau search, the first event fails the 1-tau selection due to a very small azimuthal angle between the leading jet and the missing transverse energy, the second event is rejected by the 1-tau selection because of a very small transverse mass of 14 GeV which fails a W rejection criteria of $m_T > 100 \text{ GeV}$. This small transverse mass is caused by the \cancel{E}_T vector pointing in the direction of the leading tau ($\Delta\Phi = 0.1$, $\Delta R = 0.7$).

Both selected events contain one high energetic jet with more than 350 GeV transverse momentum, and a second jet with more than 200 GeV (event 1) or nearly 100 GeV (event 2). In the first selected event, both tau leptons have a quite high BDT value greater than 0.8. They are opposite sign and have a very high invariant mass of more than 300 GeV. The second event contains one high quality tau lepton, while the second one is only slightly above the thresholds in both p_T and BDT, and it is close to the second leading jet ($\Delta R = 0.43$). Both tau leptons in this event are positively charged.

A 3-dimensional display of the two events passing all selection cuts is shown in figure 6.24

6.7.3. Interpretation

Since the 1-tau and semileptonic channel are not available for combination at the time of writing, the observed data is evaluated directly after the \cancel{E}_T selection without the vetos in the following.

The agreement between the observed data and the SM expectation is characterized by the p-value of the background-only hypothesis H_0 , which describes the probability of finding data equally or more incompatible with H_0 under the assumption that H_0 is true. As test statistic, a likelihood ratio $q = -2 \cdot \ln \frac{L_{S+B}}{L_B}$ is used with Poisson probability density functions. Systematic

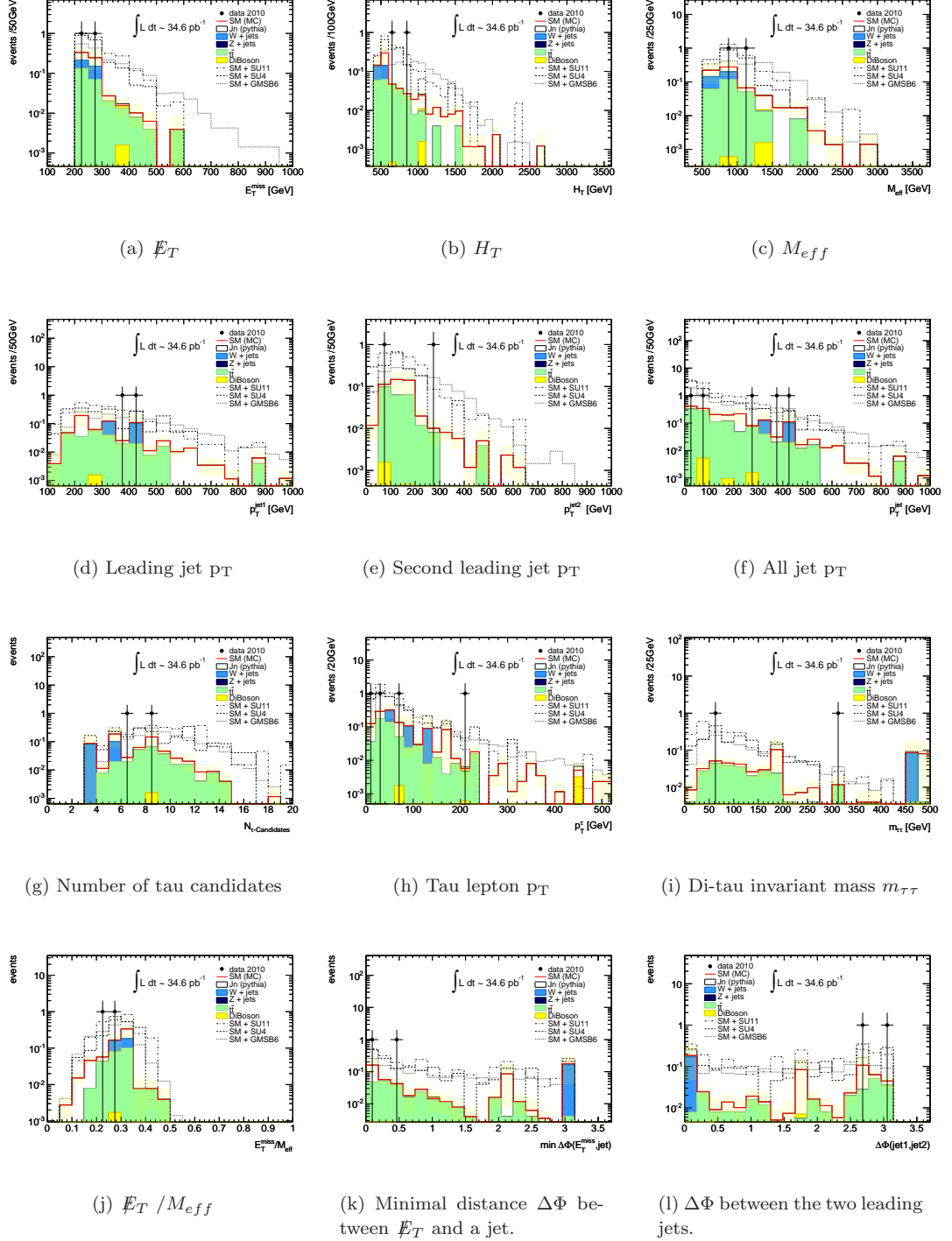
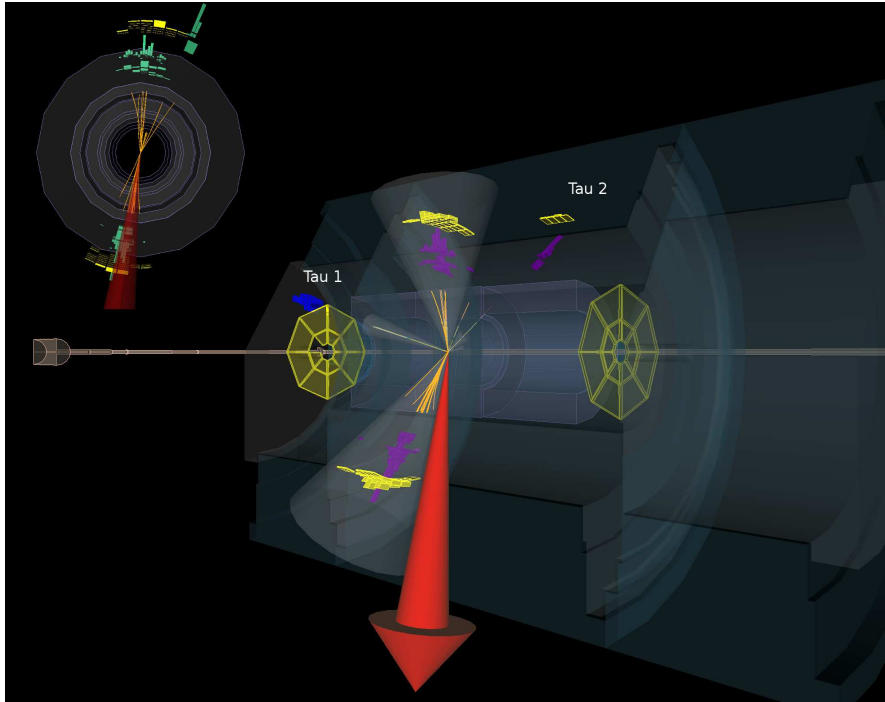
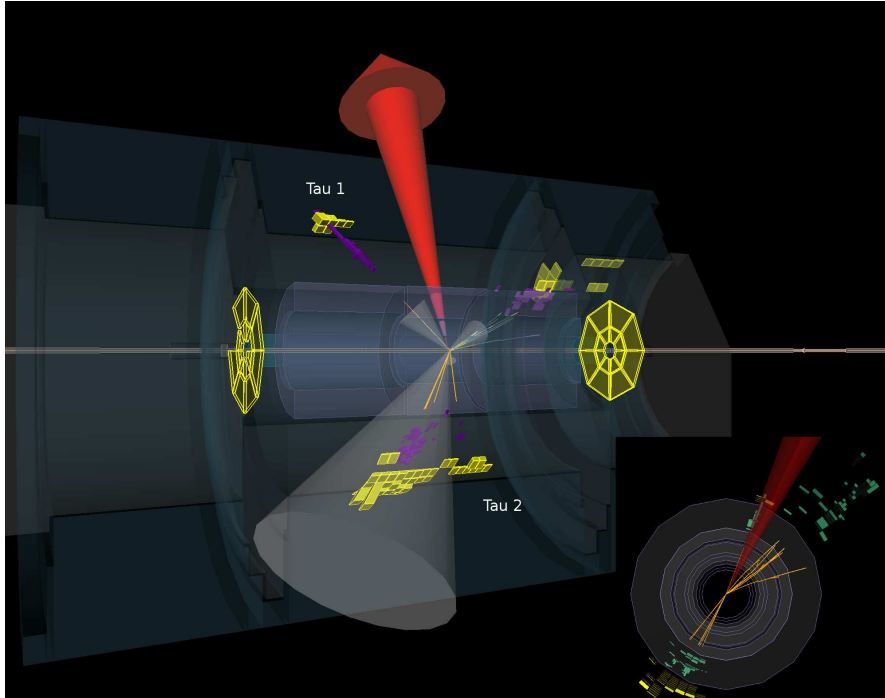


Figure 6.23. – MC description versus data in signal region.



(a) Event 1



(b) Event 2

Figure 6.24. – Event displays of selected events: the red arrow indicates the \vec{E}_T vector.

	Event 1		Event 2	
data period	I		I	
run number	167776		167680	
event number	186801762		51356017	
\cancel{E}_T	248 GeV		262 GeV	
H_T	877 GeV		624 GeV	
leading jet p_T	361 GeV		437 GeV	
2 nd jet p_T	279 GeV		97 GeV	
min $\Delta\Phi(\text{jet}, \cancel{E}_T)$	0.05		0.46	
tau properties	tau 1	tau 2	tau 1	tau 2
BDT score	0.82	0.79	0.85	0.52
Number of tracks	3	1	1	1
E_T	209 GeV	28 GeV	73 GeV	18 GeV
η	-2.17	0.79	-0.74	-0.23
Φ	1.29	1.16	1.21	-2.23
$m_{\tau\tau}$	319 GeV		73 GeV	
sign of charges	opposite		same	

Table 6.10. – Properties of observed events

uncertainties on the signal or background estimation are included by smearing the functions with the relative uncertainty.

Conventionally, H_0 (i.e. the Standard Model) is rejected if $p_B = p_{SM} < 2.87 \cdot 10^{-7}$ (one-sided limit), which corresponds to a 5σ deviation and thus a discovery of new physics. If no discovery is made, SUSY models are evaluated with the CL_S technique [127], where a tested signal hypothesis is excluded if $CL_S = \frac{CL_{S+B}}{CL_B} < 5\%$. The confidence levels CL_B and CL_{S+B} are defined such that they represent the probability with which the estimator x for the parameter to be measured lies in the confidence interval $x \pm \sigma$. The CL_S technique is a conservative approach which has the advantage (compared to CL_{S+B}) that it prevents excluding a signal to which the analysis has no sensitivity if a downward fluctuation of the background is observed. However, it does not satisfy a probability interpretation anymore. Therefore, as recommended by the ATLAS statistics forum, the so-called *power constrained limit* (PCL) [128] is also evaluated as an alternative. In this approach, a signal is excluded if $CL_{S+B} < 5\%$ under the condition that the test has sufficient sensitivity to the assumed signal. The minimal power constraint is chosen such that an observed limit is not allowed to be smaller than its -1σ expectation. This corresponds to a minimal statistical power of 16%¹¹.

With two observed events in the signal region, the p-value of the SM hypothesis p_{SM} is 0.27, so no contradiction to the Standard Model is observed. Consequently, possible limits for different mSUGRA parameter points and for GMSB6 are searched for. None of the three benchmark points can be excluded. Introducing the signal strength parameter μ such that the signal plus background hypothesis $\mu s + b$ can be tested, and iteratively calculating CL_S (PCL) for different μ until the model is not compatible with the observation, $\mu > 1.7$ (1.5), 2.6 (2.1) or 3.5 (3.2) can be excluded for SU11, SU4 and GMSB6 with the CL_S (PCL) method, respectively. Observed and expected limits of the signal strength parameters for these points are summarized in table 6.11.

	SU11	SU4	GMSB6
expected μ_{up}	0.8	1.1	1.7
observed μ_{up} (PCL)	1.5	2.1	3.2
observed μ_{up} (CL_S)	1.7	2.6	3.5

Table 6.11. – Limits on the signal strength parameter of three benchmark SUSY points.

¹¹Assuming Gaussian behaviour of the parameter to be tested.

As systematic uncertainty of the signal, these calculations include the squared sum of all downward fluctuations, which leads to 30 %, 41 % and 18 % uncertainty on the SU11, SU4 and GMSB6 expectation, respectively. Further included is the signal contamination in the sidebands used for QCD estimation, which can be large in the signal-like 0τ region used to calculate w_0 . The number of expected SU11, SU4 or GMSB6 events in this region is 56, 165 or 1 for $\mu = 1$, compared to 130 MC QCD and 42 non-QCD background events. A large signal contamination as given for SU4 leads to an overestimation of expected QCD background and thus reduced sensitivity in the signal region, yielding conservative limits. Note however that a large signal contribution in the non-QCD dominated signal-like 0τ region would also show in the non-QCD sideband investigated in section 6.5.2.

Through the signal contamination, the systematic uncertainty of the tested signal also influences the uncertainty of the background expectation.

Figure 6.25 shows the upper limit of the signal strength parameter for the two investigated mSUGRA grids, evaluated with the PCL method, overlayed with contours of $\mu_{up} = 1$ calculated both with the PCL and with the CL_S method. The ± 1 sigma bands of the expected limit are calculated from the distribution of μ_{up} values obtained in a Toy MC. Systematic uncertainties of the signal expectation include scale and PDF uncertainty as well as JES and tau efficiency and fake rate uncertainties. Other sources of systematic uncertainties are negligible compared to these (see section 6.6) and are not considered for the signal expectation. The SM background expectation includes all systematics described in section 6.6.

Points with $\mu_{up} < 1$ are excluded at 95 % CL. The excluded region is only marginally smaller

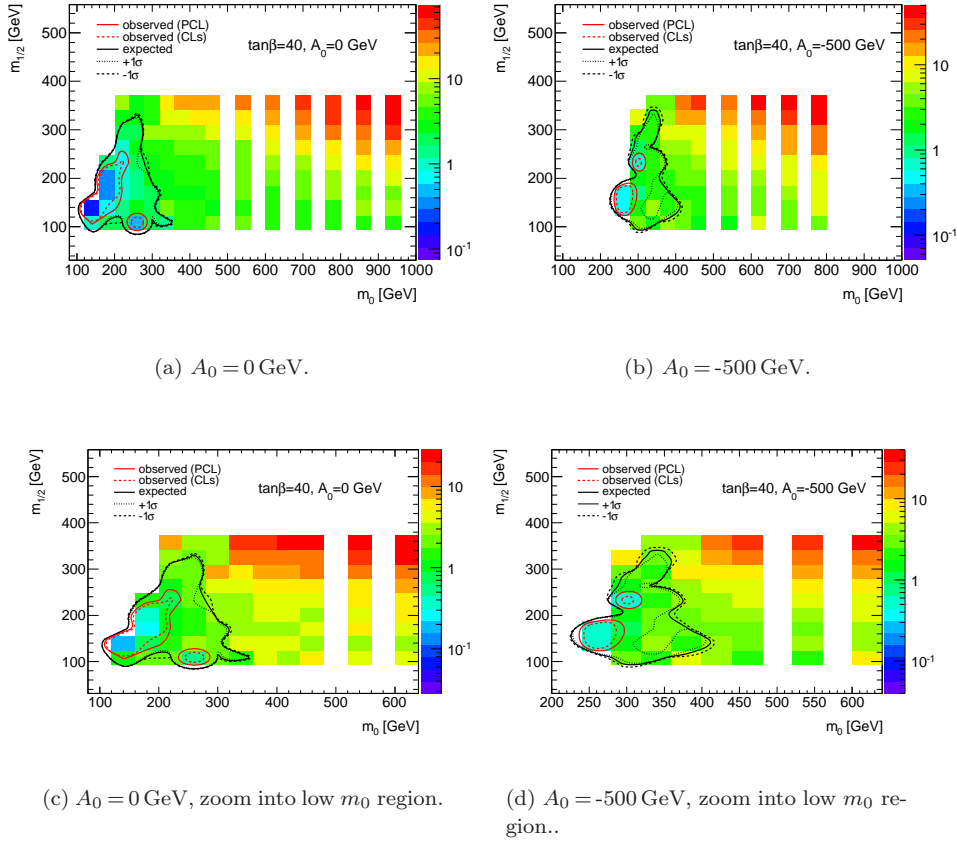


Figure 6.25. – Upper limits on the signal strength parameter μ_{up} for $\tan \beta = 40$ mSUGRA grids points: the color shows values of μ_{up} evaluated with the PCL method, the red solid (dotted) line the contour for exclusion with PCL (CL_S). Black lines are the expected limit and 1σ bands.

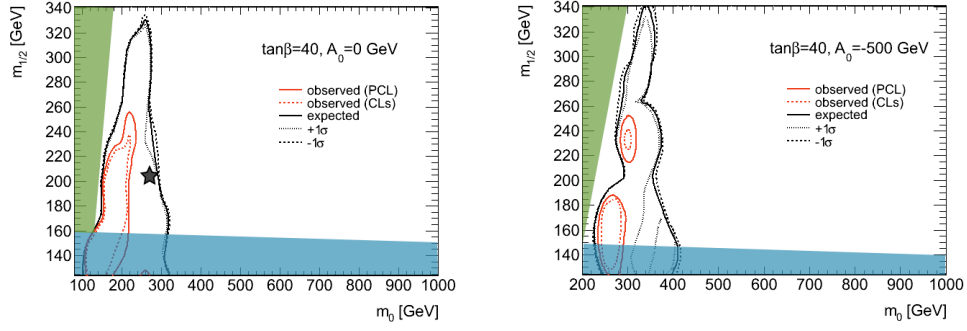
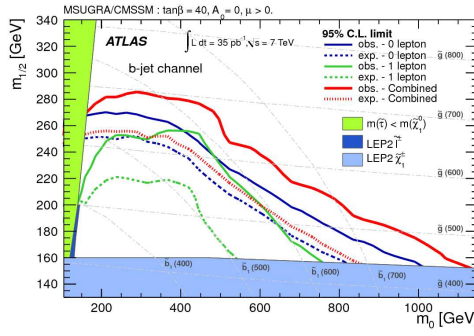
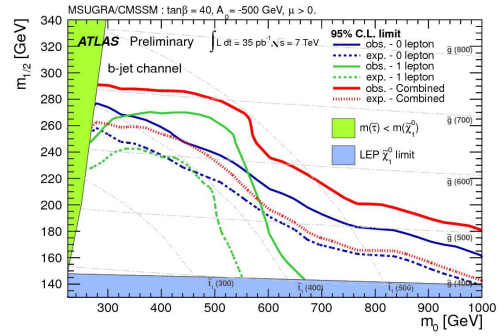
(a) $A_0 = 0$ GeV.(b) $A_0 = -500$ GeV.(c) Exclusion by ATLAS SUSY searches with b-jets, $\tan \beta = 40$, $A_0 = 0$ GeV [129].(d) Exclusion by ATLAS SUSY searches with b-jets, $\tan \beta = 40$, $A_0 = -500$ GeV [129].

Figure 6.26. – Comparison of limits from the di-tau analysis with limits from the b-jet search channel. The star in (a) marks a parameter point similar to SU11 (but for $\tan \beta$).

for CL_S compared to PCL. The observed exclusion regions are smaller than the expected limit since more data has been observed than expected from the SM alone, yet the uncertainties on both the signal and background expectation limit the sensitivity of this analysis at this early stage of data taking.

mSUGRA points excluded by the di-tau search have already been excluded recently by ATLAS SUSY searches with b-jets and missing transverse energy [126, 129]. A direct comparison is shown in figure 6.26, where (a) and (b) show the same exclusion contours as figure 6.25, but the m_0 and $m_{1/2}$ range is adjusted to the b-jet exclusion figures shown in (c) and (d). Regions excluded by LEP or by a $\tilde{\tau}_1$ LSP are marked, as well as a benchmark point in figure 6.26(a) which is identical to SU11 but for $\tan \beta = 40$ instead of 50. The limits observed in the b-jet channel are more stringent than expected (see appendix C), while the excluded region in this di-tau search is smaller. The expected exclusion, however, includes a region with low m_0 and larger $m_{1/2}$ which could not be excluded by the b-jet search. Hence with more data available, the di-tau channel can be expected to probe regions other SUSY search channels are less sensitive to, even before a combination with the other two tau search channels.

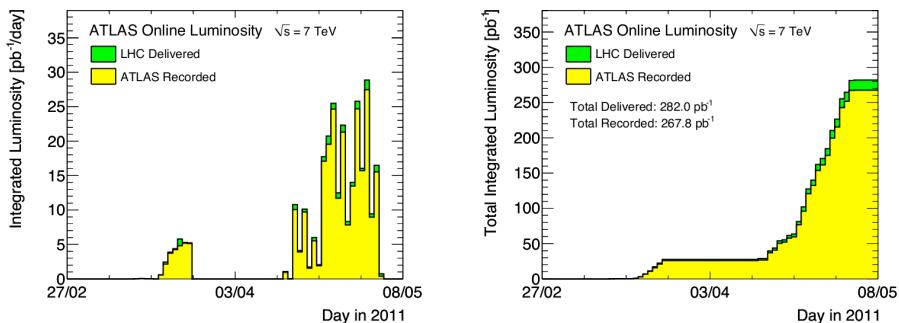
6.8. Conclusions and Outlook

A search for SUSY particles decaying into final states with two tau leptons and missing transverse energy has been performed with ATLAS data recorded in 2010 with pp collisions at a center-of-mass energy of $\sqrt{s} = 7$ TeV. This is the first result of SUSY searches with tau final states with the ATLAS detector. Although designed for a combination with dedicated 1-tau and semileptonic di-tau searches, in this thesis the di-tau search results have been interpreted standalone because results from the other channels are not available.

In a dataset corresponding to an integrated luminosity of $\int L dt = 35 \text{ pb}^{-1}$, two events were observed after applying all event selection criteria, which is in agreement with the expected number of background events of $N_{\text{SM}} = 0.77 \pm 0.19^{\text{stat}}_{-0.33}^{+0.55 \text{ syst}}$. The major contribution to the systematic uncertainty of this expectation emerges from the jet energy scale and resolution uncertainty.

Since no contradiction to the Standard Model expectation was found, upper limits on the di-tau cross section $\sigma \times BR(\tau\tau)$ in units of the theoretical values have been derived as function of m_0 and $m_{1/2}$ for two mSUGRA scenarios with $\tan\beta = 40$, $\mu > 0$ and different A_0 of 0 GeV or -500 GeV. mSUGRA points with (approximately) $m_0 < 200$ GeV and $m_{1/2} < 250$ GeV can be excluded for $A_0 = 0$ GeV at 95 % CL.

The sensitivity of the di-tau analysis is limited by large systematic uncertainties which are dominated by the jet energy scale and resolution uncertainty. Depending on the SUSY model and parameters, the signal expectation is also subject to systematic uncertainties caused by the tau efficiency or fake rate uncertainty, for which conservative estimates have been employed. These uncertainties can be expected to be significantly lower when more data is available to measure the performance of the reconstruction algorithms. The luminosity uncertainty of 11 % has already been reduced to 3.4 % for analyses using an updated version of the luminosity calculation.



(a) Luminosity versus day in 2011.

(b) Cumulative luminosity versus day in 2011.

Figure 6.27. – Luminosity developement in 2011.

The di-tau analysis is further limited by the amount of data available. Since the LHC recommenced operation after a short shutdown at the end of 2010, the integrated luminosity collected per day, shown in figure 6.27(a), is at the same order of magnitude as the complete dataset used in this thesis. About 500 pb^{-1} can be expected to be available in summer 2011, and about 1 fb^{-1} by the end of the year. More sophisticated Standard Model background estimation techniques can be performed with this larger amount of data. The QCD background can be fully determined from data, with not only the scale being measured in sidebands but also the shape of the effective mass or invariant di-tau mass being taken from the 2τ QCD region. Dedicated sidebands enriched with $t\bar{t}$, W or Z background can be defined to measure the non-QCD background contribution separately.

Furthermore, a combination of this di-tau search with the 1-tau and the semileptonic channel is foreseen. The combined sensitivity of these three tau search channels will be used to test more kinds of tau enhanced SUSY scenarios than used in this thesis, e.g. a GMSB grid is currently in production and more mSUGRA points under study. These new SUSY grids are planned to include more scenarios where the decay chain investigated in chapter 5, $\tilde{\chi}_2^0 \rightarrow \tilde{\tau}_1 \tau \rightarrow \tilde{\chi}_1^0 \tau \tau$, is kinematically allowed.

Finally, a combination of all SUSY searches performed in ATLAS with pp collisions at $\sqrt{s} = 7$ TeV taken until the end of 2013 can be expected to extend the SUSY discovery reach up to SUSY masses of the order of 1 TeV, assuming an integrated luminosity of about $\int L dt = 5 \text{ fb}^{-1}$. If a SUSY signal is discovered by the end of the $\sqrt{s} = 7$ TeV run, extraction of SUSY parameters can begin with this dataset by measurements like the one investigated in the previous chapter, and be continued after the expected LHC upgrade which allows $\sqrt{s} = 14$ TeV pp collisions. If no SUSY signal is found, a combination of results from the LHC experiments ATLAS and CMS will enable an extension of the limits on SUSY particle masses up to an energy scale where the theory loses its desired property to solve the hierarchy problem, rendering SUSY a much less attractive theory.

7. Summary

Tau lepton final states are an important contribution to the SUSY search program of the ATLAS experiment, since the production of tau leptons in proton-proton collisions at the LHC might be favoured by Supersymmetry above light lepton production. Furthermore, information about the stau mass can be extracted from a measurement of the kinematic endpoint of the di-tau invariant mass spectrum if a SUSY signal is seen.

In this thesis, final states with at least two tau leptons and missing transverse energy were investigated in terms of SUSY discovery potential as well as prospects for the measurement of a kinematic endpoint. A detailed study of three decay mode channels, the fully hadronic, semileptonic and the fully leptonic decay, yielded a combined sensitivity which enables a discovery of SUSY scenarios with stau masses up to $m_{\tilde{\tau}_1} \leq 400$ GeV and $m_{\tilde{\chi}_2^0} \leq 200$ GeV or vice versa if interpreted in mSUGRA, assuming $\int L dt = 1 \text{ fb}^{-1}$ of pp collisions with $\sqrt{s} = 10$ TeV and a systematic uncertainty on the background expectation of 50 %. The discovery reach is potentially limited by systematic uncertainties in the tau identification performance, which particularly affect the fully hadronic channel. While for a pure SUSY search in the tau channel processes producing only one tau lepton should also be taken into account, the primary goal of this study was a measurement of the endpoint of the invariant mass of two tau leptons, targeting taus from the SUSY decay chain $\tilde{\chi}_2^0 \rightarrow \tilde{\tau}_1 \tau \rightarrow \tilde{\chi}_1^0 \tau \tau$. In principle, three independent measurements can be performed in the three decay channels, yet the fully leptonic channel was found not to bear enough statistics for such a measurement with the assumed amount of accumulated data. Endpoints below about 50 GeV generally pose a problem to this measurement, since the spectrum shape then is distorted by tau reconstruction and identification threshold effects, leaving the endpoint determination via an inflection point measurement unfeasible without further adaptations. A potentially dominant source of systematic uncertainty of the endpoint result was found to be an uncertainty in the difference in tau identification efficiency of different types of tau leptons predominantly populating certain parts of the invariant mass spectrum. Such effects are negligible in the semileptonic channel, but might be large in the fully hadronic invariant mass spectrum. Two methods to fit the trailing edge of the invariant mass spectra of $\tau_{\text{had}}\tau_{\text{had}}$ and $\tau_{\text{had}}\tau_{\text{lep}}$ combinations were investigated, a binned χ^2 fit and an unbinned maximum likelihood fit. A combination of these methods was found to expose bad fit results by contradiction, while results compatible within 1σ were in most cases also consistent with the theoretical value within the statistical uncertainty of the measurement.

In the second analysis of this thesis, the fully hadronic di-tau channel was investigated in the first $\sqrt{s} = 7$ TeV ATLAS data taken between June and October 2010, corresponding to an integrated luminosity of 35 pb^{-1} . Two of the observed events passed the di-tau event selection, which is consistent with the Standard Model background expectation of $N_{\text{SM}} = 0.77 \pm 0.19_{\text{(stat)}}^{+0.55}_{-0.33} \text{(syst)}$. Interpreted in mSUGRA, limits on m_0 and $m_{1/2}$ were determined for $\tan\beta = 40$, positive higgsino mixing parameter and $A_0 = 0$ GeV as well as $A_0 = -500$ GeV. While the excluded mSUGRA region is smaller than the exclusion range obtained with the ATLAS SUSY search with b-jets using the same amount of data, the full potential of the tau search channel has yet to be exploited by a combination of the di-tau search presented here with the more inclusive search for events containing at least one tau lepton, as well as with the semileptonic di-tau channel. The analysis is further limited by large systematic uncertainties, which are being reduced by dedicated measurements at the time of writing, yielding better knowledge of the luminosity, the jet and tau lepton energy measurement as well as the tau identification efficiency and fake rate. In addition, as of today the ATLAS experiment has collected roughly ten times the amount of data used

in this thesis, enabling SUSY searches with tau leptons to advance in SUSY parameter regions not probed before. Within the next two years, Supersymmetry can be expected to either be discovered at the LHC experiments, or constrained to parameter regions less attractive in the context of extending the Standard Model.

A. Monte Carlo Datasets

Pythia dijets		Alpgen Multijets	
label	p _T range (GeV)	label	p _T range (GeV)
J0	<17	M0	unsliced
J1	17-35	M1	100-200
J2	35-70	M2	200-500
J3	70-140	M3	500-1000
J4	140-280	M4	1000-2000
J5	280-560	M5	>2000
J6	560-1120		
J7	1120-2240		
J8	>2240		

Table A.1. – QCD jet p_Tbins employed in the event generation to cover a wide p_T spectrum.

A.1. Samples with $\sqrt{s} = 14$ TeV

A.1.1. SUSY benchmark points and SM background

MC datasets ($\sqrt{s} = 14$ TeV)				MC datasets ($\sqrt{s} = 14$ TeV)			
process		σ [pb]	$\int Ldt$ [fb $^{-1}$]	process		σ [pb]	$\int Ldt$ [fb $^{-1}$]
signal				W + Jets			
SU3		18.6	27	$W \rightarrow \tau\nu$	2	504	5.6
Z + Jets	$Z \rightarrow \tau\tau$	2	56.4		3	122	4.4
		3	14.1		4	28.4	5.2
		4	3.3		5	6.1	5.5
		5	0.7				
$Z \rightarrow \mu\mu$		2	56.4	$W \rightarrow \mu\nu$	3	122	5.8
		3	14.1		4	28.4	5.4
		4	3.3		5	6.1	6.6
		5	0.7				
$Z \rightarrow ee$		2	56.4	$W \rightarrow e\nu$	2	504	6.0
		3	14.1		3	122	4.7
		4	3.3		4	28.4	5.0
		5	0.7		5	6.1	5.0
$Z \rightarrow \nu\nu$		4	18.5	QCD			
		5	3.96	M1	3	$8.9 \cdot 10^5$	$1.4 \cdot 10^{-5}$
$t\bar{t}$					4	$1.1 \cdot 10^5$	$9.4 \cdot 10^{-5}$
	$t\bar{t} \rightarrow bb + l\nu l\nu$	0	49.4		5	$1.6 \cdot 10^4$	$6.3 \cdot 10^{-4}$
		1	32	M2	3	$7.1 \cdot 10^4$	$2.1 \cdot 10^{-4}$
		2	13		4	$3.3 \cdot 10^4$	$5.3 \cdot 10^{-4}$
$t\bar{t} \rightarrow bb + l\nu qq$		3	4.2		5	$9.7 \cdot 10^3$	$1.7 \cdot 10^{-3}$
		0	197.5	M3	3	964	0.02
		1	128		4	700	0.03
		2	32.4		5	331	0.05
$t\bar{t} \rightarrow bb + qq qq$		3	16.9	M4	3	18.7	1.1
		1	128		4	15.4	1.6
		2	52.4		5	8.3	1.9
		3	16.9				

(a) SU3, Z+jets, $t\bar{t}$

(b) W+jets, QCD

Table A.2. – Cross-sections σ and generated integrated luminosity $\int Ldt$ of MC samples with full detector simulation used in the $\sqrt{s} = 14$ TeV analysis.

A.2. Samples with $\sqrt{s} = 10$ TeV

A.2.1. SUSY benchmark points and SM background

MC datasets ($\sqrt{s} = 10$ TeV)			MC datasets ($\sqrt{s} = 10$ TeV)		
process	σ [pb]	$\int Ldt$ [fb $^{-1}$]	process	σ [pb]	$\int Ldt$ [fb $^{-1}$]
signal			W + Jets		
SU3	8.2	1.23	$W \rightarrow \tau\nu$ 0	12418	0.025
Z + Jets			1	2570.4	0.073
$Z \rightarrow \tau\tau$ 0	1101	0.13	2	820.8	0.22
1	255.3	0.25	3	249.6	0.67
2	85.6	1.37	4	69.3	0.85
3	25.7	2.32	5	22.4	0.78
4	7.37	2.51	$W \rightarrow \mu\nu$ 0	12353	0.025
5	2.09	2.63	1	2629.7	0.083
$Z \rightarrow \mu\mu$ 0	1098.3	0.13	2	832.7	0.32
1	250.4	0.25	3	248.7	0.72
2	84.6	1.44	4	69.6	0.85
3	26.4	2.34	5	21.5	0.81
4	7.42	2.49	$W \rightarrow e\nu$ 0	12425	0.031
5	2.07	2.64	1	2577.2	0.061
$Z \rightarrow ee$ 0	1096.1	0.13	2	824.8	0.36
1	252.0	0.25	3	250.4	0.71
2	88.5	1.37	4	70.1	0.84
3	25.7	2.34	5	21.8	0.80
4	7.32	2.50	QCD		
5	2.11	2.61	J0	$11.7 \cdot 10^9$	$1.8 \cdot 10^{-8}$
$Z \rightarrow \nu\nu$ 0	6409.9	0.90	J1	$8.9 \cdot 10^8$	$1.2 \cdot 10^{-7}$
1	1493.4	0.15	J2	$5.6 \cdot 10^7$	$3.4 \cdot 10^{-6}$
2	504.6	0.25	J3	$3.3 \cdot 10^6$	$7.1 \cdot 10^{-5}$
3	147.6	0.68	J4	$1.5 \cdot 10^5$	$6.2 \cdot 10^{-4}$
4	41.5	2.16	J5	5122	0.043
5	11.7	2.50	J6	111.9	0.51
$t\bar{t}$			J7	1.08	93.4
$t\bar{t}$ lep	217.1	2.19	J8	0.001	79.8
$t\bar{t}$ had	182.7	1.27			

(a) SU3, Z+jets, $t\bar{t}$

(b) W+jets, QCD

Table A.3. – Cross-sections σ and generated integrated luminosity $\int Ldt$ of MC samples used in the $\sqrt{s}=10\text{TeV}$ analysis.

A.2.2. mSUGRA grid ($\sqrt{s} = 10$ TeV)

$\tan\beta = 10, A_0 = 0$ GeV, $\text{sgn}(\mu) > 0$ (part 1)										
m_0 (GeV)	$m_{1/2}$ (GeV)	LO CS (pb)	$\int L dt$ (fb $^{-1}$)	$m(\tilde{\tau}_1)$ (GeV)	$m(\tilde{\tau}_2)$ (GeV)	$m(\tilde{\chi}_1^0)$ (GeV)	$m(\tilde{\chi}_2^0)$ (GeV)	$m(\tilde{\chi}_3^0)$ (GeV)	$m(\tilde{\chi}_4^0)$ (GeV)	$m_{\tau\tau}^{\max}$ (GeV)
2210	340	1.3	23.3	2193	2208	128	190	214	323	
1470	220	4.6	6.6	1458	1468	85	147	235	277	
1285	190	8.9	3.4	1275	1283	72	126	226	262	
1100	324	0.8	38.9	1066	1086	132	244	399	423	
1100	160	20.9	1.4	1091	1099	59	104	209	243	
1070	324	0.8	39.0	1066	1086	132	244	399	423	
970	292	1.4	22.2	967	985	118	217	369	393	
940	190	9.8	2.0	934	944	73	131	256	285	
915	130	61.9	0.5	908	914	45	81	188	220	
810	160	23.9	0.8	804	813	59	106	226	255	
770	228	5.2	5.8	767	782	90	163	305	330	
730	100	371.4	0.1	724	730	31	59	163	194	
690	380	0.6	16.9	697	733	155	290	480	499	
670	196	11.7	2.6	667	681	75	136	270	297	
635	345	1.0	9.6	641	674	140	261	442	462	
580	310	1.9	5.2	586	615	125	231	404	425	
570	165	30.1	1.0	568	579	61	109	234	262	
550	100	449.0	0.4	546	553	31	58	162	193	
525	275	3.7	2.7	530	556	109	202	364	387	
510	415	0.5	57.7	528	581	170	319	525	543	
470	240	7.6	2.6	474	497	94	172	324	348	
470	132	95.4	0.3	468	478	46	82	196	226	
450	380	0.9	34.5	486	535	154	289	486	505	
430	345	1.5	19.5	444	489	139	260	447	467	
415	205	17.0	1.2	418	439	79	142	283	209	
390	310	2.8	10.7	403	444	124	230	407	428	
370	100	828.1	0.04	369	378	30	57	157	189	
360	170	43.4	1.1	362	380	63	113	241	268	
350	275	5.4	5.5	361	398	109	201	367	389	
310	240	11.2	2.7	320	353	93	171	326	349	
305	135	137.7	0.7	307	322	47	84	198	228	
280	460	0.4	12.1	325	419	188	354	578	594	114
270	205	25.3	1.2	278	308	78	141	284	309	
260	420	0.7	6.9	301	387	171	321	534	551	92
250	100	1001.8	0.2	251	263	29	56	153	186	
240	380	1.3	7.8	276	354	153	287	489	507	66
230	170	65.0	0.5	237	263	62	112	241	268	
220	340	2.4	4.1	252	322	136	254	443	463	29

Table A.4. – mSUGRA grid ($\sqrt{s} = 10$ TeV) with $\tan\beta=10$, $A_0=0$ GeV, $\text{sgn}(\mu)>0$. LO cross sections, generated luminosity, stau and neutralino masses and endpoint given for $\tilde{\chi}_2^0 \rightarrow \tilde{\tau}_1 \tau \rightarrow \tilde{\chi}_1^0 \tau \tau$ if open.

$\tan\beta = 10, A_0 = 0$ GeV, $\text{sgn}(\mu) > 0$ (part 2)										
m_0 (GeV)	$m_{1/2}$ (GeV)	LO CS (pb)	$\int Ldt$ (fb $^{-1}$)	$m(\tilde{\tau}_1)$ (GeV)	$m(\tilde{\tau}_2)$ (GeV)	$m(\tilde{\chi}_1^0)$ (GeV)	$m(\tilde{\chi}_2^0)$ (GeV)	$m(\tilde{\chi}_3^0)$ (GeV)	$m(\tilde{\chi}_4^0)$ (GeV)	$m_{\tau\tau}^{\max}$ (GeV)
190	135	200.1	0.1	196	218	46	83	196	226	163
180	260	10.1	2.0	203	258	102	187	350	372	
160	220	23.3	0.9	179	226	84	153	302	326	
150	100	2817.8	0.01	155	174	29	55	151	184	
126	500	0.3	90.8	323	362	205	386	624	639	
120	140	208.3	1.0	131	164	48	86	202	231	122
119	460	0.5	54.8	207	336	188	353	579	595	
112	420	0.8	35.4	191	309	170	320	535	552	
105	380	1.5	20.1	175	282	153	286	489	507	
98	340	2.8	8.5	159	256	136	253	444	463	
91	300	5.5	5.5	144	230	118	220	397	418	94
84	260	11.6	2.6	128	204	101	186	350	372	83
77	220	26.9	1.1	113	178	84	153	301	325	69
70	180	71.6	0.4	98	153	66	119	252	279	50
63	140	234.2	0.1	84	129	48	86	202	231	14

Table A.5. – mSUGRA grid ($\sqrt{s}=10$ TeV) with $\tan\beta=10$, $A_0=0$ GeV, $\text{sgn}(\mu)>0$. LO cross sections, generated luminosity, stau and neutralino masses and endpoint given for $\tilde{\chi}_2^0 \rightarrow \tilde{\tau}_1 \tau \rightarrow \tilde{\chi}_1^0 \tau \tau$ if open.

$\tan\beta = 30, A_0 = 0$ GeV, $\text{sgn}(\mu) > 0$										
m_0 (GeV)	$m_{1/2}$ (GeV)	LO CS (pb)	$\int Ldt$ (fb $^{-1}$)	$m(\tilde{\tau}_1)$ (GeV)	$m(\tilde{\tau}_2)$ (GeV)	$m(\tilde{\chi}_1^0)$ (GeV)	$m(\tilde{\chi}_2^0)$ (GeV)	$m(\tilde{\chi}_3^0)$ (GeV)	$m(\tilde{\chi}_4^0)$ (GeV)	$m_{\tau\tau}^{\max}$ (GeV)
900	150	35.2	0.6	828	869	53	91	167	206	176
880	250	3.0	3.3	810	861	100	180	297	324	
790	200	9.0	2.2	727	771	78	138	246	274	
730	500	0.1	71.9	681	777	208	392	596	611	
700	150	36.5	1.9	643	680	55	96	193	223	
690	450	0.3	39.2	642	729	186	350	543	559	
650	400	0.5	20.4	602	682	164	308	490	506	
610	350	1.0	10.0	563	634	143	266	435	453	
570	300	2.3	4.4	525	587	121	224	379	399	
530	250	5.5	3.6	486	540	99	182	323	344	
490	200	15.6	1.3	450	495	78	140	265	289	
450	150	56.7	1.8	411	448	55	98	207	234	
250	500	0.3	37.0	259	421	206	389	614	627	
250	450	0.5	20.1	250	396	184	347	559	574	
250	400	1.0	10.4	243	372	163	306	503	519	
250	350	1.9	5.2	336	349	141	265	448	464	
250	300	4.3	2.3	230	328	120	223	391	409	
250	200	29.8	1.7	223	290	77	139	273	295	
250	150	103.1	0.8	223	274	55	97	212	237	

Table A.6. – mSUGRA grid ($\sqrt{s}=10$ TeV) with $\tan\beta=30$, $A_0=0$ GeV, $\text{sgn}(\mu)>0$. LO cross sections, generated luminosity, stau and neutralino masses and endpoint given for $\tilde{\chi}_2^0 \rightarrow \tilde{\tau}_1 \tau \rightarrow \tilde{\chi}_1^0 \tau \tau$ if open.

$\tan\beta = 30, A_0 = -400 \text{ GeV}, \text{sgn}(\mu) > 0$										
m_0 (GeV)	$m_{1/2}$ (GeV)	LO CS (pb)	$\int L dt$ (fb ⁻¹)	$m(\tilde{\tau}_1)$ (GeV)	$m(\tilde{\tau}_2)$ (GeV)	$m(\tilde{\chi}_1^0)$ (GeV)	$m(\tilde{\chi}_2^0)$ (GeV)	$m(\tilde{\chi}_3^0)$ (GeV)	$m(\tilde{\chi}_4^0)$ (GeV)	$m_{\tau\tau}^{\max}$ (GeV)
900	150	25.1	0.8	821	867	59	108	256	275	
880	250	2.8	3.6	802	859	102	191	372	389	
790	200	8.0	2.5	718	769	80	149	324	340	
730	500	0.1	76.9	670	774	209	397	664	675	
700	150	31.0	1.0	634	678	59	109	273	289	
690	450	0.2	40.6	630	726	187	355	612	624	
650	400	0.5	20.8	590	678	165	314	559	571	
610	350	1.0	10.1	551	631	144	272	505	518	
570	300	2.2	4.6	512	584	122	231	451	465	
530	250	5.3	3.7	473	538	101	190	397	411	
490	200	15.1	1.3	434	492	80	149	341	356	
450	150	53.4	1.9	396	446	58	108	285	300	
250	500	0.3	38.5	226	414	207	393	681	692	131
250	450	0.5	20.2	217	390	185	352	628	639	145
250	400	1.0	10.4	209	366	164	311	573	585	143
250	350	2.0	5.1	202	344	142	270	518	530	127
250	300	4.4	2.3	197	323	121	229	462	475	92
250	200	31.4	1.6	191	286	79	148	348	363	
250	150	112.6	0.8	192	271	58	107	290	306	

$\tan\beta = 30, A_0 = 400 \text{ GeV}, \text{sgn}(\mu) > 0$										
m_0 (GeV)	$m_{1/2}$ (GeV)	LO CS (pb)	$\int L dt$ (fb ⁻¹)	$m(\tilde{\tau}_1)$ (GeV)	$m(\tilde{\tau}_2)$ (GeV)	$m(\tilde{\chi}_1^0)$ (GeV)	$m(\tilde{\chi}_2^0)$ (GeV)	$m(\tilde{\chi}_3^0)$ (GeV)	$m(\tilde{\chi}_4^0)$ (GeV)	$m_{\tau\tau}^{\max}$ (GeV)
900	150	38.5	0.5	825	868	51	88	159	201	
880	250	3.2	3.1	808	860	98	173	269	302	
790	200	9.7	1.5	724	769	76	132	225	258	
730	500	0.1	70.1	681	776	207	387	550	569	
700	150	38.8	1.3	640	678	54	93	183	216	
690	450	0.3	38.0	642	728	185	345	500	520	
650	400	0.5	19.6	602	680	163	303	448	469	
610	350	1.0	9.6	562	632	142	261	396	419	
570	300	2.3	4.3	523	584	120	219	344	369	
530	250	5.7	3.5	484	537	98	176	293	319	
490	200	16.2	1.2	445	490	76	135	241	270	
450	150	59.3	1.6	406	444	54	94	194	223	
250	500	0.3	37.0	261	418	205	385	569	585	175
250	450	0.5	19.8	251	392	184	343	516	533	160
250	400	1.0	10.4	242	368	162	301	463	482	134
250	350	2.0	5.0	234	344	140	260	408	429	90
250	300	4.4	2.3	227	322	119	218	355	377	
250	200	30.1	1.5	217	282	76	134	247	274	
250	150	104.8	1.0	215	266	54	94	196	224	

Table A.7. – mSUGRA grid ($\sqrt{s}=10 \text{ TeV}$) with $\tan\beta=30$, $\text{sgn}(\mu)>0$ and $A_0=-400 \text{ GeV}$ (upper table) or $A_0=400 \text{ GeV}$ (lower table). LO cross sections, generated luminosity, stau and neutralino masses and endpoint given for $\tilde{\chi}_2^0 \rightarrow \tilde{\tau}_1 \tau \rightarrow \tilde{\chi}_1^0 \tau \tau$ if open.

$\tan\beta = 50, A_0 = 0 \text{ GeV}, \text{sgn}(\mu) > 0$										
m_0 (GeV)	$m_{1/2}$ (GeV)	LO CS (pb)	$\int L dt$ (fb $^{-1}$)	$m(\tilde{\tau}_1)$ (GeV)	$m(\tilde{\tau}_2)$ (GeV)	$m(\tilde{\chi}_1^0)$ (GeV)	$m(\tilde{\chi}_2^0)$ (GeV)	$m(\tilde{\chi}_3^0)$ (GeV)	$m(\tilde{\chi}_4^0)$ (GeV)	$m_{\tau\tau}^{\max}$ (GeV)
1100	160	61.0	0.5	815	971	44	84	118	186	
970	292	1.4	21.7	705	869	118	215	330	357	
915	130	177.9	0.2	675	807	37	70	120	172	
870	260	2.6	11.5	631	779	104	188	301	327	
770	228	5.3	5.7	557	690	90	162	273	300	
730	100	6747.0	0.004	537	644	26	53	114	156	
670	196	11.7	2.6	483	601	76	135	244	271	
570	164	30.2	1.0	410	512	62	109	213	240	
510	415	0.5	57.5	347	529	171	321	508	523	
470	380	0.9	34.5	317	489	155	291	470	486	
470	132	93.1	0.4	337	424	48	83	181	209	
430	345	1.5	39.0	286	450	140	262	432	450	
390	310	2.8	10.6	255	411	125	233	394	412	
370	100	505.5	0.1	264	336	32	57	145	175	
350	275	5.5	6.6	224	371	110	203	355	374	
310	240	11.3	4.2	192	333	95	174	316	336	
270	205	25.5	1.2	161	294	79	144	275	297	
230	170	64.3	0.6	130	255	64	115	234	258	
190	135	197.2	0.2	99	216	49	85	192	217	

$\tan\beta = 50, A_0 = -400 \text{ GeV}, \text{sgn}(\mu) > 0$										
m_0 (GeV)	$m_{1/2}$ (GeV)	LO CS (pb)	$\int L dt$ (fb $^{-1}$)	$m(\tilde{\tau}_1)$ (GeV)	$m(\tilde{\tau}_2)$ (GeV)	$m(\tilde{\chi}_1^0)$ (GeV)	$m(\tilde{\chi}_2^0)$ (GeV)	$m(\tilde{\chi}_3^0)$ (GeV)	$m(\tilde{\chi}_4^0)$ (GeV)	$m_{\tau\tau}^{\max}$ (GeV)
900	600	0.04	250.0	618	867	254	481	747	758	
895	300	1.2	8.2	629	801	123	232	414	430	
850	550	0.1	145.8	580	815	231	440	698	709	
800	500	0.1	82.6	543	763	210	398	647	659	
780	250	3.3	3.1	543	696	102	191	367	383	
750	450	0.2	44.2	505	711	188	356	596	608	
700	400	0.4	22.7	468	659	166	315	545	557	
665	200	10.1	2.0	456	591	80	149	319	335	
650	350	0.9	11.0	430	608	144	273	492	505	
600	300	2.1	4.8	393	556	123	232	439	452	
550	250	5.2	3.9	356	505	101	190	385	399	
550	150	41.1	1.2	369	487	59	109	270	286	
500	200	14.9	1.3	319	454	80	149	331	346	
450	150	53.7	1.9	284	404	59	109	276	291	
350	350	1.7	6.0	151	390	143	271	507	519	74
350	300	3.6	2.8	157	371	122	230	451	464	107
350	250	8.6	2.3	165	354	100	189	395	409	73
350	200	23.1	0.9	176	338	79	149	337	352	
350	150	75.4	1.3	188	324	58	108	280	295	

Table A.8. – mSUGRA grid ($\sqrt{s}=10$ TeV) with $\tan\beta=50$, $\text{sgn}(\mu)>0$ and $A_0=0$ GeV (upper table) or $A_0=-400$ GeV (lower table). LO cross sections, generated luminosity, stau and neutralino masses and endpoint given for $\tilde{\chi}_2^0 \rightarrow \tilde{\tau}_1 \tau \rightarrow \tilde{\chi}_1^0 \tau \tau$ if open.

$\tan\beta = 50, A_0 = 400 \text{ GeV}, \text{sgn}(\mu) > 0$										
m_0 (GeV)	$m_{1/2}$ (GeV)	LO CS (pb)	$\int L dt$ (fb ⁻¹)	$m(\tilde{\tau}_1)$ (GeV)	$m(\tilde{\tau}_2)$ (GeV)	$m(\tilde{\chi}_1^0)$ (GeV)	$m(\tilde{\chi}_2^0)$ (GeV)	$m(\tilde{\chi}_3^0)$ (GeV)	$m(\tilde{\chi}_4^0)$ (GeV)	$m_{\tau\tau}^{\max}$ (GeV)
900	600	0.04	228.8	641	872	252	472	641	659	
895	300	1.4	7.1	643	803	121	216	316	347	
850	550	0.1	134.6	603	819	230	430	592	610	
800	500	0.1	76.1	565	767	208	388	542	562	
780	250	3.7	2.7	557	698	99	175	273	304	
750	450	0.2	41.4	527	714	186	346	492	513	
700	400	0.5	21.3	490	662	164	303	442	464	
665	200	11.6	1.7	470	592	76	133	229	260	
650	350	1.0	10.2	452	610	142	261	391	414	
600	300	2.2	4.6	414	558	120	219	341	366	
550	250	5.5	3.7	377	506	98	177	290	316	
550	150	48.5	1.0	383	487	54	94	186	217	
500	200	16.0	1.3	340	454	76	135	238	266	
450	150	59.6	1.7	303	402	54	94	191	220	
350	500	0.2	41.0	216	457	206	386	565	581	96
350	450	0.4	22.6	212	434	184	344	512	529	135
350	400	0.9	11.8	210	411	163	303	459	477	138
350	350	1.7	5.9	208	390	141	261	405	426	115
350	300	3.7	2.7	209	370	119	219	352	374	54
350	250	8.7	2.3	210	352	98	177	298	322	
350	200	23.3	0.9	214	335	76	135	244	271	
350	150	78.0	1.3	219	320	54	94	193	222	

Table A.9. – mSUGRA grid ($\sqrt{s}=10 \text{ TeV}$) with $\tan\beta=50$, $A_0=400 \text{ GeV}$, $\text{sgn}(\mu)>0$. LO cross sections, generated luminosity, stau and neutralino masses and endpoint given for $\tilde{\chi}_2^0 \rightarrow \tilde{\tau}_1 \tau \rightarrow \tilde{\chi}_1^0 \tau \tau$ if open.

A.3. Samples with $\sqrt{s} = 7$ TeV

A.3.1. SUSY benchmark points and SM background

MC datasets ($\sqrt{s} = 7$ TeV)			MC datasets ($\sqrt{s} = 7$ TeV)		
process	σ [pb]	$\int Ldt$ [pb $^{-1}$]	process	σ [pb]	$\int Ldt$ [pb $^{-1}$]
signal			W + Jets		
SU11	9	2221	$W \rightarrow \tau\nu$ 0	8288.1	163
SU4	59.95	833	1	1550.1	164
GMSB6	0.42	23764	2	452.1	417
$t\bar{t}$			3	121.0	417
$t\bar{t}$ lep	89.40	8605	4	30.33	429
$t\bar{t}$ had	71.39	1626	5	8.27	483
Z + Jets			$W \rightarrow \mu\nu$ 0	8288.1	167
$Z \rightarrow \tau\tau$ 0	830.13	365	1	1550.1	165
1	166.2	382	2	452.1	416
2	50.28	388	3	121.0	421
3	13.92	395	4	30.33	428
4	3.62	415	5	8.27	423
5	0.942	530	$W \rightarrow e\nu$ 0	8288.1	167
$Z \rightarrow \mu\mu$ 0	830.13	366	1	1550.1	167
1	166.2	379	2	452.1	418
2	50.28	378	3	121.0	417
3	13.92	395	4	30.33	428
4	3.62	415	5	8.27	417
5	0.942	530	QCD		
$Z \rightarrow ee$ 0	830.13	366	J0	$9.75 \cdot 10^9$	$1.4 \cdot 10^{-4}$
1	166.2	382	J1	$6.73 \cdot 10^8$	$2.1 \cdot 10^{-3}$
2	50.28	388	J2	$4.12 \cdot 10^7$	0.034
3	13.92	395	J3	$2.19 \cdot 10^6$	0.64
4	3.62	415	J4	$8.78 \cdot 10^4$	15.9
5	0.942	531	J5	2329	597
di-boson			J6	33.8	39817
WW	11.75	21263	J7	0.137	$7.8 \cdot 10^6$
WZ	3.43	72794			
ZZ	0.977	255603			

(b) W+jets, QCD

(a) SUSY benchmark points, $t\bar{t}$, Z+jets, di-bosons

Table A.10. – Cross-sections σ and generated integrated luminosity $\int Ldt$ of MC samples used in the $\sqrt{s}=7$ TeV analysis.

A.3.2. mSUGRA grid ($\sqrt{s}=7$ TeV)

$\tan\beta=40, A_0=-500$ GeV, $\mu > 0$			
m_0 (GeV)	$m_{1/2}$ (GeV)	σ (pb)	$\int L dt$ (pb ⁻¹)
240	100	12581.7	0.79
240	130	235.3	42
240	160	54.5	183
280	100	494.0	20
280	130	119.8	83
280	160	40.9	243
280	190	16.8	595
280	220	7.76	1157
280	250	3.8	2627
280	280	2.02	4943
280	310	1.09	9162
320	100	239.2	42
320	130	80.9	123
320	160	31.7	316
320	190	14.0	715
320	220	6.68	1495
320	250	3.45	2880
320	280	1.84	5429
320	310	1	9979
320	340	0.58	17216
360	100	174.2	57
360	130	61.8	162
360	160	25.4	394
360	190	11.6	781
360	220	5.75	1736
360	250	2.95	3164
360	280	1.64	6085
360	310	0.9	11082
360	340	0.51	19575
400	100	141	71
400	130	49.8	200
400	160	21.2	471
400	190	9.72	1026
400	220	4.9	2037
400	250	2.55	3915
400	280	1.39	7150
400	310	0.81	12322
400	340	0.45	22180
440	100	120.3	83
440	130	41.8	239
440	160	17.9	559
440	190	8.18	1221

(a) $240 \text{ GeV} \leq m_0 \leq 440 \text{ GeV}$

$\tan\beta=40, A_0=-500$ GeV, $\mu > 0$			
m_0 (GeV)	$m_{1/2}$ (GeV)	σ (pb)	$\int L dt$ (pb ⁻¹)
440	220	4.15	2407
440	250	2.2	4539
440	280	1.24	8049
440	310	0.72	13867
440	340	0.39	25590
520	100	94.2	106
520	130	31.2	320
520	160	13.2	755
520	190	6.14	1625
520	220	3.11	3211
520	250	1.66	6011
520	280	0.95	10505
520	310	0.54	18489
520	340	0.32	31178
600	100	81.4	123
600	130	24.8	403
600	160	9.89	1010
600	190	4.7	2122
600	220	2.32	4303
600	250	1.24	8048
600	280	0.71	14061
600	310	0.41	24232
600	340	0.22	45355
680	100	70.9	140
680	130	21.4	466
680	160	8.29	1204
680	190	3.59	2781
680	220	1.81	5512
680	250	0.93	10734
680	280	0.54	18398
680	310	0.3	33267
680	340	0.18	55433
760	100	63.9	156
760	130	18.6	537
760	160	6.96	1435
760	190	3.05	3272
760	220	1.4	7129
760	250	0.74	13478
760	280	0.41	24339
760	310	0.24	41588
760	340	0.14	42757

(b) $440 \text{ GeV} \leq m_0 \leq 760 \text{ GeV}$ **Table A.11.** – Cross-sections σ and generated integrated luminosity $\int L dt$ for mSUGRA grid points with $\tan\beta=40$, $A_0=-500$ GeV, $\mu > 0$ and a center-of-mass energy of $\sqrt{s}=7$ TeV.

B. Supplementing material

B.1. Addition to chapter 5

B.1.1. Cut-flow ($\sqrt{s} = 10$ TeV)

process	selection step					
	ΔR	EF	\cancel{E}_T	$\Delta\Phi(E_T^{miss}, \text{jet1})$	H_T	2 jets ($p_T > 40$ GeV)
SU3	49 ± 3	45 ± 3	29 ± 2	27 ± 2	20 ± 2	19.6 ± 1.8
$t\bar{t}$	725 ± 11	239 ± 6	6.0 ± 0.9	5.8 ± 0.9	2.3 ± 0.6	2.3 ± 0.6
W+jets	9916 ± 180	569 ± 22	11.1 ± 2	9.9 ± 1.8	1.2 ± 0.5	0.7 ± 0.4
Z+jets	5259 ± 62	281 ± 9	1.9 ± 0.4	1.9 ± 0.4	0.9 ± 0.3	0.7 ± 0.2
QCD	$(1.2 \pm 0.4) \cdot 10^7$	2346 ± 851	0	0	0	0
ΣBG	$(1.2 \pm 0.4) \cdot 10^7$	3435 ± 851	19 ± 2	17 ± 2	4.4 ± 0.8	3.7 ± 0.7

(a) Events selected in the fully hadronic (hh) channel, 200 pb^{-1} .

process	selection step					
	ΔR	EF	\cancel{E}_T	$\Delta\Phi(E_T^{miss}, \text{jet1})$	H_T	2 jets ($p_T > 40$ GeV)
SU3	53 ± 3	47 ± 3	17.6 ± 1.8	17.1 ± 1.7	14.5 ± 1.5	14.3 ± 1.5
$t\bar{t}$	1794 ± 15	756 ± 10	1.2 ± 0.4	1.2 ± 0.4	1.0 ± 0.4	0.9 ± 0.3
W+jets	36366 ± 344	2096 ± 45	2.0 ± 0.7	1.8 ± 0.7	1.5 ± 0.6	1.5 ± 0.6
Z+jets	8418 ± 79	526 ± 13	0.3 ± 0.2	0.3 ± 0.2	0.14 ± 0.10	0.14 ± 0.10
QCD	$(1.5 \pm 0.8) \cdot 10^5$	10 ± 6	0	0	0	0
ΣBG	$(2.0 \pm 0.8) \cdot 10^5$	3387 ± 48	3.6 ± 0.8	3.2 ± 0.8	2.6 ± 0.7	2.6 ± 0.7

(b) Events selected in the semileptonic (hl) channel, 200 pb^{-1} .

process	selection step					
	ΔR	EF	\cancel{E}_T	$\Delta\Phi(E_T^{miss}, \text{jet1})$	H_T	2 jets ($p_T > 40$ GeV)
SU3	11.2 ± 1.4	9.1 ± 1.2	6.0 ± 1.0	6.0 ± 1.0	4.6 ± 0.9	4.6 ± 0.9
$t\bar{t}$	799 ± 10	354 ± 7	3.5 ± 0.7	3.3 ± 0.7	2.1 ± 0.5	2.1 ± 0.5
W+jets	1120 ± 61	69 ± 9	0.2 ± 0.2	0.2 ± 0.2	0	0
Z+jets	436 ± 18	44 ± 4	0.35 ± 0.16	0.35 ± 0.16	0.08 ± 0.08	0.08 ± 0.08
QCD	$(3 \pm 3) \cdot 10^{-6}$	$(3 \pm 3) \cdot 10^{-6}$	0	0	0	0
ΣBG	2355 ± 64	467 ± 11	4.1 ± 0.8	3.9 ± 0.7	2.2 ± 0.5	2.2 ± 0.5

(c) Events selected in the fully leptonic (ll) channel, 200 pb^{-1} .

Table B.1. – Detailed cut flows (10 TeV selections): events expected with 200 pb^{-1} .

B.1.2. Significance Z_n in different mSUGRA regions ($\sqrt{s} = 10$ TeV selection)

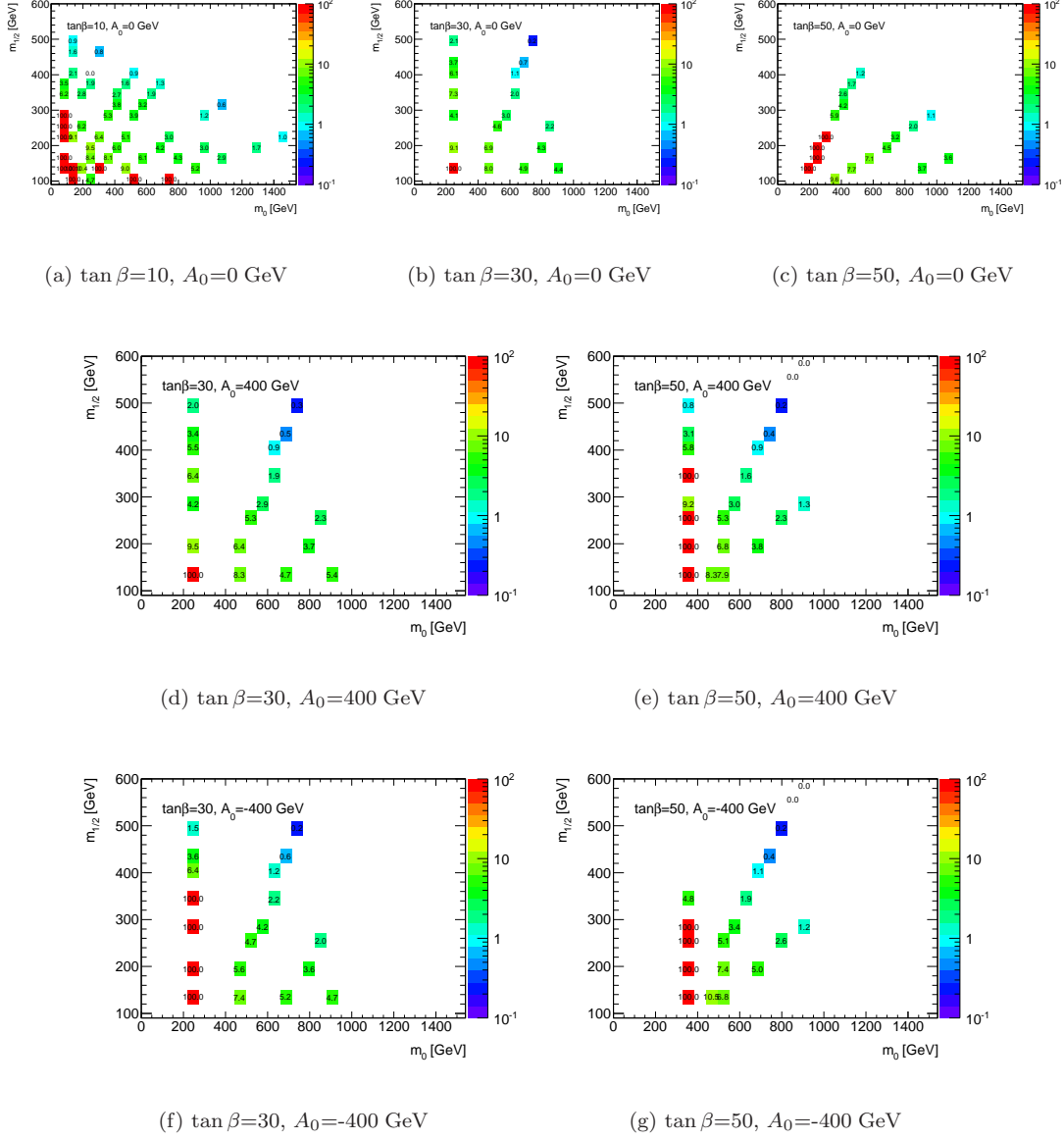


Figure B.1. – Z_n values including 30 % systematic BG uncertainty for fixed $\int L dt = 1 \text{ fb}^{-1}$.

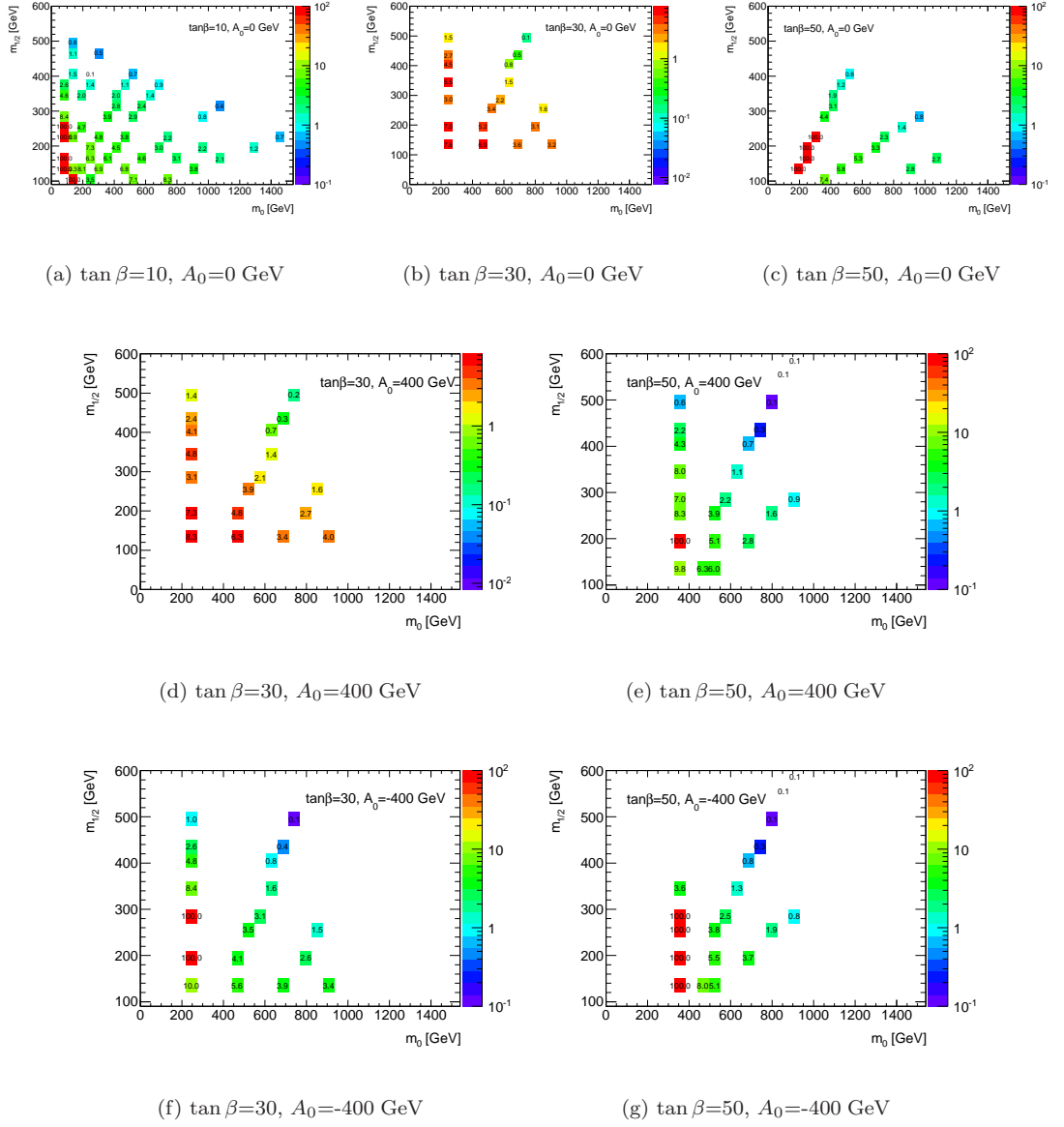


Figure B.2. – Z_n values including 50% systematic BG uncertainty for fixed $\int L dt = 1 \text{ fb}^{-1}$.

B.2. Addition to chapter 6

B.2.1. Systematic uncertainties and cut-flow ($\sqrt{s} = 7$ TeV)

sample	vetos	stat	JES +	JES -	JER	TES +	TES -	TER	ϵ_τ +	ϵ_τ -	f_τ +	f_τ -
SU11	n	± 0.22	+0.25	-0.46	-0.16	+0.13	-0.14	± 0	+0.22	-0.28	+0.36	-0.49
	y	± 0.18	+0.20	-0.32	-0.08	+0.08	-0.09	+0.08	+0.19	-0.19	+0.28	-0.28
SU4	n	± 0.31	+0.63	-0.59	-0.04	+0.13	-0.29	-0.08	+0.04	-0.08	+0.75	-0.71
	y	± 0.24	+0.42	-0.34	-0.08	+0.08	-0.25	-0.08	+0.04	-0.08	+0.46	-0.50
GMSB6	n	± 0.04	+0.06	-0.07	+0.015	+0.02	-0.019	+0.007	+0.07	-0.08	+0.02	-0.04
	y	± 0.04	+0.05	-0.05	+0.019	+0.009	-0.013	+0.003	+0.06	-0.07	+0.02	-0.04
ttbar	n	± 0.04	+0.09	-0.11	+0.004	+0.03	-0.008	+0.008	+0.004	-0.08	+0.09	-0.10
	y	± 0.03	+0.08	-0.09	+0.012	+0.02	-0.008	± 0	+0.004	-0.08	+0.09	-0.08
W+jets	n	± 0.12	+0.17	+0.08	+0.25	± 0	± 0	± 0	± 0	± 0	+0.15	-0.08
	y	± 0.12	+0.17	+0.08	+0.25	± 0	± 0	± 0	± 0	± 0	+0.15	-0.08
Z+jets	n	± 0	+0.08	± 0	+0.08	± 0	± 0	± 0	± 0	± 0	± 0	± 0
	y	± 0	± 0	± 0	+0.08	± 0	± 0	± 0	± 0	± 0	± 0	± 0
Di-boson	n	± 0.002	+0.003	± 0	+0.002	+0.002	± 0	-0.00014	± 0	± 0	± 0	-0.002
	y	± 0.002	+0.002	± 0	+0.002	+0.002	± 0	-0.00014	± 0	± 0	± 0	-0.002
Sum nonQCD	n	± 0.12	+0.35	-0.028	+0.34	+0.030	-0.008	+0.008	+0.004	-0.08	+0.25	-0.18
	y	± 0.12	+0.25	-0.004	+0.35	+0.022	-0.008	-0.00014	+0.004	-0.08	+0.24	-0.16
QCD (J3-J7)	n	± 0.10	+0.24	-0.002	+0.006	+0.004	-0.06	+0.002	± 0	± 0	+0.024	-0.19
	y	± 0.08	+0.24	-0.002	+0.005	+0.004	-0.06	+0.002	± 0	± 0	+0.024	-0.13

Table B.2. – Systematic uncertainties: absolute difference of selected events with 35 pb^{-1} before and after 1-tau veto, for jet energy scale (JES), jet energy resolution (JER), tau energy scale (TES), tau energy resolution (TER), tau identification efficiency (ϵ_τ) and fake rate (f_τ).

cuts	signal			background				
	SU11	SU4	GMSB6	ttbar	W+jets	Z+jets	di-Boson	QCD (J0-J7)
-	315±2	2098±9	14.7±0.1	5628±9	$(1.0972 \pm 0.0005) \cdot 10^6$	111838±103	567.3±0.9	$(3.664 \pm 0.003) \cdot 10^{11}$
trigger	216±2	1327±7	9.8±0.1	1615±4	11501±39	1430±11	64.7±0.3	$(4.46 \pm 0.03) \cdot 10^6$
event cleaning	215±2	1321±7	9.6±0.1	1599±4	11363±38	1394±11	63.2±0.3	$(4.46 \pm 0.03) \cdot 10^6$
$\cancel{E}_T > 100$ GeV	184±2	975±6	7.7±0.1	359±1	3097±20	80±3	13±0.1	7648±216
$p^{\text{jet1}} > 120$ GeV	174±2	881±6	6.5±0.1	251±1	2051±16	57±2	7.8±0.1	7029±168
$\geq 1 \tau$	45.2±0.8	132±2	4.57±0.08	50.3±0.5	241 ±5	18 ±1	0.77 ±0.03	740±100
$\geq 2 \tau$	6.5±0.3	9.7±0.6	2.02±0.05	3.8±0.1	5.9±0.7	2.1±0.4	0.03 ±0.006	9±3
$H_T > 450$ GeV	5.3±0.3	5.7±0.5	1.8 ±0.05	1.3 ±0.09	1.4±0.3	0.4±0.2	0.005±0.002	7±2
$\cancel{E}_T > 200$ GeV	3.2±0.2	2.4±0.3	1.4 ±0.04	0.31±0.04	0.17±0.12	0±0	0.002±0.002	0.23±0.10
veto 1-tau	2.1±0.2	1.5±0.2	1.14±0.04	0.25±0.03	0.17±0.12	0±0	0.002±0.002	0.18±0.08
veto lep-had	2.1±0.2	1.4±0.2	1.11±0.04	0.25±0.03	0.17±0.12	0±0	0.002±0.002	0.18±0.08

Table B.3. – Cut-flow (events normalized to 35 pb⁻¹).

C. mSUGRA limits

C.1. Limits from B decays

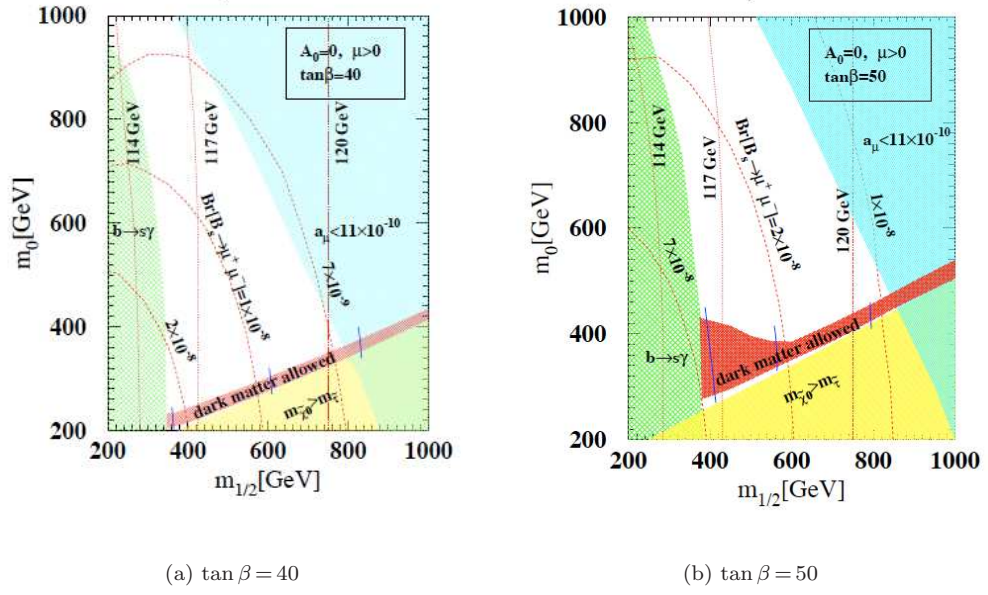
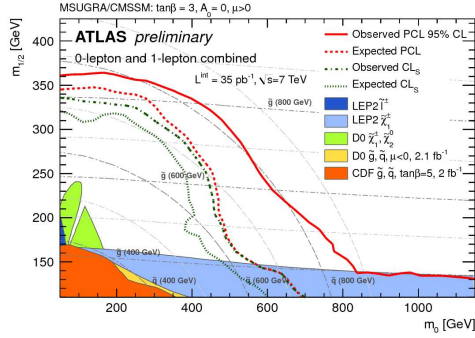
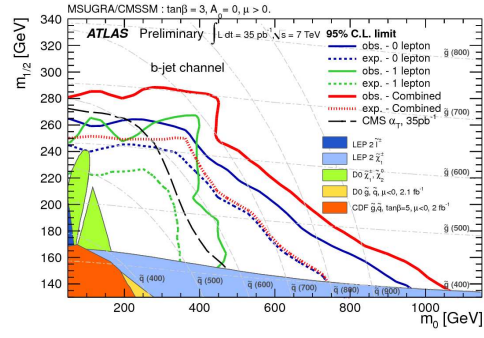


Figure C.1. – m_0 - $m_{1/2}$ plain for $\tan\beta=40$ (a) and $\tan\beta=50$ (b), $A_0=0$ and $\mu > 0$ with exclusions by $b \rightarrow s\gamma$, stau LSP or a_μ . From [16].

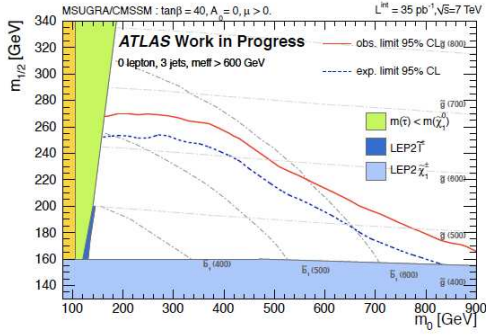
C.2. Limits from other ATLAS SUSY search channels



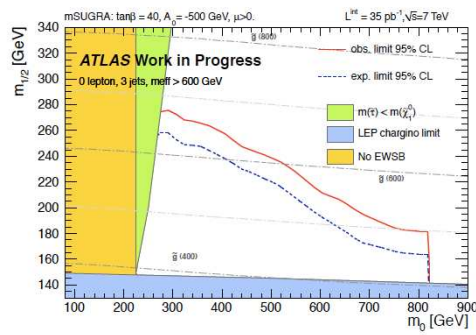
(a) Combined exclusion of ATLAS SUSY searches with 0 and 1 lepton(s), $\tan\beta = 3$, $A_0 = 0$ GeV. [130]



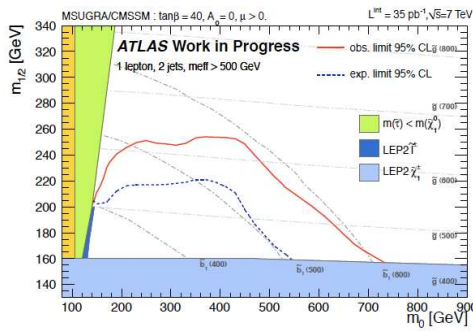
(b) Exclusion by ATLAS SUSY searches with b-jets, $\tan\beta = 3$, $A_0 = 0$ GeV [129].



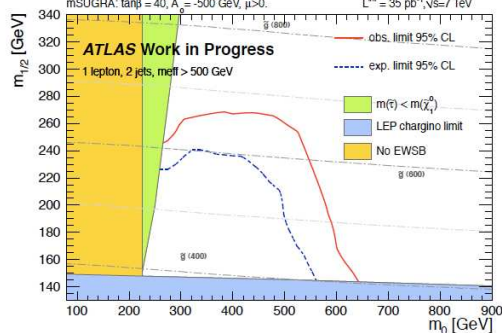
(c) Expected and observed limits ATLAS SUSY searches with b-jets, 0 lepton subchannel, $\tan\beta = 40$, $A_0 = 0$ GeV [129].



(d) Expected and observed limits ATLAS SUSY searches with b-jets, 0 lepton subchannel, $\tan\beta = 40$, $A_0 = -500$ GeV [129].



(e) Expected and observed limits ATLAS SUSY searches with b-jets, 1 lepton subchannel, $\tan\beta = 40$, $A_0 = 0$ GeV [129].



(f) Expected and observed limits ATLAS SUSY searches with b-jets, 1 lepton subchannel, $\tan\beta = 40$, $A_0 = -500$ GeV [129].

Figure C.2. – Exclusion by ATLAS SUSY searches with b-jets, light jets or light leptons in combination with missing transverse energy for positive higgsino mixing parameter, using 2010 ATLAS data.

D. One-tau and semileptonic event selection

The three SUSY search channels with tau leptons use the same baseline definitions regarding data quality, event cleaning, object definition and overlap removal. The two channels without light lepton use the same trigger and according preselection cuts on \cancel{E}_T and the leading jet p_T , while the semileptonic search uses lepton triggers. Differences arise in the tightness of the tau identification, as well as in the event selection since the different channels are naturally susceptible to a different SM background composition.

D.1. Tau identificaon

The 1-tau inclusive and semileptonic search channels use the same tau lepton identification, which differs from the tau definition used in the di-tau selection in the following aspects:

- BDT>0.7 for both 1-prong and 3-prong tau leptons
- $E_T > 20$ GeV
- electronVeto tight
- additional requirement on the energy fraction in the EM calorimeter: $E_T^{\text{EM}} / (E_T^{\text{EM}} + E_T^{\text{HAD}}) < 0.95$

D.2. SUSY event selection

D.2.1. One-tau channel

Events are selected in the 1-tau channel if they fulfill the following requirements:

- trigger: EF_j75_jetNoEF_EFxe25_noMu, $\cancel{E}_T > 100$ GeV, $p_T^{\text{jet1}} > 120$ GeV
- ≥ 1 tau lepton, no e or μ (light lepton veto)
- $p_T^{\text{jet2}} > 30$ GeV
- $\Delta\Phi(E_T^{\text{miss}}, \text{jet1}) > 0.4$, $\Delta\Phi(E_T^{\text{miss}}, \text{jet2}) > 0.4$ and $\Delta\Phi(E_T^{\text{miss}}, \tau) > 0.1$
- $\cancel{E}_T / M_{\text{eff}} > 0.25$
- $m_T(\tau, E_T^{\text{miss}}) > 100$ GeV

If there are several tau leptons present in one event, the one with the highest transverse energy is chosen to compute the transverse mass as well as the angular separation to the missing transverse energy.

Period	Trigger
tau+e channel	
MC simulation	EF_e10_medium
D	EF_e10_loose
E	EF_g17_etcut
F-I	EF_e15_medium
tau+ μ channel	
MC simulation	EF_mu10_MSonly
D	L1_mu6
E-F	EF_mu10_MSonly
G-H	EF_mu13
I	EF_mu13_tight

Table D.1. – Trigger items used in the semileptonic channel.

D.2.2. Semileptonic channel

Events are selected in the semileptonic channel if they fulfill the following requirements for either the muon channel ($\tau\mu$) or the electron channel (τe):

- trigger: different trigger items are used in different run periods, see table D.1
- exactly one tau and exactly one electron or muon
- $\cancel{E}_T > 150 / 140$ GeV ($\tau e / \tau\mu$)
- $p_T^{\text{jet}2} > 45$ GeV (τe), or $p_T^{\text{jet}1} > 40$ GeV and $p_T^{\text{jet}2} > 20$ GeV ($\tau\mu$)
- $M_{eff} > 200 / 440$ GeV ($\tau e / \tau\mu$)
- $\cancel{E}_T / M_{eff} > 0.3 / 0.24$ ($\tau e / \tau\mu$)
- $m_T(\tau, E_T^{miss}) > 60 / 40$ GeV ($\tau e / \tau\mu$)

Electrons and muons are required to have a transverse momentum of at least 20 GeV in order to be selected.

List of Figures

2.1. Hierarchy problem and unification of coupling constants	7
2.2. B / L violating couplings and proton decay	10
2.3. FCNCs in the MSSM	12
2.4. mSUGRA limits from B decays	13
2.5. Strong SUSY pair production at the LHC	17
2.6. SUSY signal and SUSY background	17
3.1. LHC acceleration chain	22
3.2. Proton-proton collisions	24
3.3. The ATLAS Detector	25
3.4. The ATLAS inner detector	26
3.5. The ATLAS Calorimeter System	28
3.6. The ATLAS Muon Spectrometer	30
4.1. Event generation and hadronization models	34
4.2. Tau identification performance: release comparison	42
4.3. Tau identification performance in $\sqrt{s} = 7$ TeV MC	43
4.4. Missing transverse energy resolution	47
5.1. Tau sources in supersymmetric processes.	50
5.2. Invariant mass and transverse momenta of signal tau leptons	51
5.3. Calibration and fit of invariant mass spectrum	56
5.4. Trigger efficiencies ($\sqrt{s} = 14$ TeV)	57
5.5. ΔR of two tau leptons	60
5.6. Selection cuts ($\sqrt{s} = 10$ TeV): N-1 spectra	62
5.7. Trigger efficiencies ($\sqrt{s} = 10$ TeV)	64
5.8. Cut flow ($\sqrt{s} = 10$ TeV selection)	64
5.9. Invariant mass fits ($\sqrt{s} = 10$ TeV)	66
5.10. Systematic uncertainties ($\sqrt{s} = 10$ TeV)	68
5.11. Invariant mass spectra: 3-body vs 2-body decays	70
5.12. Invariant mass spectra: 3-body vs 2-body decays (MC truth)	71
5.13. OS+SS spectrum shape	71
5.14. Unbinned maximum likelihood fit results	73
5.15. Toy MC for unbinned likelihood fit method	74
5.16. Discovery potential of mSUGRA ($\sqrt{s} = 10$ TeV)	76
5.17. Discovery reach in mSUGRA ($\sqrt{s} = 10$ TeV)	77
6.1. Tau identification with BDT ($\sqrt{s} = 7$ TeV)	84
6.2. Trigger efficiencies ($\sqrt{s} = 7$ TeV)	86
6.3. Event cleaning and missing transverse energy	88
6.4. Event selection ($\sqrt{s} = 7$ TeV)	90
6.5. Origin of tau leptons	91
6.6. MC validation: tau identification variables	93
6.7. MC validation: tau identification variables (2)	94
6.8. QCD sideband definition	95

6.9. QCD control regions	97
6.10. Signal-like sidebands	98
6.11. MC validation: \cancel{E}_T in control regions	98
6.12. MC validation: H_T in control regions	99
6.13. MC validation: \cancel{E}_T / M_{eff} in control regions	100
6.14. MC validation: $S_{\cancel{E}_T}$ in control regions	101
6.15. Definition of non-QCD region.	102
6.16. Standard Model background composition in control regions	102
6.17. MC validation: non-QCD control region	103
6.18. Relative jet energy uncertainties due to energy scale and resolution.	105
6.19. Number of vertices with ≥ 3 tracks in data and $t\bar{t}$ MC simulation.	108
6.20. Systematic uncertainties: pile-up ($\sqrt{s} = 7$ TeV)	108
6.21. mSUGRA sensitivity ($\sqrt{s} = 7$ TeV selection)	110
6.22. Signal systematic uncertainties as function of m_0 and $m_{1/2}$	111
6.23. MC description versus data in signal region.	113
6.24. Event displays of selected data events	114
6.25. Limits on mSUGRA parameters	116
6.26. Limits on mSUGRA parameters, comparison with b-jet search	117
6.27. Luminosity development in 2011	118
 B.1. Z_n values including 30 % systematic BG uncertainty for fixed $\int Ldt = 1 \text{ fb}^{-1}$. . .	136
B.2. Z_n values including 50 % systematic BG uncertainty for fixed $\int Ldt = 1 \text{ fb}^{-1}$. . .	137
 C.1. mSUGRA limits from B decays	141
C.2. mSUGRA limits from ATLAS SUSY searches	142

List of Tables

2.1. SM particles	4
2.2. MSSM chiral and gauge multiplets	8
2.3. mSUGRA benchmark points	15
3.1. LHC beam parameters	23
3.2. ATLAS detector performance (uptime 2010)	31
4.1. Object definition differences $\sqrt{s}=10/7$ TeV	48
5.1. SU3 characteristics	50
5.2. Calibration results	58
5.3. Cut flows ($\sqrt{s}=10$ TeV selection) and significances	63
5.4. SS to OS ratio and fake tau leptons	66
5.5. Systematic uncertainties ($\sqrt{s}=10$ TeV)	70
5.6. mSUGRA point labels ($\sqrt{s}=10$ TeV)	78
5.7. Endpoint results for different mSUGRA points ($\sqrt{s}=10$ TeV)	78
6.1. ATLAS data 2010	82
6.2. Tau identification performance in SUSY events ($\sqrt{s}=7$ TeV)	83
6.3. Tau identification performance ($\sqrt{s}=7$ TeV)	85
6.4. Cut flow ($\sqrt{s}=7$ TeV selection)	91
6.5. Data-driven QCD estimation	96
6.6. Systematic uncertainties: jet and tau energy ($\sqrt{s}=7$ TeV)	106
6.7. Systematic uncertainties: tau identification ($\sqrt{s}=7$ TeV)	107
6.8. Systematic uncertainties: overview ($\sqrt{s}=7$ TeV)	108
6.9. Cut flow: expected and observed ($\sqrt{s}=7$ TeV selection)	112
6.10. Properties of selected data events	115
6.11. Limits on SUSY benchmark points	115
A.1. QCD jets p_T slicing	123
A.2. MC samples: SUSY benchmark points and SM background, $\sqrt{s}=14$ TeV	124
A.3. MC samples: SUSY benchmark points and SM background, $\sqrt{s}=10$ TeV	125
A.4. MC samples: mSUGRA grid points, $\tan\beta=10$, $A_0=0$ GeV, $\sqrt{s}=10$ TeV	126
A.5. MC samples: mSUGRA grid points, $\tan\beta=10$, $A_0=0$ GeV, $\sqrt{s}=10$ TeV (part 2)	127
A.6. MC samples: mSUGRA grid points, $\tan\beta=30$, $A_0=0$ GeV, $\sqrt{s}=10$ TeV	127
A.7. MC samples: mSUGRA grid points, $\tan\beta=30$, $A_0=\pm 400$ GeV, $\sqrt{s}=10$ TeV	128
A.8. MC samples: mSUGRA grid points, $\tan\beta=50$, $A_0=(0/-400)$ GeV, $\sqrt{s}=10$ TeV	129
A.9. MC samples: mSUGRA grid points, $\tan\beta=50$, $A_0=400$ GeV, $\sqrt{s}=10$ TeV	130
A.10. MC samples: SUSY benchmark points and SM background, $\sqrt{s}=7$ TeV	131
A.11. MC samples: mSUGRA grid points, $\tan\beta=40$, $A_0=-500$ GeV, $\sqrt{s}=7$ TeV	132
A.12. MC samples: mSUGRA grid points, $\tan\beta=40$, $A_0=0$ GeV, $\sqrt{s}=7$ TeV	133
B.1. Detailed cut flows (10 TeV selections)	135
B.2. Systematic uncertainties (7 TeV selection)	138
B.3. Detailed cut flows (7 TeV selections)	139

D.1. Trigger items used in the semileptonic channel	144
---	-----

Bibliography

- [1] F. Halzen and A. D. Martin, “Quarks and leptons: an introductory course in modern particle physics.”, 1984.
- [2] D. J. Griffiths, “Introduction to Elementary Particles; 1st ed.”, 1987.
- [3] S. P. Martin, “A supersymmetry primer.”, 1997. [arXiv:hep-ph/9709356](#).
- [4] H. W. Baer and X. Tata, “Weak scale supersymmetry: from superfields to scattering events.”, 2006.
- [5] L. Reina, “TASI 2004 Lecture Notes: Higgs Boson Physics.” (FSU-HEP-2005-12-30), Dec 2005. [arXiv:hep-ph/0512377](#).
- [6] G. Abbiendi, “Search for the Standard Model Higgs Boson at LEP.” *Phys. Lett. B*, vol. 565 (CERN-EP-2003-011. CERN-L3-271), pp. 61–75. 22 p, Mar 2003. [arXiv:hep-ex/0306033](#).
- [7] B. Penning, “High Mass Higgs Boson Searches at the Tevatron.”, Nov 2010. Proceedings to the 21st Hadron Collider Physics Symposium 2010, Toronto, CA, [arXiv:hep-ex/1011.6307](#).
- [8] H. Flächer *et al.*. URL <http://project-gfitter.web.cern.ch/project-gfitter/GSM/>.
- [9] D. Ludwig, “The global electroweak fit and constraints on new physics with Gfitter.” *ICHEP*, p. 404. 4 p, Oct 2010. Contribution to the 35th International Conference on High Energy Physics, Paris, France, 22 - 28 July 2010, [hep-ph/1010.5678](#).
- [10] E. Komatsu, *et al.*, “Seven-Year Wilkinson Microwave Anisotropy Probe (WMAP) Observations: Cosmological Interpretation.” *ApJS*, vol. 192, Jan 2010. Submitted to Astrophysical Journal Supplement Series, [arXiv:astro-ph/1001.4538](#).
- [11] R. L. Arnowitt and P. Nath, “Supersymmetry and Supergravity: Phenomenology and Grand Unification.” (CTP-TAMU-93-52. NUB-TH-3073. SSCL-Preprint-503), Sep 1993. [arXiv:hep-ph/9309277](#).
- [12] R. Barbier, *et al.*, “R-parity violating supersymmetry.”, 2004. [arXiv:hep-ph/0406039](#).
- [13] H. K. Dreiner, C. Luhn, H. Murayama, and M. Thormeier, “Baryon triality and neutrino masses from an anomalous flavor U(1).” *Nuclear Physics B*, vol. 774 (1-3), pp. 127 – 167, 2007. ISSN 0550-3213.
- [14] M. Drees, “An Introduction to Supersymmetry.” (APCTP-96-05. KEK-TH-501), Nov 1996. [arXiv:hep-ph/9611409](#).
- [15] R. L. Arnowitt and B. Dutta. “Search for $B_s \rightarrow \mu^+ \mu^-$ and $B_d \rightarrow \mu^+ \mu^-$ Decays in 2 fb⁻¹ of pp Collisions with CDF II.” CDF Public Note 8956.
- [16] R. L. Arnowitt, B. Dutta, T. Kamon, and M. Tanaka, “Detection of $B_s \rightarrow \mu^+ \mu^-$ at the Tevatron Run II and Constraints on the SUSY Parameter Space.” *Phys. Lett. B*, vol. 538 (CTP-TAMU-2002-02), pp. 121–129. 12 p, Mar 2002. [arXiv:hep-ph/0203069](#).

- [17] T. A. Collaboration, “Absolute Lower Limits on the Masses of Selectrons and Sneutrinos in the MSSM.” *Phys. Lett. B*, vol. 544 (CERN-EP-2002-055), pp. 73–88. 23 p, Jul 2002. [arXiv:hep-ex/0207056](#).
- [18] V. Abazov *et al.* (D0), “Search for neutral Higgs bosons in the multi-b-jet topology in 5.2 fb^{-1} of $p\bar{p}$ collisions at $\sqrt{s} = 1.96 \text{ TeV}$.” (FERMILAB-PUB-10-446-E), Nov 2010. Submitted to *Phys. Lett. B*, [arXiv:hep-ex/1011.1931](#).
- [19] V. Abazov *et al.* (D0), “Search for charged Higgs bosons in top quark decays.” *Physics Letters B*, vol. 682 (FERMILB-PUB-09-393-E), pp. 278 – 286, 2009. ISSN 0370-2693. [arXiv:hep-ex/0908.1811](#).
- [20] V. Abazov *et al.* (D0), “Search for associated production of charginos and neutralinos in the trilepton final state using 2.3 fb^{-1} of data.” *Physics Letters B*, vol. 680 (FERMILAB-PUB-09-003-E), pp. 34 – 43, 2009. ISSN 0370-2693. [arXiv:hep-ex/0901.0646](#).
- [21] J. Strologas (CDF collaboration), “Search for trilepton SUSY signal at CDF.” *AIP Conference Proceedings*, vol. 1200, pp. 275–278, Oct 2009. Proceedings of the 17th International Conference on Supersymmetry and the Unification of Fundamental Interactions (SUSY 09), Boston MA, USA, June 5-10, 2009., [arXiv:hep-ex/0910.1889](#).
- [22] V. Abazov *et al.* (D0), “Search for squark production in events with jets, hadronically decaying tau leptons and missing transverse energy at $\sqrt{s} = 1.96 \text{ TeV}$.” *Physics Letters B*, vol. 680 (FERMILAB-PUB-09-268-E), pp. 24 – 33, 2009. ISSN 0370-2693. [arXiv:hep-ex/0905.4086](#).
- [23] V. Abazov *et al.* (D0), “Search for squarks and gluinos in events with jets and missing transverse energy using 2.1 fb^{-1} of $p\bar{p}$ collision data at $\sqrt{s} = 1.96 \text{ TeV}$.” *Phys. Lett. B*, vol. 660 (FERMILAB-PUB-07-668-E. 5), pp. 449–457, Dec 2007. [arXiv:hep-ex/0712.3805](#).
- [24] T. Aaltonen *et al.* (CDF), “Inclusive Search for Squark and Gluino Production in $p\bar{p}$ Collisions at $\sqrt{s} = 1.96 \text{ TeV}$.” *Phys. Rev. Lett.*, vol. 102, p. 121801, 2009. [0811.2512](#).
- [25] H. F. A. Group, “Averages of b-hadron, c-hadron, and tau-lepton Properties.” ([arXiv:1010.1589](#)), Oct 2010. [arXiv:hep-ex/1010.1589](#).
- [26] A. Dedes, H. K. Dreiner, U. Nierste, and P. Richardson, “Trilepton Events and $B_s \rightarrow \mu^+ \mu^-$: No-lose for mSUGRA at the Tevatron?” (CAVENDISH-HEP-2002-07. DAMTP-2002-79. FERMILAB-Pub-2002-129-T), Jul 2002. [arXiv:hep-ph/0207026](#).
- [27] G. Aad *et al.* (ATLAS), “Search for supersymmetry using final states with one lepton, jets, and missing transverse momentum with the ATLAS detector in $\sqrt{s} = 7 \text{ TeV}$ pp collisions.” (CERN-PH-EP-2011-013), Feb 2011. Submitted to *Phys. Rev. Lett.*, [arXiv:hep-ex/1102.2357](#).
- [28] G. Aad *et al.* (ATLAS), “Search for squarks and gluinos using final states with jets and missing transverse momentum with the ATLAS detector in $\sqrt{s} = 7 \text{ TeV}$ proton-proton collisions.”, Feb 2011. [arXiv:hep-ex/1102.5290](#).
- [29] The ATLAS Collaboration, “Combined exclusion reach of searches for squarks and gluinos using final states with jets, missing transverse momentum, and zero or one lepton, with the ATLAS detector in $\sqrt{s} = 7 \text{ TeV}$ proton-proton collisions.” (ATLAS-CONF-2011-064), Apr 2011.
- [30] W. Beenakker, R. Hoepker, and M. Spira, “PROSPINO: A Program for the Production of Supersymmetric Particles in Next-to-leading Order QCD.”, Nov 1996. [hep-ph/9611232](#).

-
- [31] W. Beenakker, R. Hopker, M. Spira, and P. M. Zerwas, “Squark and gluino production at hadron colliders.” *Nucl. Phys.*, vol. B492, pp. 51–103, 1997. [hep-ph/9610490](#).
 - [32] W. Beenakker, M. Kramer, T. Plehn, M. Spira, and P. M. Zerwas, “Stop production at hadron colliders.” *Nucl. Phys.*, vol. B515, pp. 3–14, 1998. [hep-ph/9710451](#).
 - [33] W. Beenakker *et al.*, “The Production of charginos / neutralinos and sleptons at hadron colliders.” *Phys. Rev. Lett.*, vol. 83, pp. 3780–3783, 1999. [hep-ph/9906298](#).
 - [34] M. Spira, “Higgs and SUSY particle production at hadron colliders.”, 2002. [hep-ph/0211145](#).
 - [35] T. Plehn, “Measuring the MSSM Lagrangean.” *Czech. J. Phys.*, vol. 55, pp. B213–B220, 2005. [hep-ph/0410063](#).
 - [36] H. W. Baer, F. E. Paige, S. D. Protopopescu, and X. Tata, “ISAJET 7.69: A Monte Carlo Event Generator for pp, $p\bar{p}$, and e^+e^- Reactions.”, Dec 2003. [arXiv:hep-ph/0312045](#).
 - [37] P. Bechtle, K. Desch, and P. Wienemann, “Fittino, a program for determining MSSM parameters from collider observables using an iterative method.”, Dec 2004. [hep-ph/0412012](#).
 - [38] R. Lafaye, T. Plehn, and D. Zerwas, “SFITTER: SUSY Parameter Analysis at LHC and LC.” (CERN-TH-2003-313), 2003. [hep-ph/0404282](#).
 - [39] B. Gjelsten. ”Mass determination of supersymmetric particles in ATLAS”. Ph.D. thesis, University of Oslo, 2005.
 - [40] G. Aad *et al.* (ATLAS), “Expected performance of the ATLAS experiment: detector, trigger and physics.”, 2009.
 - [41] URL <http://www.fnal.gov/>.
 - [42] URL <http://www-bd.fnal.gov/>.
 - [43] T. S. Pettersson and P. Lefèvre, “The Large Hadron Collider: conceptual design.” (CERN-AC-95-05 LHC), Oct 1995.
 - [44] O. S. Brüning, *et al.*, “The LHC design report.” (CERN-2004-003). URL <http://lhc.web.cern.ch/lhc/LHC-DesignReport.html>.
 - [45] G. Aad *et al.* (ATLAS), “The ATLAS Experiment at the CERN Large Hadron Collider.” *JINST*, vol. 3, p. S08003, 2008.
 - [46] S. Chatrchyan *et al.* (CMS), “The CMS Experiment at the CERN LHC.” *JINST*, vol. 3, p. S08004, 2008.
 - [47] K. Aamodt *et al.* (ALICE), “The ALICE Experiment at the CERN LHC.” *JINST*, vol. 3, p. S08002, 2008.
 - [48] A. A. Alves *et al.* (LHCb), “The LHCb Experiment at the LHC.” *JINST*, vol. 3, p. S08005, 2008.
 - [49] C. Lefevre, “The accelerator complex at CERN.”, 2009. URL <http://www.sciencelearn.org.nz/layout/set/lightbox/Contexts/Just-Elemental/Sci-Media/Images/Accelerator-complex-at-CERN>.
 - [50] S. Catani *et al.*, “QCD; rev. version.” (CERN-TH-2000-131), p. 115 p, May 2000. [arXiv:hep-ph/0005025](#).

- [51] “ATLAS Data Summary.” URL <https://atlas.web.cern.ch/Atlas/GROUPS/DATAPREPARATION/DataSummary/2010/records.html>.
- [52] E. Métral, “LHC beam parameters: pushing the envelope?”, 2010. Proceedings of 2010 Evian II Workshop on LHC Beam Operation, 7-9th December 2010.
- [53] F. Gianotti, Feb 2011. Talk in ATLAS weekly meeting.
- [54] D. Stump, *et al.*, “Inclusive Jet Production, Parton Distributions, and the Search for New Physics.” *J. High Energy Phys.*, vol. 10 (MSU-HEP-2003-03-03), p. 046. 50 p, Mar 2003. [arXiv:hep-ph/0303013](#).
- [55] The ATLAS Collaboration, “Measurement of the Muon Charge Asymmetry from W Bosons Produced in pp Collisions at $\sqrt{s} = 7$ TeV with the ATLAS detector.” (CERN-PH-EP-2011-036), Mar 2011. [arXiv:hep-ex/1103.2929](#).
- [56] The CMS Collaboration, “Measurement of the lepton charge asymmetry in inclusive W production in pp collisions at $\sqrt{s} = 7$ TeV.”, Mar 2011.
- [57] A. De Roeck and R. S. Thorne, “Structure Functions.”, Mar 2011. [arXiv:hep-ph/1103.0555](#).
- [58] M. L. Mangano and T. J. Stelzer, “Tools for the simulation of hard hadronic collisions.” *Annu. Rev. Nucl. Part. Sci.*, vol. 55 (CERN-PH-TH-2005-074), pp. 555–588, 2005.
- [59] V. Jain and V. Kostyukhin, “A measurement of the material in the ATLAS Inner Detector using secondary hadronic interactions in 7 TeV collisions.” (ATL-COM-PHYS-2011-243), Mar 2011.
- [60] M. Agustoni, *et al.*, “Electromagnetic energy scale in-situ calibration and performance: Supporting document for the egamma performance paper.” (ATL-COM-PHYS-2011-263), Mar 2011.
- [61] S. Aefsky and C. Amelung, “MDT and CSC Alignment Studies using Track Segments.” (ATL-COM-MUON-2011-005), Mar 2011.
- [62] G. Aad *et al.* (ATLAS), “The ATLAS Simulation Infrastructure.” *Eur. Phys. J. C*, vol. 70 (CERN-PH-EP-2010-044), pp. 823–874. 53 p, May 2010. [arXiv:physics.ins-det/1005.4568](#).
- [63] The ATLAS Collaboration, “ATLAS computing: Technical Design Report.” (ATLAS-TDR-017 ; CERN-LHCC-2005-022), 2005.
- [64] A. Buckley, *et al.*, “General-purpose event generators for LHC physics.” (CAVENDISH-HEP-10-21. CERN-PH-TH-2010-298. DCPT-10-202. HD-THEP-10-24. IPPP-10-101. KATP-40-2010. LU TP 10-28. MAN-HEP-2010-23. MCNET-11-01. SLAC-PUB-14333), Jan 2011. Submitted to Physics Reports, [arXiv:hep-ph/1101.2599](#).
- [65] L. Lonnblad, *et al.*, “Les Houches Guidebook to Monte Carlo Generators for Hadron Collider Physics.”, 2004. [arXiv:hep-ph/0403045.v2](#).
- [66] E. Boos, *et al.*, “Generic User Process Interface for Event Generators.”, Sep 2001. [arXiv:hep-ph/0109068](#).
- [67] P. Z. Skands, *et al.*, “SUSY Les Houches Accord: Interfacing SUSY Spectrum Calculators, Decay Packages, and Event Generators.” *J. High Energy Phys.*, vol. 07 (CERN-TH-2003-204. LU-TP-2003-39. SHEP-2003-24. ZU-TH-2003-15), p. 036. 29 p, Nov 2003. [arXiv:hep-ph/0311123](#).

-
- [68] S. Jadach, J. H. Kühn, and Z. Was, “TAUOLA: a library of Monte Carlo programs to simulate decays of polarized τ leptons.” *Comput. Phys. Commun.*, vol. 64 (CERN-TH-5856-90), pp. 275–299. 38 p, Sep 1990.
- [69] Z. Was, “TAUOLA for simulation of tau decay and production: perspectives for precision low energy and LHC applications.” (IFJPAN-IV-2011-1), Jan 2011. [arXiv:hep-ph/1101.1652](#).
- [70] T. Sjostrand, S. Mrenna, and P. Z. Skands, “PYTHIA 6.4 Physics and Manual.” *J. High Energy Phys.*, vol. 05 (FERMILAB-Pub-2006-052-CD-T. LU-TP-2006-13), p. 026. 570 p, Mar 2006. [arXiv:hep-ph/0603175](#).
- [71] G. Corcella, *et al.*, “HERWIG 6: an event generator for Hadron Emission Reactions With Interfering Gluons (including supersymmetric processes).” *J. High Energy Phys.*, vol. 01 (CAVENDISH-HEP-99-03. CERN-TH-2000-284. RAL-TR-2000-048), p. 010. 93 p, Nov 2000. [arXiv:hep-ph/0011363](#).
- [72] G. Corcella, *et al.*, “Herwig 6.5 release note.” (CAVENDISH-HEP-2002-17. CERN-TH-2002-270. DAMTP-2002-124. IPPP-2002-58), Oct 2002. [arXiv:hep-ph/0210213](#).
- [73] S. Moretti, K. Odagiri, P. Richardson, M. H. Seymour, and B. R. Webber, “Implementation of supersymmetric processes in the HERWIG event generator.” *J. High Energy Phys.*, vol. 04 (CAVENDISH-HEP-2002-03. CERN-TH-2001-177. DAMTP-2002-34. DCPT-2001-102), p. 028. 33 p, Apr 2002. [arXiv:hep-ph/0204123](#).
- [74] J. Butterworth, J. R. Forshaw, and M. H. Seymour, “Multiparton interactions in photo-production at HERA.” *Z. Phys. C*, vol. 72 (CERN-TH-95-82. MC-TH-96-05. UCL-HEP-96-02), pp. 637–646. 22 p, Jan 1996. [hep-ph/9601371](#).
- [75] M. L. Mangano, M. Moretti, F. Piccinini, R. Pittau, and A. Polosa, “ALPGEN, a generator for hard multiparton processes in hadronic collisions.” *J. High Energy Phys.*, vol. 07 (CERN-TH-2002-129), p. 001. 35 p, Jun 2002. [arXiv:hep-ph/0206293](#).
- [76] S. Frixione and B. R. Webber, “Matching NLO QCD computations and parton shower simulations.” *J. High Energy Phys.*, vol. 06 (CAVENDISH-HEP-2002-01. GEF-TH-2002-02. LAPP-TH-905), p. 029. 69 p, Apr 2002. [arXiv:hep-ph/0204244](#).
- [77] S. Frixione, P. Nason, and B. R. Webber, “Matching NLO QCD and parton showers in heavy flavour production.” *J. High Energy Phys.*, vol. 08 (BICOCCA-FT-2003-11. CAVENDISH-HEP-2003-03. CERN-TH-2003-102), p. 007. 70 p, May 2003. [arXiv:hep-ph/0305252](#).
- [78] K. Assamagan *et al.*, “The ATLAS Monte Carlo Project.” (ATL-COM-SOFT-2008-024), Dec 2008. To be submitted to JINST.
- [79] S. Agostinelli *et al.* (GEANT4 Collaboration), “GEANT4: A Simulation toolkit.” *Nucl. Instrum. Methods Phys. Res., A*, vol. 506 (CERN-IT-2002-003. SLAC-PUB-9350. 3), pp. 250–303. 86 p, Jul 2002.
- [80] E. Richter-Was, D. Froidevaux, and L. Poggioli, “ATLFAST 2.0 a fast simulation package for ATLAS.” (ATL-PHYS-98-131), Nov 1998.
- [81] D. Cavalli, *et al.*, “Performance of the ATLAS fast simulation ATLFAST.” (ATL-PHYS-INT-2007-005. ATL-COM-PHYS-2007-012), Jan 2007.
- [82] E. Barberio, *et al.*, “Fast shower simulation in the ATLAS calorimeter.” *J. Phys.: Conf. Ser.*, vol. 119, p. 032008, 2008.

- [83] K. Edmonds, *et al.*, “The Fast ATLAS Track Simulation (FATRAS).” (ATL-SOFT-PUB-2008-001. ATL-COM-SOFT-2008-002), Mar 2008.
- [84] W. Lampl, *et al.*, “Calorimeter clustering algorithms: Description and performance.” Tech. Rep. ATL-LARG-PUB-2008-002. ATL-COM-LARG-2008-003, CERN, Geneva, Apr 2008.
- [85] M. Cacciari, G. P. Salam, and G. Soyez, “The anti- k_t jet clustering algorithm.” *J. High Energy Phys.*, vol. 04 (LPHE-07-03), p. 063. 12 p, Feb 2008. [hep-ph/0802.1189](#).
- [86] I. Abt *et al.*, “The tracking, calorimeter and muon detectors of the H1 experiment at HERA.” *Nuclear Instruments and Methods in Physics Research Section A: Accelerators, Spectrometers, Detectors and Associated Equipment*, vol. 386 (2-3), pp. 348 – 396, 1997. ISSN 0168-9002.
- [87] The ATLAS Collaboration, “Jet energy scale and its systematic uncertainty for jets produced in proton-proton collisions at $\sqrt{s} = 7$ TeV and measured with the ATLAS detector.” (ATLAS-CONF-2010-056), Jul 2010.
- [88] E. Barberio, *et al.*, “ATLAS Calorimeter Response to Single Isolated Hadrons and Estimation of the Calorimeter Jet Scale Uncertainty.” (ATL-COM-PHYS-2011-254), Mar 2011.
- [89] The ATLAS Collaboration, “Update on the jet energy scale systematic uncertainty for jets produced in proton-proton collisions at $\sqrt{s} = 7$ TeV measured with the ATLAS detector.” (ATLAS-CONF-2011-007), Feb 2011.
- [90] G. Romeo, A. Schwartzman, R. Piegaia, T. Carli, and R. Teuscher, “Jet Energy Resolution from In-situ Techniques with the ATLAS Detector Using Proton-Proton Collisions at a Center of Mass Energy $\sqrt{s} = 7$ TeV.” (ATL-COM-PHYS-2011-240), Mar 2011.
- [91] R. Prabhu. ”Studies into tau reconstruction, missing transverse energy and photon induced processes with the ATLAS detector at the LHC.”. Ph.D. thesis, Rheinische Friedrich-Wilhelms-Universität Bonn, 2010.
- [92] C. Limbach. ”Leptonische Tau-Zerfälle in supersymmetrischen Prozessen im ATLAS-Detektor”. diploma thesis, 2009.
- [93] A. Kaczmarska, E. Richter-Was, M. Wolter, and L. Janyst, “Performance of the tau1p3p algorithm for hadronic tau decays identification with release 12.0.6.” (ATL-PHYS-INT-2008-004. ATL-COM-PHYS-2007-039), Jun 2007.
- [94] M. Heldmann and D. Cavalli, “An improved tau-Identification for the ATLAS experiment.” (ATL-PHYS-PUB-2006-008. ATL-COM-PHYS-2006-010), Dec 2005.
- [95] E. Dawe, D. O’Neil, and S. Protopopescu. “Using boosted decision trees for hadronic tau identification.” Tech. Rep. ATL-PHYS-INT-2011-004, CERN, Geneva, Jan 2011. , and references therein.
- [96] A. Kalinowski and K. Benslama, “Tau identification with the logarithmic likelihood method.” (ATL-PHYS-INT-2008-037. ATL-COM-PHYS-2008-125), Sep 2008.
- [97] A. Christov, “Electron-tau Separation for the Calorimeter Based tauRec Algorithm for the ATLAS Experiment.” (ATL-COM-PHYS-2009-045), Feb 2009.
- [98] A. Christov, *et al.*, “Performance of the tau reconstruction and identification algorithm with release 14.2.20 and mc08 data.” (ATL-COM-PHYS-2009-229), Apr 2009.
- [99] The ATLAS Collaboration, “Tau Reconstruction and Identification Performance in ATLAS.” (ATLAS-CONF-2010-086), Oct 2010.

-
- [100] G. Aad and other, “Measurement of the $W \rightarrow l\nu$ and $Z/\gamma^* \rightarrow ll$ production cross sections in proton-proton collisions at $\sqrt{s} = 7$ TeV with the ATLAS detector.” (CERN-PH-EP-2010-037), Oct 2010. [hep-ex/1010.2130](#).
 - [101] The ATLAS Collaboration, “Performance of the missing transverse energy reconstruction in proton-proton collisions at center-of-mass energy of $\sqrt{s} = 7$ TeV with the ATLAS detector.” (ATLAS-CONF-2010-039), Jul 2010.
 - [102] The ATLAS Collaboration, “Performance of the Missing Transverse Energy Reconstruction and Calibration in Proton-Proton Collisions at a Center-of-Mass Energy of 7 TeV with the ATLAS Detector.” (ATLAS-CONF-2010-057), Jul 2010.
 - [103] B. K. Gjelsten, D. J. Miller, and P. Osland, “Measurement of SUSY Masses via Cascade Decays for SPS 1a.” (ATL-PHYS-2004-029. ATL-COM-PHYS-2004-044. CERN-ATL-COM-PHYS-2004-044), 2004. [arXiv:hep-ph/0410303](#).
 - [104] C. Zendler. ”Studie zu supersymmetrischen Prozessen mit Taus im Endzustand im ATLAS-Experiment am LHC”. diploma thesis, 2007.
 - [105] T. Nattermann, K. Desch, P. Wienemann, and C. Zendler, “Measuring τ -polarisation in $\tilde{\chi}_2^0$ decays at the lh.” *Journal of High Energy Physics*, vol. 2009 (04), p. 057, 2009.
 - [106] T. Nattermann. ”Studie zu Effekten der Tau-Polarisation in Neutralino2-Zerfällen mit dem ATLAS-Experiment”. diploma thesis, 2008.
 - [107] K. Desch, T. Nattermann, P. Wienemann, and C. Zendler, “Measuring the endpoint of the di-tau mass spectrum in Neutralino2 decays with the ATLAS detector at the LHC.” (ATL-PHYS-INT-2008-008. ATL-COM-PHYS-2008-038), Mar 2008.
 - [108] W. Ehrenfeld, J. Haller, and D. Ludwig, “Expected performance of the ATLAS detector in GMSB models with tau final states.” (ATL-PHYS-PUB-2009-089. ATL-COM-PHYS-2009-570), Nov 2009.
 - [109] F. James and M. Roos, “MINUIT - a system for function minimization and analysis of the parameter errors and correlations.” *Comput. Phys. Commun.*, vol. 10 (6), pp. 343–67, 1975.
 - [110] K. Assamagan *et al.*, “The ATLAS Monte Carlo Project.” (ATL-SOFT-INT-2010-002. ATL-COM-SOFT-2008-024), Feb 2010.
 - [111] J. Linnemann. “Measures of significance in HEP and astrophysics.”, 2003. [arXiv:physics.data-an/0410303](#).
 - [112] G. Cowan, K. Cranmer, E. Gross, and O. Vitells, “Using the Profile Likelihood in Searches for New Physics.”, Jul 2010. [physics.data-an/1007.1727](#).
 - [113] P. Pirinen, “Statistical power sum analysis for nonidentically distributed correlated log-normal signals.” *The 2003 Finnish Signal Processing Symposium (FINSIG), Tampere, Finland, May 19, 2003, pp. 254-258*, pp. 254 –258, 2003.
 - [114] R. Barlow, “Extended maximum likelihood.” *Nuclear Instruments and Methods in Physics Research Section A: Accelerators, Spectrometers, Detectors and Associated Equipment*, vol. 297 (3), pp. 496 – 506, 1990. ISSN 0168-9002.
 - [115] G. Aad *et al.* (ATLAS), “Luminosity Determination in pp Collisions at $\sqrt{s} = 7$ TeV using the ATLAS Detector at the LHC.” (CERN-PH-EP-2010-069), Jan 2011. Submitted to *Journal EPJC*, [hep-ex/1101.2185](#).

- [116] The ATLAS Collaboration, “ATLAS Monte Carlo tunes for MC09.” (ATL-PHYS-PUB-2010-002), Mar 2010.
- [117] The ATLAS Collaboration, “Search for squarks and gluinos using final states with jets and missing transverse momentum with the ATLAS detector in $\sqrt{s} = 7$ TeV proton-proton collisions.” (ATL-PHYS-INT-2011-009), Feb 2011.
- [118] P. Bechtle, *et al.*, “Studying Tau Reconstruction and Identification Performance in Di-Jet, Three-Jet and Photon-Jet Events with the ATLAS Experiment.” (ATL-COM-PHYS-2011-194), Feb 2011.
- [119] G. Aad *et al.* (ATLAS), “Jet energy scale and its systematic uncertainty for jets produced in proton-proton collisions at $\sqrt{s} = 7$ TeV and measured with the ATLAS detector.” (ATLAS-CONF-2010-056), Jul 2010.
- [120] G. Aad *et al.* (ATLAS), “Jet energy resolution and selection efficiency relative to track jets from in-situ techniques with the ATLAS Detector Using Proton-Proton Collisions at a Center of Mass Energy $\sqrt{s} = 7$ TeV.” (ATLAS-CONF-2010-054), Jul 2010.
- [121] R. Piegai, G. Romeo, and A. Schwartzman, “Measurement of the Jet Energy Resolution in ATLAS using Data-Driven Techniques.” (ATL-PHYS-INT-2010-029), Mar 2010.
- [122] E. Coniavitis, *et al.*, “Reconstruction, Energy Calibration, and Identification of Hadronic Tau Decays for Winter 2011.” (ATL-COM-PHYS-2011-217), Mar 2011.
- [123] J. Butterworth, *et al.*, “Single Boson and Diboson Production Cross Sections in pp Collisions at $\sqrt{s} = 7$ TeV.” (ATL-COM-PHYS-2010-695), Aug 2010.
- [124] N. Kidonakis, “Next-to-next-to-leading soft-gluon corrections for the top quark cross section and transverse momentum distribution.” *Phys. Rev. D*, vol. 82 (11), p. 114030, Dec 2010.
- [125] S. Frixione, P. Nason, and C. Oleari, “Matching NLO QCD computations with parton shower simulations: the POWHEG method.” *J. High Energy Phys.*, Nov 2007.
- [126] B. Abbott, *et al.*, “Background estimation for searches with missing transverse energy and b -jets Supersymmetry Sensitivity/Exclusion Limit Studies in the Missing Transverse Energy and b -Jets channel.” (ATL-PHYS-INT-2011-040), Apr 2011.
- [127] A. L. Read, “Presentation of search results: the CL_s technique.” *J. Phys. G*, vol. 28 (10), pp. 2693–704, 2002.
- [128] G. Cowan, K. Cranmer, E. Gross, and O. Vitells, “Power-Constrained Limits.” (arXiv:1105.3166), May 2011. `physics.data-an/1105.3166`.
- [129] G. Aad *et al.* (ATLAS), “Search for supersymmetry in pp collisions at $\sqrt{s} = 7$ TeV in final states with missing transverse momentum and b -jets.” (CERN-PH-EP-2011-038), Mar 2011. Submitted to *Phys. Lett. B*, `hep-ex/1103.4344`.
- [130] G. Aad *et al.* (ATLAS), “Combined exclusion reach of searches for squarks and gluinos using final states with jets, missing transverse momentum, and zero or one lepton, with the ATLAS detector in $\sqrt{s} = 7$ TeV proton-proton collisions.” (ATLAS-CONF-2011-064), Apr 2011.

Acknowledgments

This work would not have been possible without the support of many people contributing in different ways:

First of all I would like to thank my supervisor Prof. Dr. K. Desch for the opportunity to work on this topic as part of the ATLAS collaboration in this exciting scientific environment at CERN, for his guidance, advice and support.

I am no less obliged to my second supervisor Dr. Peter Wienemann, whom I would like to thank for invaluable ideas and for his fascinating gift to completely engage in discussion despite his heavy work load.

I warmly thank Robindra Prabhu for scientific as well as personal advice, for being a patient motivator and a constructive critic.

I thank Xavier Portell Bueso and Michael Mazur for coordinating the effort of ATLAS SUSY searches with tau leptons. I am grateful to them and everybody contributing in that sub-group for helpful comments and fruitful discussions.

I am greatly indebted to all who took care of computer resources I used during the last four years, especially the NAF support as well as Gizo Nanava and the *hep-admins* of Bonn.

I also give my thanks to all colleagues in the Bonn Desch and the Bonn ATLAS groups, especially those of *Salon Bleue*, who created a friendly working environment and whom it has been a pleasure to work with. The work of Till and Christian was helpfully intertwined at some point with the analyses presented herein, and also Robert shared the common frustration associated with Supersymmetry analyses. Mathias provided insight into the matters of fake taus, but supported this thesis also in his capacity of first coffee machine responsible, an important task carried on by Steffen. Fond memories remain of Nina Herder, whose happy nature could cheer up the entire office and draw laughter even from Mr. Sarcasm.

Special thanks to Duc and Zong, who helped with technical and physics problems but also with their friendship, making the last few years all the more worthwhile.

Also deeply appreciated is the helpful escapism provided by my DSA friends.

Zuletzt möchte ich meiner Familie danken, insbesondere meinen Eltern, ohne deren Unterstützung weder das Studium noch diese Arbeit möglich gewesen wäre.